

Alma Mater Studiorum – Università di Bologna

DOTTORATO DI RICERCA IN

CHIMICA

Ciclo XXIX

**Settore Concorsuale di afferenza: 03/A1**

**Settore Scientifico disciplinare: CHIM/01**

**SYNTHESIS AND CHARACTERIZATION OF  
METAL-HEXACYANOMETALLATES AS  
INNOVATIVE MATERIALS FOR ANALYTICAL AND  
TECHNOLOGICAL APPLICATIONS**

**Presentata da: Dott.ssa Michela Ciabocco**

**Coordinatore Dottorato**

**Relatore**

**Prof. Aldo Roda**

**Prof. Mario Berrettoni**

**Esame finale anno 2017**

*Dedicated to my parents,  
Luigino and Rosella*

## **Candidate presentation**

During the three years of her PhD, Michela Ciabocco focused her research project on the synthesis and physicochemical characterization of new inorganic compounds based on metal-hexacyanometallates modified with semiconductors, such as TiO<sub>2</sub>.

The research carried out during the first and the second year both in the Laboratory at Bologna University (Rimini Campus) and at Miami University in Ohio, USA, under the supervision of Prof. James A. Cox, was aimed to the synthesis of metal-hexacyanometallates and to the development of silica-based films with controlled nanoarrays of cylindrical channels, in order to obtain metal-hexacyanometallates nanoparticles for electrocatalytical applications. In particular, electrocatalytic oxidation of cysteine was studied on cobalt hexacyanoferrate nanoparticles obtaining very interesting results.

Metal-hexacyanometallates and in particular indium and nickel hexacyanoferrate, have been also tested as ionic sieves, thanks to their zeolite-like interstitial sites able to easily accommodate countercations. Hence, the capability to recover selectively rare-earth elements is examined and the proposed system can selectively separate and recover erbium in presence of a different rare-earth cations mixture.

Subsequently, during the third year, the synthesis and characterization of TiO<sub>2</sub>-metal hexacyanometallates composite materials was studied in collaboration with the University of Montpellier. Properties and structures of these composite materials have been investigated by using a multi-technique approach: IR, UV-Vis, TEM, SEM, XAS, XPS, XFR and Mössbauer spectroscopy were performed. TiO<sub>2</sub> modifications with metal hexacyanometallates let us to extend the spectral response of TiO<sub>2</sub> into the visible obtaining a desirable reduction of the TiO<sub>2</sub> band gap region and considerably improving photocatalytic activity.

During the PhD, practical use of these materials was envisaged in different fields ranging from cultural-heritage protection, antibacterial, self-cleaning surfaces to electrochromic devices and photovoltaic cells, obtaining excellent results.

During the PhD, the candidate attended the School of Physical Chemistry (2015), several scientific seminars and she took part actively in four national congresses also with oral presentation. Furthermore the research activity carried out in these years is documented by seven scientific articles published in important peer-reviewed international journals. In addition, four manuscripts are in preparation and will be soon submitted.

She was also author of an oral communication at the XXVI National Congress of Analytical Chemistry.

The candidate has developed a solid understanding of the issues involved, acquiring a complete mastery of the experimental techniques, demonstrating good skills of organization and good ability to relate with external collaborators. In fact she collaborates fruitfully with other research groups in several Italian Universities, including the University of Palermo, Cagliari and Camerino and she was involved in international collaborations including the University of Montpellier (France) and Miami University, OH (USA). As a part of this collaboration, she was able to present the data during frequent meeting and write appropriate analytical reports. She also acquired excellent abilities of manuscript writing and organization of results.

She has been the co-supervisor of nine 1st level degrees thesis in “Chemistry and Technologies for Environment and Wastes” and three 2nd level degrees thesis in “Sciences and Technologies of the Industrial Chemistry” proving a great ability in coordination of the activities of the students.

Finally, my personal overall evaluation of her PhD is excellent.

***The Board expresses a score of excellence on the activity carried out by the candidate during the whole cycle of doctorate and considers her worthy to attain the PhD in Chemistry.***

# Index

<b>List of Tables</b>	<b>vi</b>
<b>List of Figures</b>	<b>vii</b>
<b>Abstract</b>	<b>xiv</b>
<b>1. Introduction</b>	<b>1</b>
1.1. Metal-Hexacyanometallates (MHCMs)	1
1.1.1. Structures of Metal-Hexacyanometallate	4
1.1.2. Synthesis methods: chemical and electrochemical synthesis	5
1.2. Physicochemical properties and application fields:	
analytical and technological applications	9
1.2.1. Magnetic functionalities of Prussian Blue analogs	9
1.2.2. Electrochromism	13
1.2.3. Thermochromism	15
1.2.4. Cation exchange	17
1.2.5. Ionic sensors	20
1.2.6. Electrocatalysis	20
1.2.7. Batteries	23
1.3. TiO <sub>2</sub> -Metal Hexacyanometallate composite materials	25
1.3.1. Photocatalysis and photocatalytic degradation of organic pollutants	26
References	29
<b>2. Work aims</b>	<b>32</b>

<b>3. Fabrication and application of modified electrodes with Indium Hexacyanoferrate (InHCF) as ion-exchanger</b>	<b>34</b>
3.1. Introduction	34
3.2. Experimental	35
3.2.1. Reagents and materials	35
3.2.2. Indium Hexacyanoferrate electrochemical synthesis	35
3.3. Results and Discussion	36
3.3.1. Modified electrodes with Indium Hexacyanoferrate: Electrochemical characterization	36
3.3.2. Indium Hexacyanoferrate reversible exchange capability	41
3.3.3. Electrochromic cell with Indium Hexacyanoferrate and Cobalt Hexacyanoferrate	43
3.4. Conclusion	44
References	44
<b>4. Electrochemical process to selectively recover rare earth-elements by using Nickel Hexacyanoferrate (NiHCF) modified electrodes as ionic sieve</b>	<b>46</b>
4.1. Introduction	46
4.2. Experimental	48
4.2.1. Reagents and materials	48
4.2.2. Nickel Hexacyanoferrate electrochemical synthesis	48
4.3. Results and Discussion	48
4.3.1. Modified electrodes with Nickel Hexacyanoferrate: electrochemical characterization	48
4.3.2. Ion-exchanging and selective recover of rare-earth elements with a Nickel Hexacyanoferrate modified electrode	53
4.4. Conclusion	56
References	57

<b>5. Electrochemically assisted deposition of an ormosil film to obtain Cobalt Hexacyanoferrate (CoHCF) nanorod array and application to electroanalysis</b>	<b>58</b>
5.1. Introduction	58
5.1.1. Sol-gel chemistry and processing	61
5.1.2. Hydrolysis and condensation	61
5.1.3. Gelation	62
5.1.4. Aging	62
5.1.5. Drying	62
5.1.6. Electrochemically assisted deposition of sol-gel films	63
5.2. Experimental	63
5.2.1. Reagents and materials	63
5.2.2. Fabrication of microporous silica sol-gel film and immobilization of nanobeads	64
5.2.3. Preparation of the ITO or GC npSG CoHCF electrode	65
5.3. Results and discussion	65
5.3.1. Characterization of the ormosil film with 20 nm channels	65
5.3.2. Film geometry	68
5.3.3. Influence of channel structure and distribution on voltammetry	69
5.3.4. Synthesis and characterization of the CoHCF nanoarray	72
5.3.5. Electrocatalytic oxidation of cysteine	78
5.4. Conclusion	81
References	83
<b>6. Physicochemical characterization of Anatase TiO<sub>2</sub>-Metal Hexcyanometallate (MHCMs) composite materials</b>	<b>85</b>
6.1. Introduction	85
6.1.1. Anatase TiO <sub>2</sub> -MHCMs composite materials	85
6.1.2. Anatase-driven charge transfer involving a spin transition in cobalt iron cyanides nanostructures	87

<b>6.2. Experimental</b>	<b>89</b>
<b>6.2.1. Reagents and materials</b>	<b>89</b>
<b>6.2.2. TiO<sub>2</sub>-Iron Hexacyanocobaltate (FeHCC) electrochemical synthesis</b>	<b>89</b>
<b>6.2.3. Chemical synthesis and deposition strategy</b>	<b>90</b>
<b>6.2.4. Chemical and electrochemical characterization of TiO<sub>2</sub>-MHCMS composite materials</b>	<b>90</b>
<b>6.3. Results and discussion</b>	<b>93</b>
<b>6.3.1. Novel Anatase TiO<sub>2</sub>-MHCMS electrochemical synthesis: TiO<sub>2</sub> as electronic and structural mediator</b>	<b>93</b>
<b>6.3.2. Chemical and electrochemical characterization of Anatase TiO<sub>2</sub>-MHCMS composite materials</b>	<b>99</b>
<b>6.3.3. Experimental evidence of the formation of composites</b>	<b>112</b>
<b>6.3.4. Reaction mechanism</b>	<b>113</b>
<b>6.3.5. Electron transfer and spin transition in MHCMS driven by Anatase TiO<sub>2</sub>: electronic and structural order effect</b>	<b>115</b>
<b>6.3.6. Photocatalytic degradation of methylene blue with Anatase TiO<sub>2</sub>-MHCMS composite materials</b>	<b>125</b>
<b>6.4. Conclusion</b>	<b>126</b>
References	128
<b>7. Conclusions and future prospects</b>	<b>130</b>
<b>APPENDIX A</b>	
<b>Synthesis of Iron Hexacyanocobaltate (FeHCC) particles and antibacterial efficiency investigation</b>	<b>131</b>
<b>1. Introduction</b>	<b>131</b>
<b>2. Experimental</b>	<b>133</b>
<b>2.1. Reagents and materials</b>	<b>133</b>
<b>2.2. Instrumentation</b>	<b>133</b>
<b>2.3. Determination of the antibacterial activity</b>	<b>134</b>
<b>2.4. Dual staining for assessment of loss of membrane integrity</b>	<b>135</b>
<b>2.5. Intracellular reactive oxygen species (ROS) measurement</b>	<b>135</b>

<b>3. Results and Discussion</b>	<b>135</b>
<b>3.1. Chemical characterization of FeHCC</b>	<b>135</b>
<b>3.2. Antibacterial activity of FeHCC against E. Coli in anaerobiosis</b>	<b>137</b>
<b>3.3. Antibacterial activity of FeHCC against E. Coli in aerobiosis</b>	<b>139</b>
<b>3.4 Antibacterial activity of FeHCC against Gram positive         and Gram negative bacteria in a rich medium</b>	<b>143</b>
<b>4. Conclusion</b>	<b>145</b>
References	146

## List of Tables

<b>Table 1</b>	Electrochromic property exhibited by Metal-Hexacyanoferrate compounds.	15
<b>Table 2</b>	Substrates to which Metal-Hexacyanoferrates show electrocatalytic property.	22
<b>Table 3</b>	$x$ best fit values in according with redox equation 3.	40
<b>Table 4</b>	Summary of the compounds studied.	100
<b>Table 5</b>	Stoichiometry of the studied compounds, obtained by XPS and XRF techniques.	100
<b>Table 6</b>	CN stretching frequencies in CoHCF and TiO <sub>2</sub> -CoHCF from curve-fitting.	102
<b>Table 7</b>	CN stretching related to different chemical features of FeHCC. $\bar{\nu}$ 1, $\bar{\nu}$ 2 and $\bar{\nu}$ 3 indicate the observed bands. Peak areas in percentage are also provided.	103
<b>Table 8</b>	Ti2p binding energy value for hexacyanometallate-TiO <sub>2</sub> composites.	106
<b>Table 9</b>	Comparison of the valence band edge binding energy of CoHCF and TiO <sub>2</sub> -CoHCF compounds at different ratios.	107
<b>Table 10</b>	Comparison of the valence band edge binding energy of FeHCC and TiO <sub>2</sub> -FeHCC compounds at different ratios.	107
<b>Table 11</b>	$E_{pc}$ and $E_{pa}$ (in Volts) for the 1:1, 10:1 and 100:1 TiO <sub>2</sub> -FeHCC compounds and the relative $E^0$ value.	111
<b>Table 12</b>	$E_{pc}$ and $E_{pa}$ (in Volts) for the 1:1, 10:1 and 100:1 TiO <sub>2</sub> -CoHCF compounds and the relative $E^0$ value.	112
<b>Table 13</b>	Selected structural parameters from EXAFS fitting results of Cobalt Hexacyanoferrate samples and Iron Hexacyanocobaltate samples.	118
<b>Table 14</b>	<sup>57</sup> Fe Mössbauer hyperfine parameters at room temperature of the measured samples.	125

## List of Figures

<b>Figure 1</b>	Cyclic voltammetry of a Glassy Carbon electrode modified with Prussian Blue using KCl 0,1 M as supporting electrolyte, scan rate: 40 mV s <sup>-1</sup> , reference electrode: Ag/ AgCl.	2
<b>Figure 2</b>	Spectra of Iron Hexacyanoferrate films on ITO-coated glass at various potentials.	3
<b>Figure 3</b>	The cubic unit cell of Metal-Hexacyanoferrate in its “soluble” form.	4
<b>Figure 4</b>	Schematic crystal structures of the cubic unit cell of Metal-Hexacyanoferrate in its “insoluble” form.	5
<b>Figure 5</b>	“In-drop” synthesis of Prussian Blue.	7
<b>Figure 6</b>	Magnetic functionalities present in Prussian blue analogs.	11
<b>Figure 7</b>	Schematic illustration of (a) the coordination geometry on Co <sup>II</sup> between six-coordinate (6-Co <sup>II</sup> ) and four-coordinate (4-Co <sup>II</sup> ) under conditions of high and low humidity and (b) the humidity-induced change in the magnetic properties.	12
<b>Figure 8</b>	Schematic illustration of a plausible pathway for a proton to travel through the hydrogen bonds of ligand water and zeolitic water molecules in the Prussian blue analog structure of M <sup>II</sup> A[M <sup>III</sup> B(CN) <sub>6</sub> ] <sub>2/3</sub> ×zH <sub>2</sub> O.	13
<b>Figure 9</b>	Schematic of the layer structure of an electrochromic window. The construction is similar to a battery. The condition shown is coloration in a cathodic material, such as tungsten oxide.	14
<b>Figure 10</b>	Schematic summary of various compounds and their redox relationships in the CoHCF system.	16
<b>Figure 11</b>	Schematic removal of cesium-137 by EIX technique.	18
<b>Figure 12</b>	Schematic depiction of alkali ion insertion mechanism in the cubic Prussian Blue analogue structure.	23
<b>Figure 13</b>	Schematic picture of the TiO <sub>2</sub> photocatalytic reaction process.	27
<b>Figure 14</b>	Continuous CV at 0.1 V s <sup>-1</sup> in a KCl/HCl solution at nominal pH ≈ 2 for the electrodeposition of a InHCF film on a GC electrode.	36

<b>Figure 15</b>	CV of an InHCF film at 0.1 V s <sup>-1</sup> in 1.0 M KCl solution.	37
<b>Figure 16</b>	CVs of InHCF films recorded at different KCl concentrations (1.0, 1.0×10 <sup>-1</sup> and 1.0×10 <sup>-2</sup> M) a) without (at native pH) and b) with 1.0×10 <sup>-2</sup> M HCl (pH = 2). The insets show the cathodic peak potentials as a function of log[K <sup>+</sup> ] which yield slopes of 56 mV/dec and 54 mV/dec for Fig. 3a and 3b.	38
<b>Figure 17</b>	CVs of InHCF films in KCl solutions (1.0, 1.0×10 <sup>-1</sup> and 1.0×10 <sup>-2</sup> M) at different nominal pH: a) pH=4.0, b) pH=0.0. The slopes of the cathodic peak potential vs log[K <sup>+</sup> ] are 72 and 80 mV/dec for figure a and b, respectively.	38
<b>Figure 18</b>	CVs of InHCF films recorded in 1.0 M (a), 1.0×10 <sup>-1</sup> M (b) and 1.0×10 <sup>-2</sup> M (c) KCl solutions at different nominal pH values (4.0-3.5-3.0-2.5-2.0-1.5-1.0-0.5-0.0).	39
<b>Figure 19</b>	CVs of InHCF films recorded in 1.0 M KCl (dashed line) and subsequently in 1.0 M HCl (solid line).	40
<b>Figure 20</b>	CVs of InHCF films in 1.0 M RbCl, ZnCl <sub>2</sub> and CsCl solutions a) and in 1.0 M LiCl, NaCl, MgCl <sub>2</sub> , NH <sub>4</sub> Cl, CaCl <sub>2</sub> , KCl, BaCl <sub>2</sub> , SrCl <sub>2</sub> and CdCl <sub>2</sub> solutions b).	41
<b>Figure 21</b>	CVs at 0.1 V s <sup>-1</sup> of an InHCF film in a) 1.0 M KCl and BaCl <sub>2</sub> solutions at native pHs, b) 1.0 M KCl and BaCl <sub>2</sub> solutions at nominal pH = 2.0 , c) in 1.0, 1.0×10 <sup>-1</sup> and 1.0×10 <sup>-2</sup> M BaCl <sub>2</sub> solutions. Insets d) and e) show an E <sub>pa</sub> (V) vs log[Ba <sup>2+</sup> ], slope of 7 mV/dec, and an E <sub>pc</sub> (V) vs log[Ba <sup>2+</sup> ], slope of 32 mV/dec.	42
<b>Figure 22</b>	The first fifty CVs of the CoHCF electrode in the cell with a InHCF electrode and 1.0 M KCl absorbed in filter paper.	44
<b>Figure 23</b>	CV of a NiHCF film at 0.1 V s <sup>-1</sup> in a 1.0 M KNO <sub>3</sub> solution.	48
<b>Figure 24</b>	CVs of NiHCF films in a) 1.0 M Al <sup>3+</sup> , b) Cr <sup>3+</sup> and c) In <sup>3+</sup> solutions at 0.1 V s <sup>-1</sup> .	49
<b>Figure 25</b>	CVs at 0.1 V s <sup>-1</sup> of a NiHCF film in 1.0 M KNO <sub>3</sub> and Er(NO <sub>3</sub> ) <sub>3</sub> solutions at native pH.	51
<b>Figure 26</b>	CVs at 0.1 V s <sup>-1</sup> of a NiHCF film in 1.0 M KNO <sub>3</sub> , RE(NO <sub>3</sub> ) <sub>3</sub> (RE=La, Dy, Gd, Er) solutions and in mixture containing rare-earth cations at native pH.	53
<b>Figure 27</b>	CVs of NiHCF film recorded in 1.0 M Cr(NO <sub>3</sub> ) <sub>3</sub> solution at 0.2 V s <sup>-1</sup> and 0.001 V s <sup>-1</sup> .	55

<b>Figure 28</b>	Sol-gel formation from the precursor solution through diffusion, aggregation and gelation process.	61
<b>Figure 29</b>	SEM image of an ITO electrode modified with APTES and 20-nm PSS. Conditions are in Experimental Section with (a) 0.5 mmol dm <sup>-3</sup> APTES reacted with an ITO surface for 15 min prior to immersion in PSS. The ormosil was deposited at 1.5 V for 20 min. (b) same as a except that no modification of the surface with APTES was done prior to immersion in PSS. The bar represents 100 nm.	66
<b>Figure 30</b>	Cyclic voltammetry of 1.0 mmol dm <sup>-3</sup> K <sub>4</sub> Ru(CN) <sub>6</sub> at bare GC; GC ormosil (20-nm channels) that was prepared from 0.5 mmol dm <sup>-3</sup> APTES; and CG ormosil (20-nm channels) that was prepared from 15 mmol dm <sup>-3</sup> APTES. Supporting electrolyte, 1.0 mol dm <sup>-3</sup> KCl; $\nu$ , 100 mVs <sup>-1</sup> .	67
<b>Figure 31</b>	Influence of APTES concentration on pore density (effective electrode area) of GC   ormosil (20-nm pores).	67
<b>Figure 32</b>	Influence of the APTES concentration on the thickness of the ormosil deposited by an electrochemically assisted process. Shown are SEM images of cross-sections of ormosil films deposited onto GC modified by treatment in A) 0.5 mmol dm <sup>-3</sup> APTES and B) 50 mmol dm <sup>-3</sup> APTES. Index bars, 200 nm.	68
<b>Figure 33</b>	Horizontal (a) and vertical (b) TEM images of a portion of the film obtained using 0.5 mmol dm <sup>-3</sup> APTES to modify the electrode. Index bars, 50 nm.	69
<b>Figure 34</b>	Evaluation of the current-limiting process in the cyclic voltammetry of 1.0 mmol dm <sup>-3</sup> K <sub>4</sub> Ru(CN) <sub>6</sub> in 1.0 mol dm <sup>-3</sup> KCl at GC ormosil (20-nm channels).	70
<b>Figure 35</b>	Chronoamperometry of 1.0 mmol dm <sup>-3</sup> K <sub>4</sub> Ru(CN) <sub>6</sub> in 1.0 mol dm <sup>-3</sup> KCl at GC ormosil (20 nm). At $t = 0$ , the applied potential, $E_{app}$ , was 0.4 V; at $t > 0$ , $E_{app} = 0.9$ V.	71
<b>Figure 36</b>	Schematic diagram of fabrication of porous template and preparation of Cobalt Hexacyanoferrate (CoHCF) nanoparticles. (a) Fabrication of 20-nm ormosil template, (b) deposition of CoHCF nanotubes, (c) obtaining the CoHCF nanoparticles, and (d) CoHCF is served as an electrode thanks to its electrochemical characteristics.	73
<b>Figure 37</b>	SEM micrographs of CoHCF obtained in 10, 20, 50 cycles and the CV study of the CoHCF modified electrodes in 1.0 mmol dm <sup>-3</sup> KCl solution. The bar represents 100 nm.	76

<b>Figure 38</b>	Schematic representation of the CoHCF electrodeposition process and the relative filling of the channels on the modified electrode surface.	77
<b>Figure 39</b>	Plot of the logarithm of the anodic peak current $i_{pa}$ vs. the logarithm of the scan rates $\nu$ for the cyclic voltammetry of CoHCF electrodeposited in GC ormosil (20-nm pores) using 10 and 50 cycles.	78
<b>Figure 40</b>	Cyclic voltamograms of the GC (ormosil, CoHCF <sub>r</sub> ) electrode in 1.0 mmol dm <sup>-3</sup> KCl at pH 2.0 in the absence and presence of cys. $\nu = 0.1 \text{ V s}^{-1}$ .	79
<b>Figure 41</b>	Calibration curve obtained during successive increments of L-Cysteine to 1.0 mmol dm <sup>-3</sup> KCl (pH=2).	80
<b>Figure 42</b>	Continuous CV at $0.1 \text{ V s}^{-1}$ in a 1.0 mM K <sub>3</sub> Co(CN) <sub>6</sub> , 1.0 mM FeCl <sub>3</sub> and 1.0 M KCl solution for the electrodeposition of a FeHCC film on a GC electrode. The inset shows the cathodic associated charge as a function of number of cycles.	94
<b>Figure 43</b>	Continuous CV at $0.1 \text{ V s}^{-1}$ in 1.0 mM K <sub>3</sub> Co(CN) <sub>6</sub> , 1.0 mM FeCl <sub>3</sub> and 1.0 M KCl solution for the electrodeposition of a FeHCC film on a GC electrode modified with TiO <sub>2</sub> film.	94
<b>Figure 44</b>	CVs at $0.1 \text{ V s}^{-1}$ of the last cycle of the electrosynthesis for FeHCC on the bare GC and on the TiO <sub>2</sub> modified GC electrode.	95
<b>Figure 45</b>	Associated charge versus the number of the cycles (100) for the electrodeposition process.	96
<b>Figure 46</b>	CV of a FeHCC film on a bare GC electrode and of a FeHCC film on a TiO <sub>2</sub> modified GC electrode performed in a 1.0 M KCl solution.	97
<b>Figure 47</b>	CVs at $0.1 \text{ V s}^{-1}$ of FeHCC and CoHCF film in a 1.0 M KCl solution.	98
<b>Figure 48</b>	CVs of TiO <sub>2</sub> -FeHCC film recorded in 1.0 M KCl solution. The inset shows the cathodic peak potentials as a function of $\log[K^+]$ which yield a slope of 47 mV/dec ( $R^2 = 0.999$ ).	99
<b>Figure 49</b>	Typical aggregate of TiO <sub>2</sub> spherical particles covered with cubic nanocrystals of CoHCF.	101
<b>Figure 50</b>	FeHCC (red curve) and CoHCF (black curve) FT/IR spectra in the 2000-2300 cm <sup>-1</sup> range.	102

<b>Figure 51</b>	TiO <sub>2</sub> -CoHCF FT/IR and TiO <sub>2</sub> -FeHCC FT/IR spectra in different molar ratios in the in the region of CN stretching frequencies.	102
<b>Figure 52</b>	XPS survey spectra of the samples TiO <sub>2</sub> :CoHCF a) and TiO <sub>2</sub> : FeHCC b) in 1:1, 10:1 and 100:1 ratios.	104
<b>Figure 53</b>	XPS Fe2p <sub>3/2</sub> and Co2p <sub>3/2</sub> spectra of 1:1 TiO <sub>2</sub> -CoHCF and TiO <sub>2</sub> -FeHCC samples.	105
<b>Figure 54</b>	N1s signal from CoHCF and FeHCC compounds. Area % of the second component of N1s (B.E. = 399.5 eV) for all the TiO <sub>2</sub> -MHCM compounds.	106
<b>Figure 55</b>	XPS valence bands of CoHCF and FeHCC compounds and of titania (0-15 eV region).	107
<b>Figure 56</b>	XAS results of the metal sites Ti, Fe, Co. Figs (a), (c) and (e) are the normalized X-Ray Absorption Near Edge (XANES) spectra while (b), (d) and (f) are the Fourier Transforms (FTs) of the Extended X-Ray Absorption Fine Structure (EXAFS) spectra.	108
<b>Figure 57</b>	XAS results of the Iron Hexacyanocobaltate (FeHCC) sample. The normalized X-Ray Absorption Near Edge (XANES) spectra are displayed in the panels (a) and (c) respectively for the Fe and Co K-edge. Panels (b) and (d) show the experimental Fourier Transforms (FTs) of the Extended X-Ray Absorption Fine Structure (EXAFS) spectra taken at the Fe and Co K-edge, respectively.	110
<b>Figure 58</b>	CVs at 0.1 V/s of 1:1 TiO <sub>2</sub> -FeHCC and 1:1 TiO <sub>2</sub> -CoHCF 1:1 in a 1.0 M KCl solution. Potentials are referred to the saturated Ag/AgCl electrode.	111
<b>Figure 59</b>	CVs at 0.1 V/s of 1:1, 10:1, 100:1 TiO <sub>2</sub> -FeHCC a) and TiO <sub>2</sub> -CoHCF b) in a 1.0 M KCl solution. Potentials are referred to the saturated Ag/AgCl electrode.	111
<b>Figure 60</b>	Schematics of two possible mechanisms for the metal hexacyanometallate interaction with Anatase particles. The red spheres are Co or Fe bonded to N atoms; the grey atoms are Co or Fe ions bonded to C atoms.	115
<b>Figure 61</b>	Normalized XANES spectra at Fe and Co K-edge for all samples.	116
<b>Figure 62</b>	EXAFS data analysis for TiO <sub>2</sub> -CoHCF and CoHCF samples. Comparison of the experimental and theoretical k <sup>2</sup> -weighted EXAFS signals and the corresponding Fourier Transform of the k <sup>2</sup> -weighted EXAFS for compounds I and II, at Fe and Co K-edges.	117

<b>Figure 63</b>	Pre-edge data for samples recorded using a pair of Si(311) crystals, at Fe and Co K-edge.	119
<b>Figure 64</b>	Room temperature <sup>57</sup> Fe Mössbauer spectra for CoHCF and TiO <sub>2</sub> -CoHCF samples.	121
<b>Figure 65</b>	XRD pattern of TiO <sub>2</sub> -CoHCF (black line) and CoHCF (red line). Crystal system: cubic, space group: F-43m, space group number: 216, a=b=c (Å)= 10.2960. * indicates the reflection peaks assigned to anatase TiO <sub>2</sub> .	122
<b>Figure 66</b>	CV obtained by using TiO <sub>2</sub> -CoHCF as working electrode, CoHCF as counter electrode, a silver-silver chloride electrode as reference, and KCl 1.0 M as supporting electrolyte (scan rate = 1.0 mV s <sup>-1</sup> ).	123
<b>Figure 67</b>	E-t curve for the reduction and the reverse oxidation by using TiO <sub>2</sub> -CoHCF as working electrode and CoHCF as counter electrode, KCl 1.0 M as supporting electrolyte. The cell were cycled at C/10 between 0.7 and -0.7 V.	124
<b>Figure 68</b>	Room temperature <sup>57</sup> Fe Mössbauer spectra for samples CoHCF (a) and TiO <sub>2</sub> -CoHCF (b) after 20 CV cycles from 1.1 to 0.0 V with a scan rate of 1.0 mV s <sup>-1</sup> . The circles and the lines represent the experimental and fitted data, respectively.	125
<b>Figure 69</b>	CoHCF-TiO <sub>2</sub> 1:10 UV-Vis spectra in the λ range between 220 and 750 nm.	126
<b>Figure 70</b>	XRD pattern of FeHCC compound.	136
<b>Figure 71</b>	IR spectra of the FeHCC powder in the region a) from 4000 to 1000 cm <sup>-1</sup> and b) of the CN group stretching.	136
<b>Figure 72</b>	TEM images of FeHCC cubic aggregates.	137
<b>Figure 73</b>	Percentage of bacterial survival under anaerobic fermentative conditions in presence of 2, 1 and 0.5 mM of KHCF and FeHCC. Control indicates the survival of E. coli in the salt medium (no additions). Data are average from triplicate experiments. Error bars represent standard deviations of duplicate incubations. Statistical significance was determined by the unpaired Student's t-test.	138

<b>Figure 74</b>	Fluorescence micrographs of dual staining with acridine orange and ethidium bromide. Upper panels: Bacteria cells treated in aerobic and anaerobic conditions for 72 h with 10 $\mu$ M of selected compounds were stained with AO/EB and visualized under fluorescence microscope at 680X magnification. The figure is representative of images obtained from at least 3 different fields for each group and from three independent experiments. Lower panels: Histogram representing the quantification of cells with damaged membranes.	140
<b>Figure 75</b>	Quantification of ROS production in aerobiosis conditions in SM and LB medium (left side) and Fluorescence micrographs after staining with dichloro-dihydro-fluorescein diacetate, DCFH-DA, (right side).	141
<b>Figure 76</b>	TEM images of collected cells from liquid culture of <i>E. coli</i> after the incubation with FeHCC.	142
<b>Figure 77</b>	Percentage of bacterial survival under aerobic (A) and anaerobic (B) conditions in presence of 1, 10, 20, 40 and 50 mM of KHCF. - indicates the survival of <i>E. coli</i> and <i>S. aureus</i> in LB medium (no additions). Data are average from triplicate experiments. Error bars represent standard deviations of duplicate incubations. Statistical significance was determined by the unpaired Student's t-test.	144

## Abstract

This thesis focuses on the synthesis, characterization and analytical and technological applications of Prussian Blue analogues (or Metal Hexacyanometallates, MHCMs), with the generic formula  $A_xM_y[B(CN)_6]_m \cdot nH_2O$  where,  $x$ ,  $y$ , and  $m$  are stoichiometric coefficients, M and B indicate transition metals and A an alkaline metal cation. Prussian Blue (PB) open framework materials exhibit unique physicochemical characteristics, that are primarily a result of the perovskite-like face-centered cubic crystal structure and represent a class of extremely versatile compounds.

Properties and structures of these chemically and electrochemically synthesized compounds, both native and composite, are investigated by using a multi-technique approach including X-ray Powder Diffraction (XRD), X-ray fluorescence spectroscopy (XRF), X-ray Absorption Spectroscopy (XAS), X-ray photoelectron spectroscopy (XPS), Scanning Electron Microscopy (SEM), Transmission Electron Microscopy (TEM), Infrared Spectroscopy (IR), Ultraviolet–visible spectroscopy (UV-Vis) and electrochemical measurements.

Electrocatalysis of targeted reactions and structural changes upon ion uptake by these MHCF nanoparticles constitute an important topic in this thesis.

The use of Prussian blue and its analogues in devices for displays and “smart” windows, environmental remediation, chemical/biological sensing, energy conversion, and magneto-optic/opto-magnetic switching is described, giving a general overview of innovative analytical and technological applications provided by such materials.

Finally, the synthesis and characterization of novel  $TiO_2$ –Metal Hexacyanometallates composite materials is studied. The electronic properties of  $TiO_2$  were substantially modified as confirmed by UV-Vis and XP-valence band data.

Practical use of these materials can be envisaged in different areas, such as antibacterial treatments, protection of historical artifacts, self-cleaning surfaces, photovoltaic cells and photoelectrochemical degradation of organic dyes in aqueous solutions under UV irradiation.



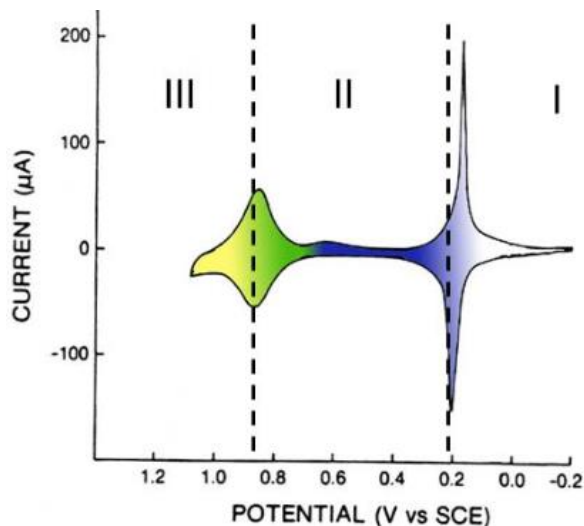
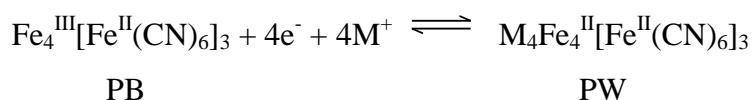


**Figure 1** Cyclic voltammetry of a Glassy Carbon (GC) electrode modified with Prussian Blue using KCl 0,1 M as supporting electrolyte, scan rate: 40 mV s<sup>-1</sup>, reference electrode: Ag/AgCl.

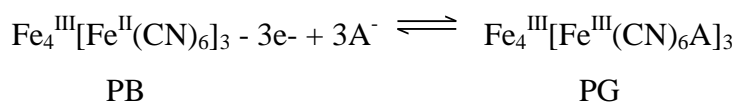
The main characteristic of PB is its ability to get oxidized and reduced in reversible way.

Three redox states can be distinguished from Fig. 1, in the potential range from 0.2 to 0.9 V (II region), the PB film exhibit a bright Prussian Blue color and it results stable.

The reduction at 0.2 V (I region) results in the discoloration of the film to give Prussian White (PW). The electron transfer upon the reduction of Prussian Blue to Prussian White is counterbalanced by the incorporation of cations (M<sup>+</sup>) into the PB film according to this equation:



When the potentials are > 0.9 V (III region), Prussian blue is oxidized to Prussian green (PG) or Berlin green. Upon the electron transfer the charge of the complex is counterbalanced by the addition of an anion (A) into the PB film, according to this equation:



The spectra of PX, PG, PB and PW are shown in Fig. 2, together with two intermediate states between blue and green.

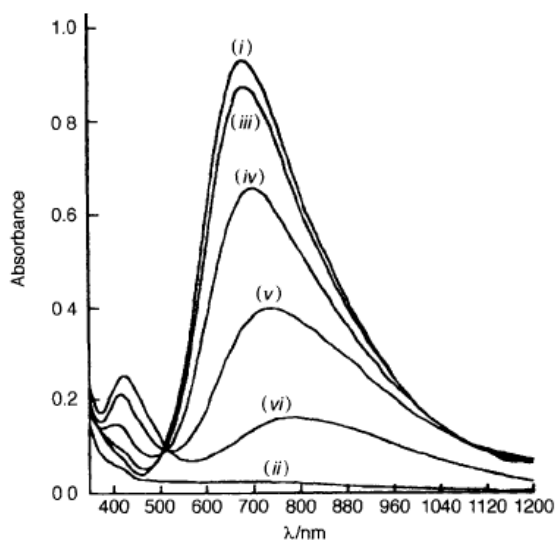


**Figure 2** Spectra of Iron Hexacyanoferrate films on ITO-coated glass at various potentials [(i) +0.50 (PB, blue), (ii) -0.20 (PW, transparent), (iii) +0.80 (PG, green), (iv) +0.85 (PG, green), (v) +0.90 (PG, green), and (vi) +1.20 V (PX, yellow) (vs. SCE)] with  $0.2 \text{ mol dm}^{-3} \text{ KCl} + 0.01 \text{ mol dm}^{-3} \text{ HCl}$  as supporting electrolyte (from *J. Chem. Soc., Dalton Trans.*, 1984, 2059)

The intense blue color in the  $\text{Fe}_4^{\text{III}}[\text{Fe}^{\text{II}}(\text{CN})_6]_3$  chromophore of PB is due to an intervalence charge-transfer (CT) absorption band centered at 690 nm.

On increase from +0.50 V to more oxidizing potentials, the original PB peak continuously shifts to longer wavelengths with diminishing absorption, while the peak at 425 nm steadily increases.<sup>4</sup>

The electrochemistry of Prussian Blue was fully investigated only some years later than 1978.<sup>4,5</sup>

Itaya et al. addressed a new versatile method for the preparation of Prussian Blue modified electrodes based on a simple electrochemical reduction of a ferric–ferricyanide solution.<sup>6</sup>

The procedure was adopted with different electrode materials (SnO<sub>2</sub>, platinum, gold, glassy carbon) and, under certain conditions, a high stability of the layer deposited through successive cycling was proved. Itaya et al.<sup>7</sup> demonstrated also the important features of Prussian Blue, in terms of analytical applications.

PB is the oldest known synthetic coordination compound, but its precise identification was complicated by three factors:

- PB is extremely insoluble but also tends to form colloids,
- Traditional synthesis tends to afford impure compositions,
- Pure PB is structurally complex.

### 1.1.1. Structures of Metal-Hexacyanometallate

The first structural investigation of Prussian Blue (PB) and its analogs dates back to 1936 when Keggin and Miles studied the X-ray pattern of iron cyanides. X-ray studies<sup>8</sup> show that Metal Hexacyanometallate-like materials form a face-centered cubic lattice nanostructure in which the high-spin metal and low-spin metal sites are both octahedral and surrounded by -NC and -CN units, with the potassium counterions and water molecules occupying the interstitial sites.

In particular Keggin and Miles found a face centered cubic (fcc) unit cell of length  $\sim 10 \text{ \AA}$ , as reported in Fig. 3:<sup>9</sup>

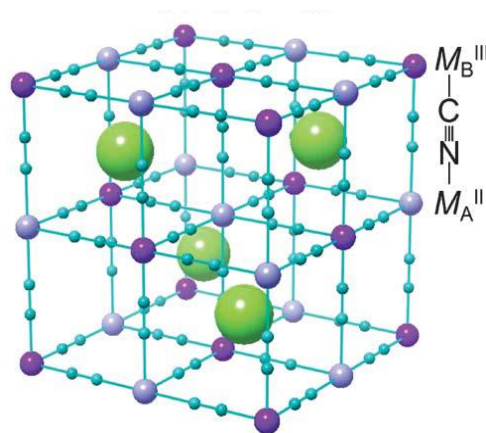


**Figure 3** The cubic unit cell of Metal-Hexacyanoferrate in its “soluble” form (1:1:1-type  $\bar{F}43m$ ).<sup>9</sup>

The structure shown in Fig. 3 represents the soluble form, in which  $M_B$  represents a transition metal in the +3 oxidation which is octahedrally coordinated to 6 carbon atoms of CN groups;  $M_A$  indicates a transition metal in +2 oxidation state which is also octahedrally coordinated to the nitrogen atoms of CN groups and alkali ion A is alternatively occupied in the interstitial sites.

The spheres which are green in color indicate monovalent cations (alkaline) intercalated into the tetrahedral cavities of the lattice to neutralize the charge of the system.

The structure previously described, defined “soluble” by Keggin and Miles,<sup>6</sup> represents only one of the two forms in which PB can be found; in fact in terms of crystallography, Prussian Blue analogs have two type of cubic crystal structures.

In the other structure, defined “insoluble” by Ludi and Güdel,<sup>10,11</sup> the coordination chemistry is the same as in Fig. 3,<sup>9</sup> where  $M_A$  and  $M_B$  represent transition metals in the +2 and +3 oxidation respectively, which are octahedrally coordinated to carbon and nitrogen atoms of CN groups respectively.<sup>12</sup>

The most significant difference is the lack of  $\frac{1}{4}$  of the groups  $[M_B(CN)_6]^{3-}$  and some of the vacancies are replaced by coordinated and non-coordinated water molecules (Fig. 4), according to Ludi and Güdel.

Ideally, the first coordinations of  $M^I$  and  $M^{II}$  are, respectively,  $\{M^I(NC)_{6-m}m(H_2O)\}$  and  $\{M^{II}(CN)_6\}$ . In the latter case, there are two types of water molecules: (i) water molecules coordinated to  $M^I$  octahedral in empty nitrogen sites and (ii) uncoordinated water molecules in interstitial positions.

Both the soluble and insoluble form shows notable physical, chemical and electrochemical properties. The magnetic and optical functionalities of these two structures are very different.

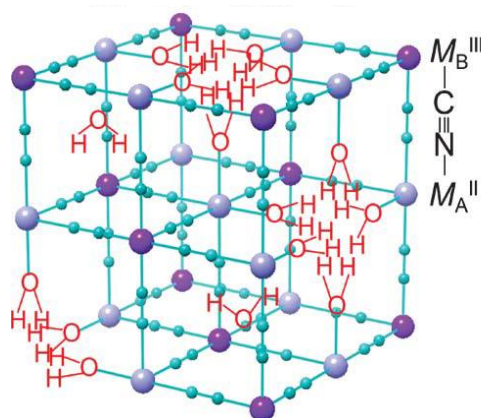


**Figure 4** Schematic crystal structures of the cubic unit cell of Metal-Hexacyanoferrate in its “insoluble” form (Vacancy-type  $Fm\bar{3}m$ ).

The terms “soluble” and “insoluble” doesn’t concern the solubility of PB analogues, they were assigned historically according to their ability to form colloidal solutions, actually PB is not soluble in any common solvent.

### 1.1.2. Synthesis methods: chemical and electrochemical synthesis

Metal-Hexacyanometallates structural properties and performances are strongly influenced by the types and contents of monovalent and multivalent cations, which depends on the conditions used for their synthesis.

Basically, the synthesis of insoluble hexacyanoferrate compounds proceeds through the reactive precipitation of two precursors: a soluble hexacyanoferrate (based on K, Na, H or  $NH_4^+$  forms) and a soluble metal salts (to be incorporated in the double-Metal Hexacyanoferrate compound).

The experimental procedure influences the properties of the final product; including the solubility/stability, the composition (ratio metal/ $K^+$ ,  $Na^+$ ,  $H^+$  or  $NH_4^+$ ), the size of nano/micro-particles (and their aggregation), the specific surface area, the density and the crystalline structure (face-centered cubic, rhombic, cubic, rhombohedral, trigonal) and its cell parameter.<sup>13</sup>

The parameters that play on the final product are the types of precursors, their molar ratio (and their concentrations), the mode (simultaneous introduction, successive addition, etc.), the order (hexacyanoferrate into metal salt solution, or reciprocal) and velocity of introduction (drop by drop, slow, fast, etc.) of their addition, the reaction temperature, the maturation (or aging), and the post-treatment (drying conditions).<sup>14</sup>

Hence, by slightly changing the experimental conditions may significantly change the characteristics of the final product.

This also means that during the synthesis of the double Metal-Hexacyanoferrate compound a variation in experimental conditions may cause (a) the co-existence of different products, for example in the case of nickel or cobalt hexacyanoferrate, and (b) the difficulty in obtaining perfectly reproducible results.

The molar ratio during the synthesis procedure may change when one of the precursors is injected drop to drop in the other compound, driving to heterogeneous materials.

This drawback can be minimized with pouring out together the two precursors at the same moment. However, some heterogeneity can locally occur in the mixing zone of the two compounds. An alternative solution would consist in the “in-drop” synthesis of the double-Metal Hexacyanoferrate.

The process consists in the mixing of the two precursors in a single drop through two needles fed at the same rate by a peristaltic pump.

Figure 5 shows the example of the synthesis of Prussian Blue by this “in-drop” method reported by Vincent et al.:<sup>13</sup> the two precursors (iron(III) chloride and potassium-hexacyanoferrate) are mixed in the drop at the extremity of the needles.

In particular, the photographs taken at different contact times, show the progressive formation of the Prussian Blue complex, together with the beige colored phase of  $FeCl_3$  and the uncolored phase of potassium hexacyanoferrate.<sup>13</sup>



**Figure 5** “In-drop” synthesis of Prussian Blue (from *Molecules* 2015, 20, 20582-20613).

Exhaustive reviews on the preparation and characterization of metal hexacyanoferrate (Cu, Zn and Ni hexacyanoferrates) have been published in the 80’s and 90’s by Loos-Neskovic research group: they reported and discussed the impact of synthesis procedures on the structure of double-Metal Hexacyanoferrate.<sup>15,16</sup>

This general chemical structure, the physical structure (cubic, face-centered cubic, trigonal, tetragonal, rhombohedral), and the size of crystallites are strongly controlled by the experimental conditions used for the synthesis of the ion-exchanger.<sup>16</sup>

Loos-Neskovic group showed that the most important and controlling parameters are the molar ratio between the precursors, the order of their addition, the presence of other chemical agents (ammonia and ammonium chloride, *etc.*), the temperature and also the pH. These parameters may impact also the stability of intermediary colloid particles and finally the size of particles. This factor is critical for example for the sorption properties of Prussian Blue analogue: hence, Lee and Streat<sup>17</sup> reported that Cs sorption capacity of potassium cobalt ferrocyanide is directly correlated to the fraction of potassium present on the ion-exchanger.

It is noteworthy that the synthesis procedure may also impact the oxidation state of iron (Fe(II) vs. Fe(III)) in the ion exchanger: the change in the precursor (ferricyanide vs. ferrocyanide) leads to different arrangements in the mesh of the crystalline structure, the vacancy of ferro-/ferri-cyanide sites, the size of ion-exchange cage, the possible incorporation of H<sub>2</sub>O molecules (which, in turn, may affect the coordination sphere and the reactivity of cyanide groups).

The type of metal may significantly impact the structure and the size of double-Metal Hexacyanoferrate crystals.

The ratio of precursors directly impacts the stability of the colloidal phase (formed during the reaction of the precursors) and the size of synthesized particles but hardly changes the type of produced metal-hexacyanoferrate.<sup>16</sup> It is generally accepted that an excess of counter metal ion (secondary metal salt containing d-metals such as Cu, Zn, Co, Fe, Ni, among the most popular) contributes to reduce the tendency of the mixture to form stable colloids and to facilitate the precipitation of the complex.

For example, Loos-Neskovic et al. compared the structure of zinc hexacyanoferrate(III) for different preparation methods with different molar ratio between the precursors (different excess of counter-metal): they most frequently found the structure to be rhombohedral but in some cases (and more specifically in the case of the presence of other cation like protons or Cs(I)) the structure changed to cubic. In addition, the chemical structure/composition was strongly affected by the experimental conditions that lead to mixtures of different salts and some changes in the crystal lattice.

The aging of the colloidal preparation (reaction of precursors, when the stoichiometry does not lead to the formation of a stable precipitate) is another way to control and increase the size of ion-exchanger particles, but the reproducibility in the synthesis procedure is more difficult to achieve.

Loos-Neskovic et al.<sup>15</sup> also reported the possible effect of the temperature and drying on the structure and composition of the Metal-Hexacyanometallates.

The expansion and the structural changes of surface properties with drying temperature was attributed to the faster evacuation of water molecules that contributes to the creation of supplementary pores and to the conversion of iron from the ferrous form to the ferric one.

In spite of huge number of publications on the chemical – physical properties of these materials, only recently authors have correlated the structure to the properties of these materials.

Onward the innovative properties and applications of several Metal-Hexacyanometallates are illustrated.

## 1.2. Physicochemical properties and application fields: analytical and technological applications

### 1.2.1. Magnetic functionalities of Prussian Blue analogs

Metal Hexacyanometallate-like materials display a wide range of important magnetic (e.g., room-temperature magnetic ordering) and magneto-optical (e.g., ferromagnetism, photoinduced (de)-magnetization) properties.<sup>18</sup> These properties are associated with the structural flexibility of their nanostructure due to the stretching and vibrational modes of the cyano-bridging ligand which allows one to improve them by selecting the appropriate electronic and magnetic configurations. The electromagnetic configurations can be tailored by external conditions, such as the magnetic field<sup>19,20</sup> and light,<sup>21,22</sup> and by changes in a specific local crystal environment (e.g., *in situ* electrochemical compositional variation occurring during the charge compensation imposed by a redox process). In the cyano-bridged metal complexes family there are a number of compounds that show charge-transfer (CT) phase transitions with an accompanying change in magnetic properties. These materials are suitable for understanding the optical control of magnetism, because the bidirectional CT transitions can be induced by photoirradiation at different photon energies.

In Metal Hexacyanoferrate complexes, "ligand-to-metal" charge transfer transitions to occur. In the electronic ground state,  $\text{Fe}(\text{CN})_6^{3-}$  has octahedral symmetry with six equivalent cyanide ligands. The LMCT excitation corresponds to a three-fold degenerate  $T_{1u}$ -symmetry excitation that does not instantaneously change the nuclear symmetry of the molecule.<sup>23</sup> While the spatial extent of the LMCT cannot be predicted *a priori*, the simplest analysis would predict the reduction of the iron atom from the ferric to the ferrous oxidation state and the oxidation of one cyanide ligand. The equivalence of the cyanide ligands, however, allows the electronic hole to hop from one ligand to another with a rate dictated by the strength of the electronic couplings between these ligands. Strong electronic coupling would lead to electron delocalization and the preservation of the octahedral symmetry found in the electronic ground state and also to the elimination of all anisotropy in the excited-state population, despite the linear polarization of the light used to generate the LMCT excited state. Alternatively, intramolecular distortion and solvation could stabilize the charge-transfer excited state, leading to electron localization and the reduction of the molecular symmetry.

As reported in detail previously, in the Metal-Hexacyanometallates periodic nanostructure, the metal  $M^I$  linked to nitrogen is generally ascribed to the high spin metallic site, while  $M^{II}$ , linked to carbon, is ascribed to the low spin site. The  $M^I/M^{II}$  ratio strongly influences the electronic and spin states of Metal-Hexacyanometallates containing alkali metals (e.g.,  $Na^+$ ,  $K^+$ , etc.). As a result, these materials tolerate different electronic spins, which limits the superexchange interactions to those across -CN bridges and allows the magnetism and coloration to be changed.<sup>24,25</sup> Elaborate theoretical analyses suggest that the local disorder associated with the structural defects, e.g., the  $\{M(CN)_6\}$  vacancies filled by  $\{(H_2O)_6\}$  clusters, plays an important role in determining the photomagnetic properties.<sup>26</sup>

The valence modulation of the  $M^I$  and  $M^{II}$  metals associated with the Metal-Hexacyanometallate lattice nanostructure can easily be performed electrochemically through the different redox processes of these materials.<sup>27</sup> This control is traditionally recognized as an *in situ* metal alkali compositional change where the  $M^I/M^{II}$  atomic composition ratio varies according to the electrochemical potential. Depending on the potential, ions are exchanged between the Metal-Hexacyanometallate nanostructure and the solution to compensate the charge lost or gained by the nanostructure during the different redox processes of these materials, leading to a potential-controlled compositional variation.

Two types of  $K^+$  sites exist during this compositional control. One type of site is adjacent to the  $Fe(CN)_{6-m}m(H_2O)$  vacancies and is preferentially occupied while the other type suffers repulsive interaction.<sup>28</sup> Thus, when all sites of the first type are occupied, which represent a fraction of about 25%, the next possibility is the occupation of the  $K^+$  sites of the nanostructure not adjacent to  $Fe(CN)_{6-m}m(H_2O)$ .<sup>28</sup>

The structural changeover that occurs *in situ* during the alkali metal composition modulation is due to the redox processes of the Metal-Hexacyanoferrate nanostructure. It is associated with a change of certain physical-chemical properties of these electromagnetic materials, such as their mechanical or magnetic properties. Among these physical properties, it is known that the magnetic properties of these materials are tunneled by the atomic composition ratio of (high spin metallic sites)/(low spin metallic sites).

Hence, Prussian Blue analogs have structural flexibility due to the stretching and vibrational modes of the cyanobridging ligand, and are classified as mixed-valence compounds due to the ligand-to-metal charge transfer mediated by the cyano ligand.

These features play important roles in the various magnetic functionalities (reported in Fig. 6), in fact several multi-functionalities with Prussian Blue analog-based magnets are demonstrated and listed below.<sup>9</sup>

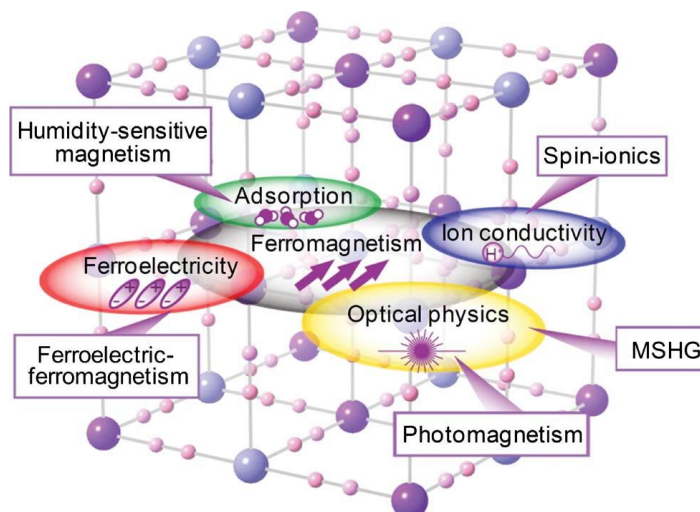


**Figure 6** Magnetic functionalities present in Prussian Blue analogs.<sup>9</sup>

(i) *Charge-transfer phase transition*: typically thermal phase transition phenomena are related to cooperativity based on the interaction between a metal ion and lattice strain. Because Prussian blue analogs have a strong cooperativity due to the bridged CN- ligand, thermal phase transitions are expected.

(ii) *Reversible photomagnetism*: several cyano-bridged bimetal assemblies, such as Cobalt Hexacyanoferrate, exhibit a photomagnetic effect. Optical control of magnetization can be realized by changing the electron spin state of a magnetic material.

(iii) *Second harmonic generation (SHG) and magnetization-induced SHG (MSHG)*: In  $A^I M_A^{II} [M_B^{III} (CN)_6]$ , the position of the A ion produces a  $\bar{4}$  rotoinversion operator, *i.e.*, the crystal structure is noncentrosymmetric.  $F\bar{3}m$ -type Prussian blue analog-based magnets are piezoelectric ferromagnets; that is, they are condensed matter with both piezoelectricity and ferromagnetism.

(iv) *Ferroelectric ferromagnetism*: to observe ferroelectric ferromagnetism, the attention is focused on hexacyanometalate-based materials because cyano-polymers are ferroelectric (at  $T_c$  5.6 K, below Curie temperature, the Metal-Hexacyanoferrates exhibit a long-range ferromagnetic ordering<sup>29</sup>).

(v) *Humidity-sensitive magnetism*:  $M_A^{II} [M_B^{III} (CN)_6]_{2/3} \cdot zH_2O$  has vacancies of  $[M_B (CN)_6]$ , which are filled with ligand water molecules coordinated to the  $M_A$  ion and non-coordinated water molecules. If a magnetic material exhibits a humidity-sensitive characteristic, then the magnetic variations can measure the humidity.

Fig. 7a schematically illustrates the geometrical change from 6-Co<sup>II</sup> to 4-Co<sup>II</sup>.

The observed  $M_s$  (saturation magnetization) value of  $4.7 \mu_B$  for Co<sup>II</sup>[Cr<sup>III</sup>(CN)<sub>6</sub>]<sub>2/3</sub>·zH<sub>2</sub>O at 80% RH (relative humidity) is due to ferromagnetic coupling between the 6-Co<sup>II</sup> ( $t_{2g}^5 e_g^2$ ,  $S = 3/2$ ) and Cr<sup>III</sup> ( $t_{2g}^3$ ,  $S = 3/2$ ). The decrease in the  $M_s$  value at low humidity is attributed to switching from ferromagnetic coupling between 6-Co<sup>II</sup> and Cr<sup>III</sup> to antiferromagnetic coupling between 4-Co<sup>II</sup> ( $e^4 t_2^3$ ,  $S = 3/2$ ) and Cr<sup>III</sup> (Fig. 7b).

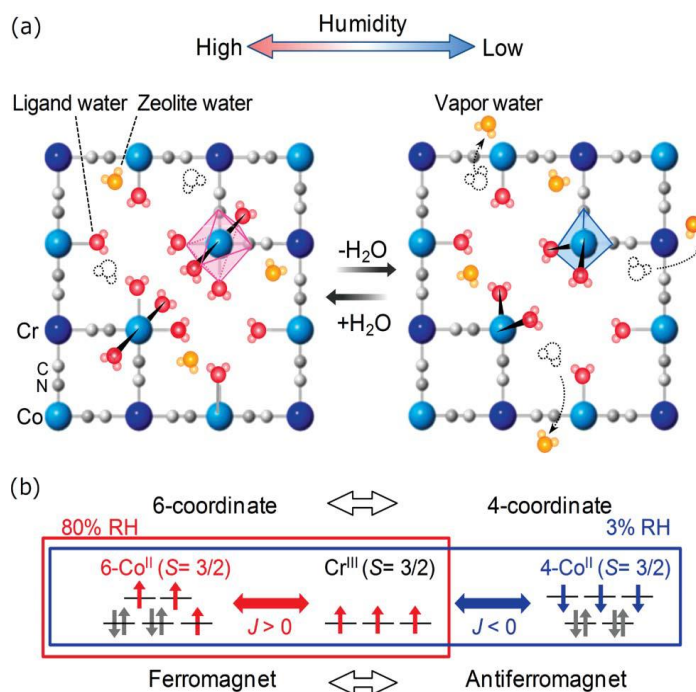


**Figure 7** Schematic illustration of (a) the coordination geometry on Co<sup>II</sup> between six-coordinate (6-Co<sup>II</sup>) and four-coordinate (4-Co<sup>II</sup>) under conditions of high and low humidity and (b) the humidity-induced change in the magnetic properties.<sup>9</sup>

(vi) *High ionic conductivity and a coupling effect between ionic conduction and magnetic ordering*: a vacancy-type Prussian Blue analog will be a useful system for observing proton conductivity because its nanoporous network structure contains water molecules, in fact materials with proton conductivity require proton carriers such as H<sup>+</sup> or H<sub>3</sub>O<sup>+</sup> provided by acidic or OH groups as well as proton-conducting pathways composed of hydrogen-bonding networks.

To deduce the mechanism of proton conduction we have to focus in the vacancy sites of [M<sub>B</sub>(CN)<sub>6</sub>]<sup>3-</sup>, the ligand water molecules coordinate to M<sub>A</sub> ions, and zeolitic water molecules exist (Fig. 8).

M<sub>A</sub> ions act as Lewis acids, and a proton is carried through the three-dimensional hydrogen bonding network composed of ligand and zeolitic water molecules.<sup>9</sup>

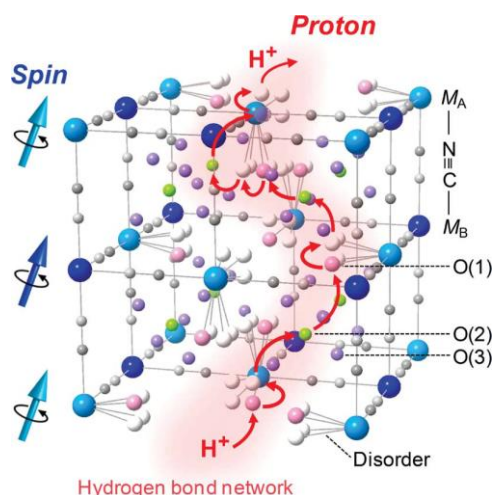


**Figure 8** Schematic illustration of a plausible pathway for a proton to travel through the hydrogen bonds of ligand water and zeolitic water molecules (red arrows) in the Prussian Blue analog structure of  $M^{II}A[M^{III}B(CN)_6]_{2/3} \cdot zH_2O$ . O(1) is the oxygen atom from the ligand water molecule, and O(2) and O(3) are the oxygen atoms of zeolitic water molecules.<sup>9</sup>

### 1.2.2. Electrochromism

Electrochromism is the property exhibited by some materials of a color change, or bleaching of color as effected either by an electron-transfer (redox) process or by a sufficient electrochemical potential. Hence it results from the generation of different visible region electronic absorption bands on switching between redox states.

In cases where more than two redox states are electrochemically available the electrochromic material may exhibit several colors and be termed polyelectrochromic.<sup>30</sup>

The term “electrochromism” was introduced in the year 1961 and the first report of the electrochemistry and electrochromism of PB film was written by Neff<sup>31</sup> in 1978.

Over the past years there has been a dramatic increase in electrochromic (EC) research activity, as seen in the large number of scientific papers and patents issued during this time. This surge in research moved from electrochromic displays to smart windows<sup>32</sup> mostly driven by the need of producing more energy efficient glazing, which can lead to a dynamic control of the transmissive materials properties.

Electrochromic materials, which change their optical properties in response to an electric field and can be returned to their original state by a field reversal, have major advantages:

- A small switching voltage (1-5 V);
- Show specular reflection;
- Possess a gray scale;
- Require power only during switching;
- Exhibit adjustable memory, up to 12-48 hours.<sup>33</sup>

Nowadays, applications of "the chromogenic family" have covered a wide and developing range of technology useful for glazing, mirrors, transparent displays and a variety of other applications.

Not surprisingly, the research field of electrochromic compounds is very broad and includes inorganic, organic, and polymeric, as well as several hybrid materials.

An electrochromic glazing device must have an ion-containing material (electrolyte) in close proximity to the electrochromic layer, as well as transparent layers for setting up a distributed electric field. Electrochemical stability can be increased by using interfacial layers. Devices are designed to shuttle ions back and forth into the electrochromic layer with applied potential. Electrochromic glazing can be fabricated from five (or less) layers consisting of two transparent conductors, an electrolyte or ion conductor, a counter electrode, and an electrochromic layer, as shown in Fig. 9.<sup>33</sup>

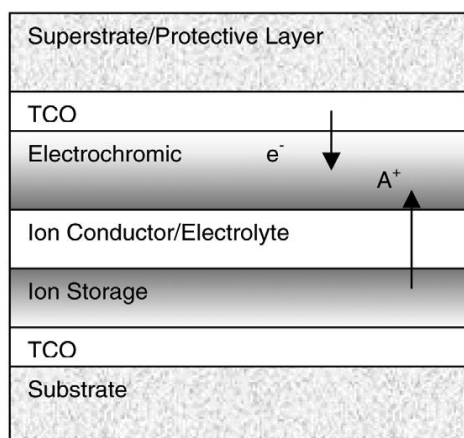


**Figure 9** Schematic of the layer structure of an electrochromic window (not to scale). The construction is similar to a battery. The condition shown is coloration in a cathodic material, such as tungsten oxide.

Examples of applications comprise flexible electrochromic on plastic for visors on motorcycle helmets,<sup>34</sup> electrochromic automotive sunroof glazing<sup>35</sup> and a type of electrochromic structure called the 'Nanocell'. This device is fashioned from photovoltaic cells so that the electrochromic can self-color when exposed to sunlight.

The cell relies on a dye-sensitized anatase titanium oxide layer, which forms a distributed *pn*-junction. Its optical density can be regulated by resistively shunting the anode and cathode of the cell.<sup>33</sup>

Onward studies revealed several analogs of PB that exhibit electrochromism; the Table 1 shows PB analogs exhibiting electrochromism and the colors shown by them<sup>36</sup> (for convention, the names of the Metal-Hexacyanoferrates are abbreviated as MHCF, where M indicates the transition metal and HCF Hexacyanoferrate anion).

**Table 1** Electrochromic property exhibited by Metal-Hexacyanoferrate compounds.

Compound	Color of the reduced species	Color of the oxidized species
<b>CuHCF</b>	red-brown	yellow
<b>NiHCF</b>	gray	yellow
<b>InHCF</b>	white	pale yellow
<b>CoHCF</b>	green	red-magenta
<b>CrHCF</b>	gray	blue
<b>PdHCF</b>	green	orange
<b>VHCF</b>	yellow	green

Cobalt Hexacyanoferrate (CoHCF) is the most interesting compound among the compounds cited in Table 1, in fact the color of the CoHCF film is dependent not only on its oxidation state but it is strongly influenced also by electrolyte counter-cations when the system is reduced.

Upon incorporation of small hydrated potassium or cesium cations, CoHCF (reduced) turns olive-brown, but in the presence of sodium and lithium ions the system is green. Coloring of cobalt compounds usually reflects the degree of solvation of Co(II) in the structures.

### 1.2.3. Thermochromism

Thermochromism is the reversible change in the color of a compound when it is heated or cooled. For inorganic compounds this transition is most often due to a change in crystalline phase, to a change in ligand geometry, or to a change in the number of molecules of solvent in the coordination sphere.

CoHCF microstructure (reduced) containing potassium or cesium is thermochromic, that is  $K_2Co^{II}[Fe^{II}(CN)_6]$  films change color from olive-brown to green upon heating (partial dehydration) above ca. 61°C (between 25-85°C). The thermochromism of cobalt compound has been explained in term of a change from more hydrated octahedral  $Co(H_2O)_6^{2+}$  to less hydrated tetrahedral  $Co(H_2O)_4^{2+}$ .

Hence, coloring of cobalt compounds usually reflects the degree of solvation of Co(II) in the structures, as detailed reported previously, explaining the thermochromism of cobalt salts.

Interstitial Co(II) is likely to be less hydrated in green-colored, sodium-containing, CoHCF films.

Since hydrated- $\text{Na}^+$  cations are relatively larger than hydrated- $\text{K}^+$  ions, they are not as easily accommodated (as hydrated- $\text{K}^+$ ) at interstices in a rigid, cubic-type, framework of Cobalt(II) Hexacyanoferrate(II). Consequently, the contribution from the hydration shell of a counteranion to the solvation environment of structural Co(II) would decrease upon sorption of sodium ions.<sup>37</sup>

The electrochemical behavior of Cobalt-Hexacyanoferrate is hard to understand. The main problem is that it is not clear what are the forms of Cobalt-Hexacyanoferrate formed in solution, and also which is the electrochemically active metal (cobalt or iron, or both). Cyclic voltammogram experiments make it impossible to get information about which metal redox reaction has occurred.

The latest theories regarding electrochemistry of Cobalt-Hexacyanoferrate were developed by Lezna et al. using the combination of multiple techniques such as IR in situ (during the acquisition of voltammograms) and XPS (X-ray Photoelectron Spectroscopy). In Fig. 10 there is a scheme with the electrochemical reactions, suggested by Lezna et al. for the high stability of  $\text{KCo}[\text{Fe}(\text{CN})_6]$  film. Three processes labeled I, II, and III are postulated as electrochemically independent, the process I and III are attributed to thin films while the process II is attributed to thick films.

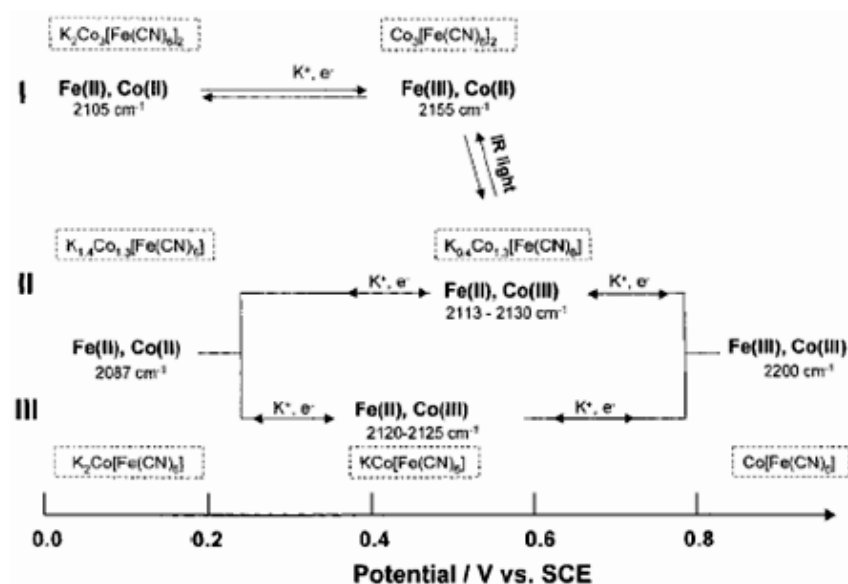


**Figure 10** Schematic summary of various compounds and their redox relationships in the CoHCF system.

The process I is already characterized, for the redox reaction involving Fe in a composition in which Co/Fe is 1.5.



The rate of this reaction is determined by the speed with which the cation  $K^+$  enters and exits the lattice, on the other hand, the oxidized form has all the tetrahedral sites free, and hence the incoming ion will not have any difficulty.

Process III involves both the cobalt and iron redox centers, and the structure identified in this Cobalt Hexacyanoferrate represents an equimolar ratio of the two metals.



#### 1.2.4. Cation exchange

The possibility that potassium intercalated in the lattice of KMHCF be replaced by a larger cation was detected for the first time in 1965,<sup>38</sup> this feature has led researchers to focus towards the possibility of forming molecular sieves, particularly useful in field of clean-up. Some Metal-Hexacyanoferrates, especially Nickel and Cobalt Hexacyanoferrates, are particularly selective towards the radioactive cesium-137, constantly generated as a byproduct in nuclear power plants.

Currently this waste is stored in special reserves, with obvious risks to the environment in case of accidental leakage hence Nickel and Cobalt Hexacyanoferrates can be used to separate radioactive cesium.

In a recent report presented by the Department of Energy of United States of America,<sup>39</sup> a new technique based on KCoHCFe, called EIX (electrochemical control of ion-exchange interactions) is used for the removal of radioactive cesium from nuclear waste. The new technique is directly based on the KCoHCFe ability to exchange  $K^+$  with  $Cs^+$  ions and it was tested on radioactive materials stored at Hanford Nuclear Reservation. A general scheme for the removal of cesium-137 by EIX technique is represented in Fig. 11.

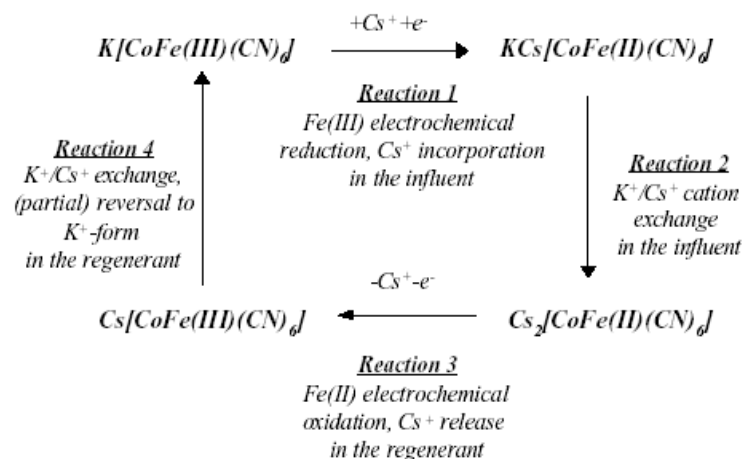


**Figure 11** Schematic removal of cesium-137 by EIX technique.

Due to the encouraging results, industries have started projects to scale up the exchange process.<sup>40,41</sup> A similar kind of behavior was also noticed for Nickel Hexacyanoferrate.<sup>42</sup>

Based on the zeolitic structure of these materials, the main mechanism involved in the binding of  $\text{Cs}^+$  (and other similar elements) consists in the ion-exchange of  $\text{K}^+$  (or  $\text{Na}^+$ ,  $\text{NH}_4^+$ ) for sorbents of general structure like  $\text{A}_x\text{M}_y[\text{Fe}(\text{CN})_6]_z \times n\text{H}_2\text{O}$  (where A is the monovalent cation ( $\text{K}^+$ ,  $\text{Na}^+$ ,  $\text{NH}_4^+$ ), M is the bivalent transition metal cation (such as  $\text{Ni}^{2+}$ ,  $\text{Co}^{2+}$ ,  $\text{Cu}^{2+}$ ,  $\text{Zn}^{2+}$ ,  $\text{Fe}^{2+}$ , etc.). It is worth highlighting the efficient “sieving” effect of the zeolitic cage associated to the crystal structure of the ion-exchangers; this contributes to the high selectivity of these materials for the recovery of Cs-type radionuclides from complex solutions (such as found in high level wastes or seawater).

Metal Hexacyanoferrate ion-exchangers have been widely studied for the recovery of Cs(I) and analogues; however, a numerous literature is also citing the possibility to use these materials for the sorption of base and precious metal ions.

It is worth noting Prussian Blue's ability to incorporate cations makes it useful as a sequestering agent for some heavy metal intoxications. Pharmaceutical-grade Prussian Blue in particular is normally used for people who have ingested thallium or radioactive cesium. According to the International Atomic Energy Agency and the U.S. Food and Drug Administration, Prussian Blue can be used as an orally ingested drug, providing a safe and effective therapy to enhance the excretion of isotopes of cesium and thallium from the intestine by means of ion exchange, so indirectly from the bloodstream by intervening in the enterohepatic circulation of caesium-137, reducing the internal residency time (and exposure) by about two-thirds.<sup>43</sup>

The ion-exchanger stability may depend on the pH, and the structure of the composite (mixed Metal Hexacyanoferrate). For example Milyutin et al.<sup>44</sup> commented that a partial dissolution of the Hexacyanoferrate compounds occurs at pH above 11.

The pH may contribute to the release of counter metals, which, in turn, affects the structure of the ion-exchanger (and its affinity or capacity to exchange metal ions, or make accessible site vacancies).

The chemical and the physical stabilities are important criteria since the change in the structure of the ion-exchanger or the change in the crystalline structure may induce diffusion limitations, metal leakage and radionuclide release. This is especially important for both sorption performance and long-term storage of metal-loaded materials.

Depending on the zeolitic structure of the ion-exchanger, its composition and the sorption mechanisms of these materials are generally controlled by diffusion, accessibility to reactive sites and surface parameters. This means that these ion-exchangers exhibit their highest efficiency and fast kinetics for sub-micron size particles.

However, as pointed by Loos-Neskovic et al.,<sup>45</sup> in some cases, the crystal structure may change during metal sorption involving much slower kinetics.

The small size of ion-exchanger particles (which depends on the mode of synthesis, as already reported previously) is a very important advantage for these materials since it allows reaching very high specific surface area, and then achieving very short equilibrium times.

Anyway, designing and managing such materials at the “nanometer” scale leads to complex problems for their management including complex recovery of materials at the end of processing flow, possible dispersion of hazardous materials (nanometer size particles, radionuclide-bearing compounds). These management and confinement issues are significantly limiting the dissemination of the technique and require developing sophisticated systems for management of these fine particles.

One solution to overcome these problems consists in immobilizing the active material (ion-exchanger micro/nanoparticles) at the surface or in the core of supports to prevent their readily dispersion.

However, the immobilization process may involve some limitations, including: reduced reactivity, low volumetric/mass density of reactive sites (dilution of active particles in/on the matrix) or slow kinetics (increased resistance to diffusion).

### 1.2.5. Ionic sensors

The development and study of electrochemical sensors which offer attractive advantages of rapid and non-invasive analysis has become an interesting area of research in recent years.<sup>46</sup>

Chemically modified electrodes (CMEs) with Prussian Blue analogues (PBAs) have been successfully employed in ion-sensing applications to introduce highly selective electrode responses.<sup>47</sup>

The studies carried out in this field turns out to be promising for Prussian blue and its analogs.<sup>48</sup> In particular copper and nickel hexacyanoferrates have been developed as sensors for ammonium ion, alkali and alkali earth cations using potentiometric and amperometric techniques.<sup>49,50</sup>

CuHCF showed a strong activity towards  $Tl^+$  ions even 100-250 times higher than that found for potassium,<sup>51</sup> this could lead to significant interest in developing sensors for the Tl(I) due the toxic nature of this element.

NiHCF is considered an effective potentiometric sensor for the determination of metal ions<sup>50</sup> and is considered an excellent candidate for separations involving alkali cations as proved in literature.<sup>52,53</sup> This property is due to its ability to deintercalate most of the intercalated ions via electrochemical modulation of the matrix charge density<sup>54</sup> and to its large ion intercalation capacity.

For this purpose, NiHCF is used in electrochemically switched ion exchange (ESIX) processes that use the selectivity of an ion intercalation compound to perform the separation. The high sensitivity and selectivity towards ions  $Na^+$  and  $K^+$  by the electroactive NiHCF thin film modified electrodes led to the development of probes for simultaneous determination of  $Na^+$  and  $K^+$  in blood and human serum<sup>55</sup> and to the development of a potentiometric method applied to the determination of potassium ion in syrup used in the treatment of body potassium deficiency.<sup>56</sup>

### 1.2.6. Electrocatalysis

Various Metal-Hexacyanoferrates deposited on electrode surfaces showed excellent electrocatalytic properties.

The zeolitic nature of PB with a cubic unit cell of 10.2 Å and with channel diameters of about 3.2 Å allows the diffusion of low molecular weight molecules (such as  $O_2$  and  $H_2O_2$ ) through the crystal.

For this reason, Itaya described PB as a three-dimensional catalyst. By taking into consideration the previous diffraction study of PB structure by Ludi et al.,<sup>57,58</sup> which demonstrated the presence of about eight uncoordinated water molecules in the unit cell of PB, Itaya hypothesized that such vacancies were responsible for the catalytic activity towards H<sub>2</sub>O<sub>2</sub>. When the molecule of hydrogen peroxide (or oxygen) penetrates the PB lattice structure, it will be located in the center of each vacancy being surrounded by four divalent high spin iron ions on average, which can bring about a catalytic reduction of H<sub>2</sub>O<sub>2</sub> via a four electron reaction.

Although this hypothesis is rather suggestive, the mechanism of catalysis of PB towards H<sub>2</sub>O<sub>2</sub> reduction is still not completely clear, probably due to the fact that, as with crosslinked organic polymers,<sup>59</sup> it is very difficult to characterize PB and there is still no complete agreement concerning its structure and its stoichiometric composition.

For many years, the structure of PB has been a subject of investigation in order to explain the electrochemical behavior and its catalytic activity.

As previously reported, Keggin and Miles<sup>60</sup> discussed the structure of PB on the basis of powder diffraction patterns. The authors distinguished between two different forms of PB, one called soluble and the other insoluble. These names, given by dye makers, do not refer to the real solubility in water but rather indicate the ease with which potassium ions peptize. The unsuitability of these terms has been much stressed and it was demonstrated that both the forms are highly insoluble ( $K_{ps} = 10^{-40}$ ).<sup>61</sup>

According to Keggin and Miles, the soluble form of PB has a cubic structure in which iron(II) and iron(III) are located on a face centered cubic lattice, where iron(II) ions are surrounded by carbon atoms and iron(III) ions are surrounded octahedrally by nitrogen atoms. The “insoluble” form differs from the “soluble” one by virtue of the excess of ferric ions which replace potassium ions in the interstitial sites.

The structure was found to be more disordered with one-fourth of the ferrocyanide sites unoccupied.

The presence of 14–16 water molecules per unit cell was demonstrated. A portion of the water molecules are filling empty nitrogen sites of the ferrocyanide vacancies, while the rest are occupying interstitial sites and represent uncoordinated water.

Moreover, no iron(III) ions were found in the interstitial sites. This conclusion seems also to be confirmed by Mossbauer and infrared studies.<sup>62,63</sup>

However, it should also be stressed that this uncertainty concerning the PB structure has also to be attributed to the fact that Prussian Blue is a generic chemical designation for a complex material with variable stoichiometry.

The structure, depending on the materials and procedure used to crystallize PB, could contain co-precipitated ions, indefinite amounts of water, hydrolyzed ferrocyanide and various vacancies in the crystal structure.

The uncertainty as to the structure of Prussian Blue has also been responsible for the uncertainty concerning the electrochemical reaction that takes place at the electrode surface.

The findings of Itaya and Neff in the 1980s had very important implications for PB catalytic activity and for its subsequent use in electroanalytical applications.

They were the first to demonstrate the possibility of depositing PB layers onto different electrode materials and showed the interesting electrocatalytic activity relative to hydrogen peroxide reduction.

These studies were the basis for the future applications of PB in sensors as a means for amperometric detection of H<sub>2</sub>O<sub>2</sub> and more generally, PB properties make these materials suitable as amperometric sensors and electrochemical detectors. The following Table 2 shows the Metal Hexacyanometallates (MHCF) with electrocatalytic properties and also the substrates to which they were found to have this property.

**Table 2** Substrates to which Metal-Hexacyanoferrates show electrocatalytic property.

MHCF	Substrates
<b>CuHCF</b>	Ascorbic acid, <sup>64</sup> NADH, Hydrazine, Hydroxylamine, Cysteine, <sup>65</sup> Glutathione <sup>66</sup>
<b>CoHCF</b>	Ascorbic acid, <sup>67</sup> Hydroquinone, <sup>68</sup> NADH, <sup>69</sup> Dopamine, <sup>70</sup> Epinephrine, <sup>70</sup> Norepinephrine, <sup>70</sup> Hydrazine, <sup>71</sup> Morphine <sup>71</sup>
<b>CoHCF modified with Ru</b>	Hydrazine, <sup>72</sup> Thiosulphate, <sup>72</sup> p-Chlorophenol <sup>72</sup>
<b>NiHCF</b>	Ascorbic acid, <sup>73</sup> Dopamine, <sup>74</sup> Hydrazine <sup>75</sup>
<b>InHCF</b>	Cysteine, <sup>76</sup> Glutathione, <sup>76</sup> 6-thiopurine, <sup>76</sup> Methimazole <sup>76</sup>
<b>Several MHCFs</b>	Hydrogen peroxide <sup>77</sup>

### 1.2.7. Batteries

Members of the family of coordination polymers called Prussian Blue analogues (PBAs) have been recently demonstrated as potential electrode materials for alkali ion batteries exploiting their stable redox properties<sup>78</sup> and large and uniform porosity.<sup>79 80</sup>

The idea to use Metal-Hexacyanoferrates in batteries derives from their open framework structure allowing for fast and reversible guest ion intercalation (Fig. 12).

Hence, several different common alkali metal ions can be reversibly inserted into these materials from aqueous electrolytes,  $\text{Li}^+$ ,  $\text{Na}^+$ ,  $\text{K}^+$  and  $\text{NH}_4^+$  and can be utilized as a cathode material for  $\text{Li}^+(\text{Na}^+)$  secondary batteries.<sup>81</sup>

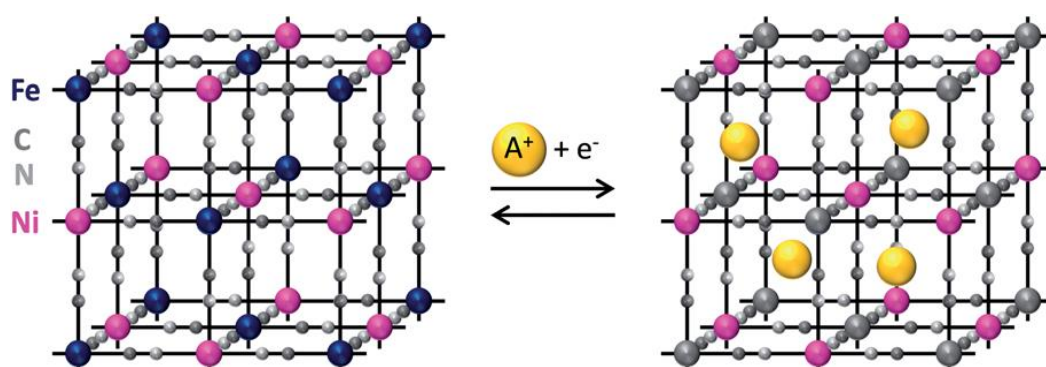


**Figure 12** Schematic depiction of alkali ion insertion mechanism in the cubic Prussian blue analogue structure. The cyanometallate vacancies and coordinated and zeolitic water molecules are omitted for clarity (from *RSC Adv.*, 2014, 4, 24955).<sup>82</sup>

For example, a thin film of Manganese Hexacyanoferrate<sup>83,84</sup> exhibits a capacity of 128(109) mA h  $\text{g}^{-1}$  and an average voltage of 3.8(3.4) V vs. Li(Na) in the  $\text{Li}^+(\text{Na}^+)$  secondary battery. In addition, PBA can store divalent alkaline-earth metal ions<sup>81,85</sup> as well as larger alkali metal ions.<sup>86,87</sup> In each case, the crystallographic lattice parameter varies only slightly, and linearly, with the concentration of the inserted ions.

However, the stiffness of the structure and the size of the interstitial sites result in only minor dimensional changes when the concentrations of the inserted ions are modified during charging and discharging. This is an important factor, it leads to the unusually long cycle lives observed in this family of materials.

These relatively inexpensive and safe high production volume materials possess remarkable electrochemical performance, operate in safe, common aqueous electrolytes, and may be inexpensively synthesized using bulk processes at moderate temperatures.

Hence, they are especially attractive for use in large-scale stationary batteries to provide storage capacity for use with the electrical power grid.<sup>88</sup>

The first studies were made on Prussian Blue alone and later coupled with Nafion as components for rechargeable batteries.<sup>44,45</sup> Final development of these systems has led to rechargeable batteries with cathodes containing Cu-FeHCF.<sup>46</sup>

In a recent report, electrochromic tungsten oxide (WO<sub>3</sub>) and Indium Hexacyanoferrate (InHCF) thin-film electrodes, in combination with a polymer electrolyte that accommodates conduction of both K<sup>+</sup> and H<sup>+</sup>, were assembled into a thin-film electrochromic battery (ECB). A typical InHCF–WO<sub>3</sub> ECB (designated as IWECB) can be charged and discharged reversibly between 0.5 and 1.5 V with a theoretical voltage of around 1.24 V.<sup>47</sup>

Success with monovalent ion insertion motivated researchers to explore these materials for divalent insertion.

Divalent ions have been shown to reversibly insert with long cycle life into Nickel Hexacyanoferrate<sup>89</sup> and PB thin films, suggesting that divalent alkaline earth cations (Mg<sup>2+</sup>, Ca<sup>2+</sup>, Sr<sup>2+</sup>, Ba<sup>2+</sup>) can reversibly insert into these materials,<sup>90,91</sup> obtaining high-rate cycling of nanoscale NiHCF electrodes with Mg<sup>2+</sup>, Ca<sup>2+</sup>, Sr<sup>2+</sup> and Ba<sup>2+</sup> ions with long cycle life and promising energy efficiency.<sup>92</sup> However, if a guest ion can carry two or three charges, the insertion reaction should store more energy than Li or Na ion batteries.

Numerous attempts have been carried out to explore potential cathode and anode materials, a key issue is the sufficient large channel structures to accommodate the storage and diffusion of the multivalent ion insertion.

Hence, our experiences with the solid state electrochemistry of Metal Hexacyanometallates and success with monovalent and divalent ion insertion made us question whether it would be possible to intercalate trivalent cations within the Metal Hexacyanometallate lattice.

In this thesis, a detailed electrochemical study about the insertion-deinsertion of trivalent cations in Nickel Hexacyanoferrate (NiHCF) lattice is reported. The study is performed in order to highlight NiHCF exchangeability properties useful in several technological applications including wastewater treatment, batteries and element purification.

### 1.3. TiO<sub>2</sub>-Metal Hexacyanometallate composite materials

Composite materials consisting of semiconductors and inorganic compounds often have attractive photo-electrochemical properties.

Among the semiconductor materials, TiO<sub>2</sub> is particularly promising due to its photo-electrochemical properties, high photo-activity, outstanding hydrophilicity,<sup>93</sup> strong redox and catalytic activity; the range of its potential applications includes catalysis, photovoltaic cells,<sup>94</sup> self-cleaning<sup>95</sup> and antifogging surface treatments.<sup>96,97</sup>

In addition, TiO<sub>2</sub> is non-toxic, chemically very stable, and easily obtained as nanometer scale particles.<sup>98</sup>

The photo-catalytic properties of TiO<sub>2</sub> are strongly affected by its structure, interface, grain size and crystallographic orientation of the exposed faces in contact with solution.<sup>99</sup> The photo-electrochemical characteristics are dependent upon porosity, morphology and the method of synthesis.<sup>100,101</sup> Surface functionalization of TiO<sub>2</sub> has been achieved with many methods including doping with metal ions or nonmetallic elements, sensitization with organic dyes or semiconductors with a small band-gap.

Several attempts have been made to deposit Metal Hexacyanometallates (MHCM) on TiO<sub>2</sub> composited films, in particular de Tacconi et al. studied the preparation, the photoelectrochemical characterization, and the photoelectrochromic behavior of Metal Hexacyanoferrate–titanium dioxide composite films (where M = Cu, Ni, In)<sup>102</sup> while Rutkowska et al. used TiO<sub>2</sub>-Nickel(II) Hexacyanoferrate(II,III) modified electrodes.<sup>103</sup>

TiO<sub>2</sub> nanoparticles functionalized with Fe<sup>II</sup>(CN)<sub>6</sub><sup>4-</sup> have been investigated in literature by electro-absorption spectroscopy. The iron complex is believed to bind the Ti<sup>IV</sup>-site via a monodentate cyanide ligand, obtaining (CN)<sub>5</sub>Fe<sup>II</sup>-CN-Ti<sup>IV</sup>(particle),<sup>104</sup> as suggested by IR and resonance Raman evidence. Other studies reported in literature dealt with thin films prepared by mixing TiO<sub>2</sub> with Metal-Hexacyanometallates.<sup>105,106</sup>

This thesis deals with the design, synthesis and characterization of new composite materials of TiO<sub>2</sub> and Metal Hexacyanometallates, in particular Cobalt Hexacyanoferrate (CoHCF) and Iron Hexacyanocobaltate (FeHCC).

Here, we will detail the synthesis procedure of both the electrochemical and chemical Anatase TiO<sub>2</sub>-CoHCF and TiO<sub>2</sub>-FeHCC, the influence upon TiO<sub>2</sub> optical properties, and the structural-electronic characterization performed with a wide range of experimental techniques.

### 1.3.1. Photocatalysis and photocatalytic degradation of toxic organic pollutants

Photocatalysis is a promising, environmentally friendly technology for the conversion of solar energy into chemical energy.<sup>107</sup> Potential applications include photodegradation of hazardous substances,<sup>108,109</sup> photocatalytic water splitting,<sup>110</sup> artificial photosynthesis, photo-induced super-hydrophilicity, and photoelectrochemical conversion.<sup>111</sup>

Relative to the history of catalysis processes, coined by Berzelius at the beginning of nineteenth century, photocatalysis remains a recent discipline, as marked by J.M. Herrmann in his introductory paper. Basically, photocatalysis differentiates from conventional catalysis by the activation of the catalytic solid, which occurs through photon absorption rather than by thermal activation. This photonic activation thus requires the use of a semiconductor material as catalyst, provided that the radiation wavelengths are greater than its band gap, which corresponds to the energy gap between both conduction and valence bands of the semiconductor.

Activating a semiconductor leads to the promotion of an electron from the valence to the conduction band, with the simultaneous creation of a photogenerated hole within the valence band.

Further, the transfer of photogenerated charge carriers to the photocatalyst surface allows redox reactions to occur with adsorbed reactants, coming from gas or liquid phase depending on the application. At the catalyst surface, the redox reactions are separated into reduction and oxidative steps, involving on one hand, conduction band electrons and adsorbed electron acceptors such as, e.g., oxygen molecules and on the other hand, valence band holes and adsorbed electron donors such as, e.g., organic molecules or more generally the targeted pollutant. Indirect oxidation reactions also occur through the formation of highly oxidative hydroxyl radicals generated by the oxidation of water by holes.

Thus, the photocatalysis discipline exists through the ability of a material, in this case a semiconductor (usually  $\text{TiO}_2$ ), to simultaneously interact with light and reactants, through both ab- and ad-sorption phenomena, respectively.

A wide variety of semiconductors have been investigated as photocatalysts in addition to traditional materials such as  $\text{TiO}_2$ ,<sup>112</sup>  $\text{WO}_3$ <sup>113</sup> and  $\text{CdS}$ .<sup>114</sup>

However, TiO<sub>2</sub> remains the most popular material and can be considered as a benchmark in the field of photocatalysis.<sup>93,115</sup>

The evolution of TiO<sub>2</sub>-based photocatalysis can be traced back to the early 1930s. In 1938, Doodeve et al. reported that active oxygen species produced on the TiO<sub>2</sub> surface can bleach dyes under UV light irradiation; TiO<sub>2</sub> was referred to as a “photosensitizer” in that publication.<sup>116</sup> The first researchers to use the terminology “photocatalyst” with respect to TiO<sub>2</sub> might be Kato and Mashio in 1956, whose report is entitled “Autooxidation by TiO<sub>2</sub> as a photocatalyst”.<sup>117</sup> In their experiments, the autooxidation of organic solvents and the simultaneous formation of H<sub>2</sub>O<sub>2</sub> were observed under the irradiation of a Hg lamp. In 1972, Fujishima and Honda reported the landmark discovery of water photolysis on a TiO<sub>2</sub> electrode,<sup>93</sup> which aroused much attention towards TiO<sub>2</sub>-based photocatalysis.

The main topic of investigation has become concentrated on how to improve the solar energy conversion efficiency to meet engineering requirements.

In general, a photocatalytic reaction consists of three steps as shown in Fig. 13.

First, photoexcitation generates electrons (e<sup>-</sup>) and holes (h<sup>+</sup>). Next, the electrons and holes migrate to the TiO<sub>2</sub> surface. Finally, the electrons and holes react with adsorbed electron acceptors and donors, respectively, to complete the photocatalytic reaction.

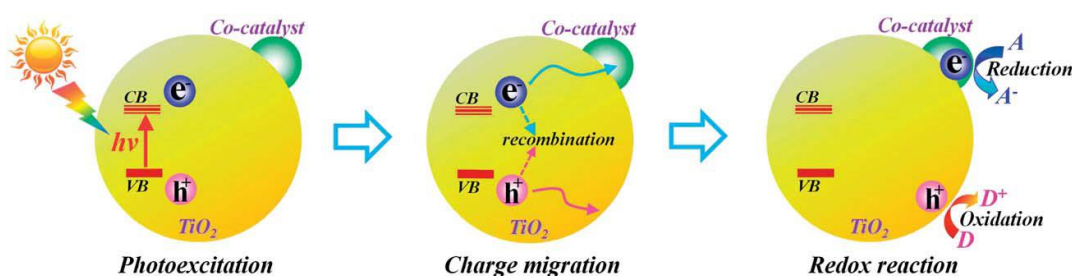


**Figure 13** Schematic picture of the TiO<sub>2</sub> photocatalytic reaction process.

Accordingly, much effort is currently focused on how to improve the light absorption, charge separation, and surface reactivity of TiO<sub>2</sub> in order to achieve outstanding photocatalytic performance.

Both spatial structuring of TiO<sub>2</sub> to increase the effective path length of incident light and band structure engineering to enhance the optical response in the UV to visible light range can induce TiO<sub>2</sub> to absorb more photons.

Attempts have been made to apply both physical concepts and spatial structuring to TiO<sub>2</sub>, all of these interesting studies revealed that well-designed nanostructures can trap photons and force them to propagate more effectively through TiO<sub>2</sub>, thus resulting in more efficient light absorption.

A limitation of TiO<sub>2</sub> is its 3.2 eV bandgap, which allows only UV light to be absorbed ( $\lambda < 387$  nm, accounting for 5% of the solar spectrum).

Recent studies proved that doping TiO<sub>2</sub> with suitable molecules, the band gap can be reduced obtaining a positive effect in the photocatalytic activity.<sup>118,119</sup>

UV-Vis spectra and the valence band measurement in the TiO<sub>2</sub>-Metal Hexacyanometallate composite materials confirm a desirable reduction of the TiO<sub>2</sub> band gap, it will be clearly detailed below in Chapter 6.

Hence, the photocatalytic degradation of some organic compounds (in particular Methylene Blue) in presence of TiO<sub>2</sub> doped by mixed Metal Hexacyanometallates is reported in this thesis.

The photodegradation by semiconductors is part of photocatalytic processes in heterogeneous phase, in particular of “*Advanced Oxidation Processes*” (AOP). This techniques involve the use of catalysts and a high energy source (UV radiation) in order to generate very reactive species such as hydroxyl radicals inducing oxidation-reduction reactions.

After this brief introduction on the structure, properties and use of Metal Hexacyanometallates, the following sections report an overview of the work carried out during the three years PhD, and in particular an in-depth description about the synthesis of Metal Hexacyanometallates and their applications for analytical and technological purposes.

- 
- <sup>1</sup> *Miscellanea Berolinensia ad Incrementum Scientiarum*, Berlin, 1710, 377.
- <sup>2</sup> D. Brown; *J. Philos. Trans.*, 1724, 33, 17.
- <sup>3</sup> Neff, V.D., *J. Electrochem. Soc.* 1978, 125 (6), 886–887.
- <sup>4</sup> Ellis, D., Eckhoff, M., Neff, V.D., *J. Phys. Chem.*, 1981, 1225–1231.
- <sup>5</sup> Rajan, K.P., Neff, V.D., *J. Phys. Chem.* 1982, 86, 4361–4368.
- <sup>6</sup> Itaya, K., Uchida, I., Neff, V.D., *Acc. Chem. Res.* 1986, 19, 162–168.
- <sup>7</sup> Itaya, K., Shoji, N., Uchida, I., *J. Am. Chem. Soc.* 1984, 106, 3423–3429.
- <sup>8</sup> S. Ohcoshi, K. Hashimoto; *The Electrochemical Society Interface*; 2002, 34.
- <sup>9</sup> H. Tokoro and Shin-ichi Ohkoshi; *Dalton Trans.*, 2011, 40, 6825.
- <sup>10</sup> A. Ludi, H. U. Güdel; *Struct. Bonding*, 1973, 14, 1.
- <sup>11</sup> A. Ludi, H. J. Buser, W. Peter, D. Schwarzenbach; *Inorg. Chem.*, 1977, 16, 2704–2710.
- <sup>12</sup> F. Herren, P. Fisher, A. Ludi, W. Halb; *Inorg. Chem.*, 1980, 19, 956.
- <sup>13</sup> Thierry Vincent, Chloë Vincent, Eric Guibal, *Molecules* 2015, 20, 20582–20613
- <sup>14</sup> Ismail, I.; El-Sourougy, M.; Moneim, N.; Aly, H. J. *Radioanal. Nucl. Chem.* 1998, 237, 97–103.
- <sup>15</sup> Loos-Neskovic, C.; Fedoroff, M.; Garnier, E. *Talanta* 1989, 36, 749–759.
- <sup>16</sup> Loos-Neskovic, C.; Fedoroff, M.; Garnier, E.; Gravereau, P. *Talanta* 1984, 31, 1133–1147.
- <sup>17</sup> Lee, E.F.T.; Streat, M. *J. Chem. Technol. Biotechnol. A* 1983, 33, 333–338.
- <sup>18</sup> D. Giménez-Romero, J. Agrisuelas, J. J. García-Jareño, J. Gregori, C. Gabrielli, H. Perrot, F. Vicente, *J. Am. Chem. Soc.* 2007, 129, 7121–7126.
- <sup>19</sup> Yamamoto, T.; Umemura, Y.; Sato, O.; Einaga, Y. *J. Am. Chem. Soc.* 2005, 127, 16065–16073.
- <sup>20</sup> Champion, G.; Escax, V.; Cartier dit Moulin, C.; Bleuzen, A.; Villain, F.; Baudelet, F.; Dartyge, E.; Verdagner, M. *J. Am. Chem. Soc.* 2001, 123, 12544–12546.
- <sup>21</sup> Sato, O.; Iyoda, T.; Fujishima, A.; Hashimoto, K. *Science* 1996, 271, 49–51.
- <sup>22</sup> Sato, O.; Kawakami, T.; Kimura, M.; Hishiya, S.; Kubo, S.; Einaga, Y. *J. Am. Chem. Soc.* 2004, 126, 13176–13177.
- <sup>23</sup> Alexander, J. J.; Gray, H. B. *J. Am. Chem. Soc.* 1968, 90, 4260–4271.
- <sup>24</sup> Sato, O.; Iyoda, T.; Fujishima, A.; Hashimoto, K. *Science* 1996, 272, 704–705.
- <sup>25</sup> Champion, G.; Escax, V.; Cartier dit Moulin, C.; Bleuzen, A.; Villain, F.; Baudelet, F.; Dartyge, E.; Verdagner, M. *J. Am. Chem. Soc.* 2001, 123, 12544–12546.
- <sup>26</sup> Herren, F.; Fischer, P.; Ludi, A.; Halg, W. *Inorg. Chem.* 1980, 19, 956.
- <sup>27</sup> Gimenez-Romero, D.; Bueno, P. R.; Garcia-Jareno, J. J.; Gabrielli, C.; Perrot, H.; Vicente, F. *J. Phys. Chem. B* 2006, 110, 2715–2722.
- <sup>28</sup> Bueno, P. R.; Gimenez-Romero, D.; Gabrielli, C.; Garcia-Jareno, J. J.; Perrot, H.; Vicente, F. *J. Am. Chem. Soc.* 2006, 128, 17146–17152.
- <sup>29</sup> S.I. Ohkoshi and K. Hashimoto, *J. Photochem. Photobiol. C: Photochem. Rev.*, 2001, 2, 71–88.
- <sup>30</sup> <sup>12</sup> R. J. Mortimer, *Chemical Society Reviews*, 1997, vol 26.
- <sup>31</sup> V. D. Neff; *J. Electrochem. Soc.*, 1978, 125, 886, 887.
- <sup>32</sup> Lampert, C.M. *Solar Energy Materials and Solar Cells*, 1998, 52 (3-4), 207–221.
- <sup>33</sup> Carl M. Lampert, *Materials today*, 7, 2004, 28–35.
- <sup>34</sup> Azens, A., et al, *Solid State Ionics* (2003) 165 (1-4), 1
- <sup>35</sup> Giron, J.-C., et al., *Electrochromic Automotive Sunroofs*. In *Proceedings of Glass Processing Days* (2003), 460
- <sup>36</sup> Kuo-Chuan Ho and Jiann-Chung Chen; *J. Electrochem. Soc.*, Vol. 145, No. 7, July 1998.
- <sup>37</sup> R. J. Kulesza, M. A. Malik, K. Miecznikowski, and A. Wolkiewicz, S. Zamponi, M. Berrettoni, R. Marassi, *J. Electrochem. Soc.*, 1996, 143, L10–12.
- <sup>38</sup> W.E. Prout, E.R. Russel and H.J. Groh, *J. Inorg. Nucl. Chem.*, 1965, 27, 473–475.
- <sup>39</sup> M.M. Benjamin, G.V. Korshin; Department of Civil and Environmental Engineering, AMSP Final Report, 1999, Project Number 55246, Grant Number DE-FG07-96ER62313.
- <sup>40</sup> R. Harjula, J. Lehto, E.H. Tusa, A. Paavola, *Nucl. Technol.*, 1994, 107, 272–278.
- <sup>41</sup> R. Harjula, J. Lehto, E. H. Tusa, A. Paavola, *Nucl. Technol.*, 1994, 107, 279–284.
- <sup>42</sup> M.T. Kelly, G.A. Arbuckle-Keil, L.A. Johnson, E.Y. Su, L.J. Amos, J.K.M. Chun and A.B. Bocarsly, *J. Electroanal. Chem.*, 2001, 500, 311–321.
- <sup>43</sup> Domokos Mathe, Krisztián Szigeti, Patent EP2675486 A2
- <sup>44</sup> Milyutin, V.; Mikheev, S.; Gelis, V.; Kozlitsin, E., *Radiochemistry* 2009, 51, 298–300.
- <sup>45</sup> Loos-Neskovic, C.; Fedoroff, M. *Solvent Extr. Ion Exch.* 1989, 7, 131–158.
- <sup>46</sup> M. Esteban, A. Castano *Environ. Int.* 35 (2009) 438–449.
- <sup>47</sup> Norma R. de Tacconi, Krishnan Rajeshwar, Reynaldo O. Lezna, *Chem. Mater.* 15 (2003) 3046–3062.
- <sup>48</sup> K. Itaya and I. Uccida, V.D. Neff, *Acc. Chem. Res.*, 1986, 19, 162–168.
- <sup>49</sup> L.M. Siperko and T. Kuwana, *Electrochim. Acta*, 1987, 32, 765–771.

- <sup>50</sup> M. Giorgetti, E. Scavetta, M. Berrettoni and D. Tonelli, *Analyst*, 2001, 126, 2168-2171.
- <sup>51</sup> M. Zadroncki, I.A. Linek, J. Stroka, P.K. Wrona and Z. Galus, *J. Electrochem. Soc.*, 2001, 148, E348-E355.
- <sup>52</sup> K. M. Jeerage, D. T. Schwartz, *Sep. Sci. Technol.* 35 (2000) 2375.
- <sup>53</sup> S. D. Rassat, J. H. Sukamto, R. J. Orth, M. A. Lilga, R. T. Hallen, *Sep. Pur. Technol.* 15 (1999) 207.
- <sup>54</sup> Jeerage, K. M. University of Washington; Seattle, WA, 2001.
- <sup>55</sup> D.R. Coon, L.J. Amos, A.B. Bocarsly and P.A. Fitzgerald-Bocarsly, *Anal. Chem.*, 1998, 70, 3137-3145.
- <sup>56</sup> R. J. Mortimer, Paulo J.S. Barbeira, Ana F.B. Sene, Nelson R. Stradiotto, *Talanta* 49 (1999) 271-275.
- <sup>57</sup> Ludi, A., Gudel, H.U., *Struct. Bond.* 1973, 14, 1-22.
- <sup>58</sup> Herren, F., Fisher, P., Ludi, A., Halg, W., *Inorg. Chem.* 1980, 19, 956-959.
- <sup>59</sup> Itaya, K., Uchida, I., Neff, V.D., *Acc. Chem. Res.* 1986, 19, 162-168.
- <sup>60</sup> Keggin, J.F., Miles, F.D., *Nature* 1936, 137, 577-578.
- <sup>61</sup> Mortimer, R.J., Rosseinsky, D.R., *J. Chem. Soc. Dalton Trans.*, 1984, 2059-2062.
- <sup>62</sup> Robin, M.B., Day, P., *Advances in Inorganic Chemistry and Radiochemistry*, 1967, 10, 247-422.
- <sup>63</sup> Duncan, J.F., Wrigley, P.W.R., *J. Chem. Soc.*, 1963, 1120-1125.
- <sup>64</sup> D.R. Shankaran, S.S. Narayanan, *Fresenius J. Anal. Chem.*, 1999, 362, 686-689.
- <sup>65</sup> S.M. Chen and C.M. Chan, *J. Electroanal. Chem.*, 2003, 543, 161-173.
- <sup>66</sup> D.R. Shankaran, S.S. Narayanan, *Bull. Korean Chem. Soc.*, 2001, 22, 816-820.
- <sup>67</sup> C.X. Cai, K.H. Xue and S.M. Xu, *J. Electroanal. Chem.* 2000, 486, 111-118.
- <sup>68</sup> M. Jiang, M. Zhou and Z. Zhau, *Ber. Bunsen-Ges. Phys. Chem.*, 1991, 95, 720-726.
- <sup>69</sup> C.X. Cai, H.X. Ju and H.X. Chen, *J. Electroanal. Chem.* 1995, 397, 185-190.
- <sup>70</sup> S.M. Chen and K.T. Peng, *J. Electroanal. Chem.*, 2003, 547, 179-189.
- <sup>71</sup> S.M. Chen, *Electrochim Acta*, 1998, 43, 3359-3369.
- <sup>72</sup> T.R.I. Castaldi, G. De Benedetto and A. Bianchini, *J. Electroanal. Chem.*, 1999, 471, 42-47.
- <sup>73</sup> D.B. Humphrey, S. Sinha and A.B. Bocarsly, *J. Phys. Chem.*, 1987, 91, 586-593.
- <sup>74</sup> D.M. Zhou, H.X. Ju and H.Y. Chen, *J. Electroanal. Chem.*, 1996, 408, 219-223.
- <sup>75</sup> X. Lin and A.B. Bocarsly, *J. Electroanal. Chem.*, 1991, 300, 325-345.
- <sup>76</sup> S. Zhanga, W.-L. Suna, W. Zhanga, W.-Y. Qia, L.-T. Jina, K. Yamamoto, S. Taob, J. Jin, *Analytica Chimica Acta* 386 (1999) 21-30.
- <sup>77</sup> R. Garjonyte and A. Malinauskas, *Sensors Actuators B*, 1998, 46, 236-241.
- <sup>78</sup> C. D. Wessells, R. A. Huggins, Y. Cui, *Nat. Commun.*, 2011, 2, 550.
- <sup>79</sup> C. D. Wessells, S. V. Peddada, R. A. Huggins, Y. Cui, *Nano Lett.*, 2011, 11, 5421.
- <sup>80</sup> Wang, Y. Lu, J. Liu, M. Xu, J. Cheng, D. Zhang, J. B. Goodenough, *Angew. Chem., Int. Ed.*, 2013, 52, 1964.
- <sup>81</sup> R. Y. Wang, C. D. Wessells, R. A. Huggins and Y. Cui, *Nano Lett.*, 2013, 13, 5748.
- <sup>82</sup> Carissa H. Li, Yusuke Nanba, Daisuke Asakura, Masashi Okubo, Daniel R. Talham, *RSC Adv.*, 2014, 4, 24955.
- <sup>83</sup> T. Matsuda and Y. Moritomo, *Appl. Phys. Express*, 2011, 4, 047101.
- <sup>84</sup> T. Matsuda, M. Takachi and Y. Moritomo, *Chem. Commun.*, 2013, 49, 2750.
- <sup>85</sup> Y. Mizuno, M. Okubo, E. Hosono, T. Kudo, H. Zhou and K. Ohishi, *J. Phys. Chem. C*, 2013, 117, 10877.
- <sup>86</sup> M. Pyrasch, A. Toutianoush, W. Jin, J. Schnepf and B. Tieke, *Chem. Mater.*, 2003, 15, 245.
- <sup>87</sup> W. Jin, A. Toutianoush, M. Pyrasch, J. Schnepf, H. Gottschalk, W. Rammensee and B. Tieke, *J. Phys. Chem. B*, 2003, 107, 12062.
- <sup>88</sup> Robert A. Huggins *Journal of The Electrochemical Society*, 164 (1) A5031-A5036 (2017).
- <sup>89</sup> R. Y. Wang, C. D. Wessells, R. A. Huggins, Y. Cui, *Nano Lett.* 2013, 13, 5748.
- <sup>90</sup> Chen, S.-M. *J. Electroanal. Chem.* 2002, 521, 29-52.
- <sup>91</sup> Mizuno, Y.; Okubo, M.; Hosono, E.; Kudo, T.; Zhou, H.; Ohishi, K. *J. Phys. Chem. C* 2013, 117, 10877-10882.
- <sup>92</sup> Richard Y. Wang, Colin D. Wessells, Robert A. Huggins, Yi Cui, *Nano Lett.* 2013, 13, 5748-5752.
- <sup>93</sup> A. Fujishima and K. Honda, *Nature*, 1972, 238, 37.
- <sup>94</sup> G. Dai, L. Zhao, J. Li, L. Wan, F. Hu, Z. Xu, B. Dong, H. Lu, S. Wang and J. Yu, *J. Colloid Interface Sci.*, 2012, 365, 46.
- <sup>95</sup> F. R. Marciano, D. A. Lima-Oliveira, N. S. Da-Silva, A. V. Diniz, E. J. Corat and V. J. Trava-Airoldi, *J. Colloid Interface Sci.*, 2009, 340, 87.
- <sup>96</sup> D. Tahk, T. I. Kim, H. Yoon, M. Choi, K. Shin and K. Y. Suh, *Langmuir*, 2010, 26, 2240.
- <sup>97</sup> Graziani, L.; Quagliarini, E.; Osimani, A.; Aquilanti, L.; Clementi, F.; Yéprémian, C.; Lariccia, V.; Amoroso, S.; D'Orazio, M., *Build. Environ.*, 2013, 64, 38.
- <sup>98</sup> M. C. Tsai, M. H. Yang, Y. W. Chang, J. K. Tzeng, C. Y. Lee, H. T. Chiu, H. C. Chen and I. N. Lin, *Mater. Chem. Phys.*, 2013, 143, 60.

- 
- <sup>99</sup> Fujishima, A.; Zhang, X.; Tryk, D. A., *Surf. Sci. Rep.*, 2008, 63, 515.
- <sup>100</sup> D. P. Serrano, G. Calleja, R. Sanz and P. Pizarro, *J. Mater. Chem.*, 2007, 17, 1178.
- <sup>101</sup> I. A. Rutkowska, A. Andrearczyk, S. Zoladek, M. Goral, K. Darowicki and P. J. Kulesza, *J. Solid State Electrochem.*, 2011, 15, 2545.
- <sup>102</sup> N.R. de Tacconi, K. Rajeshwar, R.O. Lezna, *Electrochimica Acta* 45 (2000) 3403–3411.
- <sup>103</sup> I.A. Rutkowska, M. Skunik, K. Miecznikowski, P.J. Kulesza, *ECS Trans.* 13 (2008) 185-198.
- <sup>104</sup> M. Khoudiakov, A. L. Parise and B. S. Brunshwig, *J. Am. Chem. Soc.*, 2003, 125, 4637.
- <sup>105</sup> N. R. de Tacconi, K. Rajeshwar and R. O. Lezna, *Electrochim. Acta*, 2000, 45, 3403.
- <sup>106</sup> M. Ciabocco, M. Berrettoni, D. F. Martino Chillura, M. Giorgetti, *Solid State Ionics*, 2014, 259, 53.
- <sup>107</sup> Hua Xu, Shuxin Ouyang, Lequan Liu, Pakpoom Reunchan, Naoto Umezawa, Jinhua Ye, *J. Mater. Chem. A*, 2014, 2, 12642.
- <sup>108</sup> H. H. Chen, C. E. Nanayakkara and V. H. Grassian, *Chem. Rev.*, 2012, 112, 5919–5948.
- <sup>109</sup> S. X. Ouyang and J. H. Ye, *J. Am. Chem. Soc.*, 2011, 133, 7757–7763.
- <sup>110</sup> H. Xu, X. Q. Chen, S. X. Ouyang, T. Kako, J. H. Ye, *J. Phys. Chem. C*, 2012, 116, 3833–3839.
- <sup>111</sup> X. Q. Chen, J. H. Ye, S. X. Ouyang, T. Kako, Z. S. Li, Z. G. Zou, *ACS Nano*, 2011, 5, 4310–4318.
- <sup>112</sup> U. Bach, D. Lupo, P. Comte, J. E. Moser, F. Weissortel, J. Salbeck, H. Spreitzer and M. Gratzel, *Nature*, 1998, 395, 583–585.
- <sup>113</sup> X. Q. Chen, J. H. Ye, S. X. Ouyang, T. Kako, Z. S. Li and Z. G. Zou, *ACS Nano*, 2011, 5, 4310–4318.
- <sup>114</sup> D. Chen and J. H. Ye, *Adv. Funct. Mater.*, 2008, 18, 1922–1928.
- <sup>115</sup> X. Chen and S. S. Mao, *Chem. Rev.*, 2007, 107, 2891–2959.
- <sup>116</sup> C. F. Doodeve and J. A. Kitchener, *Trans. Faraday Soc.*, 1938, 34, 902–908.
- <sup>117</sup> K. Hashimoto, H. Irie and A. Fujishima, *Jpn. J. Appl. Phys.*, 2005, 44, 8269–8285.
- <sup>118</sup> M. Berrettoni, M. Ciabocco, M. Fantauzzi, M. Giorgetti, A. Rossi, E. Caponetti, *RSC Adv.*, 2015, 5, 35435.
- <sup>119</sup> M. Khoudiakov, A. L. Parise and B. S. Brunshwig, *J. Am. Chem. Soc.*, 2003, 125, 4637.

## 2. Work aims

The main aims of this research were both the developing of novel synthesis strategies to obtain Metal Hexacyanometallates and composite films comprising of particulate semiconductors and molecular redox systems and their application for analytical and technological purposes.

A comparative discussion of the growth, characterization, and applications of the Co, Ni, In PB analogues is presented.

After a brief introduction on their solid-state chemistry, the growth of thin films of these compounds on targeted substrates is discussed. Post-deposition characterization of these materials, both native and composite, mainly by electrochemical measurements, X-ray Powder Diffraction (XRD), X-ray fluorescence spectroscopy (XRF), X-ray Absorption Spectroscopy (XAS), X-ray photoelectron spectroscopy (XPS), Scanning Electron Microscopy (SEM), Transmission Electron Microscopy (TEM), Infrared Spectroscopy (IR), Ultraviolet–visible spectroscopy (UV-Vis), is reported.

Finally, the use of these synthesized materials in devices for ion-exchangers, environmental remediation, chemical/biological sensing, energy conversion, in memory devices and magneto-optical switching is described, giving a general overview of innovative analytical and technological applications provided by such materials.

In particular, in Chapters 3 and 4 of this dissertation, the synthesis of Indium Hexacyanoferrate (InHCF) and Nickel Hexacyanoferrate (NiHCF) are discussed. These open framework materials exhibit unique physicochemical characteristics, that are primarily a result of the perovskite-like face-centered cubic crystal structure and represent excellent candidates in application involving ion exchangers and ionic sieves.

Extending the above work, in Chapter 4, a detailed electrochemical study about the insertion-deinsertion of trivalent cations in NiHCF lattice is reported in order to highlight NiHCF exchangeability properties useful in several technological applications including wastewater treatment, batteries and element purification.

In particular, it is demonstrated that Nickel Hexacyanoferrate allows for cation selective extractions, also for the rare earth elements selective recovery.

Subsequently, electrocatalysis of targeted reactions and structural changes upon ion uptake by these MHCF nanoparticles constitute an important topic in this thesis. This research project is in collaboration with prof. J. A. Cox of Miami University, OH, USA.

In particular, Chapter 5 is focused on fabrication of organically modified silica sol-gel (SG) film with templated and controlled channel size. The formation of ca. 20-nm channels normal to the electrode surface was targeted by attaching 20-nm polystyrene sulfonate (PSS) beads electrostatically to an aminopropyltriethoxysilane (APTES)-modified electrode.

Incorporation of catalysts, such as Cobalt Hexacyanoferrate, within these channels promoted the electrochemical oxidation of selected biological compounds, such as cysteine.

Finally, the synthesis and characterization of novel  $\text{TiO}_2$ -Metal Hexacyanometallates composite materials is reported in Chapter 6. This research project is in collaboration with the University of Montpellier (France), the University of Cagliari and Palermo (Italy).

The obtained experimental results highlighted that the electronic properties of  $\text{TiO}_2$  are substantially modified as confirmed in particular by UV-Vis and XP-valence band data.

Practical use of these materials can be envisaged in different areas, such as antibacterial treatments, protection of historical artifacts, self-cleaning surfaces, photovoltaic cells and photoelectrochemical degradation of potentially toxic organic dyes in aqueous solutions under UV irradiation.

It is worth noting that this is one of the first examples of the triggering of spin-crossover phenomena in Metal-Hexacyanoferrate based-molecular solids by an external stimuli other than photoexcitation and most of all one of the first studies in which a completely pure low-spin Fe(II) is obtained starting from a mix of low-spin Fe(II) and Fe(III).

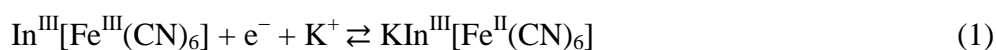
The investigation of spin transitions induced by charge transfer in molecular solids is very important because these materials may become switchable components in molecular electronics and, thanks to the significant change in the spin state induced by the charge transfer, in spintronics as well.

### 3. Fabrication and application of modified electrodes with Indium Hexacyanoferrate (InHCF) as ion-exchanger

#### 3.1. Introduction

The most studied Prussian Blue analogues are the metal-hexacyanoferrates<sup>1</sup> (*Mhcf*), with  $M = \text{Co}^{2+}, \text{Cu}^{3+}, \text{Ni}^{4+}, \text{Ru}, \text{Zn}, \text{Mn}, \text{Cr}, \text{Cd}, \text{Ho}, \text{Tm}, \text{Ga}, \text{Ce}, \text{Nd}, \text{Bi}, \text{Ag}, \text{Tb}, \text{Y}, \text{Pt}, \text{Ti}$  or  $\text{V}$ . Among these compounds, Indium-Hexacyanoferrate (InHCF) is noticeable for its particular electrochromic properties, for the ease of electrodeposition on several electrodes, for a very positive reversible redox peak (at  $\sim 0.8$  V vs Ag/AgCl reference electrode).

For modifying electrodes, InHCF can be deposited at  $\text{pH} \approx 2$  from solutions containing  $[\text{Fe}(\text{CN})_6]^{3-}$  and  $\text{In}^{3+}$  ions with KCl as the supporting electrolyte.<sup>5-12</sup> The positive branch of the voltammogram presents several reversible, narrow and well-defined peaks. The basic redox mechanism involves  $\text{K}^+$  insertion during reduction and its release during oxidation<sup>6</sup>:



During the electrochemical synthesis, the “insoluble”  $\text{In}_4[\text{Fe}(\text{CN})_6]_3$  (indium ferrocyanide) is preferentially formed; the “soluble”  $\text{KInFe}(\text{CN})_6$  is obtained by potential cycling in KCl solutions; however, mixed-type films may result as well.<sup>7</sup> It has been shown<sup>8</sup> that at  $\text{pH} \approx 2$ , a large excess of  $\text{K}^+$  and/or  $\text{H}^+$  improves electrodeposition and the stability of the solution, while the excess of  $\text{In}^{3+}$  makes the Indium Hexacyanoferrate film more stable.<sup>9</sup> InHCF films were previously obtained from solutions with  $\text{Na}^+$  and  $\text{K}^+$ ,<sup>10</sup> or with a range of mono and divalent cations<sup>11,12</sup> to study the dependence of the formation upon the counter-cations. Other reports have discussed  $\text{K}^+$  transport during the redox reactions<sup>13</sup> and the role of the different mono/divalent cations in the final properties of deposited InHCF.<sup>12</sup>

The Prussian Blue analogue InHCF has special electrochromic properties switching from yellowish in the oxidized form to colorless in the reduced form.<sup>14,15</sup> Therefore, InHCF can be used as a transparent counter-electrode for complementary electrochromic and/or electrochemical devices.

The synthesis by cyclic voltammetry (CV) of InHCF from solutions containing  $\text{K}^+$  or other mono/divalent cations is reported below. The possibility to assess whether these Prussian Blue analogues to act as reservoirs of different cations with different valence is explored.

## 3.2. Experimental

### 3.2.1. Reagents and materials

All chemicals were reagent grade from Carlo Erba ( $\text{MgCl}_2$ ,  $\text{CaCl}_2$ ,  $\text{ZnCl}_2$ ,  $\text{BaCl}_2$ ,  $\text{CdCl}_2$ ,  $\text{NaCl}$ ), Sigma-Aldrich ( $\text{K}_3\text{Fe}(\text{CN})_6$ ,  $\text{InCl}_3$ ,  $\text{CoCl}_2$ ,  $\text{KCl}$ ,  $\text{LiCl}$ ,  $\text{SrCl}_2$ ,  $\text{RbCl}$ ,  $\text{CsCl}$ ,  $\text{NH}_4\text{Cl}$ ) and Fluka ( $\text{HCl}$ ). All experiments have been performed in air, at room temperature and with deionized water.

Electrochemical measurements were made with a Model 660C (CH Instruments) electrochemical work station using a standard three-electrode electrochemical glass cell (10 ml). The substrate of the working electrode was glassy carbon (diameter  $\approx 3$  mm) or glassy indium tin oxide (ITO - squares pieces, 1.5 cm edges); a Pt counter electrode was used. All potentials were made and reported vs.  $\text{Ag}/\text{AgCl}$  in saturated  $\text{KCl}$  except for the  $\text{InHCF}/\text{CoHCF}$  case discussed below.

### 3.2.2. Indium Hexacyanoferrate electrochemical synthesis

The glassy carbon (GC) electrode was polished with a  $0.05 \mu\text{m}$  alumina slurry on a cloth and then rinsed with water; its pretreatment consisted of cycling 20 times from 1.0 V to 0.0 V at  $0.050 \text{ V s}^{-1}$  in 1.0 M  $\text{KCl}$ .  $\text{InHCF}$  film was deposited from a  $\text{pH} \approx 2$  solution that contained  $1.0 \times 10^{-3} \text{ M InCl}_3$ ,  $1.0 \times 10^{-3} \text{ M K}_3\text{Fe}(\text{CN})_6$  and 1.0 M  $\text{KCl}$ . The  $\text{pH}$  of the solution was lowered to the  $\text{pH} 1.0 - 2.0$  range (optimal for electrodeposition) by addition of  $\text{HCl}$ ; the  $\text{pH}$  was measured or determined as the nominal value.

Indium Hexacyanoferrate ( $\text{InHCF}$ ) and Cobalt Hexacyanoferrate ( $\text{CoHCF}$ ) films were prepared by dynamic electrodeposition on GC or ITO electrodes through CV scans from 1.0 V to 0.0 V at  $0.1 \text{ V s}^{-1}$ .

After rinsing with water, the electrode was cycled in 1.0,  $1.0 \times 10^{-1}$ , and  $1.0 \times 10^{-2}$  M  $\text{KCl}$  solutions to investigate the redox processes at different  $\text{KCl}$  concentrations.

$\text{CoHCF}$  films were deposited by cycling the potential 50 times between 1.0 V and 0 V at  $0.1 \text{ V s}^{-1}$  in 1.0 M  $\text{KCl}$  solutions containing  $2.0 \times 10^{-3} \text{ M CoCl}_2 \cdot 6\text{H}_2\text{O}$  and  $1.0 \times 10^{-3} \text{ M K}_3[\text{Fe}(\text{CN})_6]$ .<sup>16</sup> Also, these electrodes were rinsed with distilled water and studied by CV in different  $\text{KCl}$  solutions.

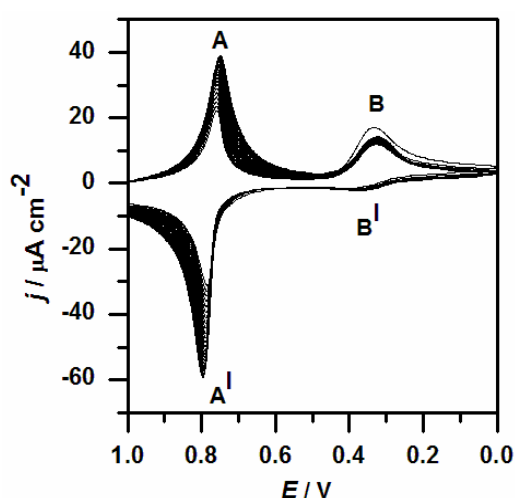
The electrochromic device consisted of an  $\text{InHCF}$  counter electrode on ITO facing an ITO with a deposited  $\text{CoHCF}$  film. The electrodes were separated by filter paper wetted with 1.0 M  $\text{KCl}$  solution in contact with a Pt wire that acted as a quasi-reference electrode.

### 3.3. Results and Discussion

#### 3.3.1 Modified electrodes with Indium Hexacyanoferrate: Electrochemical characterization

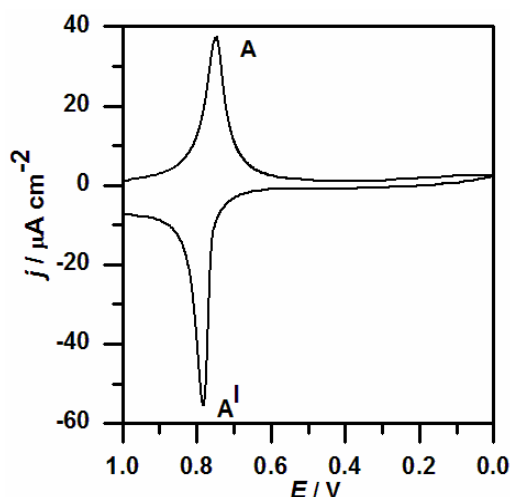
InHCF films were electrosynthesized on a GC electrode by cyclic voltammetry (CV) from solutions containing  $\text{InCl}_3$  and  $\text{K}_3\text{Fe}(\text{CN})_6$  with KCl as supporting electrolyte at  $\text{pH} \approx 2$ .

Figure 14 shows the CV scans during electrodeposition; the peak current and the associated charge slightly increase with the number of cycles for features A/A'. The redox couple A/A' is due to the species,  $\text{InHCF}^{17}$ , while B/B' is due to the  $\text{Fe}(\text{CN})_6^{4-}/\text{Fe}(\text{CN})_6^{3-}$  couple. In the first cycle,  $\text{Fe}(\text{CN})_6^{3-}$  is reduced at  $\sim +0.28$  V and then it rapidly reacts with  $\text{In}^{3+}$  ions to form  $\text{In}^{\text{III}}[\text{Fe}^{\text{II}}(\text{CN})_6]$ ; this behaviour explains the small oxidative peak B' corresponding to  $\text{Fe}(\text{CN})_6^{3-}$ . Since the properties of InHCF films are dependent upon the conditions of the electrosynthesis, we chose to synthesize InHCF by applying 50 cycles under the conditions in Fig. 14.<sup>7</sup>



**Figure 14** Continuous CV at  $0.1 \text{ V s}^{-1}$  in a KCl/HCl solution at nominal  $\text{pH} \approx 2$  for the electrodeposition of a InHCF film on a GC electrode.

The following Fig. 15 shows the CV of an InHCF film in 1.0 M KCl solution at  $\text{pH} \approx 2$ . A single reversible redox couple with narrow, well-defined peaks is observed for the reduction maximum at  $\sim +0.8$  V vs Ag/AgCl. The absence of the ferricyanide redox peaks means that no trace of the electroplating solution has been retained by the film after rinsing.



**Figure 15** CV of an InHCF film at  $0.1 \text{ V s}^{-1}$  in  $1.0 \text{ M KCl}$  solution.

The redox couple A/A' is due to the redox process given by Reaction 1.

The redox process doesn't seem to be completely reversible: the ratio of the peak heights  $I_{p_a}/I_{p_c}$  is 0.66 while the ratio of the corresponding charges  $Q_a/Q_c$  is 1.24.

This is due to the different kinetics of reduction and oxidation processes and to the different involvement of the inner and outer layers of the InHCF film, in fact by increasing the scan rate and consequently by decreasing the involved layers, the  $I_{p_a}/I_{p_c}$  ratio becomes 1.

However, a 38 mV distance between the redox peaks implies a good thermodynamic reversibility.

The shapes of the reduction and oxidation waves are different, and characteristic of a process confined to a thin layer covering the electrode.

The stability of the film by repeated CV scans at  $0.1 \text{ V s}^{-1}$  was checked. The intensity of the cathodic peak current  $I_{p_c}$  decreases monotonically with the number of cycles and reduces to 50% after 400 cycles. This phenomenon may be due to loss of electroactive material and is less pronounced in  $1.0 \times 10^{-2} \text{ M HCl}$ .

Tests were also performed in solutions with different KCl concentrations, with or without HCl, to verify whether  $\text{K}^+$  is involved in the redox reaction.

Figures 16 a and b show the CV results. The peak potentials were shifted in the negative direction with decreasing the electrolyte concentration thus confirming the role of  $\text{K}^+$  in the redox reactions.

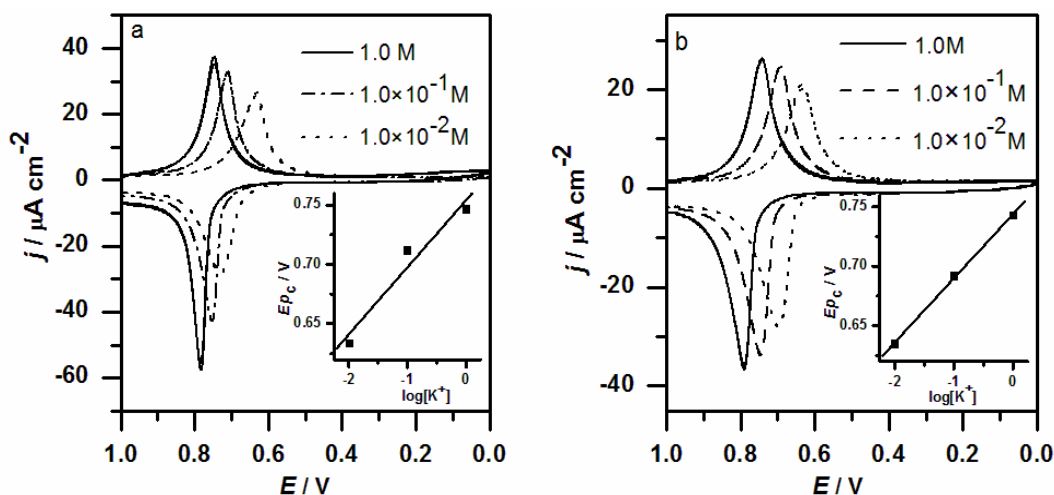


**Figure 16** CVs of InHCF films recorded at different KCl concentrations (1.0,  $1.0 \times 10^{-1}$  and  $1.0 \times 10^{-2}$  M) a) without (at native pH) and b) with  $1.0 \times 10^{-2}$  M HCl (pH = 2). The insets show the cathodic peak potentials as a function of  $\log[K^+]$  which yield slopes of 56 mV/dec and 54 mV/dec for Fig. 3a and 3b.

The Nernst equation for reaction (1) reads (in volts):

$$E = k + 0.059 \log[K^+] \quad (2)$$

Within the experimental error, our slopes of 0.054 and 0.056 V/dec are consistent with a single electron redox process involving  $K^+$ .

The pH dependence of  $K^+$  insertion in InHCF by exploring the pH range 0.0-4.0 for three KCl solutions (1.0,  $1.0 \times 10^{-1}$  and  $1.0 \times 10^{-2}$  M) was investigated.

In Figure 17, CVs at selected pH values are reported; the insets show the linear behavior of the cathodic peak potential upon  $\log[K^+]$ . In the explored pH range, the same general behavior is observed.

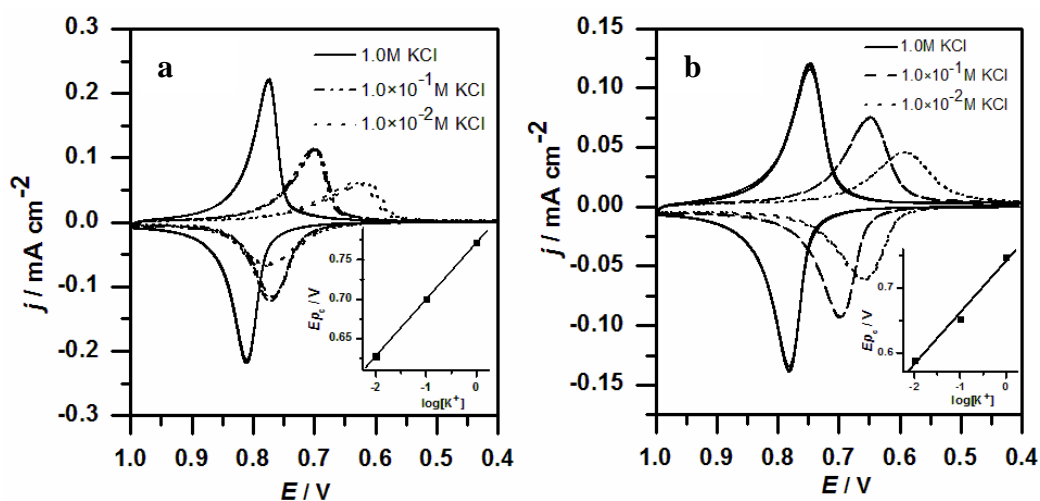


**Figure 17** CVs of InHCF films in KCl solutions (1.0,  $1.0 \times 10^{-1}$  and  $1.0 \times 10^{-2}$  M) at different nominal pH: a) pH=4.0, b) pH=0.0. The slopes of the cathodic peak potential vs  $\log[K^+]$  are 72 and 80 mV/dec for figure a and b, respectively.

The small difference in the peak morphology is ascribed to the different amount of electroactive species involved, as can be inferred by the different current scale.

The pH and  $[K^+]$  dependences shed light on the possible competition of  $H^+$  and  $K^+$  in the intercalation process. Figures 18a, b, and c show the CVs at different pH value in 1.0,  $1.0 \times 10^{-1}$ , and  $1.0 \times 10^{-2}$  M KCl, respectively.

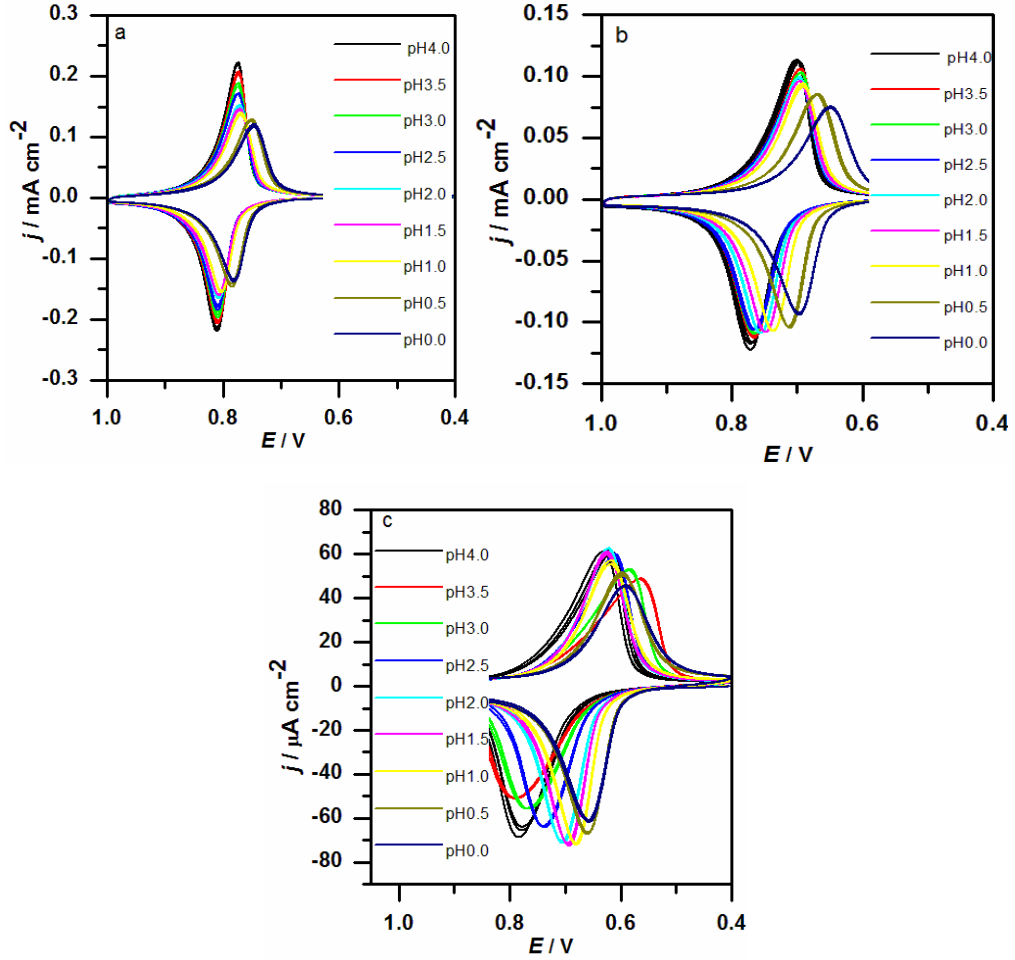
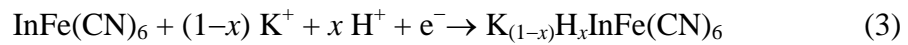


**Figure 18** CVs of InHCF films recorded in 1.0 M (a),  $1.0 \times 10^{-1}$  M (b) and  $1.0 \times 10^{-2}$  M (c) KCl solutions at different nominal pH values (4.0-3.5-3.0-2.5-2.0-1.5-1.0-0.5-0.0).

To account for the combined  $K^+/H^+$  intercalation, Reaction 1 is expanded as shown in Reaction 3.



For which the corresponding Nernst equation is given by (4):

$$E = k + (1-x) 0.059 \log[K^+] + x 0.059 \log[H^+] \quad (4)$$

The experimental value of  $x$  was obtained by fitting the experimental peak potential ( $E_p$ ) value with ones calculated with equation (4).

The calculated  $x$  values (see Table 1) show that:

1. the electrochemical intercalation involves both  $H^+$  and  $K^+$ ;
2.  $x$  decreases monotonically up to zero as pH increases;
3. when pH and pK are the same,  $K^+$  intercalation is dominant.

**Table 3**  $x$  best fit values in according with redox equation 3 (see text for details).

$x$	$1-x$	pK	pH
0.15	0.85	0.00	0.00
0.11	0.89	0.00	0.50
0.02	0.98	0.00	1.00
0.01	0.99	0.00	1.50
0.00	1.00	0.00	2.00
0.00	1.00	0.00	2.50
0.00	1.00	0.00	3.00
0.00	1.00	0.00	3.50
0.00	1.00	0.00	4.00
0.56	0.44	1.00	0.00
0.31	0.69	1.00	0.50
0.13	0.87	1.00	1.00
0.10	0.90	1.00	1.50
0.08	0.92	1.00	2.00
0.06	0.94	1.00	2.50
0.07	0.93	1.00	3.00
0.06	0.94	1.00	3.50
0.04	0.96	1.00	4.00
1.00	0.00	2.00	0.00
0.63	0.37	2.00	0.50
0.31	0.69	2.00	1.00
0.20	0.80	2.00	1.50
0.18	0.82	2.00	2.00
0.21	0.79	2.00	2.50
0.29	0.71	2.00	3.00
0.35	0.65	2.00	3.50
0.12	0.88	2.00	4.00

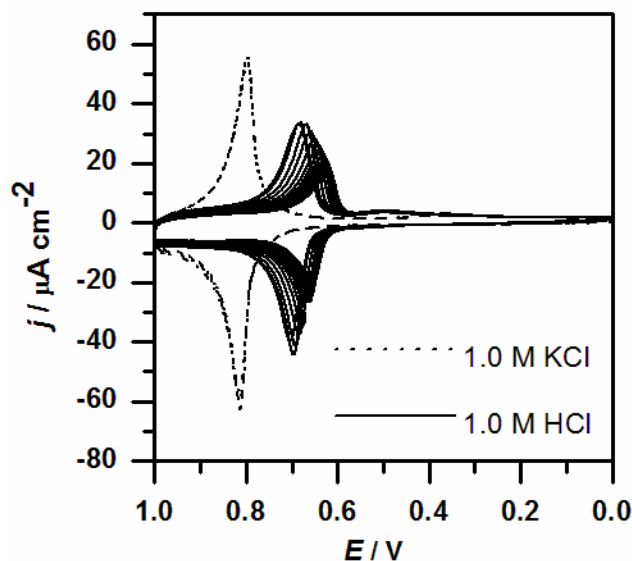


**Figure 19** CVs of InHCF films recorded in 1.0 M KCl (dashed line) and subsequently in 1.0 M HCl (solid line).

Figure 19 compares a CV recorded in 1.0 M KCl with a sequence of scans subsequently performed in 1.0 M HCl solution. In 1.0 M HCl, the peak height decreases for each scan unit reaching a stable value after about 15 cycles.

This trend in HCl is due to the greater affinity of  $K^+$  than for  $H^+$  toward intercalation in InHCF and to the contribution of the mixed species  $K_{(1-x)}H_xInFe(CN)_6$  in the first scans in HCl where  $x$  is noticeably different from the stable value of 1 it eventually will reach.

The subsequent CV recorded in the starting 1.0 M KCl solution overlaps the first one.

The kinetics of  $K^+$  intercalation has been explored by CVs performed with scan rates  $\nu$  in the  $0.001 - 0.500 \text{ V s}^{-1}$  range in 1.0 M KCl solutions at nominal pH values of 1.0, 2.0, 3.0, and 4.0, where  $H^+$  intercalation is negligible.

The peak heights were linearly dependent upon  $\nu^{1/2}$  at low scan rates and dependent upon  $\nu$  at high scan rates.

At high scan rates, the limiting factor is the supply of  $K^+$  at the electrode/solution interface (semi-infinite linear diffusion) while at low scan rates the limiting factor becomes the diffusion rate of  $K^+$  in InHCF. In the second case we have a surface confined electrochemical process. The transition from the confined process to the  $K^+$  supply depending process occurs roughly at the same  $\nu$  in different KCl solutions.

### 3.3.2 Indium Hexacyanoferrate reversible exchange capability

To investigate the electrochemical behavior in the presence of different mono or divalent metal cations, a CV was initially recorded in 1.0 M KCl; a second CV was subsequently performed with 1.0 M solutions of other cations, and finally a last CV scan was repeated in 1.0 M KCl. This protocol allows evaluation of the affinities of the test cations relative to that of  $K^+$ . Furthermore, the dependence of CVs upon the concentration has been studied for each metal cation in the  $1.0 - 1.0 \times 10^{-2}$  M range.

The CV study of InHCF was extended to supporting electrolyte cations other than  $K^+$  and  $H^+$ . The results are shown in Fig. 20 a and b. The replacement of  $K^+$  ions with another cation causes substantial changes in the peak shape and position. The shift in the peak potential relates to the ionic potential of the cation,<sup>18</sup> as has been noted previously for other Prussian Blue type of compounds.<sup>19,20</sup> Almost a linear dependence both for mono and divalent cations except for  $Li^+$  and  $Mg^{2+}$  was observed. It is worth noting that the findings of Fig. 20 must be referred only to the peak potentials and not to the peak intensity because the experiments were performed by using different InHCF film modified electrodes.

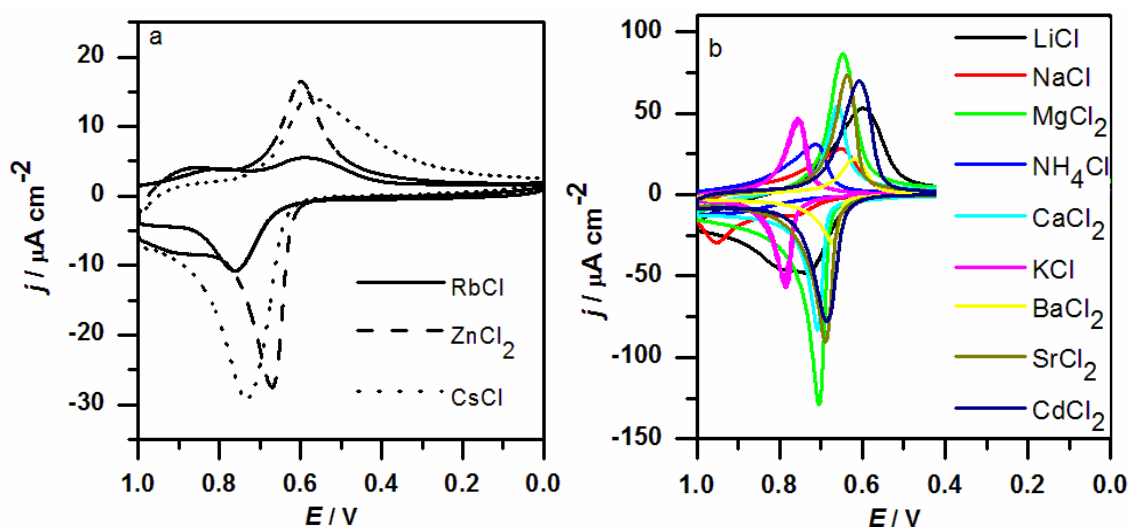
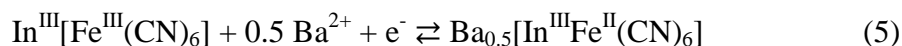


**Figure 20** CVs of InHCF films in 1.0 M RbCl, ZnCl<sub>2</sub> and CsCl solutions a) and in 1.0 M LiCl, NaCl, MgCl<sub>2</sub>, NH<sub>4</sub>Cl, CaCl<sub>2</sub>, KCl, BaCl<sub>2</sub>, SrCl<sub>2</sub> and CdCl<sub>2</sub> solutions b) at 0.1 V s<sup>-1</sup>.

When the final experiment in nominally neutral 1.0 M KCl is performed after testing in solutions with the other cations, CVs are obtained which are similar to the original one in KCl. The intensities in the final experiment are sometimes reduced, as expected for loss of the electroactive material; however, the phenomenon is absent when the experiments are run in 1.0 M KCl at pH  $\approx$  2.0. Figure 21 illustrates this behaviour in the case of barium chloride. The redox mechanism involves Ba<sup>2+</sup> insertion during reduction and its release during oxidation, in according with the following redox reaction:



The Nernst equation for reaction (5) reads (in volts)

$$E = k + 0.5 (0.059 \log[\text{Ba}^{2+}]) \quad (6)$$

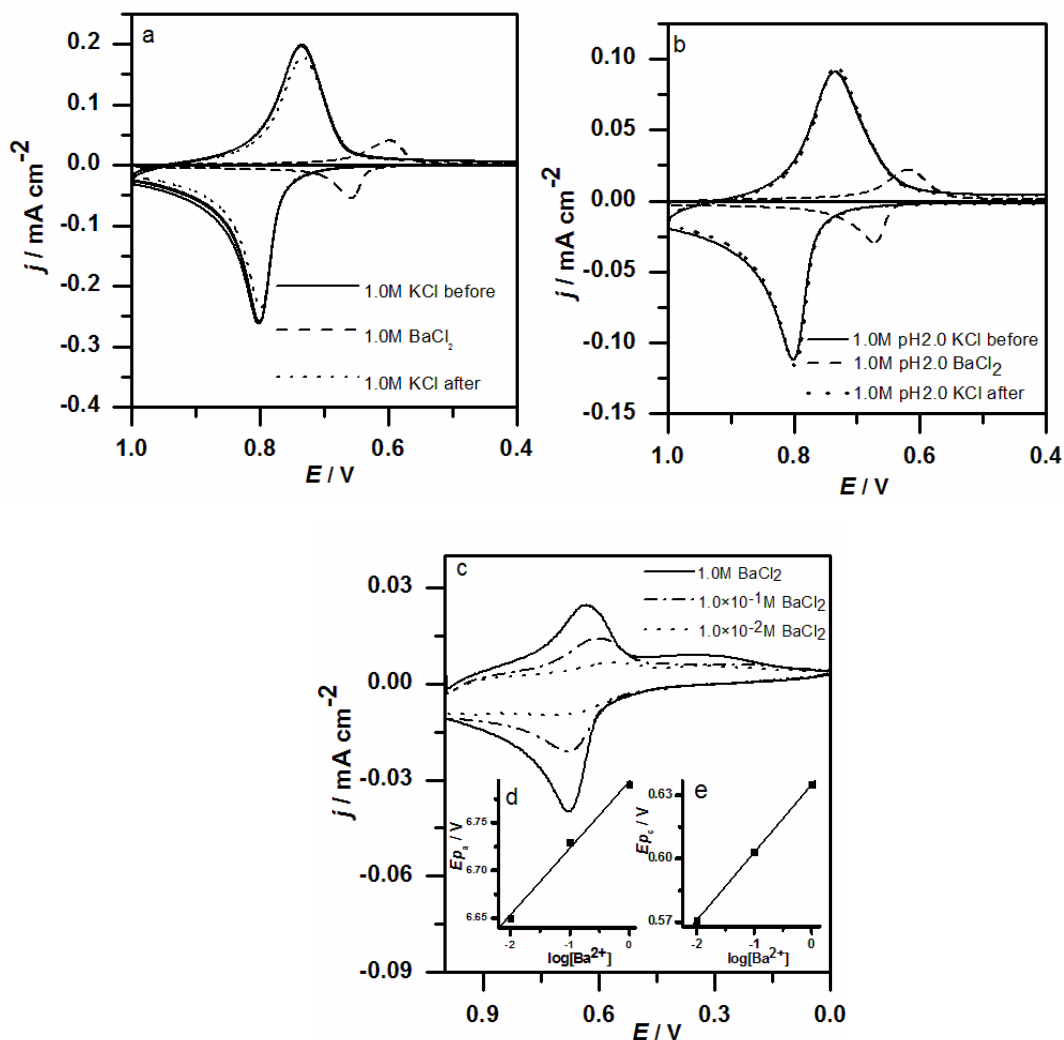


**Figure 21** CVs at 0.1 V s<sup>-1</sup> of an InHCF film in a) 1.0 M KCl and BaCl<sub>2</sub> solutions at native pH, b) 1.0 M KCl and BaCl<sub>2</sub> solutions at nominal pH = 2.0, c) in 1.0, 1.0 × 10<sup>-1</sup> and 1.0 × 10<sup>-2</sup> M BaCl<sub>2</sub> solutions. Insets d) and e) show an  $E_{p_a}$  (V) vs  $\log[\text{Ba}^{2+}]$ , slope of 7 mV/dec, and an  $E_{p_c}$  (V) vs  $\log[\text{Ba}^{2+}]$ , slope of 32 mV/dec.

The  $\text{Ba}^{2+}$  CVs have smaller intensities corresponding to a reduced insertion of  $\text{Ba}^{2+}$  and/or a thinner electroactive layer.

The CVs in  $\text{BaCl}_2$  solutions reported in Fig. 21 correspond to a stable behaviour achieved in about 10 cycles during which a substantial reduction of peak intensities and a decrease of the peaks potentials is observed (a similar phenomenon has been illustrated in Fig. 19). All the non- $\text{K}^+$  cations exhibit similar behaviours. The dependence of  $E_{p_c}$  upon the concentration of the monovalent cations ( $\text{Li}^+$ ,  $\text{Na}^+$ ,  $\text{K}^+$ ,  $\text{Rb}^+$ ,  $\text{Cs}^+$  and  $\text{NH}_4^+$ ) yield slopes in the 38 - 128 mV/dec range.

The predicted slope for divalent cations would be 59/2 mV/dec. Our data agree well with expectations in the case of  $\text{Sr}^{2+}$  and  $\text{Ba}^{2+}$  but higher slopes are found for  $\text{Cd}^{2+}$ ,  $\text{Sr}^{2+}$  and  $\text{Ca}^{2+}$ . From the morphology of the curves, it is possible to note a quasi-reversible process and consequently kinetic factors such as the electron transfer coefficient can influence the nernstian slope value.

As matter of fact, for all the investigated bivalent cations we never observe a partial substitution of In, coordinated to N atom, by the new other cations, as already observed in the case of  $\text{PB}^{21}$  where Iron coordinated to N atom, was partially replaced by  $\text{Ni}^{2+}$  and  $\text{Cd}^{2+}$  when cycled in solutions containing this cations.

The perfect electrochemical reversibility confirms the absence of any substitution of In, at least, in the time scale of the experiments; nevertheless the kinetic process may be is too slow to be detected. Further experiments will be needed in order to asses this hypothesis.

### **3.3.3 Electrochromic cell with Indium Hexacyanoferrate and Cobalt Hexacyanoferrate**

As a final part of this study, two Prussian Blue type of films were combined in a single cell in order to obtain a prototype of an electrochromic cell.

In the electrochromic window design, the window is an electrochemical cell in which two conducting glass panes are separated by an electrolyte material.

A film of InHCF (counter electrode) and a film of CoHCF (working electrode) was deposited on each of two ITO glasses. The electrolyte was 1.0 M KCl absorbed on filter paper separating the two films.

Figure 22 shows the CVs relative to the Pt quasi-reference electrode, which are characteristic of the CoHCF insoluble form.<sup>22</sup> Subsequent scans are similar, implying that the working electrode is stable.

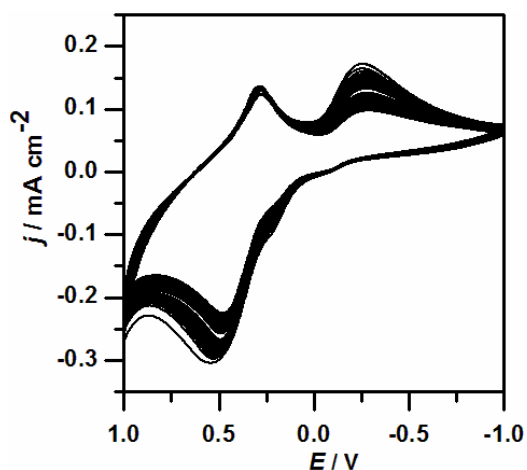


**Figure 22** The first fifty CVs of the CoHCF electrode in the cell with a InHCF electrode and 1.0 M KCl absorbed in filter paper.

The ITO/InHCF electrode changes transparency and color with charge but permits to study a wide range of electrochromic Prussian Blue analogues thanks to its capability to host and reversibly exchange different mono/divalent cations.<sup>23</sup> This is an example of electrochromic cell or “smart window”, as coined by Svensson and Granqvist<sup>24</sup> to describe windows that own electrochromism character, meaning they can change transmittance under different voltage.

### 3.4 Conclusion

The electrochemical behavior of InHCF has been investigated in detail.

InHCF films electrodeposited at nominal pH  $\approx$  2.0 are very stable in 1.0 M KCl acid solutions. In pure KCl, the CV peak intensities decrease by  $\sim$  50% in about 400 CV cycles and then stabilize. The influence of pH in the 0.0 - 4.5 range reveals a competition between insertion of H<sup>+</sup> and K<sup>+</sup>, leading to the formation of the mix compound  $K_{(1-x)}H_x\text{InFe}(\text{CN})_6$  that undergoes the following redox reaction:



The relative amounts of intercalated H<sup>+</sup> and K<sup>+</sup> have been evaluated from CVs at different pH and pK values (see Table 3).

Kinetics of the intercalation processes were also studied in 1.0 M KCl at different pH by changing the CV scan rate,  $\nu$ .

A linear dependence of intensity upon  $\nu$  at low scan rates and a  $\nu^{1/2}$  dependence at high scan rates is observed, as expected for a reaction that is a pure surface process (no diffusion limiting factor) at low scan rate that transitions to one where the diffusion of the counter ion in the film limits the current in the upper scan rate limit.

KInHCF reversibly exchanges the following cations:  $\text{Li}^+$ ,  $\text{Na}^+$ ,  $\text{K}^+$ ,  $\text{Rb}^+$ ,  $\text{Cs}^+$ ,  $\text{NH}_4^+$ ,  $\text{Mg}^{2+}$ ,  $\text{Ca}^{2+}$ ,  $\text{Sr}^{2+}$ ,  $\text{Ba}^{2+}$ ,  $\text{Cd}^{2+}$ ,  $\text{Zn}^{2+}$  and  $\text{H}^+$ . Relative to  $\text{K}^+$ , the intercalation kinetics of all the other cations is more sluggish and the CV peaks have lower currents.

However, the original performances are mostly restored when the electrode with the foreign cation is cycled in 1.0 M KCl solution. This capability of InHCF to reversibly exchange many monovalent and divalent cations makes it an excellent candidate for electrochromic devices or batteries needing a reservoir of these cations.

Finally, an electrochromic cell with CoHCF and InHCF films electrodeposited on two ITO glass electrodes separated by 1.0 M KCl electrolyte absorbed in filter paper was designed and assembled; as expected, the CV response of the CoHCF electrode is consistent with the electrochemical studies of this compound.

Future studies will use this type of cell to explore the electrochromic behavior of CoHCF in the presence of different cations in solution.

---

<sup>1</sup> De Tacconi NR, Rajeshwar K, Lezna RO (2003) *Chem. Mater* 15:3046-3062.

<sup>2</sup> Berrettoni M, Giorgetti M, Zamponi S, Conti P, Ranganathan D, Zanolto A, Saladino ML, Caponetti E (2010) *J PhysChem C* 114:6401–6407.

<sup>3</sup> Guadagnini L, Tonelli D, Giorgetti M (2010) *Electrochim Acta* 55:5036–5039.

<sup>4</sup> Zamponi S, Berrettoni M, Kulesza PJ, Miecznikowski K, Malik MA, Makowski O, Marassi R (2003) *Electrochim Acta* 48:4261–4269.

<sup>5</sup> Kulesza PJ, Faszynska M (1988) *J ElectroanalChem* 252:461-466.

<sup>6</sup> Malik MA, Horanyi G, Kulesza PJ, Inzelt G, Kertesz V, Schmidt R, Czirok E (1998) *J ElectroanalChem* 452:57-62.

<sup>7</sup> Kurdakova VV, Kondrat'ev VV, Levin OV, Malev VV (2002) *Russ J Electrochem* 38:1192–1199.

<sup>8</sup> Chen LC, Tseng KS, Ho KC (2002) *J Solid State Electrochem* 7:1-5.

<sup>9</sup> Tseng KS, Chen LC, Ho KC (2006) *Electroanalysis* 18:1306-1312.

<sup>10</sup> Chen SM (1996) *J ElectroanalChem* 417:145-153.

<sup>11</sup> Malev V, Kurdakova V, Kondratiev V, Zigel V (2004) *Solid State Ionics* 169:95–104.

<sup>12</sup> Chen SM (2002) *J ElectroanalChem* 521:29–52.

<sup>13</sup> Czirak E, Beskai J, Kulesza PJ, Inzelt G, Wolkiewicz A, Miecznikowski K, Malik MA (1996) *J ElectroanalChem* 405:205-209.

<sup>14</sup> Wang JY, Yu CM, Hwang SC, Ho KC, Chen LC (2008) *Solar Energy Materials & Solar Cells* 92:112–119.

<sup>15</sup> Jin Z, Dong S (1990) *ElectrochimActa* 35:1057-1060.

<sup>16</sup> Kulesza PJ, Malik MA, Miecznikowski K, Wolkiewicz A (1996) *J ElectrochemSoc* 143:L10-L12.

<sup>17</sup> Zhang S, Sun W, Zhang W, Qi W, Jin L, Yamamoto K, Tao S, Jin J (1999) *AnalyticaChimicaActa* 386:21-30.

<sup>18</sup> Chen SM, Chan CM (2003) *J ElectroanalChem* 543:161-173.

<sup>19</sup> Rutkowska IA, Stroka J, Galus Z (2008) *ElectrochimActa* 53:3870-3878.

<sup>20</sup> Barcena-Soto M, Scholz F (2002) *J ElectroanalChem* 521:183-189.

<sup>21</sup> Dostal A, Hermes M, Scholz F (1996) *J ElectroanalChem* 415:133-141.

<sup>22</sup> Kulesza PJ, Zamponi S, Malik MA, Berrettoni M, Wolkiewicz A, Marassi R (1998) *ElectrochimActa* 43:919-923.

<sup>23</sup> M. Ciabocco, M. Berrettoni, S. Zamponi, J. A. Cox, S. Marini, *Journal of Solid State Electrochemistry* 17 (2013) 2445-2452.

<sup>24</sup> E. L. Runnerstrom, A. Llordés, S. D. Lounis, D. J. Milliron, *Chem. Commun.*, 2014,50, 10555-10572.

## **4. Electrochemical process to selectively recover rare earth-elements by using Nickel Hexacyanoferrate (NiHCF) modified electrodes as ionic sieve**

### **4.1 Introduction**

The development and study of electrochemical sensors which offer attractive advantages of rapid and non-invasive analysis has become an interesting area of research in recent years.<sup>1</sup>

Chemically modified electrodes (CMEs) with Prussian blue analogues (PBAs) have been successfully employed in ion-sensing applications to introduce highly selective electrode responses.<sup>2</sup> The exchange of alkali cations during the redox reactions is the basis for the ion selectivity of these compounds.

In particular, nickel(II) hexacyanoferrate(II, III), NiHCF, is a mixed-valent inorganic analog of Prussian blue<sup>3,4</sup> useful for several technological applications, such as charge storage,<sup>5,6</sup> electroanalysis,<sup>7</sup> ion exchanger,<sup>8,9</sup> electrocatalysis,<sup>10,11</sup> and chemical sensor,<sup>12,13</sup> including electrochemical and biochemical sensing.

NiHCF films can be easily obtained on different electrodes by electrodeposition through potential cycling.<sup>14</sup> Studies indicate that NiHCF is deposited on an electrode in a rigid ordered structure having zeolitic properties<sup>15</sup> of macro-molecular crystal structures. Electrochemical reduction requires cation intercalation,<sup>16</sup> whereas oxidation requires cation expulsion, in both cases to maintain charge neutrality within the Metal Hexacyanoferrate matrix. The presence of two peaks, evident in  $K^+$  containing electrolytes, should be attributed to the existence of two stable forms of ferrocyanides, both electroactive and the peak at more positive potentials can be attributed to the major  $K^+$  presence.<sup>17</sup>

On the contrary, NiHCF voltammetric responses yield single sets of peaks in lithium and sodium electrolytes, reflecting the lower abilities of hydrated  $Li^+$  and  $Na^+$  to undergo ion pairing with Metal Hexacyanoferrates.<sup>18</sup> The ultrafast intercalation of  $Na^+$  and  $Rb^+$  in a thin film of NiHCF and the intercalation kinetics analysis were also reported in literature and they were ascribed to the high cation diffusion constant in the solid.<sup>19</sup>

NiHCF is characterized by well-defined, reversible and reproducible responses in different supporting electrolytes, its electrochemical behavior depends selectively on the type and on the concentration of the cation.

NiHCF is an excellent candidate for separations involving alkali cations as proved in literature.<sup>20,21</sup> This property is due to its ability to de-intercalate most of the intercalated ions via electrochemical modulation of the matrix charge density<sup>22</sup> and to its large ion intercalation capacity.

For this purpose, NiHCF is used in electrochemically switched ion exchange (ESIX) processes that use the selectivity of an ion intercalation compound to perform the separation.

Hence, our experiences with the solid state electrochemistry of Metal Hexacyanometallates and success with monovalent and divalent ion insertion made us question whether it would be possible to intercalate trivalent cations within the Metal Hexacyanometallate lattice and motivated us to explore these materials also for trivalent insertion.

While divalent ions have been shown to reversibly insert with long cycle life into Nickel Hexacyanoferrate<sup>23</sup> and PB thin films, suggesting that divalent alkaline earth cations ( $Mg^{2+}$ ,  $Ca^{2+}$ ,  $Sr^{2+}$ ,  $Ba^{2+}$ ) can reversibly insert into these materials,<sup>24,25</sup> no work demonstrates insertion of a range of trivalent ions in Nickel Hexacyanoferrate.

In this chapter, a detailed electrochemical study about the insertion-deinsertion of trivalent cations, and in particular rare earth elements (REE) in NiHCF lattice is reported in order to highlight its exchangeability properties useful in several technological applications including wastewater treatment, batteries and element purification.

The research was aimed at the possibility to use Nickel Hexacyanoferrates (NiHCF) as ionic sieves, for the rare earth elements selective recovery.

In fact, the growing industrial applications of the rare earth elements (REE) led to a growing interest in the research of new technologies for separation and recovery of rare earths. REEs are never found as free metals in the earth's crust and their naturally occurring minerals consist of mixtures of various REEs and non-metals.

The proposed procedure is focused on the selective separation of REEs through a very simple process and consisting in a loop of two electrochemical steps.

## 4.2. Experimental

### 4.2.1 Reagents and materials

All chemicals were reagent grade from Sigma-Aldrich ( $\text{NiCl}_2$ ,  $\text{K}_3\text{Fe}(\text{CN})_6$ ,  $\text{Er}(\text{NO}_3)_3$ ), Alfa-Aesar ( $\text{Gd}(\text{NO}_3)_3$ ,  $\text{La}(\text{NO}_3)_3$ ,  $\text{Dy}(\text{NO}_3)_3$ ), and Merck ( $\text{KNO}_3$ ). All experiments have been performed in air, at room temperature, and with deionized water.

### 4.2.2 Nickel Hexacyanoferrate electrochemical synthesis

Electrochemical measurements were performed by using a Model 660C (CH Instruments) electrochemical workstation and a standard three-electrode electrochemical glass cell (10 mL). The substrate materials of working electrode were glassy carbon (diameter=3 mm) or a 60 pores per inch (ppi) RVC (reticulated vitreous carbon) 3D mesh (1.0 cm×1.0 cm×3.0 cm, specific surface area  $4000 \text{ m}^2\text{m}^{-3}$ ) rinsed under ultrasound in alcohol followed distilled water prior to use. In the case of RVC, the electrical contact is ensured by Pt wire glued by epoxy conductive resin. A Pt counter electrode was used.

All potentials were recorded vs. Ag/AgCl in saturated KCl. The glassy carbon (GC) electrode was polished with a  $0.05 \mu\text{m}$  alumina slurry on a cloth and then rinsed with water; its pre-treatment consisted of cycling 20 times from 1.0 V to 0.0 V at  $0.050 \text{ V s}^{-1}$  in 1.0 M  $\text{KNO}_3$ . NiHCF film was deposited from a solution that contains  $1.0 \times 10^{-3} \text{ M NiCl}_2 \times 6\text{H}_2\text{O}$ ,  $1.0 \times 10^{-3} \text{ M K}_3\text{Fe}(\text{CN})_6$ , and 1.0 M  $\text{KNO}_3$  as supporting electrolyte.

## 4.3. Results and Discussion

### 4.3.1 Modified electrodes with Nickel Hexacyanoferrate (NiHCF): Electrochemical characterization

Figure 23 shows the cyclic voltammogram of a NiHCF film cycled in 1.0 M  $\text{KNO}_3$  solution. In view of the previous reports,<sup>26</sup> the following approximate formulas,  $\text{K}_2\text{Ni}^{\text{II}}[\text{Fe}^{\text{II}}(\text{CN})_6]$  and  $\text{KNi}^{\text{II}}_{1.5}[\text{Fe}^{\text{II}}(\text{CN})_6]$ , can be assigned to two predominant forms of electrodeposited NiHCF films.

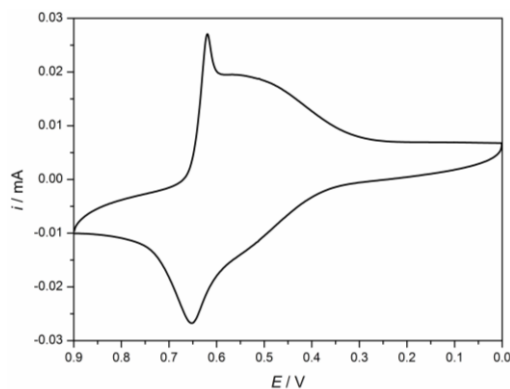


**Figure 23** CV of a NiHCF film at  $0.1 \text{ V s}^{-1}$  in a 1.0 M  $\text{KNO}_3$  solution.

To investigate the electrochemical behavior in the presence of different trivalent metal cations, CVs are recorded in various supporting electrolytes containing 1.0 M  $\text{Al}^{3+}$ ,  $\text{Cr}^{3+}$  and  $\text{In}^{3+}$ . A CV was initially recorded in 1.0 M KCl; a second CV was subsequently performed with 1.0 M solutions of other different trivalent cation, and finally a last CV scan was repeated when the electrode was switched back to the native solution containing  $\text{K}^+$ . This protocol allows to check the reversibility of the process and hence the evaluation of the affinities of the test cations relative to that of  $\text{K}^+$ .

The results are shown in Fig. 24 a, b and c for  $\text{Al}^{3+}$ ,  $\text{Cr}^{3+}$  and  $\text{In}^{3+}$ . The replacement of  $\text{K}^+$  ions with another cation causes substantial changes in the peak shape and position. The shift in the peak potential relates to the ionic potential of the cation, as has been noted previously for other Prussian Blue type of compounds or probably it may be due to the developing of new modified sites, as reported in the literature.<sup>27</sup>

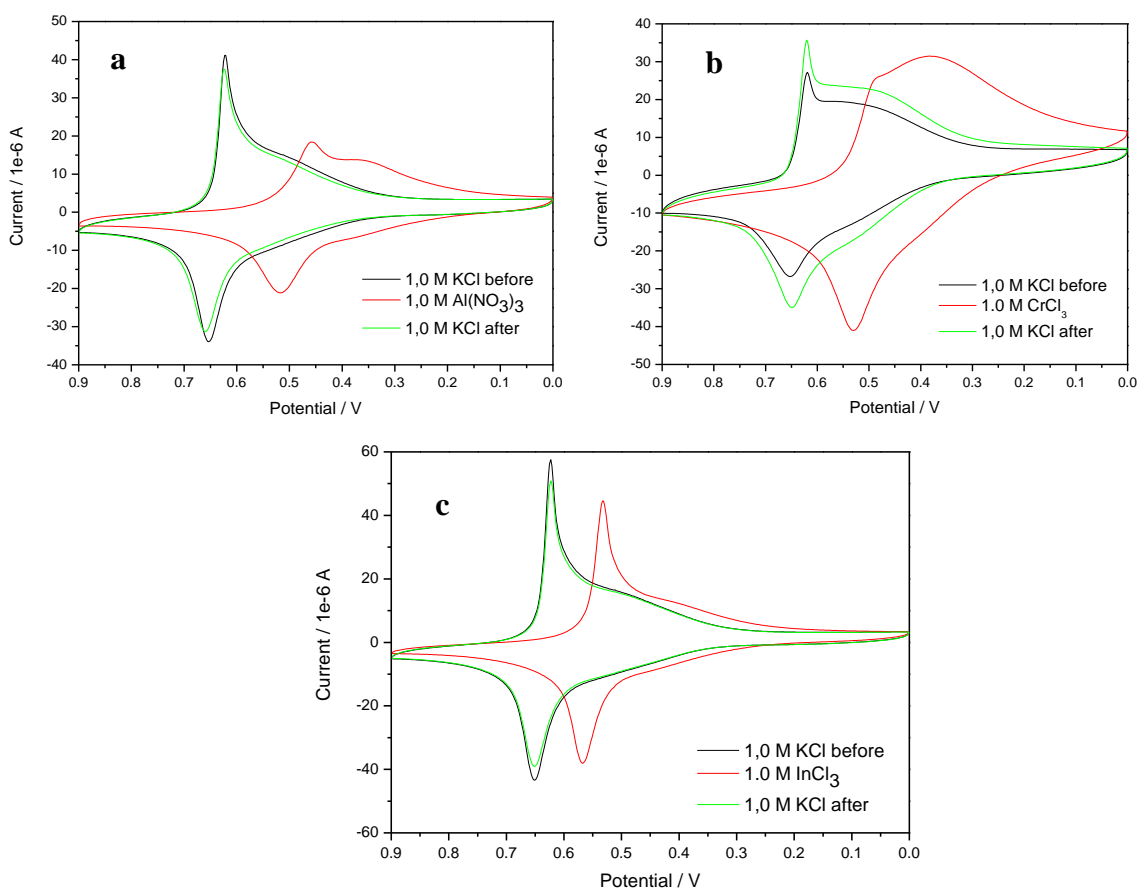


**Figure 24** CVs of NiHCF films in a) 1.0 M  $\text{Al}^{3+}$ , b)  $\text{Cr}^{3+}$  and c)  $\text{In}^{3+}$  solutions at 0.1  $\text{V s}^{-1}$ .

When the final experiment in nominally neutral 1.0 M KCl is performed after testing in solutions with the other cations, CVs are obtained which are similar to the original one in KCl. The intensities in the final experiment are sometimes reduced, as expected for loss of the electroactive material.

Cyclic voltammograms (CVs) demonstrate reversible insertion of all the investigated cations in NiHCF. Both the insertion voltages and the qualitative shapes of the CVs vary significantly as a function of the insertion ion. The presence of multiple cathodic and anodic peaks at different voltages in the data suggests that there are multiple electrochemical processes during the ion insertion, corresponding to ions inserting into these electrochemically distinct sites in the structure. However, the current understanding of ion insertion in PB analogues provides no comprehensive explanation for why electrochemical properties vary so significantly with the choice of insertion ion. The Rietveld refinement results reported in literature<sup>28</sup> suggest that vacancies and water molecules may facilitate ion insertion, but the detailed mechanism of ion insertion in PB analogues remains a topic of ongoing studies.

The kinetics of the intercalation relative to the different monovalent cations have been explored by CVs performed with scan rates in the 0.001–0.500 V s<sup>-1</sup> range in 1.0 M solutions. The peak heights were linearly dependent upon the scan rate at low scan rates and dependent upon the square root of the scan rate at high scan rates, according to the following Randles-Sevcik equation, describing the effect of scan rate on the peak current  $I_p$  in cyclic voltammetry:

$$i_p = 0.4463nFAc(nFvD/RT)^{1/2}$$

$n$  = Number of electrons

$F$  = Faraday's Constant 96,485 C/mole

$A$  = Electrode Area cm<sup>2</sup>

$D$  = Analyte Diffusion Coefficient (cm<sup>2</sup> s<sup>-1</sup>)

At high scan rates, the limiting factor is the supply of the monovalent cation at the electrode/solution interface (semi-infinite linear diffusion) while at low scan rates the limiting factor becomes the diffusion rate of the monovalent cation in NiHCF. In the second case, we have a surface-confined electrochemical process.

The peak separation,  $\Delta E_p = E_{pa} - E_{pc}$  became wider at higher scan rates than at lower scan rates, indicating a limitation arising from charge transfer kinetics.

These results suggest that the reaction kinetics change from a surface process to a diffusion-controlled process.

Subsequently, the stability of the film by repeated CV scans at  $0.1 \text{ V s}^{-1}$  was checked. Extended cycling of trivalent ions over 100 cycles demonstrates the high structural integrity of NiHCF even after such extended cycling. There is no evidence to suggest a change in crystal structure or decrease in crystallinity after cycling.

As a matter of fact, for all the investigated monovalent cations, a partial substitution of Ni, coordinated to the N atom, is never observed by the other new cations, as already observed in the case of PB where the iron coordinated to nitrogen atom was partially replaced by  $\text{Ni}^{2+}$  and  $\text{Cd}^{2+}$  when cycled in solutions containing these cations. The perfect electrochemical reversibility confirms the absence of any substitution of Ni, at least, in the time scale of the experiments; nevertheless, the kinetic process may be too slow to be detected.

To investigate the electrochemical behavior in presence of different rare earth cations, the previously detailed protocol was carried on, hence a CV was initially recorded in  $1.0 \text{ M KNO}_3$ ; a second CV was subsequently performed in  $1.0 \text{ M}$  solutions of rare earth cations, and finally the last CV scan was repeated in  $1.0 \text{ M KNO}_3$ . This protocol allows us the evaluation of the possible replacement of  $\text{K}^+$  with the tested rare-earth cations and, in the last step, the reversibility of the process. This procedure has been applied to different rare earth elements cations such as  $\text{La}^{3+}$ ,  $\text{Gd}^{3+}$ ,  $\text{Dy}^{3+}$  and  $\text{Er}^{3+}$ . These elements were chosen for their important applications and represent examples of light-group rare-earth elements “LREE” and heavy-group rare-earth elements “HREE”. Figure 25 shows the stability/reversibility process toward to the erbium nitrate.

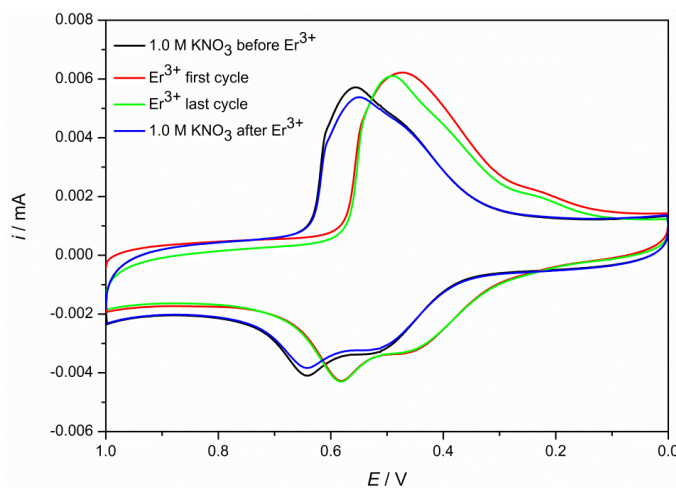


**Figure 25** CVs at  $0.1 \text{ V s}^{-1}$  of a NiHCF film in  $1.0 \text{ M KNO}_3$  and  $\text{Er}(\text{NO}_3)_3$  solutions at native pH.

The first cycle recorded in KNO<sub>3</sub> (black line) is almost coincident with the last (blue line) recorded after performing 100 cycles in a solution containing Er<sup>3+</sup> cations; thus confirming the perfect cation exchange reversibility and the stability of NiHCF in Er<sup>3+</sup> almost for 100 CVs.

Also in this case, the first (red line) and the last cycle (green line) are almost superimposed.

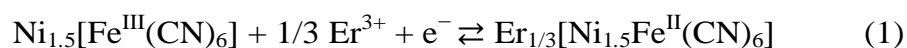
A perfect stability is observed with all the investigated cations. This feature, together with the perfect electrochemical reversibility, confirmed by the absence of any substitution of Ni or Fe, is a basic requirement in order to test these devices as selective molecular sieves.

Furthermore, the dependence of CVs upon the cation concentration has been studied for each rare-earth cation in the 1.0-1.0×10<sup>-2</sup> M range in order to assess the role of the rare earth cation in the electrochemical process.

The replacement of K<sup>+</sup> ions with another cation causes substantial changes in the peak shape and position.

The peak potentials shift can be related either to the radius of the hydrated cation, as has been noted previously for other Prussian Blue type of compounds<sup>29</sup> or to the ionic potential (ratio of ionic charge to radius) as reported by Scholz et al.<sup>30</sup>

The redox mechanism involves Er<sup>3+</sup> insertion during reduction and its release during oxidation, in accordance with the following redox reaction:



The Nernst equation for reaction (1) reads (in Volts)

$$E = k + \left( \frac{0.059}{3} \log[\text{Er}^{3+}] \right) \quad (2)$$

All the experiments, therefore, confirm the insertion/de-insertion mechanism of the tested rare earth elements as proved by the Nernstian slope values very close to the theoretical one of 19 mV.

This is a consequence of the zeolitic structure of the NiHCF characterized by open channels whose chemical-physical characteristics constitute the driving force for ion discrimination: the nature and the size of the ion are the limiting factors in order to be inserted into the structure.

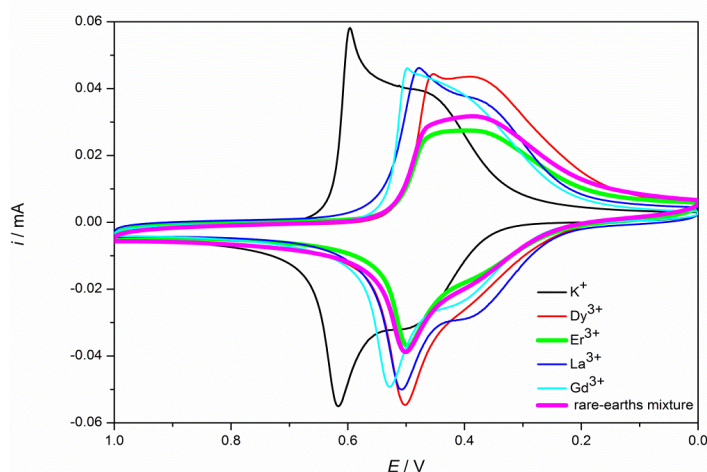
### 4.3.2 Ion-exchanging and selective recover of rare-earth elements with a Nickel Hexacyanoferrate modified electrode

Figure 26 reports the CVs of NiHCF films in 1.0 M  $\text{La}(\text{NO}_3)_3$ ,  $\text{Gd}(\text{NO}_3)_3$ ,  $\text{Dy}(\text{NO}_3)_3$  and  $\text{Er}(\text{NO}_3)_3$  solutions at  $0.1 \text{ V s}^{-1}$  and in a mixture containing all the investigated rare earth elements.

As matter of fact, the peak position and the morphology strongly depends on the nature of rare earth cations.

It is worth noting the perfect analogy between the CV in the solution containing the  $\text{Er}^{3+}$  alone and in the mixture containing all the rare earth elements.

The experiment is notable in order to hypothesize the selectivity of NiHCF toward to a specific cation.



**Figure 26** CVs at  $0.1 \text{ V s}^{-1}$  of a NiHCF film in 1.0 M  $\text{KNO}_3$ ,  $\text{RE}(\text{NO}_3)_3$  ( $\text{RE}=\text{La}$ ,  $\text{Dy}$ ,  $\text{Gd}$ ,  $\text{Er}$ ) solutions and in mixture containing rare-earth cations at native pH.

In order to check the feasibility and reliability of selective  $\text{Er}^{3+}$  recover from a mixture containing REE cations, experiments have been run by using a “Reticulated Vitreous Carbon“ (RVC) electrode as working electrode, providing very large electrochemical active surface and area/volume ratio.

Despite the dramatic increase of the electrochemical active surface, the electrochemical deposition leads to a similar CV morphology than the one reported in Figure 23 with well-defined peaks and with greater anodic and cathodic current intensities.

The procedure consists of performing initially CVs in 1.0 M  $\text{KNO}_3$ ; subsequently CVs in the solution containing the equimolar mixture of  $\text{La}^{3+}$ ,  $\text{Gd}^{3+}$ ,  $\text{Dy}^{3+}$  and  $\text{Er}^{3+}$ , and going back, CVs in 1.0 M  $\text{KNO}_3$ . At the beginning, this protocol was carried on for 20 cycles.

The analysis of the  $\text{KNO}_3$  solutions rare earth cation-free, performed by X-ray fluorescence and ICP-OES, indicated an  $\text{Er}^{3+}$  concentration of about 0.1 M in 20 cycles, and the total absence of the other rare earth cations. Hence in 20 cycle, 10%  $\text{Er}^{3+}$  has been recovered from an equimolar mixtures of  $\text{La}^{3+}$ ,  $\text{Gd}^{3+}$ ,  $\text{Dy}^{3+}$  and  $\text{Er}^{3+}$ .

The following measurements confirm that  $\text{Er}^{3+}$  concentration is proportional to the performed cycles number.

It is worth noting that by increasing the oxidation state of the insertion ion from +1 to +3, a negligible impact on insertion chemistry in NiHCF is observed.

This aspect is counterintuitive since the charge state is usually the strongest determining factor of electrochemical insertion in other materials. These observations suggest a high degree of charge screening, likely from water molecules in the hydration shell or in the structure which minimizes the electrostatic interaction between the insertion ion and the host ions that make up NiHCF. The unhydrated crystal ionic radii of the multivalent insertion ions in octahedral geometry<sup>31</sup> are smaller than the channel radius in NiHCF, so if the ions are not hydrated, all of these ions should be able to diffuse through the channels.

However, these ions are most likely at least partially hydrated since there appears to be a high degree of charge screening that enables the rapid insertion kinetics of trivalent ions. This is supported by the Rietveld refinement results reported in literature,<sup>28</sup> which suggest that trivalent ions require additional hydration to remain in the structure. It is unclear if hydrated insertion ions are diffusing through alternative pathways, such as the proposed ferricyanide vacancy pathway<sup>32</sup> or if ions are hydrated only along the axes during diffusion.<sup>33</sup>

The first pathway is supported by X-ray fluorescence (XRF) data providing the stoichiometry of the compounds, and in particular it is worth underlining that Ni/Fe stoichiometric ratio approaches the limit value (1.8) of the so called "insoluble" form, rich in vacancies of the  $\text{Fe}(\text{CN})_6^{3-}$  group, and the value is far from 1, that is characteristic of the so called "soluble" form.

As previously reported, depending upon the degree of peptization, Metal hexacyanoferrates can be described in the "soluble" and the "insoluble" form.

Basically, the insoluble form lacks one-fourth of the  $\text{B}(\text{CN})_6^{3-}$  units, which are replaced by coordinated and noncoordinated water molecules.

In addition, many of the multivalent ion CVs exhibit multiple cathodic and anodic peaks at distinct voltages, as shown in Fig. 27, which is consistent with ions inserting into multiple distinct crystallographic sites (consistent with the structural results and with the electrochemical results obtained at different scan rates shown in Fig. 27) or undergoing different degrees of dehydration during insertion.<sup>33</sup>

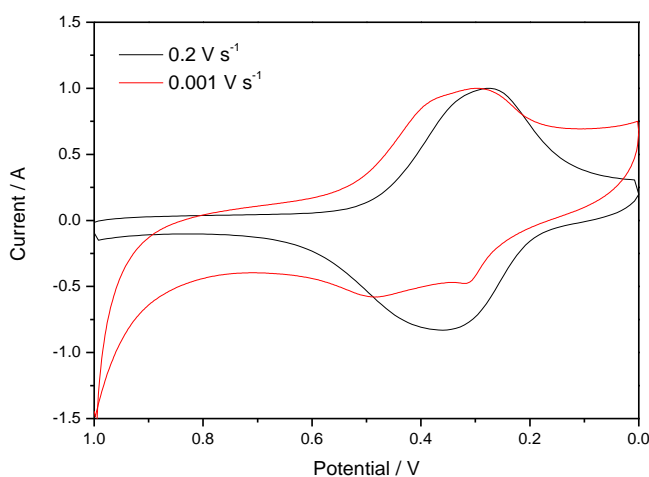


**Figure 27** CVs of NiHCF film recorded in 1.0 M Cr(NO<sub>3</sub>)<sub>3</sub> solution at 0.2 V s<sup>-1</sup> (red line) and 0.001 V s<sup>-1</sup> (black line).

The variations in insertion voltage and kinetics of different multivalent ions reflect the complex mechanisms during multivalent ion insertion, and these mechanisms remain a topic of ongoing study.

Anyway, the experiments point toward a novel vacancy-mediated ion insertion mechanism that reduces electrostatic repulsion and helps the observed rapid ion insertion. The results suggest a new approach to multivalent ion insertion that may help to advance the understanding of this complex phenomenon.

### 4.3 Conclusion

Physical and structural properties make NiHCF ideal for monovalent and trivalent ion reversible electrochemical insertion, never before observed in any material.

Cyclic voltammograms demonstrate reversible insertion of different trivalent ions, most of which come from the rare earth series of elements.

The shapes of the cyclic voltammograms are generally more poorly defined than those of monovalent ion insertion, and trivalent ions appear to insert gradually over a wider range of voltages.

Each voltammogram exhibits multiple cathodic and anodic peaks separated by 100 to 300 mV, which suggests a complex insertion mechanism with more thermodynamically distinct insertion sites for each ion. This may correspond to variations in the level of dehydration required for ions to be inserted into different sites within the structure.

Findings demonstrated that it is possible to exchange  $K^+$  reversibly and selectively with a rare-earth cation present in solution under cyclic voltammetry experiments.

It is worth noting a perfect stability of the NiHCF film in the investigated rare earth cations. This feature, together with the perfect electrochemical reversibility, confirmed by the absence of any substitution of Ni or Fe, plays a key role in this study and represents the basic requirement in order to test these devices as selective molecular sieves.

The possibility to modulate the metal linked to N or C in Metal-Hexacyanometallates, let to give the theoretical base for a systematic investigation in order to search for selective electrodes toward to other rare earth cations.

The particular characteristic of this process based on a closed cycle, let to realize flow systems using limited quantities of restoring solutions.

- 
- <sup>1</sup> M. Esteban, A. Castano *Environ. Int.* 35 (2009) 438-449.
- <sup>2</sup> Norma R. de Tacconi, Krishnan Rajeshwar, Reynaldo O. Lezna, *Chem. Mater.* 15 (2003) 3046-3062.
- <sup>3</sup> A. B. Bocarsly, S. Sinha, *J. Electroanal. Chem.* 137(1982)157.
- <sup>4</sup> S. Sinha, B. D. Humphrey, A. B. Bocarsly, *Inorg. Chem.* 23(1984)203.
- <sup>5</sup> Richard Y. Wang, Colin D. Wessells, Robert A. Huggins, Yi Cui, *Nano Lett.* 2013, 13, 5748–5752.
- <sup>6</sup> Shenglan Yu, Yong Li, Yunhao Lu, Ben Xu, Qiuting Wang, Mi Yan, Yin Zhu Jiang, *Journal Power Sources* 275 (2015) 45-49.
- <sup>7</sup> Mohammad Hossein Mashhadizadeh, Taher Yousefi, Ahmad Nozad Golikand, *Electrochim Acta* 59 (2012) 321– 328.
- <sup>8</sup> T. Vincent, C. Vincent, Y. Barré, Y. Guari, G. Le Saout, E. Guibal, *J. Mater. Chem. A*, 2014, 2, 10007.
- <sup>9</sup> Senliang Liao, Chunfeng Xue, Yonghong Wang, Junlan Zheng, Xiaogang Hao, Guoqing Guan, Abudula Abuliti, Hui Zhang, Guozhang Ma, *Separation and Purification Technology* 139 (2015) 63–69.
- <sup>10</sup> Annamalai Senthil Kumar, Palani Barathi, K. Chandrasekara Pillai, *Journal of Electroanalytical Chemistry* 654 (2011) 85–95.
- <sup>11</sup> N.S. Sangeetha, S.Sriman Narayanan, *Analytica Chimica Acta* 828 (2014) 34–45.
- <sup>12</sup> Roger J. Mortimer, Paulo J.S. Barbeira, Ana F.B. Sene, Nelson R. Stradiotto Talanta 49 (1999) 271–275.
- <sup>13</sup> Jin Qiang Ang, Binh Thi Thanh Nguyen, Chee-Seng Toh, *Sensors and Actuators B* 157 (2011) 417– 423.
- <sup>14</sup> M.A. Malik, K. Miecznikowski, P.J. Kulesza, *Electrochim. Acta* 45 (2000) 3777.
- <sup>15</sup> L. F. Schneemeyer, S. E. Spengler, D. W. Murphy, *Inorg. Chem.* 24(1985)3044.
- <sup>16</sup> Marcin A. Malik, Pawel J. Kulesza, Roberto Marassi, Francesco Nobili, Krzysztof Miecznikowski, Silvia Zamponi, *Electrochimica Acta* 49 (2004) 4253–4258
- <sup>17</sup> P. J. Kulesza, K. Brajter, E. Dabek-Zlotorzynska, *Anal Chem.* 59(1987)2776.
- <sup>18</sup> J. Bácskai, K. Martinez, E. Czirok, G. Inzelt, P. J. Kulesza, M. A. Malik, *J. Electroanal. Chem.* 385(1995)241.
- <sup>19</sup> Takayuki Shibata and Yutaka Moritomo, *Chem. Commun.* 2014, 50, 12941
- <sup>20</sup> S. D. Rassat, J. H. Sukamto, R. J. Orth, M. A. Lilga, R. T. Hallen, *Sep. Pur. Technol.* 15(1999)207.
- <sup>21</sup> L. J. Amos, A. Duggal, E. J. Mirsky, P. Ragonesi, A. Bocarsly, P. A. Fitzgerald-Bocarsly, *Anal Chem.* 60(1988)245.
- <sup>22</sup> Jeerage, K. M. University of Washington; Seattle, WA, 2001
- <sup>23</sup> R. Y. Wang , C. D. Wessells , R. A. Huggins , Y. Cui , *Nano Lett.* 2013 , 13 , 5748 .
- <sup>24</sup> Chen, S.-M. *J. Electroanal. Chem.* 2002, 521, 29–52.
- <sup>25</sup> Mizuno, Y.; Okubo, M.; Hosono, E.; Kudo, T.; Zhou, H.; Ohishi, K. *J. Phys. Chem. C* 2013, 117, 10877–10882
- <sup>26</sup> Zamponi S, Berrettoni M, Kulesza PJ, Miecznikowski K, Malik MA, Makowski O, Marassi R (2003) *Electrochim. Acta* 48:4261-4269
- <sup>27</sup> R. W. Murray, in A. J. Bard Ed. “*Electroanalytical Chemistry Series vol. 13*).
- <sup>28</sup> *Adv. Energy Mater.* 2015, 5, 1401869
- <sup>29</sup> Ciabocco M, Berrettoni M, Zamponi S, Cox JA (2013) *J Solid State Electrochem* 17:2445-2452
- <sup>30</sup> Scholz F, Dostal A (1995) *Angew Chem* 107:2876-287
- <sup>31</sup> R. D. Shannon , *Acta Crystallogr. Sect. A* 1976 , 32 , 751
- <sup>32</sup> S.-I. Ohkoshi , K. Nakagawa , K. Tomono , K. Imoto , Y. Tsunobuchi , H. Tokoro , *J. Am. Chem. Soc.* 2010 , 132 , 6620
- <sup>33</sup> F. Scholz , A. Dostal , *Angew. Chem. Int. Ed.* 1996 , 34 , 2685

## **5. Electrochemically assisted deposition of an ormosil film to obtain Cobalt Hexacyanoferrate (CoHCF) nanorod array and application to electroanalysis**

### **5.1 Introduction**

Sol-gel-based porous materials have found many applications in chemistry, biology and material science as chemical sensors, chromatographic stationary phases, adsorbents, catalytic supports and nanosize reactors.<sup>1-6</sup> Sol-gel chemistry has been first discovered in 1840s by Ebelman<sup>7</sup> that synthesized glass-like substrate, SiO<sub>2</sub>, during hydrolysis of tetraethylortosilicate (TEOS) at low pH; however, extensive study in this field was since 1930. Further, research showed that inorganic gels formed a network with characteristic porosity,<sup>8</sup> which was proved by Hurd in 1938.<sup>9</sup> He proposed a new theory of a polymeric networks formed by silicic acid surrounded by liquid phase. Sol-gel chemistry received significant interest when the monolithic gels were formed at room temperature and converted to a glass by continuous drying of the gel in 1970s.<sup>10-12</sup>

Rapid expansion of sol-gel technology allowed to synthesize wide range of homogeneous inorganic oxide materials at low temperature and obtain specific properties, such as optical transparency, chemical durability, hardness, thermal resistance and tailored porosity.<sup>12,13</sup> Nowadays, sol-gel process is used to obtain wide range of composite materials of controlled morphology e.g. aerogel, xerogels, thin and thick films, nm-size particles and monoliths, which exhibit specific electronic and optical properties.<sup>14-24</sup>

Application of organic-inorganic hybrids in electrochemistry has received a lot of attention as a potential electrode modifiers, because of their porosity displaying large surface area and mechanical stability.<sup>18,19, 25-34</sup> The high number of organic functional groups and open structure increases the sensitivity of electrochemical response, allowing fast access of the analyte and incorporation of catalyst used in electrochemical sensors and biosensors.<sup>28,35,36</sup> Additionally, application of specific organic alkoxy silanes can improve the detection of the analyte and discriminate potential interferences.<sup>37-44</sup> Of great importance for sensing and catalysis is to fabricate thin films of controlled porosity that will provide direct access to the electrode surface and exhibit size exclusion properties. A typical mesoporous silica sol-gel films with ordered channels are prepared by dip-coating or spin-coating of surfactant doped sol precursor solution onto the electrode surface.<sup>45-48</sup>

Walcarius and coworkers<sup>49</sup> reported an easy and fast way of electrochemical deposition, which induces a self-assembly of surfactant-templated (organo)silica thin films on the electrode surface, creating mesopore channels oriented perpendicular to the electrode surface. His work was based on previous report by Mandler and coworkers,<sup>50</sup> that obtained sol-gel film, based on electrochemical generation of condensation catalyst, hydroxyl ions. This was achieved by applying a constant negative potential, which caused a local increase in pH near the electrode surface and allowed controllable deposition of methyltrimethoxysilane film, MeTMOS, at the electrode surface.

However, Walcarius and coworkers<sup>49</sup> further explored surfactant-templated mesopores film formation process obtaining pores normal to the electrode surface and showed that the specific thickness (100 nm) of the film is strictly dependent on deposition time (10 s), suitable cathodic potential and electrode material.

The fundamental step in controlling the porosity is the selection of the pH for the catalysis of sol-gel processing. Acid catalysis yields microporous solids, whereas under basic conditions the product is mesoporous. The difference is related to the relative rates of the hydrolysis and condensation steps of metal alkoxide precursors. When the process is base catalyzed, a relatively rapid condensation reaction leads to a highly branched product that is less compact than that formed when rapid hydrolysis under acidic conditions dominates. Hence, when the goal is to coat an electrode with a sol-gel film, control of the pH at the surface via an electrochemical reaction is a useful method.

As initially reported by Mandler and coworkers, formation of a sol-gel film on a conducting surface can be performed by applying a sufficiently negative potential to a weakly buffered sol to generate hydroxide ion that catalyzes the deposition. Likewise, at a positive potential, hydrogen ion generation catalyzes the formation of microporous sol-gel films. Cox and coworkers,<sup>51</sup> showed that application of suited positive potential can create microporous sol-gel film of controlled thickness and pores that are perpendicular to the electrode surface.

To extend the range of pore size in sol-gel films, templates have been employed; examples include organized surfactants and latex beads.

The goal is to obtain nanostructured particles for their improved electronic, optical, and electrocatalytic properties based upon their size, distribution, and morphology.

Due to the increased surface area and/or nanosize effect, these materials show increased reactivity than their bulk counterparts. Several synthesis strategies have been studied; common examples include electrospinning method and solvothermal synthesis.

However, they require expensive equipment and/or harmful organic chemicals; hence, a number of studies have targeted the development and implementation of simple synthesis strategies for fabrication of catalytically active, nanostructured materials.

Among these initiatives is the use of synthesis within spatially confined domains and particularly relevant to the present study is the processing of sol–gels with additives to the precursor sol that result in controlled nanodomains in films.

Electrochemically assisted deposition of a sol–gel film in combination with polystyrene templates has been used to achieve films of controlled porosity.

In particular, thin films of organically modified silica with 20-nm channels were fabricated in this work by combining electrochemically assisted sol–gel processing of a trimethylmethoxysilane precursor with modification of a glassy carbon electrode by electrostatic attachment of 20-nm sulfonated polystyrene (PSS) beads as templates to a sub-monolayer of 3-aminopropyltriethoxysilane (APTES). PSS and APTES were dissolved from the dried film in chloroform.

The pore geometry was sufficiently well defined to permit immobilization of electrochemical catalysts within the void volumes.

In the current study, Cobalt Hexacyanoferrate (CoHCF) nanorods were electrochemically grown within these channels, obtaining nanosized CoHCF.

Among the Metal Hexacyanoferrates, CoHCF is of particular interest from both fundamental and practical perspectives due to several reasons: both cobalt and iron exist in two oxidation states (II, III) leading to a multitude of compound stoichiometries and redox situations; CoHCF has unique electrochromic properties with color changes not only dependent on the oxidation states of the Co and Fe redox centers, but also on the nature of the co-cation imbibed by the compound during electroreduction.

CoHCF shows reversible thermochromism in the temperature range of 25–85°C; it exhibits the phenomenon of the reversible photoinduced magnetization; and importantly, CoHCF shows good electrocatalytic activity toward a variety of biologically important substrates, such as ascorbic acid, dopamine, *b*-nicotinamide adenine dinucleotide, nitrite, hydrazine, *p*-chlorophenol, and hydroxylamine etc.

Hence, the electrocatalytic activity of nanosized CoHCF was investigated and compared to that of the corresponding bulk material; in this study the test system was the oxidation of L-cysteine.

### 5.1.1 Sol-gel chemistry and processing

The sol-gel processing is based on growth of inorganic networks, which involved three step process. First, the colloidal suspension (particles in range of 1 μm to 1 nm) of precursor solution (sol) is prepared. Then the sol solution undergoes gelation step and forms networks by in a liquid phase (gel)<sup>11</sup> (Fig. 28). There are two main sol-gel precursors used in film formation: organic alkoxy silanes (MeTMOS) and the most commonly used inorganic tertaalkoxy silane (TEOS, TMOS).<sup>52</sup> However, other alkoxides precursors such as borates, titanates and aluminates are also used with combination of TEOS.

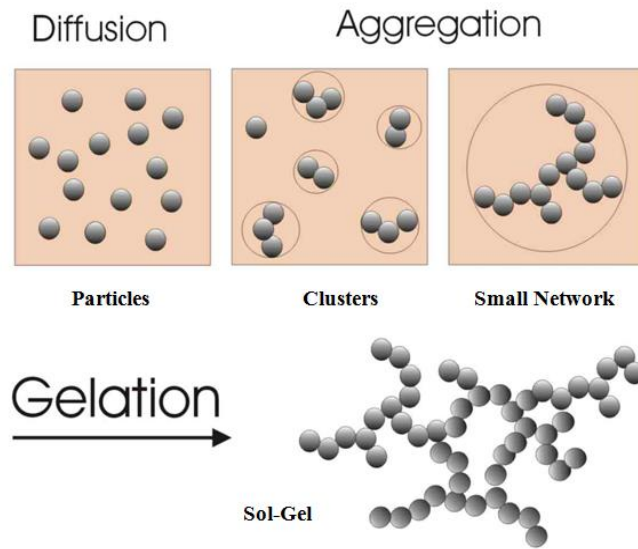
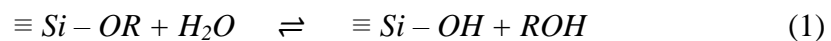


**Figure 28** Sol-gel formation from the precursor solution through diffusion, aggregation and gelation process.

### 5.1.2 Hydrolysis and condensation

Sol-gel processing is usually described by three reactions: hydrolysis, condensation and polycondensation that are catalyzed by acid ( $H^+$ ) or base ( $OH^-$ ), as illustrated in the reactions below 1-3. The type of the catalyst changes the structure and properties of sol-gel material.

#### HYDROLYSIS



#### ALCOHOL CONDENSATION



#### WATER CONDENSATION



Typically hydrolysis and condensation reaction occurs spontaneously and almost simultaneously. However, at low pH the rate of hydrolysis reaction is much faster than condensation resulting in protonation of alkoxide group, which withdraws electron density from silicon atom making it subjected to water attack. Next, the condensation reaction undergoes substitution of protonated silanol groups.

On the other hand, at high pH, in the presence of base catalyst, water dissociates to produce hydroxyl anion, which attack silicon atom. The rate of the condensation reaction is relatively faster and involves nucleophilic attack of deprotonated silanol groups on neutral silicate. The rate of hydrolysis and condensation is very important and in electrochemically assisted deposition of sol-gel films results in different porosity of the film.

### **5.1.3 Gelation**

After hydrolysis and condensation resulting silica particles form a clusters, which further aggregate and form a silica networks in gelation process. This can be determined by initial increased viscosity and low elasticity of sol. The gel elasticity increases with time; however, it is very difficult to predict gel time. One of the most popular techniques measuring the gelation time is viscoelastic response of the gel as a function of shear rate, reported by Sacks and Sheu.<sup>53,54</sup>

### **5.1.4 Aging**

The aging process occurs long after the gel point, during which the number of networks increases due to the polymerization or further condensation reaction. This is due to the high number of labile hydroxyl group. Next, the expulsion of liquid from pores and spontaneous shrinkage of gel are known as a syneresis. This process is increased with temperature and concentration of precursor in the sol. Further formation of large particles is known as a coarsening process, which is affected by the pH, temperature, concentration and type of the precursor. The last stage is the transformation step when the liquid separates from the solid into two phases. Typically during the aging process, the effective surface area decreases and the pores size increases.<sup>56,57</sup>

### **5.1.5 Drying**

Further shrinkage of gel occurs during the drying process, which involves loss of water and alcohol. The rapid evaporation of the liquid from the pores can change the structure of the gel and causing cracking.<sup>58</sup>

### **5.1.6 Electrochemically assisted deposition of sol-gel films**

Modification of the electrode surface with sol-gel films was typically achieved by spin-coating or dip-coating methods.<sup>52,59</sup>

As previously described, novel routes for electrochemical deposition of sol-gel films have been developed by Mandler and coworkers.<sup>60</sup> They induced the deposition of sol-gel films by applying positive or negative potential, which caused local decrease or increase of pH near the electrode surface due to the oxidation or reduction of water.<sup>61,62</sup>

Application of this method allowed for synthesis of wide range of sol-gel films on many different conductive surfaces from many different precursors such as zirconia, silica and titania.<sup>62-64</sup> These films were successfully applied in dye entrapment, corrosion protection and electroanalysis. The main advantage of this method over dip-coating and spin-coating is nm thick sol-gel film which can be obtained by controlling the value of applied potential and deposition time. Additionally, specific porosity of the film can be achieved by inclusion of surfactant and polystyrene spheres.<sup>49,65</sup>

## **5.2. Experimental**

### **5.2.1 Reagents and materials**

The precursor to the formation of the organically modified silica (ormosil) film was trimethylmethoxysilane (99%) from Sigma-Aldrich (Milwaukee, WI) with 2-propanol (99.5 %) as the diluent (Alfa Aesar, Ward Hill, MA). Prior to electrochemically assisted deposition of the ormosil, the electrode surface was modified, first, with 3-aminopropyltriethoxysilane (99%), APTES, obtained from Sigma-Aldrich (St. Louis, MO) and, second, with 20-nm-diameter sulfonated polystyrene beads, PSS, obtained in an 8%(w/v) suspension from the Molecular Probes® unit of Life Technologies Corp. (Eugene, OR). The other chemicals were reagent grade.

Cyclic voltammetry was performed with glassy carbon (GC) electrodes, 3.0 mm diameter, obtained from Bioanalytical Systems (West Lafayette, IN).

The ormosils imaged by electron microscopy were deposited on indium tin oxide (ITO) sheets from Delta Technologies, Limited (Stillwater, MN).

The ITO was cut into ca. 1.5 cm squares, a portion of which was isolated with a 0.5-cm (diameter) O-ring to serve as the working electrode. A 1-cm cylinder in an opening above the O-ring was connected to a sample cell (Teflon).

### 5.2.2 Fabrication of microporous silica sol-gel film and immobilization of nanobeads

The electrodes were modified by the following sequence: chemisorption of aminopropyltriethoxysilane (99%), APTES, ion-exchange of sulfonated polystyrene, PSS, onto the positively charged APTES sites, electrochemically assisted deposition of the ormosil, and removal of the APTES and PSS.

Unless otherwise stated, the first of these steps was the chemisorption of 0.5–50 mmol dm<sup>-3</sup> APTES solution in methanol on the electrode for 20 min. After rinsing, 20 nm (dia.) beads of PSS was immobilized by ion-exchange onto the APTES sites by immersion in a 1:1 dilution of the commercial 20 nm PSS suspension in water for 30 s.

Subsequently, an ormosil film on this modified electrode was deposited by an electrochemically assisted process adapted from Mandler and coworkers but with H<sup>+</sup> as the catalyst and with a template for the channels.

Hence, the GC|APTES-PSS electrode was rinsed and transferred to an aged (for 60 min) sol that was prepared by mixing 5.0 mL of 0.1 mol dm<sup>-3</sup> LiClO<sub>4</sub> in 2-propanol with 2.5 mL H<sub>2</sub>O, adjusting the pH to 5.0 with 0.1 mol dm<sup>-3</sup> HCl, and slowly adding 2.0 mL of trimethylmethoxysilane. A potential of 1.5 V vs. Ag | AgCl (to generate hydronium ion as the processing catalyst) was applied for 20 min during which the solution was stirred slowly to avoid inhomogeneities in the deposited film.

The formation of the film is accompanied by a decrease in the current during the first 15 min, which is due to gradual blocking of the electrode surface areas not protected with PSS.

The importance of the H<sup>+</sup>-catalyzed sol-gel formation is that the resulting ormosil phase is microporous, which makes this portion of the film essentially an insulator so that only the template channels are electrochemically active pathways.

Copious evolution of gas was not observed under this condition.

The electrode was slowly withdrawn while potential was still applied, and the excess sol was removed by capillary action onto a tissue contacted to the electrode casing. Finally, the electrode was air-dried overnight, and the APTES-PSS was dissolved in chloroform. After rinsing with fresh chloroform, the film was dried overnight.

It should be noted that the potential must be selected to prevent excessive generation of gaseous products. Indeed, the intentional generation of H<sub>2</sub> has been used, as shown in literature, to form macropores during electrochemically assisted formation of a sol-gel film.

### 5.2.3 Preparation of ITO or GC|npSG|CoHCF electrodes

The deposition of the Cobalt Hexacyanoferrate (CoHCF) film onto the GC electrode coated with an ormosil film with templated, 20-nm pores, GC|ormosil (20-nm pores), was performed in a freshly prepared solution containing  $3.0 \times 10^{-4} \text{ mol dm}^{-3}$   $\text{K}_3\text{Fe}(\text{CN})_6$  and  $3.0 \times 10^{-4} \text{ mol dm}^{-3}$   $\text{CoCl}_2$ .

When the test electrode was GC coated with ormosil that lacked template channels, this solution was  $2.5 \times 10^{-3} \text{ mol dm}^{-3}$   $\text{K}_3\text{Fe}(\text{CN})_6$  and  $2.5 \times 10^{-3} \text{ mol dm}^{-3}$   $\text{CoCl}_2$ . The supporting electrolyte was  $1.0 \text{ mol dm}^{-3}$  KCl in both cases.

Electrochemical deposition of CoHCF was by cyclic voltammetry over the range 0.0–0.9 V at a scan rate of  $0.1 \text{ V s}^{-1}$  for 50 cycles. After modification, the electrodes were rinsed and transferred to  $1.0 \text{ mol dm}^{-3}$  KCl for storage.

Prior to reuse of the electrodes, the ormosil films were removed by sonication for 10 min in a NaOH solution and polishing the treated surface to a mirror-like surface with an aqueous alumina slurry of different sizes (0.3 and 0.05  $\mu\text{m}$ ) on a polishing cloth.

The restoration of the surface was verified by obtaining the reversible, one-electron oxidation signature for the cyclic voltammetry of  $1.0 \text{ mmol dm}^{-3}$   $\text{Ru}(\text{CN})_6^{4-}$  in  $1.0 \text{ mol dm}^{-3}$  KCl at  $100 \text{ mV s}^{-1}$ . The criteria for a clean surface were five replicate cycles with peak current agreement to within 3% of that at the original bare electrode and a peak separation of 59–65 mV.

All electrochemical measurements were performed on solutions that were deaerated with nitrogen gas. The potentials were measured and reported vs. an Ag|AgCl,  $3 \text{ mol dm}^{-3}$  KCl reference electrode from Bioanalytical Systems (West Lafayette, IN).

## 5.3. Results and discussion

### 5.3.1 Characterization of the ormosil film with 20 nm channels

First of all, in the present study a comparison of ATR spectra of bare glassy carbon (GC), GC modified with APTES and PSS, and the modified electrode after treatment with chloroform was made. Of importance is that an overnight soaking in chloroform followed by air-drying removed the APTES and PSS to below the detection limit of the instrument. This dissolution process results in open channels in the ormosil-modified electrode.

From the obtained results, it was hypothesized that the channels were cylindrical and comprised the only electroactive portion of the film when electrochemically assisted sol-gel processing was used at a positive potential where the catalyst that is generated is hydrogen ion.<sup>66</sup>

In particular, SEM images are recorded in order to study the surface morphology of the modified electrode with and without APTES. After modification with 0.5 mmol dm<sup>-3</sup> APTES and PSS (20-nm), the ITO surface shown in Fig. 29a was obtained. The important feature is that the diameter of the channels at the outer surface of the ormosil (20 nm from Image-Pro Plus® software) is that of the cross-section of the PSS templating agent.

Image 29b is that of a blank (same conditions as Fig. 29b except APTES was absent); at the resolution of the instrument, no evidence of a pore structure is observed.

The results in Fig. 29b demonstrate two points. First, 20-nm PSS does not adsorb to the electrode when it is not modified with APTES. Second, deposition of the ormosil at a positive potential where hydrogen ion is the electrochemically generated catalyst of the sol-gel process gives a compact film on the electrode. The same results were obtained when GC rather than ITO was the electrode.

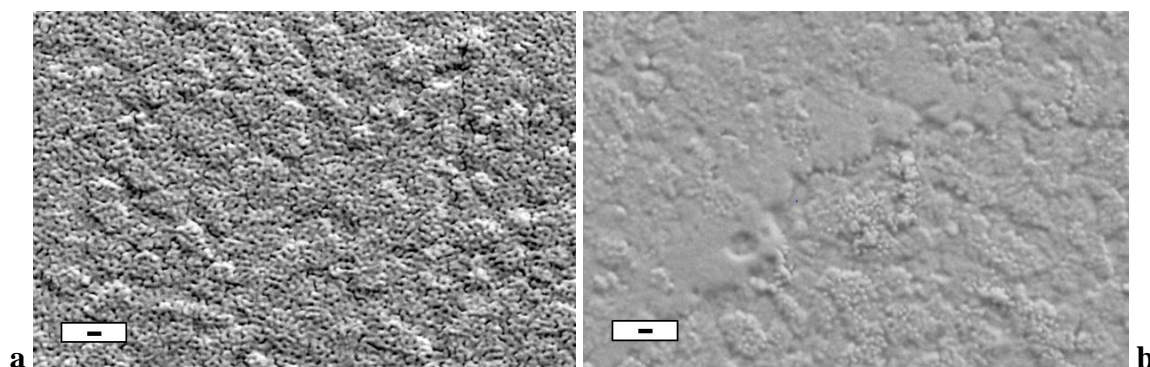


**Figure 29** SEM image of an ITO electrode modified with APTES and 20-nm PSS. Conditions are in Experimental Section with (a) 0.5 mmol dm<sup>-3</sup> APTES reacted with an ITO surface for 15 min prior to immersion in PSS. The ormosil was deposited at 1.5 V for 20 min. (b) same as a except that no modification of the surface with APTES was done prior to immersion in PSS. The bar represents 100 nm.

In a further extension of our previous studies,<sup>66,67</sup> a systematic evaluation of the influence of APTES on the density of the pores was made in this investigation. The influence of APTES concentration used to modify the electrode on the cyclic voltammetry of Ru(CN)<sub>6</sub><sup>4-</sup> in 1.0 mol dm<sup>-3</sup> KCl was investigated (Fig. 30).

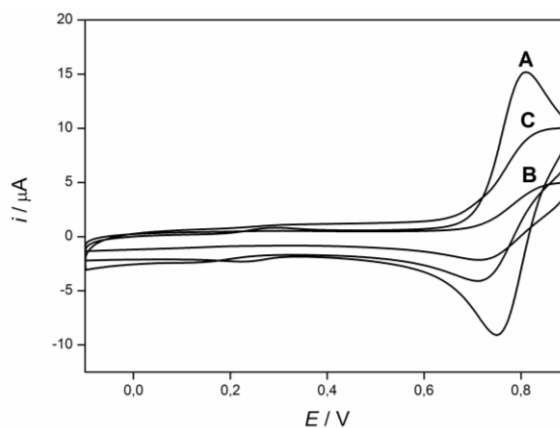


**Figure 30** Cyclic voltammetry of  $1.0 \text{ mmol dm}^{-3} \text{ K}_4\text{Ru(CN)}_6$  at (A) bare GC; (B) GC | ormosil (20-nm pores) that was prepared from  $0.5 \text{ mmol dm}^{-3}$  APTES; and (C) CG | ormosil (20-nm pores) that was prepared from  $15 \text{ mmol dm}^{-3}$  APTES. Supporting electrolyte,  $1.0 \text{ mol dm}^{-3} \text{ KCl}$ ;  $\nu$ ,  $100 \text{ mVs}^{-1}$ . Conditions are detailed in Experimental Section.

The increase in current with increase in APTES concentration over the range  $0 - 15 \text{ mmol dm}^{-3}$  is illustrative of the role of APTES on the population of surface-immobilized PSS nanoparticles and, hence, on the resulting pore density. When the electrode was not modified with APTES prior to immersion in PSS, a passivating (non-porous) ormosil film was obtained, which is consistent with the image in Fig. 29b. Increasing the APTES concentration to  $30 \text{ mmol dm}^{-3}$  resulted in only a small increase in peak current for the oxidation of  $\text{Ru(CN)}_6^{4-}$ . Either the adsorption isotherm for APTES is nonlinear or the packing of PSS in a monolayer approaches a limit when  $30 \text{ mmol dm}^{-3}$  is used to modify the electrode (Fig. 31). The standard deviations of the peak currents for electrodes modified with  $0.5, 5.0, 15,$  and  $30 \text{ mmol dm}^{-3}$  APTES are  $0.2, 0.1, 0.4,$  and  $0.5 \text{ }\mu\text{A}$ , respectively.

A surprising result was observed when  $50 \text{ mmol dm}^{-3}$  APTES was used to modify the base electrode. The peak current for the oxidation of  $\text{Ru(CN)}_6^{4-}$  drastically decreased (Fig. 31).

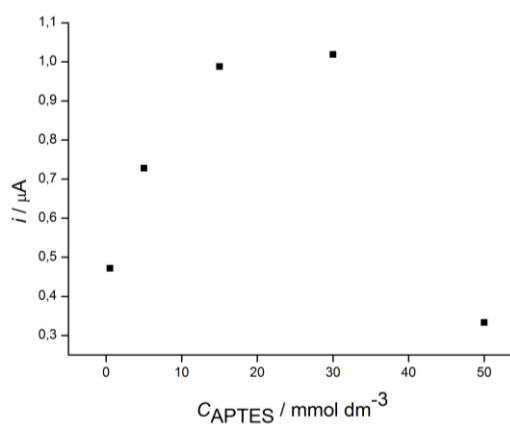


**Figure 31** Influence of APTES concentration on pore density (effective electrode area) of GC|ormosil (20 nm channels).

In this case the standard deviation was  $0.2 \mu\text{A}$ . That is, the ormosil film prepared under this condition apparently was not permeable to  $\text{Ru}(\text{CN})_6^{4-}$ . Consistent with these electrochemical data, SEM imaging of the surface demonstrated that a compact, nonporous film was formed when  $50 \text{ mmol dm}^{-3}$  APTES was used to modify the electrode.

### 5.3.2 Film geometry

SEM images of cross-sections of ormosil films prepared after treatment with  $0.5 \text{ mmol dm}^{-3}$  and with  $50 \text{ mmol dm}^{-3}$  APTES were compared to determine whether the quantity of PSS that is immobilized prior to the electrochemically assisted deposition of the ormosil influenced the film thickness (Fig. 32).

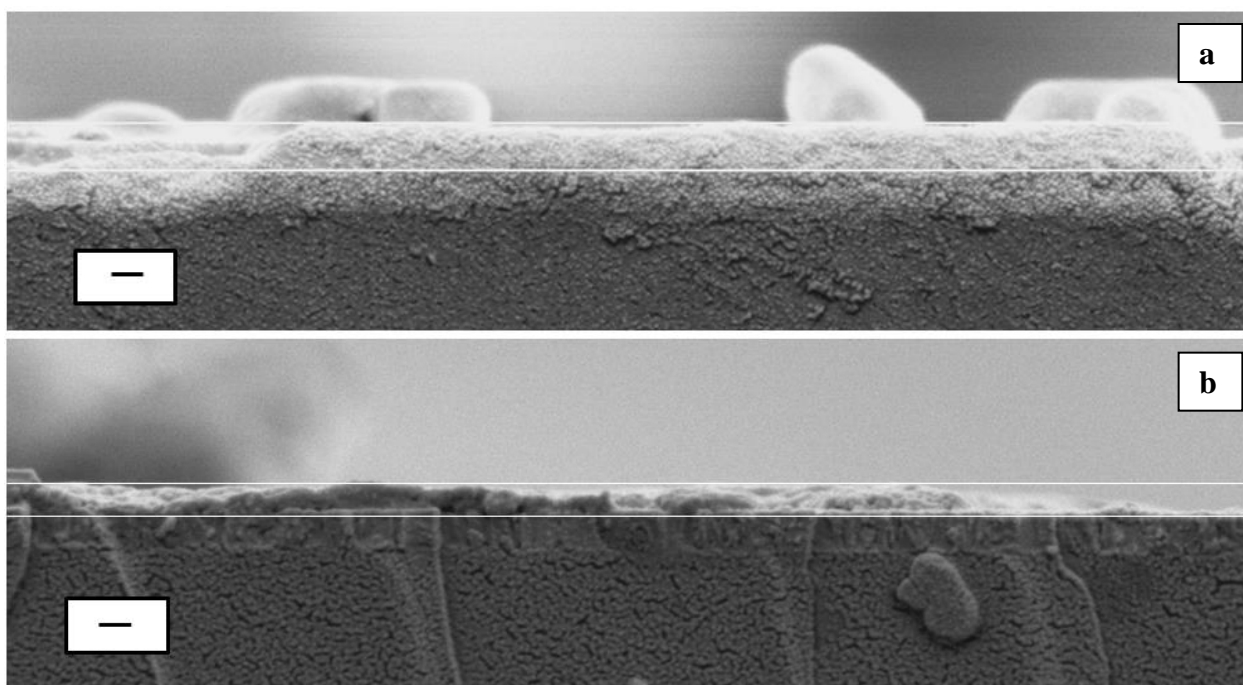


**Figure 32** Influence of the APTES concentration on the thickness of the ormosil deposited by an electrochemically assisted process. Shown are SEM images of cross-sections of ormosil films deposited onto GC modified by treatment in a)  $0.5 \text{ mmol dm}^{-3}$  APTES and b)  $50 \text{ mmol dm}^{-3}$  APTES. Following modification with APTES, adsorption of PSS and deposition of an ormosil was performed as described in the caption to Fig. 1. Index bars, 200 nm.

When  $0.5 \text{ mmol dm}^{-3}$  was used to modify the electrode and the film was deposited as described in the Experimental section, the thickness was 270 nm. At the higher concentration, the thickness, while too inconsistent to accurately estimate, is generally below 50 nm.

Excess PSS that results from a high population of APTES sites on the ITO electrode clearly disrupts the electrochemically assisted processing of  $(\text{CH}_3)_3\text{SiOCH}_3$ .

Perhaps when the PSS is tightly packed on the electrode surface or is stacked in a multilayer, the  $(\text{CH}_3)_3\text{SiOCH}_3$ , which is the precursor to the ormosil, is blocked from reaching the acidified zone at the electrode surface. Instead, the hydrogen ion catalyst must transport across the PSS layer by, for example, site-to-site diffusion. The resulting ormosil film can be predicted to be thinner than when the sol-gel processing occurs directly at the acidified surface, and the PSS will not template a pore structure in that ormosil forms above it.

Attempts to elucidate the pore geometry by SEM imaging of a film cross-section were unsuccessful. Instead, a portion of the film was mechanically removed from the electrode and imaged by TEM (Fig. 33). The horizontal image, Fig. 33a, suggests that the channels are cylindrical. These apparent channels do not appear as open cylinders because of an anomaly that occurs because removal of the film skews the film geometry.

The vertical image, Fig. 33b, does show open channels at the ormosil surface with a diameter in the 20-nm range.

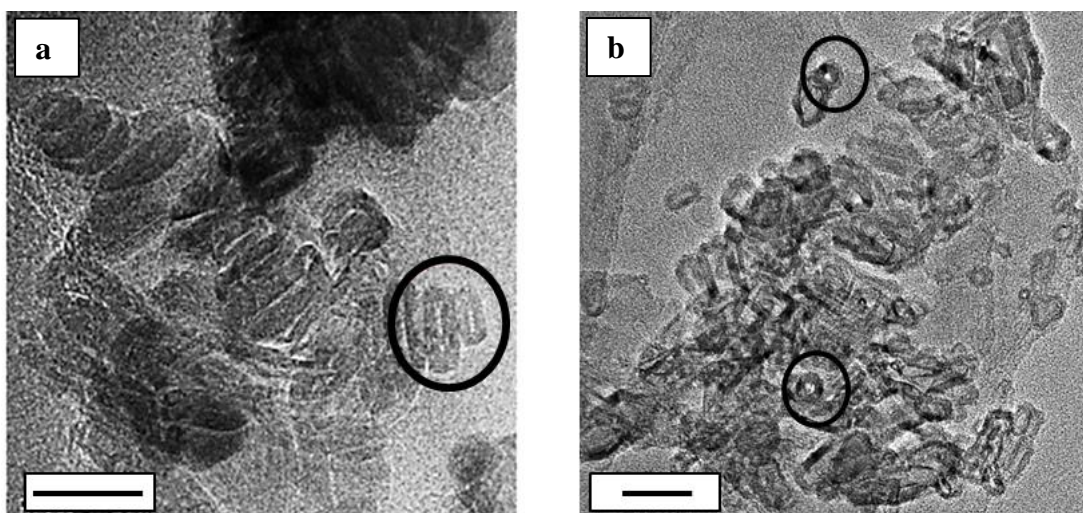


**Figure 33** Horizontal (Fig. 33a) and vertical (Fig. 33b) TEM images of a portion of the film obtained using  $0.5 \text{ mmol dm}^{-3}$  APTES to modify the electrode. Conditions are detailed in Experimental Section. Index bars, 50 nm.

### 5.3.3 Influence of channel structure and distribution on voltammetry

The experiments displayed in Fig. 30 involving the CV of  $\text{Ru}(\text{CN})_6^{3-}$  as a function of pore density were expanded to elucidate the current-limiting process at the GC|ormosil (20 nm) electrode. First, the influence of scan rate,  $\nu$ , on the peak current,  $i_{\text{pa}}$ , for the oxidation of  $\text{Ru}(\text{CN})_6^{3-}$  was determined (Fig. 34). In the  $\nu$ -range,  $5\text{--}100 \text{ mVs}^{-1}$ , the slope of the plot of  $\log i_{\text{pa}}$  vs.  $\nu$  is 0.42, which approaches the theoretical value of 0.5 for a current limited by semi-infinite linear diffusion.

Below  $5 \text{ mV s}^{-1}$ ,  $i_{\text{pa}}$  is nearly independent of  $\nu$ , which generally is an indicator of radial diffusion as the current-limiting process.

However, this interpretation is for a conventional electrode where the surface of the electrode directly contacts the bulk solution. The present study is in the category of nanoscale electrochemistry, which includes both the use of single electrodes at the base of nanopores in various materials and nanoarrays of electrodes.

The topic is the subject of a recent review.<sup>68</sup> Of relevance to the present study, White and coworkers have described mass transfer to an electrode at the base of a single nanopore.<sup>69,70</sup> Here, the nanopore was an inverted cone (where the pore radius is greater than that of the electrode surface). The parameters that must be considered are the following:  $\delta$ , the diffusion layer thickness where  $\delta \approx (2Dt)^{1/2}$ ;  $r_o$ , radius of the nanopore; and  $d_p$ , depth of the nanopore. When  $\delta > 10(r_o + d_p)$ ,<sup>69</sup> the current is limited by radial diffusion, in which case it reaches steady state; that is, in terms so the present study, if the prediction for a single nanopore applies to the array in the ormosil, the current that is developed in CV for the oxidation of  $\text{Ru}(\text{CN})_6^{3-}$  would reach a plateau and be independent of  $\nu$  in that  $r_o$  is 10 nm and  $d_p$  is ca. 200 nm. Moreover, converting  $\nu$  to an experimental time,  $t_{\text{expt}}$ , by  $t_{\text{expt}} = RT/\nu F$ ,<sup>69,71</sup> and assuming  $D \approx 10^{-6} \text{ cm}^2\text{s}^{-1}$  yields a prediction of radial diffusion at all  $\nu$ -values in Fig. 34.

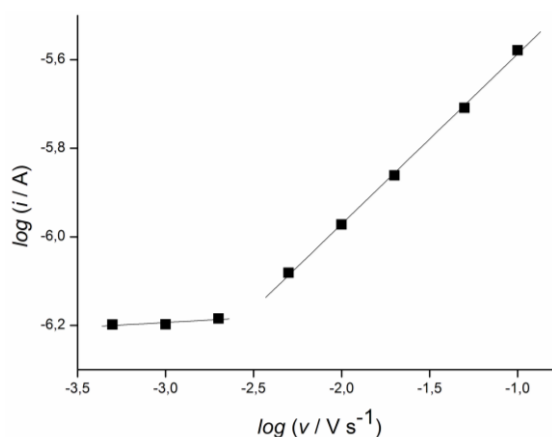


**Figure 34** Evaluation of the current-limiting process in the cyclic voltammetry of  $1.0 \text{ mmol dm}^{-3}$   $\text{K}_4\text{Ru}(\text{CN})_6$  in  $1.0 \text{ mol dm}^{-3}$  KCl at GC/ormosil (20-nm channels).

The above prediction is not followed at  $\nu$ -values  $> 5 \text{ mVs}^{-1}$ ; that linear diffusion observed experimentally at  $\nu > 5 \text{ mV s}^{-1}$  is a result of the array structure of the channels in the ormosil film. Designating  $x_{\text{sep}}$  as a representative distance between the pores, if  $\delta > x_{\text{sep}}$ , the diffusion layers around the channels overlap in which case linear diffusion to the outer surface of the ormosil film limits the current alone or in combination with radial diffusion.

The slope of 0.42 of the portion of Fig. 34 at  $\nu > 5 \text{ mVs}^{-1}$  indicates that linear diffusion resulting from overlapping diffusion layers is dominant in this region.

Under the conditions used to deposit the ormosil in Fig. 34,  $x_{\text{sep}} \approx 100 \text{ nm}$ .

Thus, even at the highest  $\nu$  in Fig. 34,  $100 \text{ mVs}^{-1}$ , at which  $\delta = 2 \cdot 10^4 \text{ nm}$ , the diffusion layers of the array overlap.

Linear diffusion because of overlap of diffusion layers previously was observed with films of poly(styrene) prepared from a diblock copolymer of poly(styrene) and poly(methylmethacrylate) where 10-nm (radius) channels were separated by an average of 36 nm and  $\nu$  was below  $100 \text{ mVs}^{-1}$ . As in the present study, the depth of the channels was much less than the thickness of the diffusion layer.

Extending this analysis to interpret the apparent onset of radial diffusion at  $\nu < 5 \text{ mVs}^{-1}$  in Fig. 34 results in an anomaly in that linear diffusion should continue to be the current-limiting process. For example, at  $1 \text{ mVs}^{-1}$ , the value of  $t_{\text{expt}}$  is approximately 26 s.

When  $D$  is approximated as  $10^{-6} \text{ cm}^2\text{s}^{-1}$ , the value of  $\delta$  is about  $7 \cdot 10^4 \text{ nm}$ , which greatly exceeds  $x_{\text{sep}}$ . The factor that is not accounted for in this treatment is convection.

In that the experiments were performed with the electrochemical cell on the bench top rather than isolated from environmental factors that cause some degree of convection, maintaining a diffusion-limited process for a time such as 26 s is not realistic. Indeed, the onset of convection is probably at times in the range 1-5 s.

Chronoamperometry corroborates this interpretation. As shown in Fig. 35, the current for the oxidation of  $\text{Ru}(\text{CN})_6^{3-}$  approaches steady state as  $t$  approaches 1 s. An additional factor is that the negative-going scans in CVs at  $\nu < 5 \text{ mV s}^{-1}$  do not re-trace the current plateaus for the oxidation of  $\text{Ru}(\text{CN})_6^{3-}$ , which is strong evidence that the product is dispersed by convection.

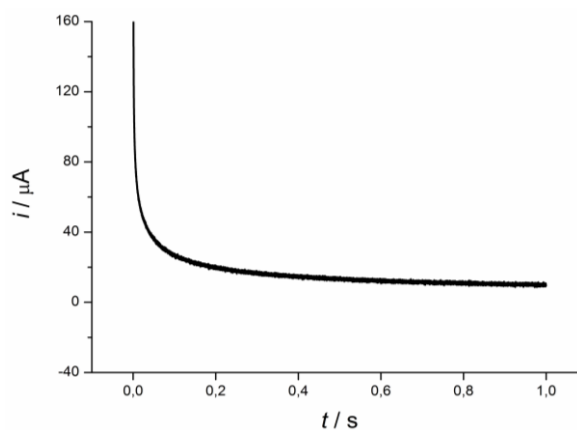


**Figure 35** Chronoamperometry of  $1.0 \text{ mmol dm}^{-3} \text{ K}_4\text{Ru}(\text{CN})_6$  in  $1.0 \text{ mol dm}^{-3} \text{ KCl}$  at GC|ormosil (20 nm). At  $t = 0$ , the applied potential,  $E_{\text{app}}$ , was  $0.4 \text{ V}$ ; at  $t > 0$ ,  $E_{\text{app}} = 0.9 \text{ V}$ .

Overall, these data suggest that radial diffusion at a nanoscale is unlikely to be attained at slow scan rates unless the electrochemical cell is isolated from environmental causes of convection.

At the nanoscale, this problem is certainly more significant than with micron-scale electrodes and/or arrays.

As an example where radial diffusion was achieved, Mirkin and coworkers<sup>72</sup> obtained steady-state (current plateau) CVs of  $2 \text{ mmol dm}^{-3} \text{ Ru(NH}_3)_6^{3+}$  at an 850 nm Ag electrode in a nanowell formed by etching the Ag held in a glass capillary, but the stronger evidence was that the anodic and cathodic current plateaus were superimposed at  $50 \text{ mVs}^{-1}$ .

Given that the envisioned application of these electrodes is to fabricate arrays that serve as catalytic, size-exclusion films, future work will be aimed at developing nanoarrays with channel diameters in the 10-20 nm range and channel separation sufficient to provide non-overlapping diffusion layers.

#### **5.3.4 Synthesis and characterization of CoHCF nanoarray**

Modification of a glassy carbon (GC) electrode with a film of an organically modified silica (ormosil) with a 20-nm channels, herein designated as GC|ormosil (20-nm channels), provided a template for the synthesis of a nanoarray of Cobalt Hexacyanoferrate (CoHCF).

As shown previously, cylindrical channels normal to the electrode surface are formed, presumably because the electrochemically assisted processing results in channels that are essentially shadows of the immobilized PSS.

Hence, the pore diameter, 20 nm, is the same as that of the PSS templates. In the present study, SEM images of replicate films in comparison to images of the PSS-APTES modified surfaces showed that the efficiency of pore formation was about 99%; that is, very few cases of collapse between adjacent channels occurs.

The nanochannels of the ormosil-coated electrode were further modified by electrochemical deposition of CoHCF as previously detailed in the Experimental Section.

The following Fig. 36 shows a schematic diagram of fabrication of porous template and preparation of CoHCF nanoparticles.

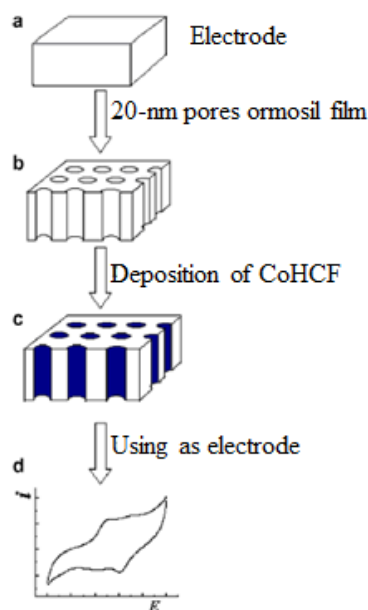


**Figure 36** Schematic diagram of fabrication of porous template and preparation of CoHCF nanoparticles. (a) fabrication of 20-nm ormosil template, (b) deposition of CoHCF nanotubes, (c) obtaining the CoHCF nanoparticles, and (d) CoHCF was served as an electrode thanks to its electrochemical characteristics.

Cyclic voltammetry (CV) in the potential range 0.0-1.0 V and with scan rate of 0.1 V s<sup>-1</sup> was employed in a conventional three-electrode configuration.

Different degrees of filling the 20-nm channels in the ormosil with CoHCF were achieved through variation of the number of cycles; generally, 10, 20 or 50 cycles were applied. The current observed for the cyclic voltammetry of CoHCF served to monitor the quantity that was deposited. In this regard, the redox processes can involve both iron and cobalt centers in accord with the following reaction scheme:<sup>73</sup>



The notation (CoFe)<sup>ox number</sup> regardless of which metal atom is in the oxidized form represents the actual situation in the case of the Cobalt Hexacyanoferrate (CoHCF) compounds, in which a mixture of both Co<sup>III</sup>/Co<sup>II</sup> and Fe<sup>III</sup>/Fe<sup>II</sup> metal ions with a different ratio can coexist depending on the synthetic route.

In CoHCF, the Fe<sup>III</sup> center is always electrochemically active, while the redox process related to the couple Co<sup>III</sup>/Co<sup>II</sup> becomes allowed only for compounds crystallized in the so-called insoluble form.

The insoluble form presents defects caused by the absence of 1/4 of the Fe(CN)<sub>6</sub><sup>4-</sup> groups, replaced by water molecules, which allows the swelling of the structure caused by the contraction of the Co-N bond length while reducing to Co<sup>II</sup>.

Real samples are usually constituted by a solid solution in which the insoluble and soluble forms coexist, giving rise to CVs that show a more complex morphology due to both the redox processes of  $\text{Fe}^{\text{III}}/\text{Fe}^{\text{II}}$  and  $\text{Co}^{\text{III}}/\text{Co}^{\text{II}}$  couples.

The surface morphology and the mechanism of formation of CoHCF were studied by scanning electron microscopy (SEM). The bottom of the 20 nm channels comprises the portion of the GC|ormosil (20-nm pore) electrode surface that is electrochemically active.

The morphology of the electrochemically deposited CoHCF on this electrode was influenced by the nanoporous structure of the ormosil film. That is, the 20 nm channels acted as templates for the deposition of nanoparticles of CoHCF.

When the quantity of the CoHCF that was deposited was limited by applying only 10 cycles (Fig. 38) under the above-described CV conditions, its formation was exclusively in the channels. The morphology and CV signature in  $1.0 \text{ mmol dm}^{-3}$  KCl (Figs. 37A and 37D, respectively) were characteristic of CoHCF nanoparticles,<sup>73</sup> this behavior was already observed for CoHCF nanoparticles supported on carbon nanotubes.<sup>74</sup>

In the CV, a small anodic peak at of about 0.57 V is shown; the boundary surface can be considered rich in defects, resulting in the higher concentration of  $\text{Co}^{\text{III}}$  with respect to  $\text{Fe}^{\text{III}}$ , this condition can lead to a CV that shows only one redox couple at the potential attributed to the reduction of  $\text{Co}^{\text{III}}$ . The analogous data for 20 cycles (Figs. 37B and 37E) and 50 cycles (Figs. 37C and 37F) illustrate a change in CoHCF structure as the deposit extends onto the outer surface of the ormosil.

During the CV scans, a progressive modification of the curve morphology has been observed. This finding can be ascribed to the conversion of the starting nanocompound to a bulk-like species. Hence, when 20 cycles were used to deposit CoHCF, these data show a mix of nanoparticles and the cubic structure that is characteristic of bulk-form CoHCF deposited on bare electrode surfaces.<sup>73</sup>

When 50 cycles were employed, the latter are the dominant features. The corresponding bulk compound presents a more complex oxidation process involving two species that are attributed to the  $\text{Fe}^{\text{III}}/\text{Fe}^{\text{II}}$  and  $\text{Co}^{\text{III}}/\text{Co}^{\text{II}}$  couples, as usually reported in the literature.<sup>73,75-77</sup>

Overall, the SEM data evolve from CoHCF nanoparticles to aggregates of cubic structure as the deposit transitions from being confined to within the 20-nm channels to being deposited on the outer surface of GC|ormosil (20-nm channels).

Consistent with the above hypothesis, the CV signature changes from that of nanoparticulate CoHCF in 0.1 mol dm<sup>-3</sup> KCl, in which only a single redox process of CoHCF attributed to the Co<sup>III</sup>/Co<sup>II</sup> couple occurs,<sup>78</sup> to the typical shape of the CV of bulk-form CoHCF obtained by chemical synthesis or by electrodeposition on bare electrodes, namely reduction peaks at 0.65 V and at 0.45 V.

With bulk-form CoHCF, the redox process involves two different transition metals, i.e. the Fe and Co centers.

Fe<sup>III</sup> center is always electrochemically active, whereas the redox process related to the Co<sup>III</sup>/Co<sup>II</sup> couple is active only for compounds crystallized in the so-called “insoluble form”, for which the cubic structure of the CoHCF has less than 1:1 stoichiometry due to the lack of one-fourth of the Fe(CN)<sub>6</sub><sup>3-</sup> groups.<sup>73</sup>

Under conditions where the CoHCF is electrochemically formed only within the 20-nm channels, this sub-stoichiometric insoluble structure is prevalent because of the spatially restricted environment, which accounts for the shape of the CV in Fig. 37A.

In contrast, when the quantity of CoHCF that is on the outer surface of the ormosil (e.g. with 50 cycles applied, as described above) greatly exceeds that in the channels (Fig. 38), the features of the CV reflect those of the stoichiometric (soluble) form where the two oxidation peaks are separated.

The peak potentials are shifted toward positive values relative to those observed for a CoHCF film on GC. The shift reflects some resistance to charge transport through the nanoscale pores.

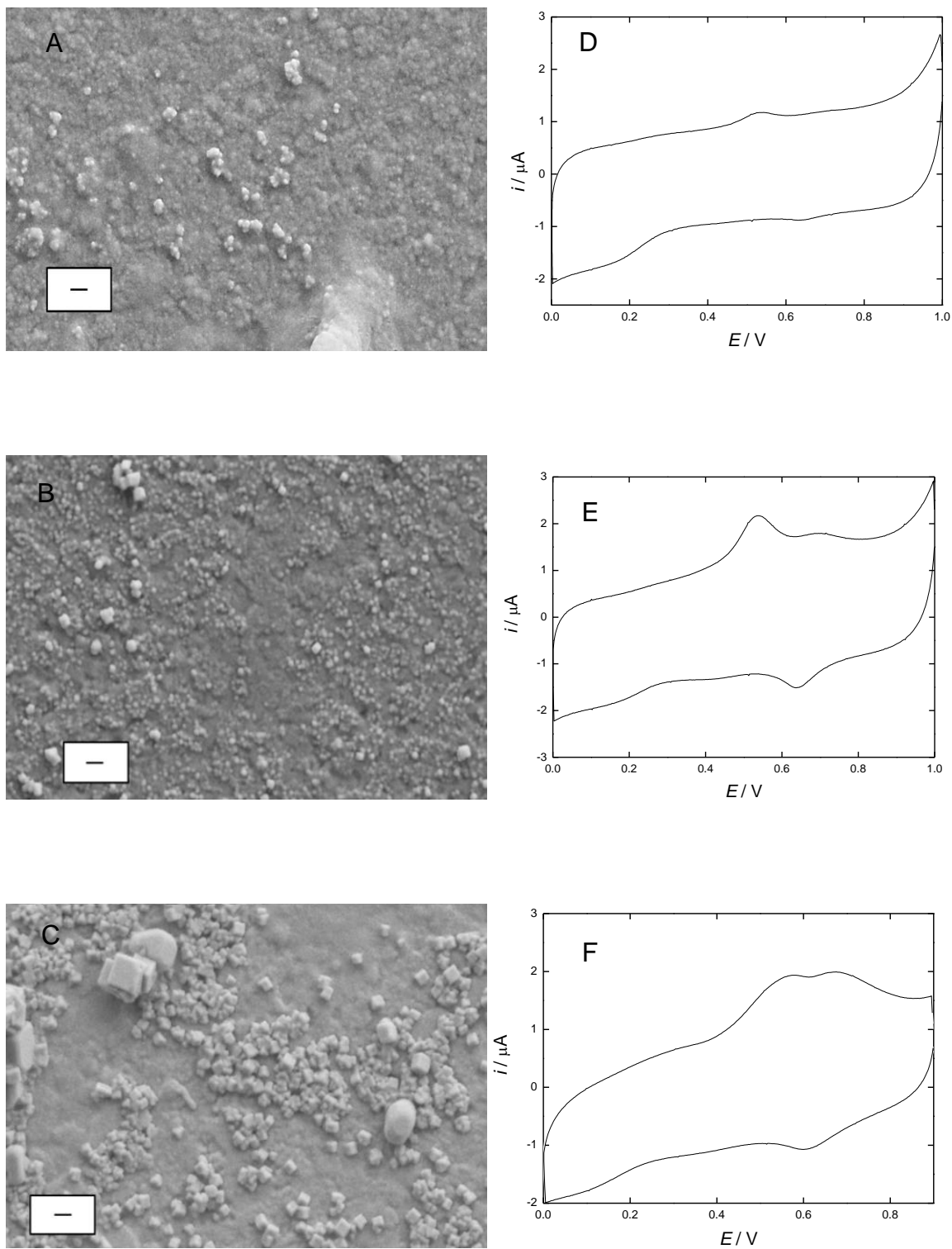


**Figure 37** SEM micrographs of CoHCF obtained in A) 10, B) 20, C) 50 cycles and the CV study of the CoHCF modified electrodes in  $1.0 \text{ mmol dm}^{-3}$  KCl solution. The bar represents 100 nm

A schematic representative of this electrodeposition process is shown in Fig. 38.

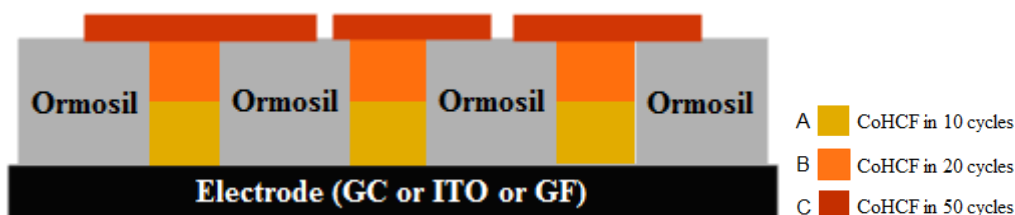


**Figure 38** Schematic representation of the CoHCF electrodeposition process and the relative filling of the channels on the modified electrode surface.

The current-limiting processes in the cyclic voltammetry of CoHCF confined in the channels (10-cycle deposition) and spilled over the top of the ormosil (50-cycle deposition) were evaluated. The system is somewhat analogous to that of a redox polymer film on an electrode, which was treated in detail by Vorotyntsev et al.<sup>79</sup> Cyclic voltammetry over the  $\nu$ -range  $0.1 - 5 \times 10^{-3} \text{ V s}^{-1}$  was performed, and  $i_{pa}$  was measured. The behavior was analyzed by examining  $\log i_{pa}$  as a function of  $\log \nu$ . If the CoHCF behaves as a metallic conductor, the slope of the  $\log i_{pa}$  vs.  $\log \nu$  plot will be 1.0. In fact in the case of fast electron and counter-ions transport into the film, the slope of the  $\log i_{pa}$  vs.  $\log \nu$  plot approaches to 1.0. It is worth underlining that this case requires electron self-exchange kinetics to be sufficiently fast on the time scale of the experiment to not limit the current as well as facile mobility of a counter ion within the deposit. Such a situation is ideal for CoHCF to act as a redox mediator. However, when the currents are limited by electron transport over the  $\nu$ -range studied, the slope of such plot should approach 0.5. In the case of slow electron exchange between neighboring redox centers the rate of charge transport into the film obeys formal diffusion law, where  $D_e$ , the diffusion coefficient for the transport of electrons through the redox active layer, should be considered as the rate of propagation of oxidation/reduction front. The same takes place in the case of counter-ion limiting charge transport processes. The rate of charge propagation is determined by ionic diffusion with diffusion coefficient  $D_i$ .<sup>80</sup>

In general, when the combination of the electron self-exchange (or electron diffusion) and counter ion diffusion occur, the charge transport is limited by an effective diffusion coefficient,  $D_{eff}$ , including both components,  $D_e$  and  $D_i$ .

The result (Fig. 39) is that with CoHCF confined to the pores and with spillover onto the top of the film the slope is of intermediate value between that for a metallic conductor and for a system limited by  $D_{eff}$ .

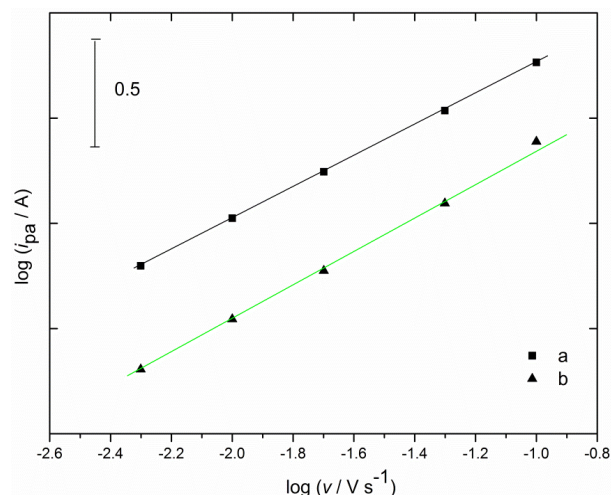


**Figure 39** Plot of the logarithm of the anodic peak current  $i_{pa}$  vs. the logarithm of the scan rates  $\nu$  for the cyclic voltammetry of CoHCF electrodeposited in GC|ormosil (20-nm pores) using 10 (black line) and 50 (green line) cycles.

Specifically, linear regression analysis results in the following: 10 deposition cycles (slope, 0.74;  $R^2$ , 0.999) and 50 deposition cycles (slope, 0.63;  $R^2$ , 0.999). Either electron self-exchange kinetics or counter ion transport causes some departure from the ideal case. The greater departure from the ideal case is when the CoHCF is deposited on the outer surface of the ormosil as well as within the channels. Here, the higher surface area relative to the nanorod array yields a commensurately higher current. The current path is exclusively through the CoHCF nanorods within the channels because the ormosil phase is non-conducting.

The result is that counter ion mobility and/or electron self-exchange kinetics within the nanorod phase play a greater role in limiting the current than when the CoHCF is deposited only within the channels of the GC|ormosil (20-nm channels).

### 5.3.5 Electrocatalytic oxidation of cysteine

It is well known that MHCs promote electrocatalytic activity of several analytes, and, therefore, find extensive use in analytical chemistry.<sup>81,82</sup> In order to evaluate the electrocatalytic activity of the GC|ormosil (20-nm channels) electrode modified with Cobalt Hexacyanoferrate, CoHCF nanorods, herein designated as GC|(ormosil, CoHCF<sub>r</sub>), L-cysteine (cys) was selected as model compound.

Figure 40 shows the cyclic voltammograms of GC|(ormosil, CoHCF<sub>r</sub>) in 0.1 mol dm<sup>-3</sup> KCl at pH 2.0 (adjusted with HCl) in presence and absence of cys at 0.1 V s<sup>-1</sup>. The cys concentrations ranged from 30-150 μmol dm<sup>-3</sup>. With the addition of cys, an increase of  $i_{pa}$  at 0.78 V is observed as the cys concentration increases.

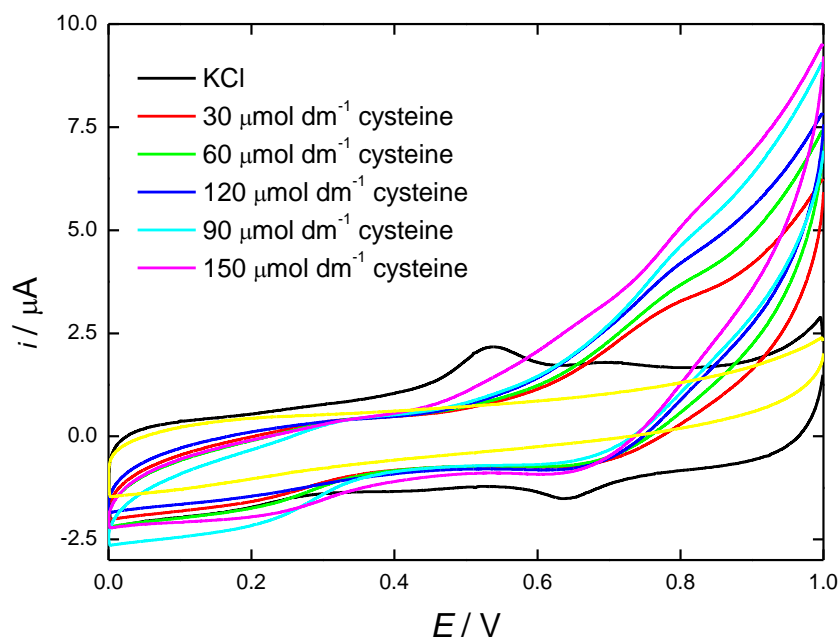


**Figure 40** Cyclic voltammograms of the GC|(ormosil, CoHCF<sub>r</sub>) electrode in 1.0 mmol dm<sup>-3</sup> KCl at pH 2.0 in the absence (black curve) and presence of cys.  $\nu = 0.1 \text{ V s}^{-1}$

The voltammetric behavior is consistent with a CoHCF-mediated oxidation of cys as the electrode process. That is, on the addition of cys, an enhancement in the anodic current corresponding to Equation 1 is observed, whereas in the reverse scan the corresponding two reduction waves are attenuated. These changes result from the chemical regeneration of  $\text{CoFe}^{\text{V}}$  and the concomitant diminution of  $\text{CoFe}^{\text{VI}}$  (Reaction 2).



The anodic current generated in the mediated oxidation of cys electrooxidation process can be attributed to the oxidation of the thiol present in the cys structure as reported by Shi et al.<sup>82</sup> A mediated oxidation can yield cysteic acid, which does not passivate an electrode surface,<sup>83</sup> whereas at bare GC oligomer that strongly adsorbs to the surface is the probably product.

Figure 41 shows the calibration curve obtained by CV of cys at a GC|(ormosil, CoHCF<sub>r</sub>) electrode. The linear least squares analysis of these data gave the following information: slope,  $1.68 \times 10^{-8} \mu\text{A } \mu\text{mol dm}^{-3}$ ;  $R^2$ , 0.999; and intercept,  $2.72 \times 10^{-6} \mu\text{A}$ .

The sensitivity of the calibration curve is comparable to similar systems in which iron(III) oxide core–Cobalt Hexacyanoferrate shell nanoparticles have been employed to modify a carbon paste electrode and used as an electrocatalytic transducer for the electrocatalytic oxidation of L-cysteine.<sup>84</sup>

Moreover, it is comparable to an indium tin oxide electrode coated with a nanoscale sol-gel film modified by inclusion of Cobalt Hexacyanoferrate, which catalyzes the oxidation of 5-hydroxytryptophan (5-HTPP).<sup>81</sup>

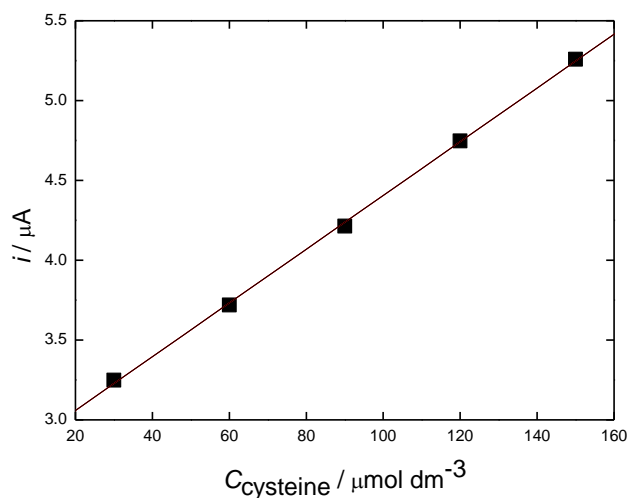


**Figure 41** Calibration curve obtained during successive increments of L-Cysteine to  $1.0 \text{ mmol dm}^{-3}$  KCl (pH=2)

At pH=2 cys also is oxidized at carbon-based electrodes. The anodic current, which probably resulted from a weak interaction of carbon and sulfur atom, was generated from direct electron transfer between L-cysteine and carbon surface.<sup>84,85</sup>

However, the anodic peak resulting from this direct electrooxidation of cys decreased on prolonged potential cycling. Because of this passivation the electrooxidation of cys at bare carbon electrodes is of limited value for development of an analytical procedure for cys.

In contrast, consecutive CVs for the oxidation of cys at GC|(ormosil, CoHCF<sub>r</sub>) gave stable anodic currents. With 1, 10, 20, 30, 40, and 50 cycles at  $0.1 \text{ Vs}^{-1}$ , the respective anodic currents were 3.2, 3.2, 3.1, 3.1, 3.0 and 3.0  $\mu\text{A}$ . The reusability of the immobilized metal nanoparticles in catalytic reactions is a standing challenge. In this case, the catalyst continues to show a high activity even after 50 cycles.

Regarding the analytical results at GC|(ormosil, CoHCF<sub>r</sub>), the LOD is well-below the concentration range in Fig. 41, and the intercept, which is due to the oxidation of the mediator, is high relative to the signal from cys oxidation. Hence, this LOD only reflects the linearity and the standard deviation of the data points in Fig. 41.

For analytical measurements in the  $\text{nmol dm}^{-3}$  range with a mediator, amperometry under potentiostatic conditions is superior because the background current in the absence of the analyte decays to zero thereby enhancing the signal-to-noise ratio.<sup>83,86</sup>

## 5.4 Conclusion

Electrochemically assisted deposition of an ormosil film from  $(\text{CH}_3)_3\text{SiOCH}_3$  onto a surface modified by a distribution of 20-nm PSS beads resulted in a film with cylindrical channels that formed above the APTES-immobilized PSS.

The distribution of the channels was controlled via the surface coverage of GC or ITO by APTES, which in turn was determined by its concentration during the modification of the base electrode.

As the concentration of APTES in the modification medium was increased (and, hence, the quantity of PSS deposited), the channel density in the ormosil film increased initially, but a point was reached where a non-porous ormosil was deposited. Imaging the electrode modified with APTES and PSS showed that the deposition of a non-porous ormosil film occurred when the APTES coverage resulted in the immobilization of densely packed PSS.

The oxidation of  $\text{Ru}(\text{CN})_6^{3-}$  at an electrode modified with a nanoarray of channels gave a current limited primarily by linear diffusion. When CV at scan rates below  $5 \text{ mV s}^{-1}$  was performed, a steady-state current was developed; however, rather than reflecting an onset of radial diffusion in this time domain, the steady-state current was due to convection caused by environmental factors.

Subsequently, the electrochemical synthesis of Cobalt Hexacyanoferrate nanorods (CoHCF) within the 20-nm channels of the template organically modified silica film (ormosil) on glassy carbon electrodes is reported.

These channels have a distribution that can be pre-determined by the selection of the templating agent used to modify the surface of the electrode upon which the ormosil film is deposited by an electrochemically assisted process.

The number of the collapsed channels is very few, and they do not affect the electrochemical deposition process or subsequent voltammetric studies.

The electrochemical active surface area comprises only the bottom of the channels so the potentiodynamic electrochemical synthesis of CoHCF can be restricted to the inside of these channels by controlling the number of cycles that are employed.

Hence, in this modified electrode, the amount of the electrochemically deposited CoHCF can be modulated within the channels, in order to obtain either CoHCF nanorods or CoHCF bulk. With an increase in the number of cycles, the deposition process will eventually spill over to the surface of the film.

The process that limits the oxidation of the CoHCF was investigated by cyclic voltammetry as a function of scan rate,  $\nu$ , in  $0.1 \text{ mol dm}^{-3}$ .

The ideal case for a mediator is that it acts like a metallic conductor in which case  $i_{pa}$  is directly proportional to  $\nu$ . In the present case,  $i_{pa} \propto \nu^{0.74}$ , which illustrated that either electron self-exchange kinetics or, perhaps, counterion diffusion within the CoHCF causes a departure from ideality.

Nevertheless, the mediated oxidation of cys by CoHCF was limited by linear diffusion when this analyte was at concentrations up to at least  $0.15 \text{ mmol dm}^{-3}$ .

As a consequence, the anodic current intensity due to the electrocatalytic oxidation of cys shows a perfect linear correlation with the cys concentration, as proved by the calibration curve in the range from  $30$  to  $150 \text{ } \mu\text{mol dm}^{-3}$ .

Moreover, there was no evidence of electrode passivation when 50 cycles were applied in  $0.15 \text{ mmol dm}^{-3}$  cys whereas at bare carbon electrodes, the oxidation of cys rapidly passivates the surface.

In comparison with other electrodes, or especially the bare electrode, not modified with a nanorod array, experiments show as direct electrooxidation of cys decreased on prolonged potential cycling.

Because of this passivation, the electrooxidation of cys at bare carbon electrodes is of limited value for development of an analytical procedure for L-cysteine. In fact, in literature is well known that cysteine oxidation at bare electrodes also yields passivating films.

As matter of fact, the higher stability of this modified electrode makes it appropriate for electroanalytical applications because the catalyst continues to show a high activity even after a huge number of cycles.

It is likely that the product of the mediated oxidation is cysteic acid that does not adsorb to the surface rather than an oligomer. Facile oxygen transfer in conjunction with electron transfer may promote the former, whereas the spatial restrictions of the 20-nm pores may block polymerization.

- <sup>1</sup> Y. Xia, B. Gates, Y. Yin and Y. Lu, *Adv. Mater.*, 2000, 12, 693
- <sup>2</sup> A. Corma, *Chem. Rev.*, 1997, 97, 2373
- <sup>3</sup> T. J. Barton, L. M. Bull, W. G. Klemperer, D. A. Loy, B. McEnaney, M. Misono, P. A. Monson, G. Pez, G. W. Scherer, J. C. Vartuli and O. M. Yaghi, *Chem. Mater.*, 1999, 11, 2633
- <sup>4</sup> K. Moller and T. Bein, *Chem. Mater.*, 1998, 10, 2950
- <sup>5</sup> G. A. Ozin, A. Kuperman and A. Stein, *Angew. Chem., Int. Ed. Engl.*, 1989, 28, 359
- <sup>6</sup> M. M. Collinson, in *Handbook of Advanced Electronic and Photonic Materials, and Devices*, Ed. H. S. Nalwa, 5, Academic Press, 2001, 163
- <sup>7</sup> M. Ebelman, *Ann. Chimie Phys.* 1846, 16, 129
- <sup>8</sup> T. Graham, *J. Chem. Soc.* 1864, 17, 318
- <sup>9</sup> C. B. Hurd, *Chem. Rev.* 1938, 22, 403
- <sup>10</sup> L. L. Hench, J. K. West, *Chem. Rev.*, 1990, 90, 35
- <sup>11</sup> O. Lev, M. Tsionsky, L. Rabinovich, V. Glezer, S. Sampath, I. Pankratov, J. Gun, *Anal. Chem.*, 1995, 67, 1, 22A
- <sup>12</sup> C. J. Brinker, G. W. Scherer, *Sol-Gel Science: The Physics and Chemistry of Sol-Gel processing*, New York, 1990
- <sup>13</sup> C. J. Brinker, G. W. J. Scherer, *Non-Crystalline Solids*, 1985, 70, 301
- <sup>14</sup> D. Avnir, L. C. Klein, D. Levy, U. Schubert and A. B. Wojcik, *Chemistry of Organic Silicon Compounds*, Wiley, Chichester, UK, 1998, 2, 2317
- <sup>15</sup> J. Wen, G. L. Wilkes, *Chem. Mater.*, 1996, 8, 1667
- <sup>16</sup> C. Sanchez, F. Ribot, *New J. Chem.*, 1994, 18, 1007
- <sup>17</sup> C. Sanchez, F. Ribot, B. Lebeau, *J. Mater. Chem.*, 1999, 9, 35
- <sup>18</sup> M. M. Collinson, *CRC Crit. Rev. Anal. Chem.*, 1999, 29, 289
- <sup>19</sup> O. Lev, Z. Wu, S. Bharathi, V. Glezer, A. Modestov, J. Gun, L. Rabinovich and S. Sampath, *Chem. Mater.*, 1997, 9, 2354
- <sup>20</sup> J. Livage, C. Roux, T. Coradin, S. Fennouh, S. Guyon, L. Bergogne, A. Coiffier and O. Bouvet, *Mater. Res. Soc. Symp. Proc.*, 2001, 651, T1
- <sup>21</sup> J. D. Mackenzie, E. P. Bescher, *J. Sol-Gel Sci. Technol.*, 1998, 13, 371
- <sup>22</sup> J. D. Mackenzie, *Polym. Mater. Sci. Eng.*, 1993, 70, 380
- <sup>23</sup> S. Mann, S. L. Burkett, S. A. Davis, C. E. Fowler, N. H. Mendelson, S. D. Sims, D. Walsh, N. T. Whilton, *Chem. Mater.*, 1997, 9, 2300
- <sup>24</sup> S. Yano, K. Iwataand, K. Kurita, *Mater. Sci. Eng. C*, 1998, 6, 75
- <sup>25</sup> M. M. Collinson, *Advanced Electronic and Photonic Materials and Devices*, Academic Press, 2001, 5, 163
- <sup>26</sup> M. M. Collinson, *Trends Anal. Chem.*, 2002, 21, 30
- <sup>27</sup> A. Walcarius, *Electroanalysis*, 1998, 10, 1217
- <sup>28</sup> J. Wang, *Anal. Chim. Acta*, 1999, 399, 21
- <sup>29</sup> A. Walcarius, J. Bessiere, *Chem. Mater.*, 1999, 11, 3009
- <sup>30</sup> A. Walcarius, *Electroanalysis*, 2001, 13, 701
- <sup>31</sup> A. Walcarius, *Encyclopedia of Nanoscience and Nanotechnology*, American Scientific Publishers, 2004, 2, 857
- <sup>32</sup> L. Rabinovich, O. Lev, *Electroanalysis*, 2001, 13, 265
- <sup>33</sup> M. M. Collinson, *Mikrochim. Acta*, 1998, 129, 149
- <sup>34</sup> M. M. Collinson, A. R. Howells, *Anal. Chem.*, 2000, 72, 702A
- <sup>35</sup> S. Sayen, M. Etienne, J. Bessiere, A. Walcarius, *Electroanalysis*, 2002, 14, 1521
- <sup>36</sup> A. Walcarius, M. Etienne, S. Sayen, B. Lebeau, *Electroanalysis*, 2003, 15, 414
- <sup>37</sup> B. Barroso-Fernandez, M. Theresa Lee-Alvarez, C. J. Seliskar, W. R. Heineman, *Anal. Chim. Acta*, 1998, 370, 221
- <sup>38</sup> M. Etienne, J. Bessiere, A. Walcarius, *Sens. Actuators, B*, 2001, B76, 531
- <sup>39</sup> C. Hsueh and M. M. Collinson, *J. Electroanal. Chem.*, 1997, 420, 243
- <sup>40</sup> C. L. Lin, P. Tien, L. K. Chau, *Electrochim. Acta*, 2004, 49, 573
- <sup>41</sup> R. Makote, M. M. Collinson, *Chem. Mater.*, 1998, 10, 2440
- <sup>42</sup> M. D. Petit-Dominguez, H. Shen, W. R. Heineman, C. J. Seliskar, *Anal. Chem.*, 1997, 69, 703
- <sup>43</sup> S. Sayen, C. Gerardin, L. Rodehuser, A. Walcarius, *Electroanalysis*, 2003, 15, 422
- <sup>44</sup> H. Wei, M. M. Collinson, *Anal. Chim. Acta*, 1999, 397, 113
- <sup>45</sup> M. Ogawa, *Supramol. Sci.*, 1998, 5, 247
- <sup>46</sup> D. Zhao, P. Yang, D. I. Margolese, B. F. Chmelka, G. D. Stucky, *Chem. Commun.*, 1998, 2499
- <sup>47</sup> N. Nishiyama, S. Tanaka, Y. Egashira, Y. Oku, K. Ueyama, *Chem. Mater.*, 2002, 14, 4229

- 
- <sup>48</sup> J. C. Brinker, D. R. Dunphy, *Curr. Opin. Colloid Interference Sci.*, 2006, 11, 126
- <sup>49</sup> A. Walcarius, E. Sibottier M. Etienne, J. Ghanbaja, *Nature Materials*, 2007, 6, 602
- <sup>50</sup> R. Shacham, D. Avnir, D. Mandler, *Adv. Mater.*, 1999, 11, 384
- <sup>51</sup> J. A. Cox, K. M. Wiaderek, B.L. Mehdi, B. P. Gundorf, D. Ranganathan, S. Zamponi, M. Berrettoni, *J. Solid State Electrochem.*, 2011, 15, 2409
- <sup>52</sup> C.J. Brinker, G. C Frye, J. Hurd, C. S. Ashley, *Thin Solid Films*, 1991, 201, 97
- <sup>53</sup> H. Bissig, R. V., F. Scheffold, P. Schurtenberger, V. Trappe, *Soft Condensed Matter*
- <sup>54</sup> M. D. Sacks, R. S. Sheu, *Science of Ceramic Chemical Processing*, Wiley, United States, 1986
- <sup>55</sup> M. D. Sacks, R. S. Sheu, *J. NonCryst. Solids*, 1987, 92, 383
- <sup>56</sup> J. D. Wright, N. A. J. M. Sommerdijk, *Sol-gel Materials, Chemistry and Applications*, Gordon and Breach Science Publishers, 2001
- <sup>57</sup> C. J. Brinker, G. W. Scherer, *Sol-Gel Science: Physics and Chemistry of Sol-Gel Processing*, Academic Press, United States, 1990
- <sup>58</sup> D. Rolison, B. Dunn, *J. Mater. Chem.*, 2001, 11, 963
- <sup>59</sup> H. Schmidt, *Struc. Bond.* 1992, 77, 119
- <sup>60</sup> D. Mandler, *Isr. J. Chem.*, 2010, 50, 306
- <sup>61</sup> R. Shacham, D. Avnir, D. Mandler, *Advanced Materials*, 1999, 11, 384
- <sup>62</sup> R. Shacham, D. Mandler, D. Avnir, *Chem. Eur. J.*, 2004, 10, 1936
- <sup>63</sup> R. Shacham, D. Avnir, D. Mandler, *J. Sol-Gel Sci. Technol.*, 2004, 31, 329
- <sup>64</sup> R. Shacham, D. Mandler, D. Avnir, *C. R. Chim.*, 2010, 13, 237
- <sup>65</sup> M. Kanugo, M. M. Collinson, *Chem. Commun*, 2004, 548
- <sup>66</sup> Mehdi BL, Rutkowska IA, Kulesza PJ, Cox JA (2013) *J Solid State Electrochem* 17:1581-1590
- <sup>67</sup> Rutkowska IA, Sek JP, Mehdi BL, Kulesza PJ, Cox JA (2014) *Electrochimica Acta* 122:197-203
- <sup>68</sup> Murray RW (2008) *Chem Rev* 108:2688-2720
- <sup>69</sup> Zhang B, Zhang Y, White HS (2004) *Anal Chem* 76:6229-6238
- <sup>70</sup> Zhang B, Zhang Y, White HS (2006) *Anal Chem* 78:477-483
- <sup>71</sup> Bard AJ, Faulkner LR (2001) *Electrochemical methods* 2<sup>nd</sup> ed. Wiley & Sons, New York
- <sup>72</sup> Noël JM, Velmurugan J, Gökmeşe E, Mirkin MV (2013) *J Solid State Electrochem* 17:385-389
- <sup>73</sup> Berrettoni M, Giorgetti M, Zamponi S, Conti P, Ranganathan D, Zanotto A, Saladino ML, Caponetti E (2010) *J Phys Chem* 114:6401-6407
- <sup>74</sup> De Tacconi NR, Rajeshwar K, Lezna RO (2003) *Chem Mater* 15:3046-3062
- <sup>75</sup> Yang M, Jiang J, Yang Y, Chen X, Shen G, Yu R, *Biosensors and Bioelectronics* 21 (2006) 1791–1797
- <sup>76</sup> Chen SM (1998) *Electrochim Acta* 43: 3359-3369
- <sup>77</sup> Pyrasch M, Toutianoush A, Jin W, Schnepf J, Tieke B (2003) *Chem Mater* 15: 245-254
- <sup>78</sup> Berrettoni M, Giorgetti M, Cox JA, Ranganathan D, Conti P, Zamponi S (2012) *J Solid State Electrochem* 16:2861-2866
- <sup>79</sup> Vorotyntsev MA, Daikhin LI, Levi MD (1992) *J Electroanal Chem* 332: 213-235
- <sup>80</sup> Kondratiev VV, Tikhomirova AV, Malev VV (1999) *Electrochim Acta* 45:751-759
- <sup>81</sup> Ranganathan D, Zamponi S, Berrettoni M, Mehdi BL, Cox JA (2010) *Talanta* 82:1149-1155
- <sup>82</sup> Shi G., Lu J, Xu F, Sun W, Jin L, Yamamoto K, Tao S, Jin J (1999) *Anal Chim Acta* 391:307-313
- <sup>83</sup> Cox JA, Gray TJ (1990) *Anal Chem* 62:2742-2744
- <sup>84</sup> Sattarahmady N, Heli H (2011) *Anal Biochem* 409:74–80
- <sup>85</sup> Gao ZN, Zhang J, Liu WY (2005) *J Electroanal Chem* 580:9–16
- <sup>86</sup> Gorski W, Aspinwall CA, Lakey JRT, Kennedy RT (1997) *J Electroanal Chem* 425:191-199

## **6. Physicochemical characterization of Anatase TiO<sub>2</sub>-Metal Hexacyanometallate (MHCMs) composite materials**

### **6.1 Introduction**

#### **6.1.1 Anatase TiO<sub>2</sub>-MHCMs composite materials**

Composite materials consisting of semiconductors and inorganic compounds have often attractive photo-electrochemical properties. Among the semiconductor materials, TiO<sub>2</sub> is particularly promising due to its photo-electrochemical properties, high photo-activity, outstanding hydrophilicity<sup>1</sup>, strong redox and catalytic activity; the range of its potential applications includes catalysis, photovoltaic cells,<sup>2</sup> self-cleaning<sup>3</sup> and antifogging surface treatments.<sup>4,5</sup>

In addition, TiO<sub>2</sub> is non-toxic, chemically very stable, and easily obtained as nanometer scale particles.<sup>6</sup>

The photo-catalytic properties of TiO<sub>2</sub> are strongly affected by its structure, interface, grain size and crystallographic orientation of the exposed faces in contact with solution.<sup>7</sup> The photo-electrochemical characteristics are dependent upon porosity, morphology and the method of synthesis.<sup>8,9</sup>

Surface functionalization of TiO<sub>2</sub> has been achieved with many methods including doping with metal ions or nonmetallic elements, sensitization with organic dyes or semiconductors with a small band-gap.

TiO<sub>2</sub> modifications with transition metals have extended the spectral response of TiO<sub>2</sub> well into the visible region also improving photocatalytic activity.<sup>10,11,12</sup>

The incorporation of transition metals in the titania crystal lattice may result in the formation of new energy levels between VB and CB, inducing a shift of light absorption towards the visible light region.

Anatase results more efficient than rutile in the photocatalysis,<sup>13</sup> hence is more widely used than rutile in many applications, among which is the synthesis of supported catalysts, due to its remarkably higher specific surface area.

The aim of this study is the design, synthesis and characterization of new composite materials of TiO<sub>2</sub> and Metal Hexacyanoferrates.

Among the Metal Hexacyanoferrates, Cobalt Hexacyanoferrate (CoHCF) has been extensively studied in literature due to its interesting chemical and electrochemical properties.<sup>14</sup>

CoHCF exhibits excellent reversible redox centers (at both Fe and Co site) and its electrochemical activity is affected by electrolyte cation as proved by Kulesza et al.<sup>15</sup> CoHCF films can be easily fabricated on various surfaces and the traditional methods to prepare it include chemical and electrochemical deposition.<sup>16,17</sup>

On the contrary, Iron Hexacyanocobaltate, FeHCC presents a cubic structure similar to that of CoHCF, in which both metal centers are octahedrally coordinated by the cyanide groups, but they are differently coordinated to carbon and nitrogen, in fact cobalt and iron atoms are coordinated by six carbon and six nitrogen atoms, respectively providing significantly different properties. The electrochemistry of FeHCC has not been extensively investigated in literature, contrary to CoHCF.

However, it is reported in papers dealing with Cs sorption probed by Mössbauer spectroscopy<sup>18</sup> and its removal in waste solutions through a process involving the precipitation of cesium.<sup>19</sup> It is worth highlighting the well-known electrochemical activity of iron centers in FeHCC while cobalt atoms in aqueous electrolytes display no activity.<sup>20</sup>

Widmann et al. investigated the behavior of solid mixtures  $KM[HCF]_{1-x}[HCC]_x$  where  $M = Ni, Fe, Cu$  showing the redox activity of high spin iron centre  $Fe^{2+}/Fe^{3+}$  occurs. This activity is observed by cyclic voltammetry only in freshly synthesized FeHCC; after 2 days the peak system of low-spin iron appears, obviously due to a partial decomposition to Prussian green revealed by a change in color to light green.<sup>21</sup>

Several attempts have been made to deposit MHCM on  $TiO_2$  composited films, in particular de Tacconi et al. studied the preparation, the photoelectrochemical characterization, and the photoelectrochromic behavior of Metal Hexacyanoferrate–titanium dioxide composite films (where  $M = Cu, Ni, In$ )<sup>22</sup> and Rutkowska et al. used  $TiO_2$ -Nickel(II) Hexacyanoferrate(II,III) modified electrodes.<sup>23</sup>

$TiO_2$  nanoparticles functionalized with  $Fe^{II}(CN)_6^{4-}$  have been investigated in literature by electro-absorption spectroscopy. The iron complex is believed to bind at the  $Ti^{IV}$ -site via a mono-dentate cyanide ligand, obtaining  $(CN)_5Fe(II)-CN-Ti(IV)$  particle,<sup>24</sup> as suggested by IR and resonance Raman evidence. Other studies dealt with thin films prepared by mixing  $TiO_2$  with Metal-Hexacyanometallates.<sup>25,26</sup>

To the best of our knowledge, no investigation of the CoHCF–TiO<sub>2</sub> composites has been reported in literature while a detailed electrochemical study of their FeHCC–TiO<sub>2</sub> counterparts has appeared.<sup>26</sup>

Based on the above premises, this thesis reports novel synthesis procedures of both the electrochemical and chemical Anatase TiO<sub>2</sub>-CoHCF and TiO<sub>2</sub>-FeHCC, the influence upon TiO<sub>2</sub> optical properties, and the structural-electronic characterization performed with a wide range of experimental techniques in order to develop new technological applications.

### **6.1.2 Anatase-driven charge transfer involving a spin transition in cobalt iron cyanides nanostructures**

Successes in synthesizing new metal-cyanide solids, clusters and low-dimensionality cyanide arrays has obtained a great deal of attention.<sup>27</sup> In this context, coordination complexes showing two close-lying electronic states differing in charge distribution represent an appealing field of investigation since they offer an opportunity for studies of the factors that control spin conversion between these states.

The family of Cobalt Hexacyanoferrates undergoes a well characterized charge transfer induced spin transition (CTIST) that can be activated either thermally or optically.<sup>28,29</sup>

The transition,  $\text{Fe}^{2+}(\text{LS})\text{-CN-Co}^{3+}(\text{LS}) \rightarrow \text{Fe}^{3+}(\text{LS})\text{-CN-Co}^{2+}(\text{HS})$ , where HS and LS denote high spin and low spin, respectively, involves a spin change on the cobalt site, correlated to a charge transfer between the Fe and Co which induces the  $\text{Co}^{\text{II}}(\text{S}=3/2)$  -  $\text{Co}^{\text{III}}(\text{S}=0)$  switching, with a subsequent structural significant change attributed to the Co–N bond length upon the high spin (HS) - low spin (LS) switching and leading to a reversible expansion of the lattice.

This elastic process in the core is thought to induce a magnetomechanical response in the magnetic shell.<sup>30</sup> Generally, the difference in the energy of the two spin states is furnished by photoexcitation, and an irradiation energy of 1 eV (red light) is enough for the spin transition to occur between the two stable states.<sup>31</sup>

For instance, a spin transition followed by strong changes in the magnetisation has been observed upon illuminating a Cobalt Hexacyanoferrate sample with a proper light, a fact that has led to applications in memory devices and magneto-optical switching.<sup>32</sup>

The temperature is not the only external strain able to trigger CTIST: it is possible also by varying the pressure or replacing the alkali cation inserted in the 3D structure, as shown in literature.<sup>33</sup> Anyway, if the electronic structure of the transition-metal ion in both ground and metastable state is now well-known, questions still remain on the charge transfer mechanism.

The Prussian Blue (PB) analogue  $\text{KCo}[\text{Fe}(\text{CN})_6]$  nanodispersed with anatase  $\text{TiO}_2$  has excited a great interest recently,<sup>34</sup> leading to the electron transfer within the pairs  $\text{Co(II)-HS-Fe(III)-LS}$  and  $\text{Co(III)-LS-Fe(II)-LS}$ . This study represents one of the first examples where an external stimulus other than the photoexcitation, and in particular anatase  $\text{TiO}_2$ , triggers spin-crossover phenomena in Metal-Hexacyanoferrate based-molecular solid.

The electronic excitations collectively propagate through the crystal leading to a new long-lived phase. The experimental evidence of this effect is supported by previous high resolution XANES and EXAFS results, the latter highlighted a consistent change (10 %) of the Co-N first shell bond distance and making evidence of the local charge changes and local structural modification in  $\text{TiO}_2$ -modified samples. The practical significance of the charge-transfer materials is very important because a functional material property can be induced by external stimuli opening new directions in chemical inventions of new stimuli-switchable devices.<sup>35</sup> Materials undergoing a photoinduced phase-transition, for instance, are an attractive research subject in the fields of inorganic chemistry, solid-state chemistry, and materials science,<sup>36,37</sup> whereas photomagnetic materials (optical switching magnets), experiencing a magnetic transition upon an optical stimulus, could be applied in new optical recording technologies such as opto-magnetic memories and optical computers.

In this study, we will highlight how it is possible to induce a structural order along the Co-NC-Fe-CN-Co chain by simply synthesizing a composite material where CoHCF nanoparticles are dispersed on Anatase  $\text{TiO}_2$ . This effect is confirmed by  $^{57}\text{Fe}$  Mössbauer spectroscopy, which clearly indicates a change in the oxidation state at the iron centre on going from pure CoHCF to the  $\text{TiO}_2$ -CoHCF composite.

The electron transfer through the cyanide bridge to produce  $\text{Co}^{\text{II}}\text{-Fe}^{\text{III}}$  magnetic pairs and the corresponding spin transition are associated with a different population of the d orbitals and especially of the antibonding  $e_g^*$  ones.

This leads to important geometrical changes around the transition metal.

In this solid material, the electronic and structural changes accompanying the spin transition propagate throughout the solid through short and long range interactions and the cooperativity of the transition is provided by intercluster interaction.

To the best of our knowledge, this is the first study in which a completely pure low-spin Fe(II) is obtained starting from a mix of low-spin Fe(II) and Fe(III).

The investigation of spin transitions induced by charge transfer in molecular solids is very important because these materials may become switchable components in molecular electronics and, thanks to the significant change in the spin state induced by the charge transfer, in spintronics as well.

## **6.2. Experimental**

### **6.2.1 Reagents and materials**

All chemicals used in this work were reagent grade and were used as received from Sigma-Aldrich (FeCl<sub>2</sub>, K<sub>3</sub>[Co(CN)<sub>6</sub>], K<sub>3</sub>[Fe(CN)<sub>6</sub>], CoCl<sub>2</sub>, KCl, anatase TiO<sub>2</sub> 99%) and from Fluka (TiCl<sub>4</sub>, >99.0%).

Deionized water was used throughout this work. All experiments were carried out at room temperature and in air.

### **6.2.2 TiO<sub>2</sub>-Iron Hexacyanocobaltate (FeHCC) electrochemical synthesis**

CoHCF dynamic electrodeposition is reported in several scientific papers and its ease of synthesis by electrochemical deposition is well known. The morphology and the CV features are preserved for long time contrary to FeHCC.

FeHCC film electrodeposition through cyclic voltammetric (CV) can be considerably improved by electrodepositing FeHCC on a TiO<sub>2</sub> modified electrode.

In particular, Anatase TiO<sub>2</sub> film has been obtained by using TiCl<sub>4</sub> as precursor. The aqueous hydrolysis of TiCl<sub>4</sub>, as indicated in the following reaction, represents a process to produce nanostructured polycrystalline TiO<sub>2</sub>. An aqueous solution of TiCl<sub>4</sub> was dropped on to the electrode surface and allowed to dry (these operations are carried out under the hood) in order to obtain an adherent TiO<sub>2</sub> film on the GC surface.

This process is run at room temperature and yield Anatase-phase particles because of the lower reaction temperature<sup>38</sup> as proved by the EDX spectra.

The film formation takes place in according to the following reaction:



For the dynamic electrodeposition through cyclic voltammetric (CV) of the FeHCC film, the selected TiO<sub>2</sub> modified electrode (GC, or ITO, or GF) is cycled from 1.2 V to -0.4 V potential at a rate of 0.1 V/s, in the modification solution which contains 1.0 mM K<sub>3</sub>Co(CN)<sub>6</sub>, 1.0 mM FeCl<sub>3</sub> and 1.0 M KCl as supporting electrolyte.

### 6.2.3 Chemical synthesis and deposition strategy

Iron Hexacyanocobaltate and Cobalt Hexacyanoferrate were chemically synthesized by a co-precipitation method by adding dropwise 0.05 M water solution of FeCl<sub>2</sub> or CoCl<sub>2</sub> to an equivalent amount of K<sub>3</sub>[Co(CN)<sub>6</sub>] or K<sub>3</sub>[Fe(CN)<sub>6</sub>] and stirring at room temperature. When the two solutions were in contact, a yellow or a brick-red suspension was obtained.

All precipitates were allowed to stand for a night and air-dried at ambient conditions to improve the formation of the TiO<sub>2</sub>-MHCM bond. Subsequently, they were carefully washed several times with deionized water to remove the unreacted salts and centrifuged to separate the solid product. Finally, the precipitate was dried at 80°C.

TiO<sub>2</sub>-FeHCC and TiO<sub>2</sub>-CoHCF were obtained in a similar way starting with a TiO<sub>2</sub> suspension to which a water solution of FeCl<sub>2</sub> or CoCl<sub>2</sub> and an equivalent amount of K<sub>3</sub>[Co(CN)<sub>6</sub>] or K<sub>3</sub>[Fe(CN)<sub>6</sub>] were added drop wise and stirred at room temperature<sup>26</sup>.

These TiO<sub>2</sub>-MHCM compounds were synthesized in three different molar ratios: 1:1:1, 10:1:1 and 100:1:1 (where the notation indicates the TiO<sub>2</sub>:K<sub>3</sub>Fe(CN)<sub>6</sub>:CoCl<sub>2</sub> in the case of TiO<sub>2</sub>-CoHCF composite). Hereafter, the composites will be identified by the notation 1:1, 10:1, 100:1.

### 6.2.4 Chemical and electrochemical characterization of TiO<sub>2</sub>-MHCMs composite materials

The characterization was performed by a multi-technique approach.

In particular, Transmission Electron Microscopy (TEM) experiments were performed on a high resolution transmission electron microscope (HR-TEM) JEOL JEM-2100 operating at 200 kV. Before analysis, the samples were dispersed in isopropanol and deposited on a 300-mesh holey carbon-coated nickel grid. Elemental analysis was carried out using an energy dispersive X-ray detector (Energy Dispersive Spectroscopy, EDS), Oxford mod. 6498, on a 30 mm<sup>2</sup> area.

Infrared spectra (IR) were recorded with a Jasco FT/IR-4600 PLUS spectrometer working in transmission mode. At least 32 scans were typically taken between  $4000\text{ cm}^{-1}$  and  $500\text{ cm}^{-1}$  with a resolution of  $1\text{ cm}^{-1}$ . Powder spectra were recorded by using KBr pellets, containing about 1% w/w of the sample.

The pellets were produced by compressing with 5 ton for about 20 s the powders in a stainless steel mold of 13 mm in diameter; no pressure effects have been observed by using a manually operated hydraulic press (Specac Ltd., Orpington Kent, UK). The spectrum of pure KBr was taken as a background reference.

UV-Vis spectra were recorded in the 220–700 nm range with a HELIOS  $\alpha$  THERMO SPECTRONIC instrument.

Thermogravimetric analyses (TGA) were carried out in a Perkin Elmer TGA7 thermogravimetric analyzer. Samples (between 5 and 10 mg) were heated from 25 to  $400^\circ\text{C}$  at  $5^\circ\text{C}/\text{min}$  under flowing nitrogen ( $20\text{ cm}^3/\text{min}$ ).

X-ray photoelectron spectroscopy (XPS) analyses were performed with a Thetaprobe spectrometer (Thermo Fisher Scientific, Waltham MA, USA) at the University of Cagliari. The samples were mounted as pellets on a copper bi-adhesive tape. Spectra were collected using a  $300\text{ }\mu\text{m}$  spot size Al  $K\alpha$  monochromatic beam operated at 4.7 mA and 15 kV. A flood gun was used for charge compensation. Survey spectra were acquired in fixed analyzer transmission mode (FAT) using a pass energy (PE) of 200 eV, while the high-resolution spectra of C1s, Cl2p, Co2p, Fe2p, K2p, N1s, O1s, Ti2p were collected with a PE of 100 eV selecting the standard lens mode; the full-width at half-maximum of the peak height, FWHM, of the silver  $\text{Ag}3d_{5/2}$  signal for the high-resolution spectra was 0.83 eV. The linear response of the instrument was checked with periodic calibrations performed according to ISO 15472:2001.<sup>39</sup>

Binding energy values were corrected by referencing the aliphatic carbon to 285 eV. Data were acquired under computer control (Avantage v 3.45).

The spectra were processed using CASAXPS software.<sup>40</sup> An iterated Shirley – Sherwood<sup>41</sup> background subtraction routine was performed before applying a fitting procedure using a combination of Gaussian and Lorentzian shapes. Composition was calculated using the first-principle method<sup>42</sup> and assuming a homogeneous sample. Peak areas were corrected for the sensitivity factors calculated using the Scofield's photoionization cross-sections,<sup>43</sup> the asymmetry parameters,<sup>44</sup> the inelastic mean free paths (IMFP) and the intensity/energy response of the analyzer as detailed in the literature.<sup>45</sup>

IMFP were calculated according to Seah et al.<sup>46</sup> The accuracy of the resulting atomic concentrations is estimated to be within  $\pm 10\%$ .

X-Ray absorption measurements have been recorded at the XAFS beamline at Elettra Synchrotron (Basovizza, Trieste, Italy). The storage ring operated at 2.0 GeV in top up mode with a typical current of 300 mA. The data were recorded at Ti K-edge (4965 eV), Fe K-edge (7112 eV) and Co K-edge (7709 eV) in transmission mode using ionization chamber. Samples for XAS measurements were solid pellets, prepared by mixing the material (15 mg) with cellulose filler (100 mg). XAS spectra were deglitched, calibrated, and normalized using the Athena program.<sup>47</sup>

X-ray powder diffraction (XRD) patterns were collected with the  $\text{CuK}\alpha$  radiation on a Philips X'Pert Pro diffractometer. Diffraction patterns were collected between  $5^\circ < 2\theta < 70^\circ$ , where most reflections of MHCs diffraction patterns appear. Cell parameters were obtained by pattern matching using the Unitcell computer program.<sup>48</sup>

X-ray fluorescence elemental analysis was performed with a Shimadzu 800HS. Transmission  $^{57}\text{Fe}$  Mössbauer spectra were recorded at room temperature with a  $^{57}\text{Co}(\text{Rh})$   $\gamma$ -ray source in the constant acceleration mode. The velocity scale was calibrated using the magnetic six line spectrum of a high-purity iron absorber. The values of isomer shift ( $\delta$ ), quadrupole splitting ( $\Delta$ ), full line width at half-maximum ( $\Gamma$ ) and relative resonance area (RA), determined by fitting the experimental data to appropriate combinations of Lorentzian lines with a nonlinear least-square method, are reported in Table 14. The values of the isomer shift ( $\delta$ ) are given relative to  $\alpha$ -Fe.

About the electrochemical measurement, an aqueous suspension of the sample was dropped on the glassy carbon electrode; after drying, an adherent deposit was covering the electrode surface. Before deposition, the glassy carbon surface was polished with a 0.05  $\mu\text{m}$  alumina slurry on a microcloth polishing pad and rinsed with deionized water.

Electrochemical measurements were carried out with a CH Instrument, model 660c, through a standard three-electrode electrochemical glass cell (10  $\text{cm}^3$ ) comprising a glassy carbon electrode (with a 3 mm diameter) as working electrode and a Pt auxiliary electrode; the reference was a silver–silver chloride electrode ( $\text{Ag}/\text{AgCl}$ ) in a saturated solution of potassium chloride. All the potentials will be referred to the  $\text{Ag}/\text{AgCl}$  electrode.

In particular, for galvanostatic measurements, electrochemical tests were performed either in a three electrode glass cell, or in a two electrodes Swagelok teflon cell at room temperature using an MPG2 potentiostat from BioLogic.

Electrodes for galvanostatic measurements were composed of the active material (80% by weight, w/w), acetylene black (14% w/w, Y50A), and polytetrafluoroethylene PTFE (6% w/w, Alfa Aesar) as binder. The mixture was rolled into thin sheets and punched into circular electrodes 6.35 mm in diameter. The typical electrode mass was 4-6 mg. The TiO<sub>2</sub>-CoHCF electrode was used as the working electrode, whereas CoHCF electrodes were used as both the reference and the counter electrode. Whatman glass fiber disks were used as the separator, and a 1.0 M KCl aqueous solution as the electrolyte.

For galvanostatic measurements, the cells were cycled at capacities approaching theoretical values at low C-rates (C/10) between 0.7 and -0.7 V. The specific capacities presented hereafter have been calculated from the content of active material (80 wt%), and referred to the amount of Fe. For cyclic voltammetry (CV), all cells were cycled at 1 mV s<sup>-1</sup>.

### **6.3. Results and discussion**

#### **6.3.1 Novel Anatase TiO<sub>2</sub>-MHCMS electrochemical synthesis: TiO<sub>2</sub> as electronic and structural mediator**

Cobalt Hexacyanoferrate (CoHCF) dynamic electrodeposition is reported in several papers and its ease of synthesis by electrochemical deposition is well known.

The morphology and the CV features are preserved for long time contrary to FeHCC. This study proved that FeHCC film electrodeposition through cyclic voltammetric (CV) can be considerably improved by electrodepositing FeHCC on a TiO<sub>2</sub> modified electrode.

In particular, Anatase TiO<sub>2</sub> film has been obtained by using TiCl<sub>4</sub> as precursor.

FeHCC films have been electrosynthesized in 100 cycles on a cleaned GC electrode by cyclic voltammetry (CV) in solutions containing 1.0 mM K<sub>3</sub>Co(CN)<sub>6</sub>, 1.0 mM FeCl<sub>3</sub>, and 1.0 M KCl as supporting electrolyte.

Figure 42 shows the CV scans during electrodeposition and the background in 1.0 M KCl solution; the peak current and the associated charge (reported in the inset of Fig. 42) slightly increase with the number of cycles.

Only one reversible redox system can be observed. The response is associated with the intercalation of electrolyte K<sup>+</sup> cations.

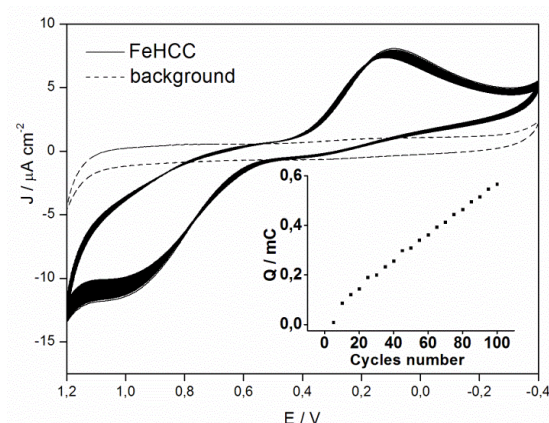


**Figure 42** Continuous CV at  $0.1 \text{ V s}^{-1}$  in a  $1.0 \text{ mM K}_3\text{Co(CN)}_6$ ,  $1.0 \text{ mM FeCl}_3$  and  $1.0 \text{ M KCl}$  solution for the electrodeposition of a FeHCC film on a GC electrode. The inset shows the cathodic associated charge as a function of number of cycles.

A GC electrode modified with Anatase  $\text{TiO}_2$  film has been subsequently used as working electrode to electrosynthesize FeHCC films. The conditions are the same of the previous FeHCC electrodeposition on the bare GC.

Figure 43 shows the CV scans during electrodeposition on the  $\text{TiO}_2$  modified GC electrode; the peak intensity and the associated charge deeply increase with the number of cycles, as shown in the inset in Fig. 43.

The associated charge increase is greater than the electrodeposition on bare GC, as shown in the Fig. 42 and Fig. 43 insets.

Increasing values of the current with the increasing number of scans prove the growth of the film thickness.

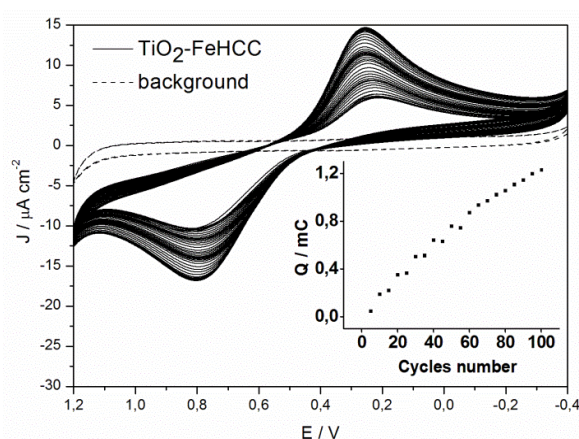


**Figure 43** Continuous CV at  $0.1 \text{ V s}^{-1}$  in  $1.0 \text{ mM K}_3\text{Co(CN)}_6$ ,  $1.0 \text{ mM FeCl}_3$  and  $1.0 \text{ M KCl}$  solution for the electrodeposition of a FeHCC film on a GC electrode modified with  $\text{TiO}_2$  film. The inset shows the associated charge as a function of number of cycles.

It is worth noting that the modification of GC by  $\text{TiO}_2$  film does not alter the voltammetric shapes shown in Fig. 42.

Figure 44 compares the last CV cycle (the 100<sup>th</sup>) of a FeHCC film on a bare GC electrode **a**) and on an Anatase TiO<sub>2</sub> modified GC electrode **b**).

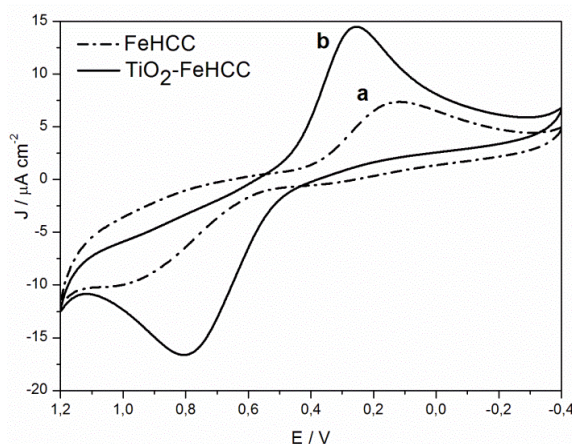


**Figure 44** CVs at 0.1 V s<sup>-1</sup> of the last cycle of the electrosynthesis for FeHCC on the bare GC **a**) and on the TiO<sub>2</sub> modified GC electrode **b**).

The comparison highlights a smaller cathodic and anodic peak separation by using an Anatase TiO<sub>2</sub> modified GC electrode. In this case, the morphology of the process seems more reversible, probably because of the modification of the electrode surface with TiO<sub>2</sub> acting as electronic and structural mediator, thus favoring the decreasing of the resistance to the electron transfer.

The redox mechanism involves K<sup>+</sup> insertion during reduction and its release during oxidation, according to the following reaction:



regardless of which metal atom is in the oxidized form.

The notation (CoFe)<sup>ox number</sup> is conserved for analogy with Cobalt Hexacyanoferrate, although in Iron Hexacyanocobaltate only the Fe center is always electrochemically active.

Figure 45 compares the increase of the passed charge versus the number of the cycles (100) for the electrodeposition process both on bare GC and on TiO<sub>2</sub> modified GC electrode. In both the electrodeposition processes, the passed charge increases as the number of the cycles increases and the increase is greater by using a TiO<sub>2</sub> modified GC electrode. This behavior can be ascribed to the greater electroactive surface due to the TiO<sub>2</sub> film.

The charge increase on TiO<sub>2</sub> modified GC electrode shown in Fig. 45 shows two different growth rates as indicated by the different slopes of the interpolation lines.

In the first 60 cycles the growth rate is higher, because the TiO<sub>2</sub> porous surface must be completely covered, after that the growth rate is due only to the film growth.

The growth rate decrease is due to a lower electroactive surface and to a possible different electrochemical kinetics. Similar behavior is observed in the case of the bare GC electrode. For this electrode two regions of different growth rate are observed in a shorter time scale.

In conclusion, the bare GC surface results totally covered in only 10 cycles because the electroactive surface is considerably smaller, while 60 cycles are needed in the case of a TiO<sub>2</sub> modified electrode.

The thickness of the electrodeposited FeHCC film on the electrode can be modulated by varying the number of cycles.

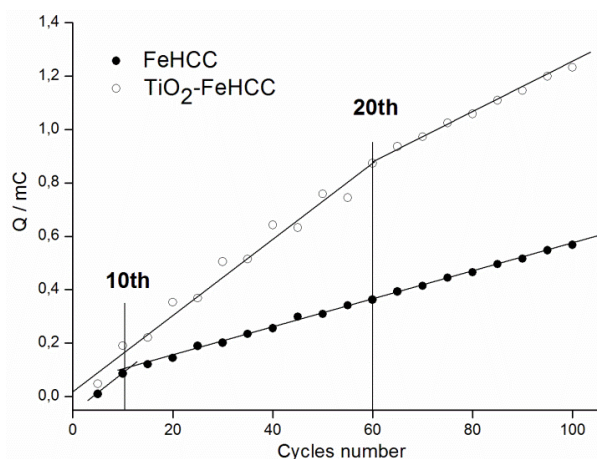


**Figure 45** Associated charge versus the number of the cycles (100) for the electrodeposition process. • - bare GC and o - TiO<sub>2</sub> modified GC electrode.

Figure 46 compares the last cycle (the 100<sup>th</sup>) of the FeHCC electrodeposition process to a cyclic voltammogram of the same electrode recorded in a 1.0 M KCl solution. The CVs on the bare GC (Fig. 46a) show a dramatic decrease of the current intensity, probably due to the loss of the electroactive material. The loss is so great that prevents the resolution of any voltammetric wave.

The poor stability and adherence of FeHCC to the GC electrode is already reported in literature by Kasem and al.<sup>49</sup>

Otherwise by using a TiO<sub>2</sub> modified GC electrode (Fig. 46b), only a small decrease of the current intensity is observed, and the morphology is perfectly preserved.

A stability test consisting in a continuous CVs, shows a slight decrease of the peak intensity as the number of cycles increases and the main electrochemical features can be observed up to 50 cycles. At this stage of research it is not clear if the electrode loses the electrochemical active compound (FeHCC) or the  $\text{TiO}_2$  film.

As matter of fact a single well-defined redox couple is observed (Fig. 46b).

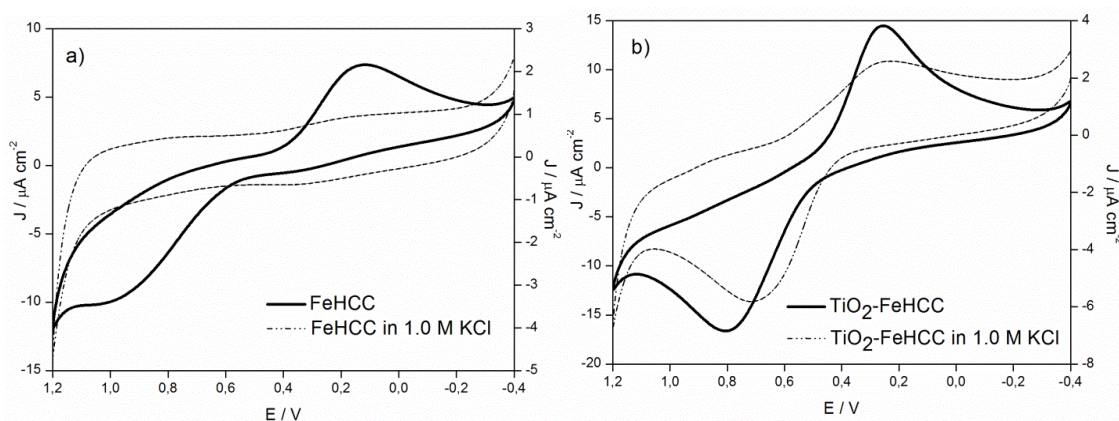


**Figure 46** CV of a FeHCC film on a bare GC electrode a) and of a FeHCC film on a  $\text{TiO}_2$  modified GC electrode b) performed in a 1.0 M KCl solution (dotted line), compared to the last cycle of the respective electrodeposition process (solid line).

Figure 46 b) shows a shift of the peak potential ( $E_p$ ) in the oxidation process towards cathodic potentials.

The different morphology of the oxidation and reduction peaks may be related to the dynamics of the  $\text{K}^+$  insertion/de-insertion. In the reduction process of the iron Hexacyanocobaltate film,  $\text{K}^+$  must enter into FeHCC film to provide a charge balance during reduction., while during the oxidation,  $\text{K}^+$  leaves the film.

The broader shape of the reduction peak can be explained by the fact that the cation insertion is less facile than the release.

As a matter of fact, more complex voltammetric morphologies are sometimes observed for the FeHCC electroformed film. The voltammetric waves recall the analogy with CoHCF compound. The simple electrochemical response so far detailed for electrodeposited film of FeHCC can be spoiled by the presence of more redox centers. In fact, more complex voltammetric morphologies are sometimes observed for the FeHCC electroformed film.

In particular, Fig. 47 compares the corresponding CV for FeHCC (solid line) and for CoHCF (dotted line). In this case the voltammetric waves recall the analogy with CoHCF compound.

As seen in the literature, the different redox waves are assigned to Cobalt and Iron. In fact, although the FeHCC electrodeposition processes have been performed in the same conditions, the morphology of the CVs can result very different, they can show either one wave (Fig. 46b) or two ones (Fig. 47, solid line) in the reduction process.

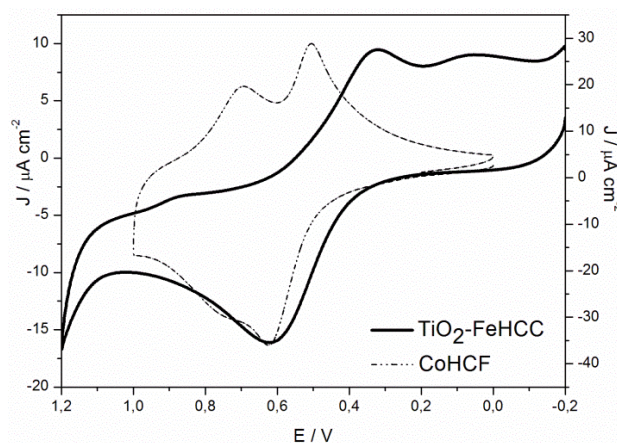


**Figure 47** CVs at  $0.1 \text{ V s}^{-1}$  of FeHCC (solid line) and CoHCF (dotted line) film in a 1.0 M KCl solution.

Respect to the electrochemical behavior of CoHCF film where two electroactive centers coexist ( $\text{Co}^{\text{III}}/\text{Co}^{\text{II}}$ ,  $\text{Fe}^{\text{III}}/\text{Fe}^{\text{II}}$ ) in the case of FeHCC film, probably the split of the reduction process can be ascribed to the simultaneously presence of two different FeHCC species (for example the soluble and insoluble species and/or their solid solutions).

To gain a complete understanding of FeHCC material, a FeHCC powder sample was synthesized following the reported procedures for the chemical solution synthesis.

Therefore, we exploited a possible chemical deposition procedure to obtain a homogeneous mixture of FeHCC- $\text{TiO}_2$  at the GC electrode.

To a cleaned GC (glassy carbon) or ITO (indium tin oxide) electrode, a volume of 0.02 mL of FeHCC and  $\text{TiO}_2$  dispersion was needed to be retained on the top of the electrode in order to obtain a smooth and uniform surface.

By using ITO electrodes, the best results were obtained. Figure 48 shows the CV of an  $\text{TiO}_2$ -FeHCC composite electrode in 1.0 M KCl solution at native pH on ITO electrode. The CV retains the same morphology of the electroformed FeHCC.

The inset of Fig. 48 shows the cathodic peak potential in function of the logarithm of the  $K^+$  concentration ( $1.0$ ,  $1.0 \cdot 10^{-1}$ ,  $1.0 \cdot 10^{-2}$  M) in order to verify whether the  $K^+$  is effectively involved in the redox reaction 3.

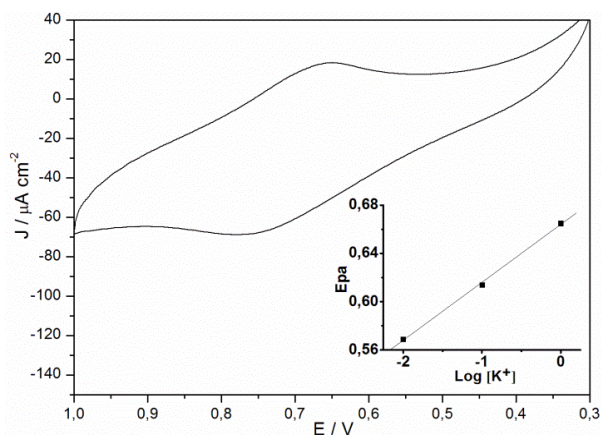


**Figure 48** CVs of  $TiO_2$ -FeHCC film recorded in 1.0 M KCl solution. The inset shows the cathodic peak potentials as a function of  $\log[K^+]$  which yield a slope of 47 mV/dec ( $R^2 = 0.999$ ).

The peak potentials are shifted in a negative direction with decreasing the electrolyte concentration in agreement with the involvement of  $K^+$  ions in the redox reactions.

Indeed the cyclic voltammogram shows a potential peaks shift toward to lower values very close to 59 mV per decade of  $K^+$  ion concentration, characteristic of a monoelectronic process.

### 6.3.2 Chemical and electrochemical characterization of Anatase $TiO_2$ -MHCs composite materials

Chemically synthesized Anatase  $TiO_2$ -FeHCC and  $TiO_2$ -CoHCF compounds were characterized by a multi-technique approach.

In particular, Table 4 lists the  $TiO_2$ -FeHCC and  $TiO_2$ -CoHCF composite materials synthesized in different ratios and summarizes the techniques used for their characterization. The results of the thermogravimetric analyses and the XRD are also included.

TGA allows the determination of the number of water molecules included in the structure of the Metal Hexacyanometallate. In Table 4 the XRD column reports the cell parameter,  $a$ , referred to the cubic structure, calculated by the unit cell program.

The diffractogram of the 100:1  $TiO_2$ :FeHCC sample is not available being the concentration of FeHCC too low in this composite. The cell parameters,  $a$ , assume a value very close to 10 Å, typical of Metal Hexacyanometallate compounds.

Table 5 provides the stoichiometry of the compounds as measured by X-ray fluorescence (XRF) and X-ray photoelectron spectroscopy (XPS).  $K^+$  is missing in the XRF data due to limitations of the experimental set up.

The low intensity of the cobalt signal, Co2p, did not allow calculation of the surface composition of the  $TiO_2$ -FeHCC sample in 100:1 ratio. The elemental ratios calculated with XPS and XRF are in reasonable agreement.

**Table 4** Synoptic table of the compounds studied.

Sample	CV	IR	UV-Vis	TGA ( $nH_2O$ )*	XAS	XRD $a / \text{\AA}^*$	XPS	TEM	
$TiO_2$ -CoHCF	1:1	X	X	X	3,0	X	10.07	x	X
	10:1	X	X	X	6,5		10.30	x	X
	100:1	X	X	X	7,8		10.26	x	X
$TiO_2$ -FeHCC	1:1	X	X	X	5,2	X	10.30	x	X
	10:1	X	X	X	6,3		10.13	x	X
	100:1	X	X	X	7,4		-	x	X

\*The last digit is only partially significant due to the statistical error.

**Table 5** Stoichiometry of the studied compounds, obtained by XPS and XRF techniques.

Sample	$TiO_2$ :MHCM Ratio	XPS			XRF*	
		Formula	Co/Fe	N/Fe	Co/Fe	Co/Fe
$TiO_2 + CoHCF$	1:1	$K_{1,2}Co_{1,3}[Fe(CN)_6]$	1.3	6.5	$Co_{1,1}[Fe(CN)_6]$	1.1
	10:1	$K_1Co_{1,5}[Fe(CN)_6]$	1.5	6.3	$Co_{1,2}[Fe(CN)_6]$	1.2
	100:1	$K_{0,7}Co_{1,5}[Fe(CN)_6]$	1.5	5.9	$Co_{1,4}[Fe(CN)_6]$	1.4
			Fe/Co	N/Co		Fe/Co
$TiO_2 + FeHCC$	1:1	$K_{0,7}Fe_{0,7}[Co(CN)_6]$	0.7	6.2	$Fe_{0,8}[Co(CN)_6]$	0.8
	10:1	$K_{0,3}Fe_{0,8}[Co(CN)_6]$	0.8	5.8	$Fe_{1,6}[Co(CN)_6]$	1.6
	100:1	-	-	-	$Fe_{1,32}[Co(CN)_6]$	1.3

\* $K^+$  is not detected.

All the synthesized compounds, that is  $TiO_2$ -FeHCC and  $TiO_2$ -CoHCF in different ratios, were fully characterized by TEM, IR, UV-Vis, XAS, XPS and cyclic voltammetry (CV) in order to provide evidence of their formation, to determine the morphology of the aggregates, to verify the formation of the compounds and to shed a light on the effect of the FeHCC and CoHCF doping agents.

### ➤ Transmission Electron Microscopy (TEM)

Samples were characterized by transmission electron microscopy (TEM) and energy dispersive spectroscopy (EDS) to provide evidence for the presence of the Metal Hexacyanometallate and to characterize the morphology of particles and aggregates.

In particular EDS analyses performed upon various aggregates demonstrate the co-presence of Fe, Co, and Ti.

The following observations apply both to FeHCC and to CoHCF compounds:

1. aggregates of TiO<sub>2</sub>-CoHCF (1:1 ratio) and TiO<sub>2</sub>-FeHCC (1:1 ratio) consist of typical spherical TiO<sub>2</sub> particles covered with grains of cubic CoHCF and FeHCC;
2. in 1:1 samples, many isolated clusters of CoHCF or FeHCC with cubic structure and 100÷200 nm in size are observed; however, FeHCC has less isolated clusters than CoHCF;
3. in 10:1 samples; TiO<sub>2</sub> aggregates are larger, ranging from 100 to 600 nm, and consist of 5÷20 TiO<sub>2</sub> spherical particles; Fig. 49a is a micrograph of TiO<sub>2</sub> and CoHCF in 10:1 ratio showing an aggregate of spherical TiO<sub>2</sub> particles covered with cubic nanocrystals of CoHCF;
4. In 100:1 samples, rare CoHCF or FeHCC particles and TiO<sub>2</sub>-CoHCF or TiO<sub>2</sub>-FeHCC aggregates are present, as shown in Fig. 49b. These CoHCF or FeHCC particles are larger than in the 1:1 and 10:1 samples.

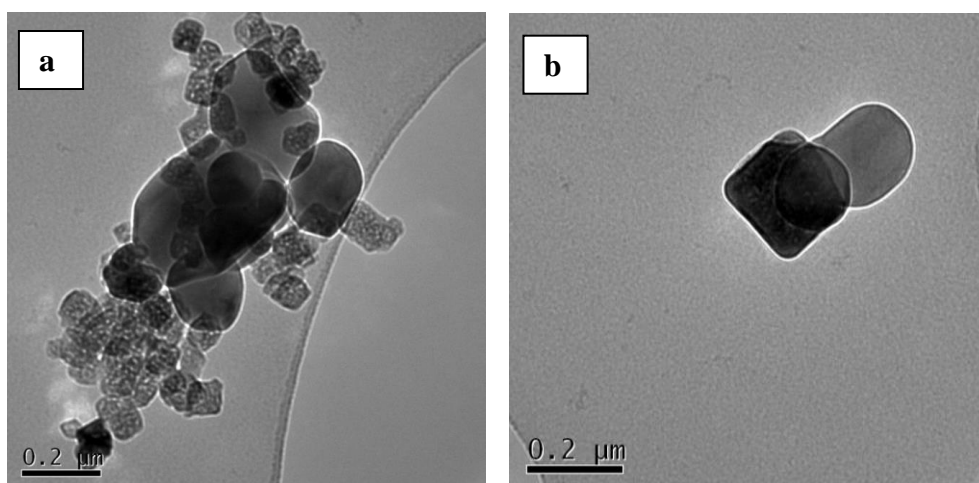


**Figure 49** a) Typical aggregate of TiO<sub>2</sub> spherical particles covered with cubic nanocrystals of CoHCF (10:1 ratio), b) Magnification at 30.000x of the sample referring to a cubic particle of CoHCF bonded to a TiO<sub>2</sub> spherical particle. TiO<sub>2</sub>-CoHCF are in 100:1 ratio.

#### ➤ **Fourier transform Infrared Spectroscopy (FT/IR)**

For sake of clarity and comparison, each Fourier transform infrared (FT/IR) spectrum presented below is overturned and individually normalized to its top transmittance value. Fig. 50 shows the spectra of FeHCC (red curve) and CoHCF (black curve) in the bulk form.

Spectra in Fig. 50 agree with data from the literature.<sup>14,26</sup>

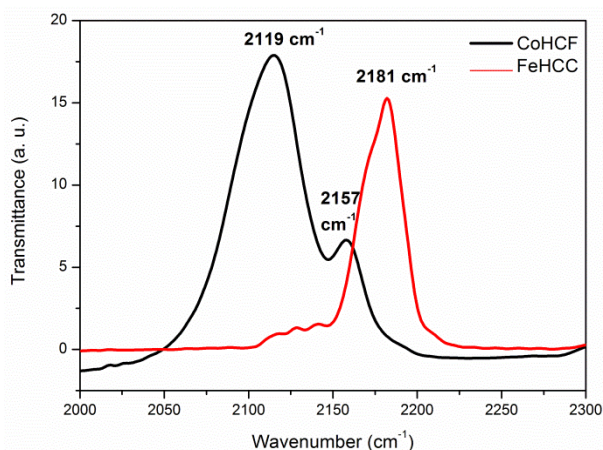


**Figure 50** FeHCC (red curve) and CoHCF (black curve) FT/IR spectra in the 2000-2300  $\text{cm}^{-1}$  range.

Fig. 51 a and b show the normalized IR transmission spectra in the region of the CN stretching frequencies for  $\text{TiO}_2$ -CoHCF and  $\text{TiO}_2$ -FeHCC, respectively, in different molar ratios (1:1, 10:1 and 100:1).

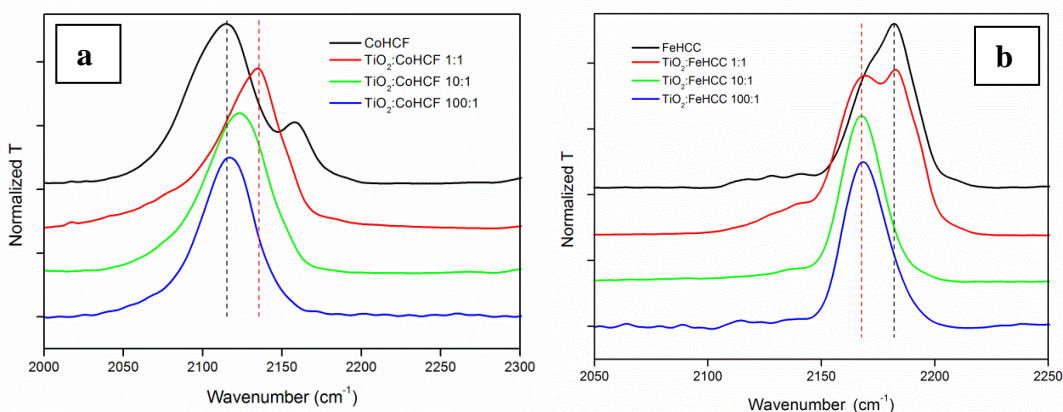


**Figure 51** a)  $\text{TiO}_2$ -CoHCF FT/IR and b)  $\text{TiO}_2$ -FeHCC FT/IR spectra in different molar ratios in the region of CN stretching frequencies.

**Table 6** CN stretching frequencies in CoHCF and  $\text{TiO}_2$ -CoHCF from curve-fitting.

Stretching	$\text{Fe}^{\text{II}}\text{-CN-Co}^{\text{II}}$ $\bar{\nu} / \%$	$\text{Fe}^{\text{II}}\text{-CN-Co}^{\text{III}}$ $\bar{\nu} / \%$	$\text{Fe}^{\text{II}}\text{-CN-Co}^{\text{III}}$ $\bar{\nu} / \%$	$\text{Fe}^{\text{II/III}}\text{-CN-Ti}$ $\bar{\nu} / \%$	$\text{Fe}^{\text{III}}\text{-CN-Co}^{\text{II}}$ $\bar{\nu} / \%$
Bulk	2081 / 11	2102 / 36	2119 / 33	2133 / 0	2157 / 20
1:1	2081 / 20	2102 / 16	2119 / 28	2133 / 35	2157 / 1
10:1	2081 / 15	2102 / 17	2119 / 37	2133 / 31	2157 / 0
100:1	2081 / 20	2102 / 8	2119 / 66	2133 / 0	2157 / 6

In the bulk CoHCF compound, all the bands due to the possible combinations  $\text{Fe}^{\text{II/III}}\text{-CN-Co}^{\text{II/III}}$  were detected and assigned (see Table 6).

In 1:1 and 10:1, the bands at  $2157 \text{ cm}^{-1}$  disappear, the bands at 2081, 2102 and  $2119 \text{ cm}^{-1}$  remain nearly the same, a new band at  $2133 \text{ cm}^{-1}$  appears, probably due a  $\text{Fe}^{\text{II/III}}\text{-CN-Ti}$  bond. In 100:1 compound the band distribution density is similar to the bulk one.

These findings fully agree with the XPS results (see the XPS section) and are consistent with the pictures emerging from the TEM analyses. In fact, in the 100:1 compound, the CoHCF particles bonded to TiO<sub>2</sub> are very few while clusters of isolated CoHCF are mostly detected.

Table 7 reports the same data for the observed CN stretching bands in FeHCC, without any assignment to a definite chemical structure, the bands are indicated only as  $\bar{\nu}$  1,  $\bar{\nu}$  2 and  $\bar{\nu}$  3 because no reference data have been found in literature. Anyway, the whole IR band is in agreement with Berrettoni et al.<sup>26</sup>

The difference in the relative intensity of the bands, especially relevant in the case of FeHCC, can be due to different particle size (i.e. the bulk surface features).

**Table 7** CN stretching related to different chemical features of FeHCC.  $\bar{\nu}$  1,  $\bar{\nu}$  2 and  $\bar{\nu}$  3 indicate the observed bands. Peak areas in percentage are also provided.

Stretching	$\bar{\nu}$ 1 / %	$\bar{\nu}$ 2 / %	$\bar{\nu}$ 3 / %
Bulk	2167 / 21	2169 / 0	2181 / 79
1:1	2167 / 28	2169 / 38	2181 / 34
10:1	2167 / 26	2169 / 74	2181 / 0
100:1	2167 / 28	2169 / 44	2181 / 27

In bulk compound, two stretching bands are observed at 2181 and 2167 cm<sup>-1</sup>.

The intensity of the band at 2181 cm<sup>-1</sup>, the dominant one in bulk FeHCC, decreases by dilution with TiO<sub>2</sub> while the intensity of the band at 2169 cm<sup>-1</sup>, absent in bulk FeHCC, increases; the latter band is tentatively assigned to the FeHCC-TiO<sub>2</sub> bond.

The intensity of the band at 2167 cm<sup>-1</sup> is not influenced by the concentration, as shown in Table 7, so it can be referred to the FeHCC in bulk.

In the case of FeHCC we observe a net shift between CN in the bulk form and CN in the TiO<sub>2</sub>-linked form. Furthermore, the shift is inversely proportional to the FeHCC concentration. The spectra of the samples with CoHCF have more features than those with FeHCC, corresponding to a relatively minor complexity of the latter.

#### ➤ X-ray photoelectron spectroscopy (XPS)

X-ray photoelectron spectra were acquired with the full set of compounds. Survey spectra of TiO<sub>2</sub>-CoHCF and TiO<sub>2</sub>-CoHCF in 1:1, 10:1 and 100:1 ratios are shown in Fig. 52a and b respectively.

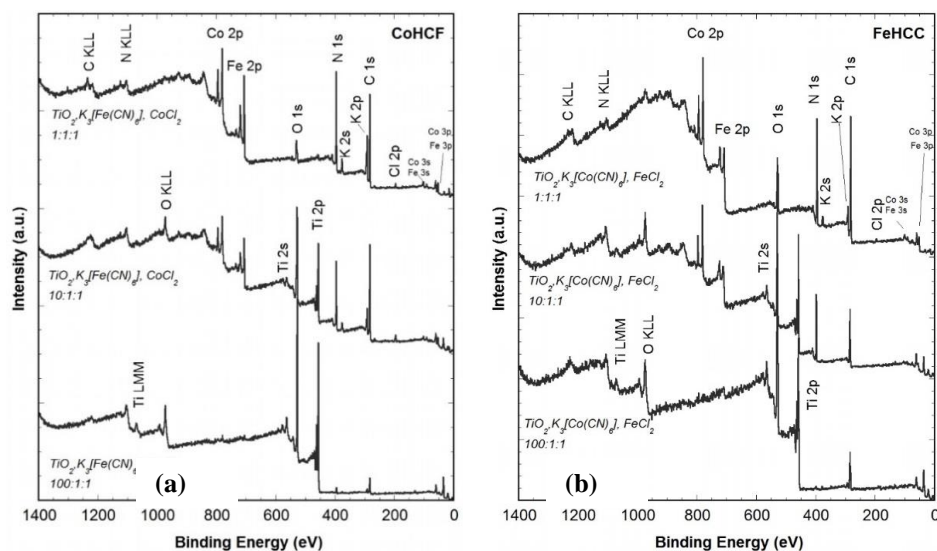


**Figure 52** XPS survey spectra of the samples  $\text{TiO}_2\text{:CoHCF}$  a) and  $\text{TiO}_2\text{:FeHCC}$  b) in 1:1, 10:1 and 100:1 ratios. X-ray source used: monochromatic  $\text{AlK}\alpha$ .

Signals from all the elements that belong to the compounds C, N, O, Fe, Co, Ti, K and a small amount of Cl have been detected. These elements are revealed on the surfaces of  $\text{TiO}_2\text{-FeHCC}$  aggregates at all dilutions. The quantitative analyses are summarized in Table 5; a fairly good agreement with the energy dispersive spectroscopy data, compatible with the experimental uncertainties of the two techniques is obtained.

To obtain information about the chemical state of the elements, the spectra of iron, cobalt, nitrogen and titanium were curve fitted. Parameters such as the Gaussian-Lorentzian ratio and the full width at half height (FWHM) of a component were obtained from the spectra of reference compounds taken under identical acquisition conditions.

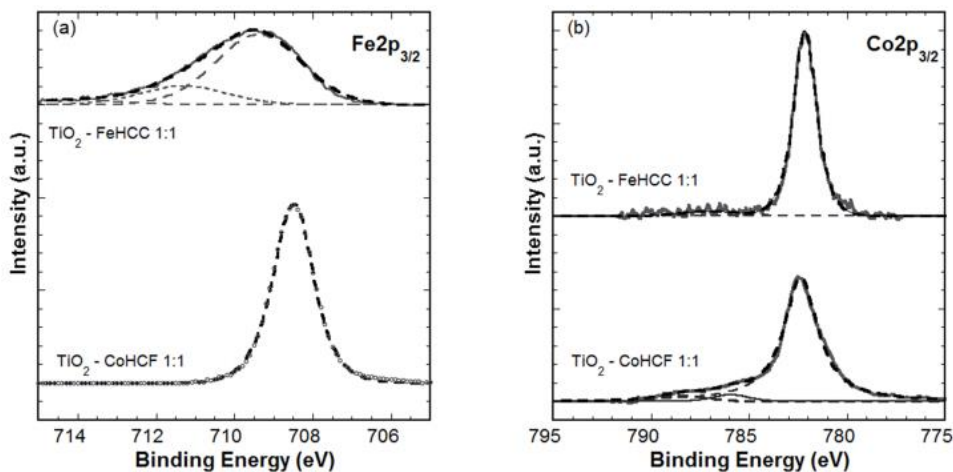
### Iron

Fig. 53a shows, as examples, the fitting of the  $\text{Fe}2p_{3/2}$  signals in the 1:1  $\text{TiO}_2\text{-CoHCF}$  and  $\text{TiO}_2\text{-FeHCC}$  samples.

The  $\text{Fe}2p_{3/2}$  peak of the bulk CoHCF (not shown) indicates the presence of  $\text{Fe}^{\text{II}}$  (B.E. = 708.4 eV) and  $\text{Fe}^{\text{III}}$  (B.E. = 710.0 eV), in agreement with literature;<sup>50,51</sup> this agrees with the IR spectra of CoHCF in the bulk form. The absence of  $\text{Fe}^{\text{III}}$  in  $\text{TiO}_2\text{-CoHCF}$  samples with 1:1 (Fig. 53a) and 10:1 ratios confirms the IR results. The presence of a component at 710 eV in the 100:1 sample (not shown), associated with the presence of  $\text{Fe}^{\text{III}}$ , is also in agreement with the IR findings.

The line shape of  $\text{Fe}2p_{3/2}$  in the FeHCC compounds is very different from that in CoHCF (Fig. 53a): the peaks are asymmetric, the full-width at half height (FWHM) is greater, and peak positions are shifted to higher binding energies.

Curve fitting procedures performed according to literature<sup>52,53</sup> lead to the conclusion that both Fe<sup>II</sup> at 709.0 eV and Fe<sup>III</sup> at 710.5 eV are present at the surface of FeHCC particles.



**Figure 53** XPS Fe<sub>2p<sub>3/2</sub></sub> (a) and Co<sub>2p<sub>3/2</sub></sub> (b) spectra of 1:1 TiO<sub>2</sub>-CoHCF and TiO<sub>2</sub>-FeHCC samples.

### Cobalt

In Fig. 53b curve fitted Co<sub>2p<sub>3/2</sub></sub> signals of 1:1 TiO<sub>2</sub>-CoHCF and TiO<sub>2</sub>-FeHCC samples are reported as examples. In the CoHCF compounds, the Co<sub>2p<sub>3/2</sub></sub> feature has a main component at  $782.0 \pm 0.2$  eV together with shake-up satellites peaks at higher binding energies. These satellites suggest the existence of Co(II).<sup>54,55,56</sup> No significant chemical shift is observed for Co<sup>II</sup> and Co<sup>III</sup>-CN complexes<sup>57</sup> but the co-presence of Co<sup>III</sup>, which was revealed by IR spectroscopy, is supported by the difference in binding energy,  $\Delta E = \text{Co}2p_{1/2} - \text{Co}2p_{3/2}$ , which is about 15.6 eV, intermediate between the value reported for Co<sup>II</sup> (16 eV) and the one for Co<sup>III</sup> (15 eV). The absence of satellites in the Co<sub>2p<sub>3/2</sub></sub> feature of the FeHCC compounds (Fig. 53b) and a binding energy separation  $\text{Co}2p_{1/2} - \text{Co}2p_{3/2}$  of 15 eV strongly implies that cobalt is present as Co<sup>III</sup> in these compounds.

### Nitrogen

N<sub>1s</sub> signal for CoHCF and FeHCC samples without TiO<sub>2</sub> shows a single component at  $398.3 \pm 0.2$  eV; in the presence of TiO<sub>2</sub>, a second small component appears at a higher binding energy ( $399.5 \pm 0.2$  eV) (Fig. 54a,b). The most intense signal could be ascribed to nitrogen of the cyano-groups coordinating a transition metal.<sup>58</sup> The weaker signal might be assigned to the M-CN-Ti surface complexes, as described by Macyka et al.<sup>59</sup>

The intensity of the second component increases from TiO<sub>2</sub>-MHCM 1:1 to TiO<sub>2</sub>-MHCM 100:1 (Fig. 54c) and the increase of the intensity is more pronounced in the case of TiO<sub>2</sub>-CoHCF than for TiO<sub>2</sub>-FeHCC samples.

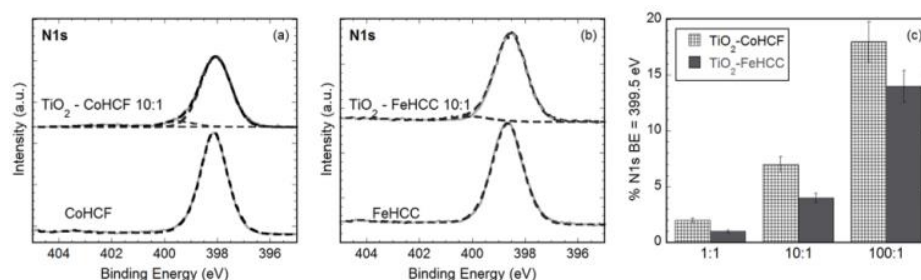


**Figure 54** N1s signal from CoHCF (a) and FeHCC (b) compounds. c) area % of the second component of N1s (B.E. = 399.5 eV) for all the TiO<sub>2</sub>-MHCM compounds.

## Titanium

Ti2p peaks (not shown) were curve fitted, after Shirley-Sherwood background subtraction, with a doublet (Ti2p<sub>1/2</sub> – Ti2p<sub>3/2</sub>) separated by 5.7 eV due to spin-orbit coupling. Each peak is symmetric; the binding energy of Ti2p<sub>3/2</sub> peak is found at 458.8 eV in the 1:1 samples, as for TiO<sub>2</sub>, and shifts to 459.2 eV in the 100:1 samples. The effective invariance of the above parameters could be due to the fact that the Ti2p signal is mainly due to the unbounded TiO<sub>2</sub> particles.

**Table 8** Ti2p binding energy value for Metal Hexacyanometallate-TiO<sub>2</sub> composites.

Ti2p <sub>3/2</sub> binding energy value (eV ± 0.2)		
TiO <sub>2</sub> :MHCM	FeHCC	CoHCF
1:1	458.9	458.8
10:1	458.8	458.8
100:1	459.2	459.1

## XP-Valence Band

XP-valence bands of TiO<sub>2</sub> and TiO<sub>2</sub>-MHCM compounds have been recorded and results are shown hereafter (Fig. 55 and 56).

Pure TiO<sub>2</sub> valence band edge shows the presence of two peaks, separated by ~2 eV that could be ascribed to π (nonbonding) and σ (bonding) O2p orbitals.<sup>60</sup>

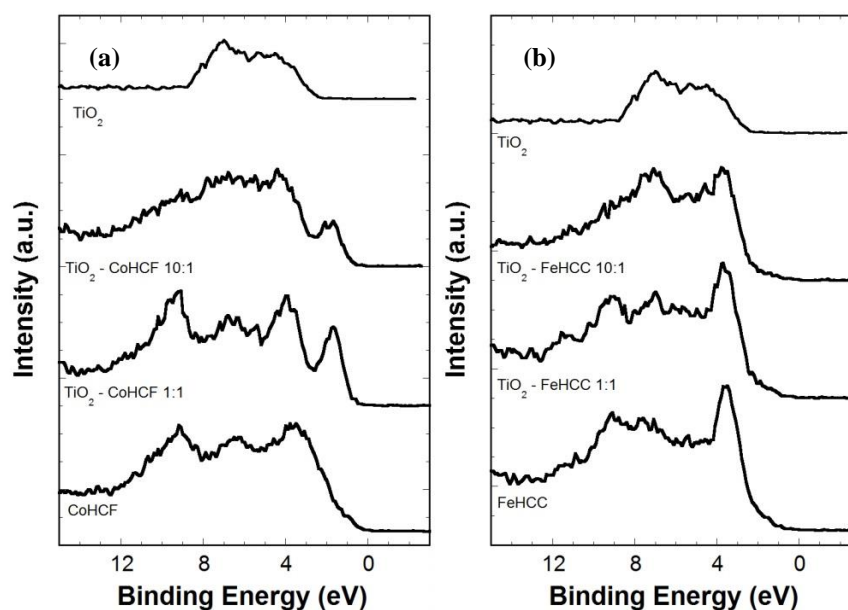
### CoHCF and FeHCC compounds

Fig. 55a shows the valence bands of Cobalt Hexacyanoferrate without TiO<sub>2</sub> and in the mixtures 1:1 and 1:10 with TiO<sub>2</sub>. The valence band of commercial TiO<sub>2</sub> (Sigma Aldrich) is provided for comparison. The band is due to the overlapping of the contributions due to Co-N σ and π bonding electrons, with Fe-C σ and π bonding and Co non – bonding electrons.<sup>61</sup> Relative to pure TiO<sub>2</sub>, the edge shifts to lower binding energies in bulk CoHCF and its mixtures with TiO<sub>2</sub> (Table 9).

**Table 9** Comparison of the valence band edge binding energy of CoHCF and TiO<sub>2</sub>-CoHCF compounds at different ratios.

Sample	Valence Band Edge binding energy (eV ± 0.2)
CoHCF	2.0
TiO <sub>2</sub> :CoHCF 1:1	1.2
TiO <sub>2</sub> :CoHCF 10:1	1.2
TiO <sub>2</sub>	3.2

Fig. 55b shows the valence bands of the Iron Hexacyanocobaltate compounds.



**Figure 55** XPS valence bands of CoHCF a) and FeHCC b) compounds and of commercial titania (0-15 eV region).

Also in this case a complex band between 0 and 12 eV is observed for pure FeHCC; in analogy with CoHCF, it is assigned to the overlapping of the bands due to Co-C  $\sigma$  and  $\pi$  bonding electrons with Fe-C  $\sigma$  and  $\pi$  bonding electrons.

A shift toward lower energies of the edge is also observed (Table 9) in the TiO<sub>2</sub>-MHCM composites relative to pure TiO<sub>2</sub>; a difference of 0.7 eV is observed between the edge of bulk CoHCF and that of bulk FeHCC.

**Table 10** Comparison of the valence band edge binding energy of FeHCC and TiO<sub>2</sub>-FeHCC compounds at different ratios.

Sample	Valence Band Edge binding energy (eV ± 0.2)
FeHCC	1.3
TiO <sub>2</sub> :FeHCC 1:1	1.3
TiO <sub>2</sub> :FeHCC 10:1	1.9
TiO <sub>2</sub>	3.2

### ➤ X-ray absorbance spectroscopy (XAS)

Relevant information on about the binding between  $\text{TiO}_2$  and the Metal Hexacyanometallates can be gained by using an elemental analytical technique such as the X-ray Absorption Spectroscopy.<sup>62</sup>

In this case, all the three metal sites (Ti, Fe, Co) can be monitored and the results are shown in Fig. 56.

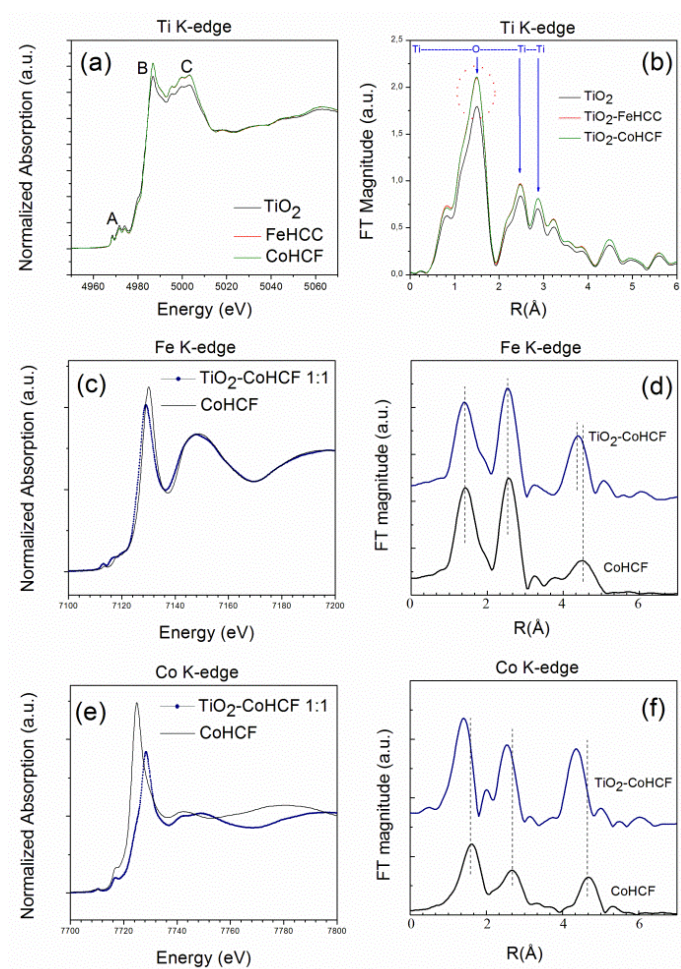


**Figure 56** XAS results of the metal sites Ti, Fe, Co. Figs (a), (c) and (e) are the normalized X-Ray Absorption Near Edge (XANES) spectra while (b), (d) and (f) are the Fourier Transforms (FTs) of the Extended X-Ray Absorption Fine Structure (EXAFS) spectra.

The normalized XANES spectra are given in the left column of Fig. 56 (a, c, e) whereas the right column provides the Fourier Transforms (FTs) of the Extended X-Ray Absorption Fine Structure (EXAFS) spectra.

Of the composite samples, only the spectra of  $\text{TiO}_2$ -MHCM 1:1, taken as the most representative, are reported. The normalized curves at the Ti K-edge (panel (a)) give evidence that the presence of FeHCC or CoHCF modifies the local environment of titanium, in comparison with that of pure Anatase phase.

This is evident from the pre-edge structures (A peak), the main absorption edge (B) and the resonance (C) but the modification at the Ti site with either FeHCC or CoHCF dopant is essentially the same.

The comparison of the Fourier Transform curves of the EXAFS signals relatives to the K-edge of Ti confirms minor but significant modifications of the local structure of Ti.

This is showed in the panel (b) where the FTs, which are related to the radial atomic distribution around the selected (photo-absorber) atom, display peaks intensity increasing following FeHCC or CoHCF doping. This might be due to a decreasing of the structural order in the three shells as indicated in Fig. 56b.

By tuning the x-ray beam to a precise metal edge, complementary information is available at the Fe and Co K-edges for both TiO<sub>2</sub>-FeHCF 1:1 and TiO<sub>2</sub>-CoHCF 1:1 samples.

Panels (c), (d), (e), (f) display a selection of the XAS analysis concerning the CoHCF composites; comparison with bulk CoHCF is also provided. All panels indicate modification relative to the bulk sample of the XAS spectra, thus confirming the occurrence of a substantial interaction between TiO<sub>2</sub> and CoHCF.

A close inspection of the figures reveals the following details of the TiO<sub>2</sub>-CoHCF binding: (1) the Fe local site is basically the same upon TiO<sub>2</sub> addition as seen from the XANES in the panel c but a shift towards lower energy of the curve is evidenced, indicating a partial reduction to Fe(II); (2) unlike the Fe, the Co local environment changes upon TiO<sub>2</sub> addition, as the overall shape of the XANES curve of panel (e) is strongly modified; furthermore, no changes in the pre-edge peak position has been detected and therefore the Co is in the Co(II) site.

The trend observed in the XANES data is confirmed by the corresponding FTs curves. The Fe display (panel (d)) similar peak positions and intensities, with the exception of the 3rd peak at  $\sim 5 \text{ \AA}$ , assigned to the Fe–Co distance, which decreases upon doping with TiO<sub>2</sub>. On the contrary, all three peaks displayed in the panel (f) shift to lower distances, providing evidence for shorter bond lengths of the first, second and third shells around cobalt.

Similar comments apply to the comparison of the Fe and Co K-edges in FeHCC and TiO<sub>2</sub>-FeHCC. The analysis, available in Fig. 57, leads to the same conclusions if we swap the Co with Fe site. In this case the Fe site changes significantly upon TiO<sub>2</sub> doping while the Co one does not, as clearly visible from the XANES curve of Fig. 57, panels (c) and (d).

This experimental finding is interesting and can be explained by considering the local probe characteristic of a XAS experiment. Regardless the long range structure, the XAS indicates that significant changes occur only at the metal site (either Co or Fe), which is linked to the N side of the CN moieties of the cyanide bridge.

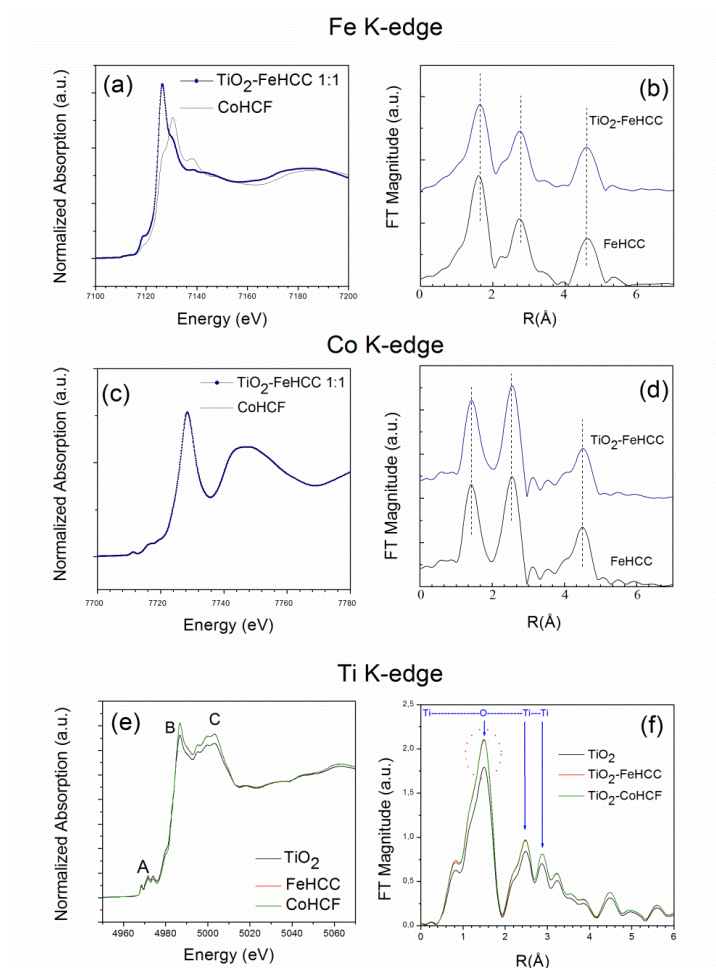


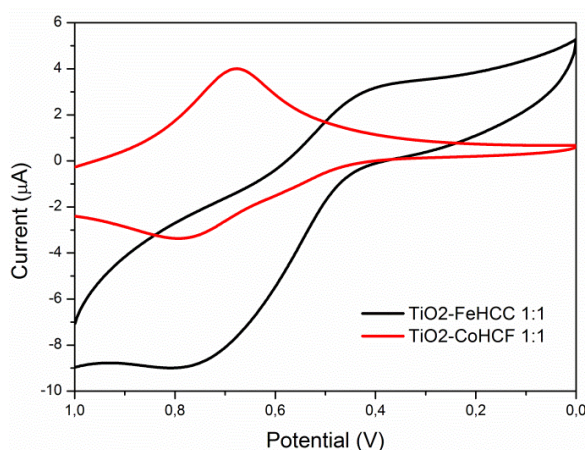
**Figure 57** XAS results of the Iron Hexacyanocobaltate (FeHCC) sample. The normalized X-Ray Absorption Near Edge (XANES) spectra are displayed in the panels (a) and (c) respectively for the Fe and Co K-edge. Panels (b) and (d) show the experimental Fourier Transforms (FTs) of the Extended X-Ray Absorption Fine Structure (EXAFS) spectra taken at the Fe and Co K-edge, respectively.

### ➤ Cyclic Voltammetry (CV)

Electrochemical test were performed in order to give evidence of the formation of MHCM clusters on the  $\text{TiO}_2$  surface.

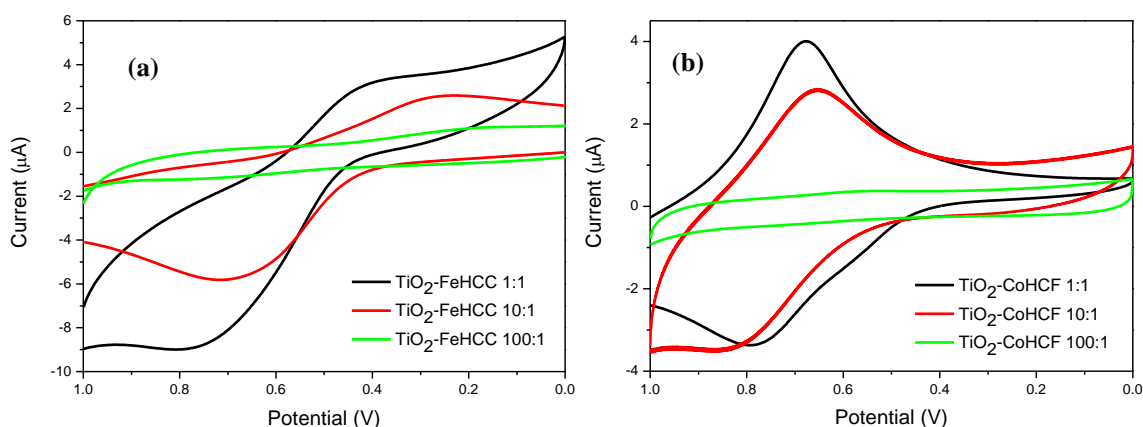
In particular, chemically synthesized Anatase  $\text{TiO}_2$ -FeHCC and  $\text{TiO}_2$ -CoHCF compounds were deposited on glassy carbon, as reported in the Experimental section, and characterized by cyclic voltammetry.

Fig. 58 shows the cyclic voltammograms for  $\text{TiO}_2$ -FeHCC (black line) and  $\text{TiO}_2$ -CoHCF (red line), both in a 1:1  $\text{TiO}_2$ -MHCM ratio.



**Figure 58** CVs at 0.1 V/s of TiO<sub>2</sub>-FeHCC 1:1 (black line) and TiO<sub>2</sub>-CoHCF 1:1 (red line) in a 1.0 M KCl solution. Potentials are referred to the saturated Ag/AgCl electrode.

Fig. 59a and b provide CVs of TiO<sub>2</sub>-FeHCC and TiO<sub>2</sub>-CoHCF in 1:1, 1:10, 1:100 molar ratios respectively, in 1.0 M KCl solution. It is worth noting that in all cases, only a single reversible redox system is observed.



**Figure 59** CVs at 0.1 V/s of 1:1 (black line), 10:1 (red line), 100:1 (green line) TiO<sub>2</sub>-FeHCC a) and TiO<sub>2</sub>-CoHCF b) in a 1.0 M KCl solution. Potentials are referred to the saturated Ag/AgCl electrode.

Table 11 and 12 report the  $E_{p_c}$  and  $E_{p_a}$  (in Volts) values for the 1:1, 10:1 and 100:1 TiO<sub>2</sub>-FeHCC and TiO<sub>2</sub>-CoHCF compounds respectively and the relative  $E^0$  values calculated as  $(E_{p_a} + E_{p_c})/2$ .

**Table 11**  $E_{p_c}$  and  $E_{p_a}$  (in Volts) for the TiO<sub>2</sub>-FeHCC compounds and the relative  $E^0$  value.

TiO <sub>2</sub> -FeHCC	$E_{p_c}$	$E_{p_a}$	$E^0$
1:1	0.364	0.787	0.575
10:1	0.261	0.708	0.484
100:1	0.207	0.735	0.471

**Table 12**  $E_{pc}$  and  $E_{pa}$  (in Volts) for the  $TiO_2$ -CoHCF compounds and the relative  $E^0$  value.

$TiO_2$ -CoHCF	$E_{pc}$	$E_{pa}$	$E^0$
1:1	0.679	0.784	0.732
10:1	0.655	0.835	0.745
100:1	0.529	--	--

CVs were also performed in solution with different KCl concentrations (1.0,  $1.0 \times 10^{-1}$ ,  $1.0 \times 10^{-2}$  M) to verify the role of  $K^+$ . For both compounds, the peak potentials shifted in the negative direction with decreasing the electrolyte concentration, thus confirming that the redox process is associated with the intercalation of electrolyte  $K^+$  cations. Within the experimental error, the slopes of 56 mV and 52 mV are consistent with a single electron redox process assisted by  $K^+$ . Similar results were obtained for  $TiO_2$ -FeHCC and  $TiO_2$ -CoHCF in 10:1 molar ratio (not shown).

### 6.3.3 Experimental evidence of the formation of composites

First of all, findings prove how feasible and reliable is the synthesis of composite materials based on  $TiO_2$  particles modified by CoHCF or FeHCC. In fact, electrochemical results and TEM micrographs give evidence of the formation of MHCM clusters on the  $TiO_2$  surface. The optimum  $TiO_2$ -MHCM ratio is found between 1:1 and 10:1 since in these molar ratios the spherical particles of  $TiO_2$  are covered by cubic nanocrystals of MHCM. Furthermore, the composite materials show a red shift of the threshold absorption edge in the UV region, due to a decrease of the titanium dioxide band gap.

The waves of cyclic voltammetry and their dependence upon the  $K^+$  concentration demonstrate the successful synthesis of both CoHCF and FeHCC.<sup>14,26</sup>

Only a single quasi-reversible redox system is detected both in FeHCC and in CoHCF.

In bulk CoHCF, two redox processes due to the  $Fe^{III}/Fe^{II}$  and  $Co^{III}/Co^{II}$  couples, respectively, can be observed; the second one becomes electroactive only when the compound is crystallized in the so called “insoluble form”<sup>63</sup> or in nano-sized form.<sup>14</sup>

In bulk CoHCF, the peak potential and the  $E^0$  values allow to assign the redox wave to  $Fe^{III}/Fe^{II}$  couple.<sup>14</sup> In the FeHCC compounds, the observed redox wave is still due the iron center, as confirmed by the  $E^0$  values, while the cobalt center is non electroactive.<sup>26</sup>

Hence the observed redox waves in TiO<sub>2</sub>-FeHCC and TiO<sub>2</sub>-CoHCF are always due just to the Fe<sup>III</sup>/Fe<sup>II</sup> couple.

From the CVs of TiO<sub>2</sub>-FeHCC (Fig. 59a and Table 11) it is worth noting that, with increasing the TiO<sub>2</sub>/FeHCC ratio, the kinetics of cation insertion becomes slower, since the cathodic peak shifts toward more negative potentials, while the kinetics of its release is faster, since the anodic peak shifts toward more negative potentials. Also the E° values show a negative shift in going from 1:1 to 10:1 composites, and no further changes in the 100:1 composite.

The redox process is characterized by a relative high peak separation, in accordance with the published literature,<sup>26</sup> while the peak shapes reflect the difference in the TiO<sub>2</sub>-FeHCC synthesis. Actually, the modified electrode was realized by chemical synthesis (see Experimental paragraph for details) while in the published literature,<sup>26</sup> the TiO<sub>2</sub>-FeHCC composite electrodes were electrochemically synthesized in situ on a TiO<sub>2</sub> thin film. In the case of TiO<sub>2</sub>-CoHCF (Fig. 59b and Table 12), both cation insertion and release become more difficult at least for 1:1 and 10:1 compounds, while in 100:1 ratio the CV shape prevents the resolution of the voltammetric wave. In this case, as expected, the E° values remain constant.

#### 6.3.4 Reaction Mechanism

IR, XPS and XAS and XANES results allow to tentatively identify possible reaction mechanisms for the formation of the composites. In the case of CoHCF and, more generally, in the case of Metal Hexacyanoferrates, the morphology of CN stretching band reflects the complexity of their structure. Actually, the possible co-presence of different linear chains, for example Fe<sup>III</sup>-CN-Co<sup>II</sup> or Fe<sup>II</sup>-CN-Co<sup>III</sup>, made possible by the redox properties of the two redox metal centers, leads to different chemical environments for the CN groups.<sup>14</sup>

Further complexity can arise for the possible co-presence of the soluble and insoluble structure. On the other hand, in FeHCC the iron center is the only electroactive species; hence, the chemical differences in the chains are less than in the case of CoHCF.

The formation of MHCM cluster on the TiO<sub>2</sub> surface causes a clear modification of the IR spectra. The change in the intensity, that might be assigned to the different amounts of MHCM added and hence to the different degree of interaction with the TiO<sub>2</sub>, is accompanied by a band shift towards lower wavenumbers and a shape morphology change (Fig. 51a and b).

IR results are in agreement with the XPS that allows to distinguish between Fe–CN (CoHCF) and Fe–NC (FeHCC) and confirm the absence of Fe<sup>III</sup> in TiO<sub>2</sub>-CoHCF samples with 1:1 (Fig. 53a) and 10:1 ratios and the presence of Fe<sup>III</sup> in the 100:1 sample. XPS and IR identification of cobalt species are also in agreement for both FeHCC and CoHCF samples. Furthermore XPS analyses provide the evidence of the interaction between nitrogen and titanium: cyanide groups may act as ligands for titanium ions at the surfaces, forming M–CN–Ti bonds, as also shown by the band shift towards lower wavenumbers and shape morphology change in IR spectra. The involved reaction might be thought as a nucleophilic substitution reaction with titanium ions playing the role of central ions and Hexacyanoferrate anions acting as ligands.

The combined XANES and EXAFS analysis at the Ti K-edge of Fig. 56 and 57 show that the presence of MHCM modifies the local environment of the titanium, relative to that in pure Anatase. This suggests the same type of binding between the Anatase and either FeHCC or CoHCF cubes. The analysis at the metal (Fe and Co) K-edges shows modification in the XAS spectra respect to the pure CoHCF sample (and the same holds true for the FeHCC case), thus confirming the occurrence of a close interaction between TiO<sub>2</sub> and CoHCF (or FeHCC). Overall, these findings are explained by considering a close interaction between the anatase and the FeHCC or CoHCF cubes, most likely through the N side of the CN moieties, as previously evidenced by the IR and XPS analyses.

On the basis of these findings two mechanisms for the Metal Hexacyanoferrate (FeHCC or CoHCF) interaction to the Anatase particles can be proposed.

According to the first mechanism, the HCC or HCF salt reacts with either Fe(III) or Co(III) respectively to give the mixed hexacyanometallate (I step, Fig. 60a) and subsequently the insoluble species, consisting in a dendrimer-like structure, reacts with the N terminals (II step, Fig. 60a). It is worth noting that the role of the vacancies is important because they suppress the perfectly cubic structure and increase the surface adhesion.

The presence of ion vacancies, and their concentration, in Metal Hexacyanoferrates certainly affects a range of properties.<sup>64</sup> However, one may imagine another mechanism: the HCC or HCF salt reacts with anatase particles (I step, Fig. 60b) and, subsequently, the Metal Hexacyanometallate FeHCC or CoHCF synthesis occurs (II step, Fig. 60b).

Presently, it is not possible to determine which of these two mechanisms is the predominant one.

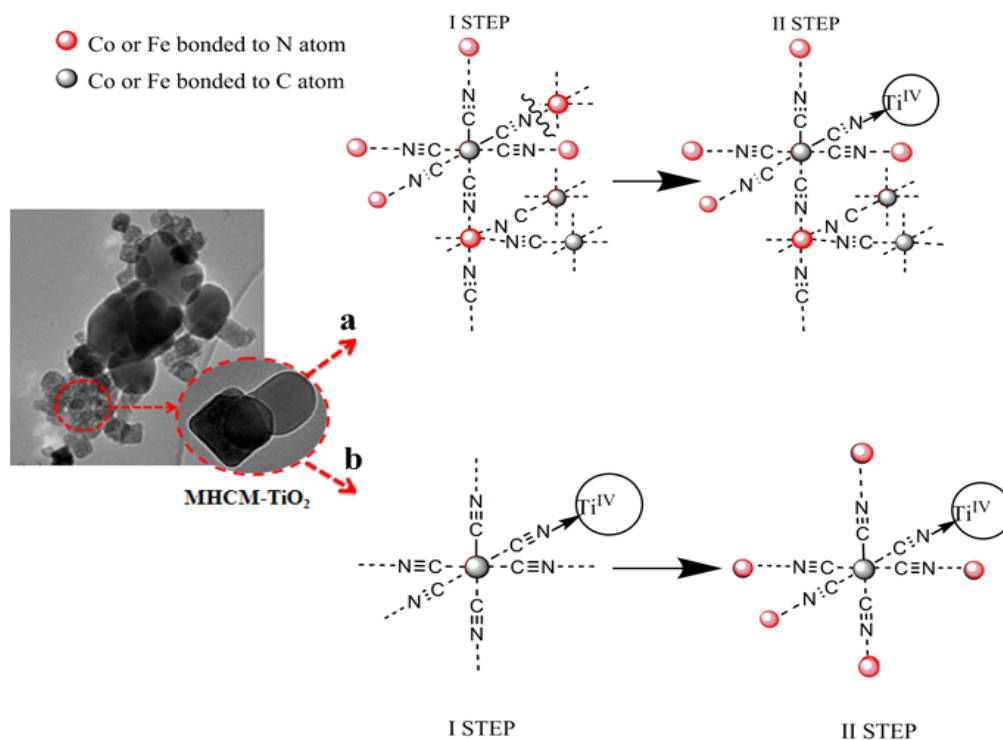


**Figure 60** Schematics of two possible mechanisms for the Metal Hexacyanometallate interaction with Anatase particles. The red spheres are Co or Fe bonded to N atoms; the grey atoms are Co or Fe ions bonded to C atoms.

### 6.3.5 Electron transfer and spin transition in MHCMs driven by Anatase $\text{TiO}_2$ : electronic and structural order effect

The Prussian Blue (PB) analogue  $\text{KCo}[\text{Fe}(\text{CN})_6]$  nanodispersed with anatase  $\text{TiO}_2$  has excited a great interest recently, leading to the electron transfer within the pairs  $\text{Co(II)-HS-Fe(III)-LS}$  and  $\text{Co(III)-LS-Fe(II)-LS}$ .

It represents one of the first examples where an external stimulus other than the photoexcitation triggers spin-crossover phenomena in Metal-Hexacyanoferrate based-molecular solid.

The electronic excitations collectively propagate through the crystal leading to a new long-lived phase. The experimental evidence of this effect is supported by high resolution XANES and EXAFS results, the latter highlighted a consistent change (10 %) of the Co-N first shell bond distance.

The following Fig. 61 displays the x-ray absorption near-edge spectra (XANES) of the four samples at both metal edges (Fe and Co).

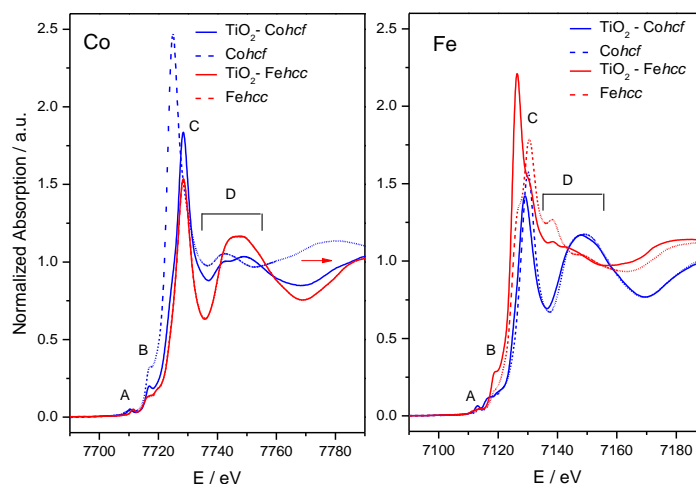


**Figure 61** Normalized XANES spectra at Fe and Co K-edge for all samples.

All spectra are characterized by a pre-edge peak A, the edge region B corresponding to the rising part of the spectrum, the edge resonance C which is associated to the continuum, and the region D which is associated to multiple scattering events of the photo-electron. As seen from the Co K-edge, spectra are modified in both shape and position of the main features with the largest difference arising from the Cobalt Hexacyanoferrate while compared to the TiO<sub>2</sub>-doped Cobalt Hexacyanoferrate sample (blue lines). This suggests a strong modification of the local charge associated to the cobalt ion whereas little modifications are seen at the Fe K-edge, apart from changes in the local charge associated to the Fe, providing evidence for a close interaction between the Co site and the anatase, which in turn may produce changes in the formal oxidation states of the two metals. The same holds true while considering the Fe-K edge spectra, but in this case, the Iron Hexacyanocobaltate (FeHCC) samples are the ones where a significant difference appeared. This is related to the structure of the investigated Metal Hexacyanometallate: in the Metal Hexacyanoferrate the N-side of the cyanide bridge is linked to the cobalt. On the contrary, the N-side is coordinated by the iron in Hexacyanocobaltate. Overall, these findings provide evidence for a close interaction between Ti (of the anatase) and the metal attached to the N-side of the hexacyanometallate linear chain, which is in line with IR and XPS data.<sup>65</sup>

The local structural site of both Fe and Co have been analysed using EXAFS.

Fig. 62 displays the comparison of the  $k^2$ -extracted EXAFS signals to the theoretical ones for TiO<sub>2</sub>-CoHCF and CoHCF samples at both Fe and Co edge. The corresponding Fourier Transform signals are indicated at the bottom.

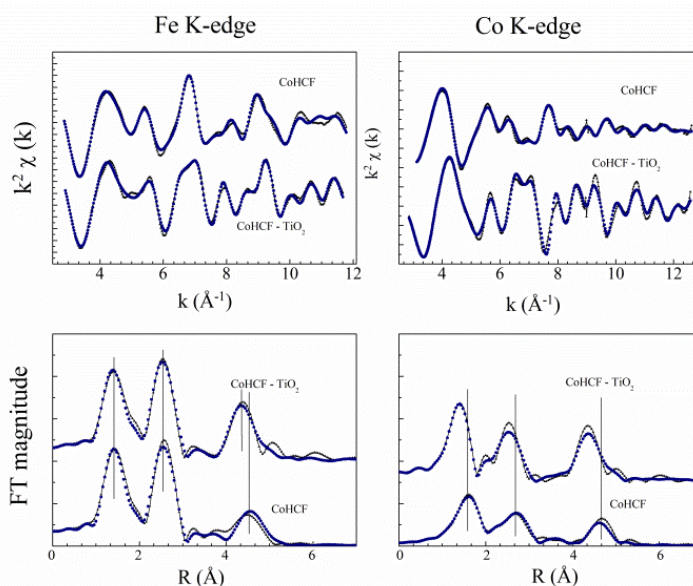


**Figure 62** EXAFS data analysis for  $\text{TiO}_2$ -CoHCF and CoHCF samples. Comparison of the experimental (-) and theoretical (...)  $k^2$ -weighted EXAFS signals (upper panels) and the corresponding Fourier Transform (lower panels) of the  $k^2$ -weighted EXAFS for compounds I and II, at Fe and Co K-edges.

The EXAFS curves are characterized by a superposition of several main oscillations, and the corresponding FT curves confirm the presence of three main peaks, which originate by the almost perfect cube structure of Metal Hexacyanoferrate.

The position of the peaks are not the same in CoHCF and in  $\text{TiO}_2$ -doped CoHCF, indicating a modification of the structure upon the Anatase doping.

In particular at the Co K-edge, all three peaks shift to lower distances, providing evidence for bond lengths shortening of the first, second and third shells around the cobalt. This fact is close correlated to a possible spin transition. On the contrary, at the Fe site only the 3rd peak at about 5 Å, which corresponds to the Fe--Co mutual distance, is seen to decrease upon  $\text{TiO}_2$  doping.

The EXAFS spectrum of MHCFs is a peculiar one and it requires a specific analysis<sup>66</sup> concerning the electron scattering from strongly correlated systems, such as the Metal Hexacyanoferrates.

As indicated by the best-fit in Fig. 62, the theoretical curves match well within the experimental ones, demonstrating the reliability of the present EXAFS data analysis.

Table 13 reports some relevant structural parameters (the first 3 shells) for all samples as obtained by the best-fitting procedures.

**Table 13** Selected structural parameters from EXAFS fitting results of Cobalt Hexacyanoferrate samples and Iron Hexacyanocobaltate samples. The estimated parameter errors are indicated in parentheses.

Shells		TiO <sub>2</sub> -CoHCF	CoHCF	TiO <sub>2</sub> -FeHCC	FeHCC
1 <sup>st</sup>	Fe-C / Å	1.872(6)	1.892(5)	-	-
	Co-C / Å	-	-	1.868(2)	1.859(4)
2 <sup>nd</sup>	C≡N / Å	1.171(5)	1.166(5)	1.19(1)	1.19(1)
3 <sup>rd</sup>	Co-N / Å	1.891(7)	2.084(5)	-	-
	Fe-N / Å	-	-	2.087(3)	2.061(4)

The Fe-C first shell interatomic distance in TiO<sub>2</sub>-CoHCF and CoHCF sample is almost the same, with values of 1.892(5) and 1.872(6) Å, respectively. On the contrary, a large difference has been found in the Co-N interaction. The observed value of 2.084(5) Å for the pristine CoHCF material shortens to 1.891(7) Å in the TiO<sub>2</sub> doped sample. This significant difference is found to be correlated to a spin transition from Co high spin (S=3/2) to Co (low spin, S= 1/2) which is accompanied by a variation of the Co-N bond length, as observed previously.<sup>67,68</sup>

In this case, a partial electron transfer, from Co<sup>II</sup>-LS to Fe<sup>III</sup> should be observed, which in turn trigger the formation of Co<sup>III</sup>-LS. This spin transition is not observed in TiO<sub>2</sub>-FeHCC and FeHCC sample, i.e.: while the FeHCC is doped with TiO<sub>2</sub>. In such a case the first shell distance at both Fe and Co do not changes significantly upon doping the pristine material.

The C≡N bond lengths, ranging from 1.166(5) to 1.19(1) in all the four samples, are found to be comparable to the values quoted for this class of materials.

The EXAFS Debye Waller generally increase in several structural parameters after the TiO<sub>2</sub> doping, demonstrating an increase of the structural disorder. This is evident from a comparison of the EXAFS bond variance associated to the first shell Fe-C and Co-C distances.

Overall, the EXAFS analysis indicates a consistent shortening (about 10 %) of the Co-N bond length in CoHCF sample upon the TiO<sub>2</sub> addition and that the Fe-C-N portion of the Fe-C-N-Co linear chains vibrate in the same way around the equilibrium position.

Also, the TiO<sub>2</sub> doping trigger some structural disorder in both CoHCF and FeHCC.

Detailed electronic information can be gained by the analysis of the pre-edge peaks and both Fe and Co K-edge XAS spectra.

Hence, high resolution XANES spectra have been recorded at the same beamline but using a pair of Si(311) crystals in the fixed-exit monochromator, ensuring a better experimental resolution.

Fig. 63 shows the pre-edge side of the XANES spectra at both Co (left) and Fe (right) K-edge. Generally speaking pre-edge peaks of the first row transition metal are due to dipole-forbidden 1s-3d transition which become possible by p-d hybridisation if distortion from a centrosymmetry takes place.<sup>69</sup> In our case, because both Co and Fe are in almost perfect octahedral symmetry, those weak pre-edge peak are due most likely to quadrupole allowed 1s-3d transition.<sup>16</sup>

The Co pre-edge features are characterized by a single peak mainly, with different intensity and position in the studied samples. In the pristine CoHCF (Co<sup>II-HS</sup>), the peak moves towards higher energy and thus an oxidation (to Co<sup>III-LS</sup>) takes place.

On the contrary, no changes of the edge energy nor the intensity are observed in the TiO<sub>2</sub>-modified FeHCC sample: the Co oxidation state remains unchanged. It is also interesting to note the shift in the peak position (about 1 eV) observed for Co<sup>III</sup> coordinated by 6 N (as in the FeHCC sample) respect to the 6 C coordinated Co<sup>III</sup> sample (TiO<sub>2</sub>-CoHCF sample). This is due to a crystal field effect: the C-bonded of the cyanide ligand produces a larger crystal field respect to the N-bonded one, and thus the peaks move towards higher energy.

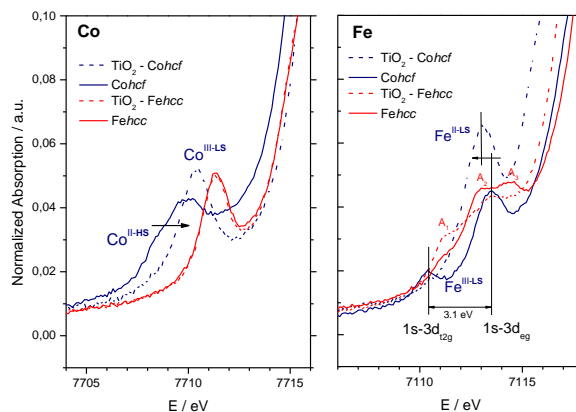
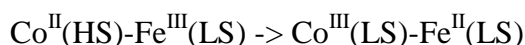


**Figure 63** Pre-edge data for samples recorded using a pair of Si(311) crystals, at Fe and Co K-edge.

The pre-edge features at the Fe K-edge are more complicated but a close inspection provides the clear evidence of the reduction of the Fe<sup>III</sup> to Fe<sup>II</sup> in the TiO<sub>2</sub>-modified CoHCF sample, respect to the pristine. This allows to explore the possible charge transfer among the two metals: an oxidation of Co<sup>II</sup> and a reduction of Fe<sup>III</sup> have been evidenced.

Overall this result well combined to the outcome of the EXAFS data analysis. In fact, the anatase doping of the CoHCF sample has caused a major shortening of the Co-N bond length, which is a well-known experimental finding correlated to a Co spin transition.<sup>14,15</sup>

TiO<sub>2</sub> induces an electronic charge transfer concomitant to a significant shortening of the Co-N bond length from 2.08 Å (Co<sup>II-HS</sup>) to 1.91 Å (Co<sup>III-LS</sup>) and with a subsequently shortening of the cell parameters from 10.28 to 9.96 Å. Overall the charge transfer involving the spin transition in CoHCF can be indicated as:



FeHCC and TiO<sub>2</sub>-modified FeHCC, red lines, are subject to changes related to the symmetry at the Fe site, but none at the Co site. This is also evidenced by the pre-edge curves. More information at the Fe site can be deduced by the high resolution spectra which allowed to identify three peaks (A1, A2 and A3) which are expected for High-Spin (HS) ferrous complexes. The three peaks are due to the 1s-3d<sub>t<sub>2g</sub></sub> (<sup>4</sup>T<sub>1g</sub> state) and to the 1s-3d<sub>e<sub>g</sub></sub> (<sup>4</sup>T<sub>2g</sub> and <sup>4</sup>T<sub>1g</sub> states). Eventually, the pre-edge data at the Fe k-edge support the LS state of Iron for TiO<sub>2</sub>-CoHCF and CoHCF sample (6C coordinated) and the HS state for TiO<sub>2</sub>-FeHCC and FeHCC samples (6N coordinated).

<sup>57</sup>Fe Mössbauer spectroscopy was used to highlight the charge transfer mechanism in Cobalt Hexacyanoferrate (CoHCF) when synthesized in presence of Anatase TiO<sub>2</sub>.

Figure 64 shows the Mössbauer spectra recorded at room temperature for CoHCF (a) and TiO<sub>2</sub>-CoHCF (b) samples. The quadrupole split spectrum of CoHCF can be fitted with two spectral contributions: a dominant quadrupole doublet with a relatively large quadrupole splitting of 0.43 mm/s (cf. Table 14) which is typical of ferric iron in Metal Hexacyanoferrates, and a second minor singlet (or an unresolved doublet) with parameters in the typical range of low spin ferrous iron in Metal Hexacyanoferrates.

It is important to remember that, in low-spin Fe(II) and Fe(III) in an octahedral environment, such as in Metal Hexacyanoferrates, the d orbitals are split into lower t<sub>2g</sub> and higher e<sub>g</sub> levels.

The d<sup>6</sup> electron configuration of Fe(II) corresponds to a complete filling of the t<sub>2g</sub> states, and the arising of a quadrupole splitting can be ascribed only to distortion of the octahedral coordination or to the presence of different ligand in a non-symmetric arrangement.

In the case of Fe(III), the d<sup>5</sup> electron configuration results in a non-spherical distribution of the d electron population, producing a notable quadrupole splitting.

Moreover, ferricyanides usually undergo a Jahn-Teller distortion in order to further stabilize the paired electrons in two of the  $t_{2g}$  levels ( $d_{xy}$ ,  $d_{xz}$ ,  $d_{yz}$ ), which further contributes to the quadrupole splitting.

Differently from the spectrum of CoHCF, the spectrum of sample  $\text{TiO}_2$ -CoHCF is a singlet with the typical parameters of ferrous iron in Metal Hexacyanoferrates. Using an unresolved doublet with a very small quadrupole splitting in the fitting of the spectrum, provides an improved quality of the fit. The arising of a small quadrupole splitting can be explained by the possible presence of a minor distortions and/or vacancies in the coordination of the iron centers.

The comparison of these results thus reveals a completely different oxidation state of the iron in the two samples, with a complete reduction of the iron to Fe(II) when the PB analogue is prepared in the presence of  $\text{TiO}_2$ , confirming the electron transfer induced by  $\text{TiO}_2$  along the Co-NC-Fe-CN-Co chain.

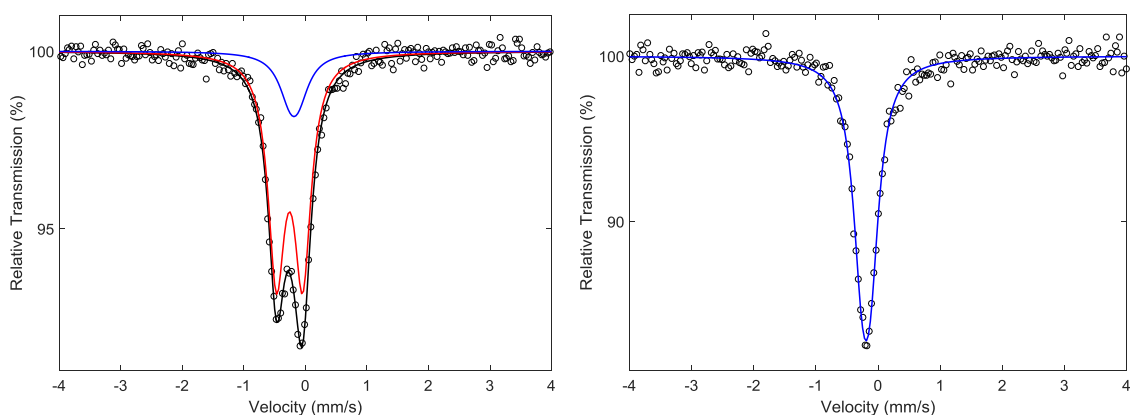


**Figure 64** Room temperature  $^{57}\text{Fe}$  Mössbauer spectra for samples CoHCF (a) and  $\text{TiO}_2$ -CoHCF (b). The circles and the lines represent the experimental and fitted data, respectively.

XRD analyses confirm the success of the synthesis and allow the identification of lattice changes in the structure of CoHCF in the two investigated samples.

The XRD patterns of CoHCF and  $\text{TiO}_2$ -CoHCF shown in Fig. 65, are consistent with the typical  $fcc$  lattice of MHCs.

The reflection peaks attributed to  $\text{TiO}_2$  are also highlighted in the pattern of  $\text{TiO}_2$ -CoHCF. Anatase is the only polymorph of  $\text{TiO}_2$  identified in the sample.

The cell parameter  $a$  determined by pattern matching is 10.29 and 10.10 Å for CoHCF and  $\text{TiO}_2$ -CoHCF, respectively, in the typical range of most Metal Hexacyanometallates.

The observed values suggest a shortening of the Co–N bond length in TiO<sub>2</sub>-CoHCF compared to CoHCF.

The transition Fe<sup>3+</sup>-CN-Co<sup>2+</sup>(HS) to Fe<sup>2+</sup>-CN-Co<sup>3+</sup>(LS), involves a change in both the oxidation and the spin state on the Co center, with a subsequent significant change in the Co–N bond length and thus a shrinking of the lattice. In this case, co-precipitation on anatase TiO<sub>2</sub> seem to induce an electronic charge transfer concomitant to a significant shortening of the Co–N bond length from 2.08 Å ((Co(II)-HS) to 1.91 Å (Co(III)-LS) with a subsequent shortening of the cell parameters, in line with previous results.

A close inspection of the reflection peaks reveals a rhombohedral distortion of the *fcc* lattice, which is indicated by the splitting of the (220), (420), (440), and (620) reflections. This splitting is more pronounced in the TiO<sub>2</sub>-CoHCF compound.

The rhombohedral structure is the result of a distortion of the characteristic, *fcc* crystal structure of PBAs along the body diagonal triggered by the asymmetric electrostatic potential induced within the cubic framework.

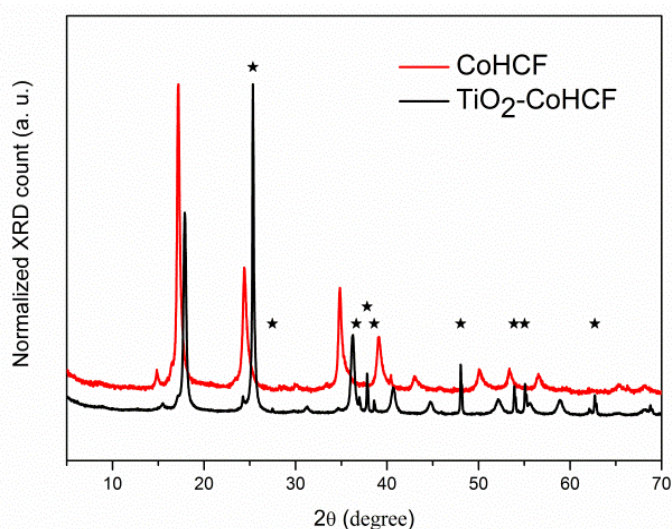


**Figure 65** XRD pattern of TiO<sub>2</sub>-CoHCF (black line) and CoHCF (red line). Crystal system: cubic, space group: F-43m, space group number: 216, a=b=c (Å)= 10.2960. \* indicates the reflection peaks assigned to Anatase TiO<sub>2</sub>.

It is worth underling that both XRD and Mössbauer spectroscopy show the successful synthesis of TiO<sub>2</sub>-CoHCF with no impurities.

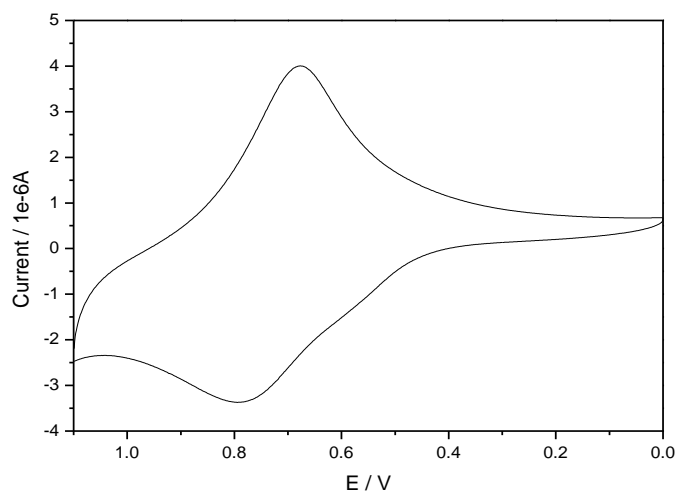
In particular, Mössbauer spectroscopy, which is usually more sensitive than XRD in the detection of amorphous and nanosized impurities, clearly indicates the absence of other Fe-containing impurities in the sample.

Figure 66 shows the three-electrodes CV (cyclic voltammetry) of a cell constituted of a TiO<sub>2</sub>-CoHCF working electrode, a CoHCF counter electrode and a silver–silver chloride (Ag/AgCl) in a saturated solution of potassium chloride reference electrode, with an aqueous solution of KCl 1.0 M as the electrolyte. The CV shape shows a single reversible redox process characteristic of the iron centres in TiO<sub>2</sub>-CoHCF, as confirmed by the E<sub>0</sub> values, contrary to bulk CoHCF, in which two redox processes due to the Fe(III)/Fe(II) and Co(III)/Co(II) redox couples are usually well distinguished.

Anyway, a closer inspection of the oxidation process reveals a shoulder at 0.57 V vs Ag/AgCl, which may be referred to cobalt, highlighting a possible mix of the so called “soluble” and “insoluble” species.

It is worth noting that the Co(III)/Co(II) couple becomes electroactive only when the compound is crystallized in the so called “insoluble form” or in the nano-sized form.

Subsequent scans are similar, implying that the working electrode is stable, while the current intensity increases slightly with time, indicating a gradual involvement of the innermost layers of the electroactive CoHCF material with successive scans.



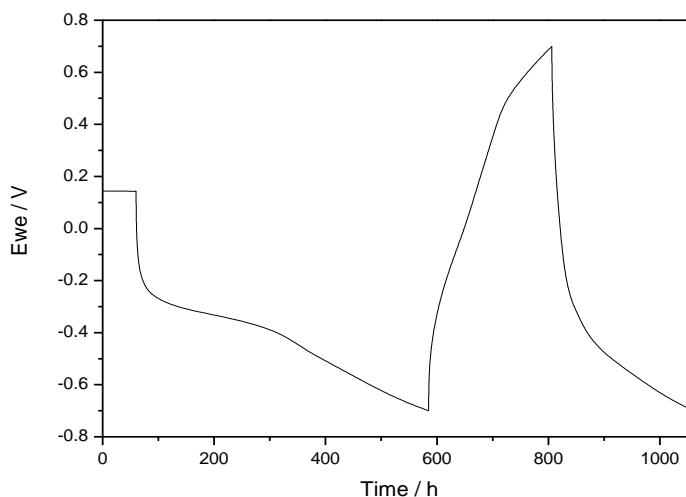
**Figure 66** CV obtained by using TiO<sub>2</sub>-CoHCF as working electrode, CoHCF as counter electrode, a silver–silver chloride electrode as reference, and KCl 1.0 M as supporting electrolyte (scan rate = 1.0 mV s<sup>-1</sup>).

Figure 67 shows the typical E–t curve for the galvanostatic cycling of a cell containing TiO<sub>2</sub>-CoHCF as the working electrode and CoHCF as the counter electrode in a two electrodes Swagelock teflon cell. Here, the potential is applied between two CoHCF electrodes, but the working one is nanodispersed on Anatase TiO<sub>2</sub>.

Obviously, the difference in electrochemical potential of two electrodes containing the same electroactive material should be zero, hence this galvanostatic measurements further highlights the key role of the presence of TiO<sub>2</sub> during synthesis on the redox state of the metal centers in the preparation of CoHCF.

The typical E-t curve shows the first discharge, much longer in time than the charge and the following discharge processes, evidencing two successive processes: first the voltage drops down to about -0.3 V, where a voltage plateau is observed, and subsequently decreases as the reaction proceeds.

During the following charge, the derivative signal evidences two redox couples which can be attributed to the redox couples Co(III)/Co(II) and Fe(III)/Fe(II), as already observed by CV.



**Figure 67** E-t curve for the reduction and the reverse oxidation by using TiO<sub>2</sub>-CoHCF as working electrode and CoHCF as counter electrode, KCl 1.0 M as supporting electrolyte. The cell were cycled at C/10 between 0.7 and -0.7 V.

In order to follow the evolution of the oxidation state of the iron centers during the electrochemical tests, Mössbauer spectra were recorded at room temperature for both CoHCF (a) and TiO<sub>2</sub>-CoHCF (b) electrodes after 20 continuous CV cycles from 1.1 to 0.0 V vs Ag/AgCl with a scan rate of 1.0 mV s<sup>-1</sup> (Fig. 68).

The Mössbauer spectrum of the cycled CoHCF electrode shown in Figure 68 is different from that of the pristine sample. Even though it can still be interpreted in terms of two quadrupole doublets, the dominant doublet with the large splitting has now parameters (cf. Table 14) in the typical range of high spin Fe(III).

The unresolved doublet, on the contrary, has virtually the same parameters of that observed initial sample, with the exception of slightly narrower linewidth.

A slightly narrower linewidth characterizes also the Mössbauer spectrum of sample TiO<sub>2</sub>-CoHCF after 20 CV cycles, which is on the contrary characterized by the same parameters of pristine TiO<sub>2</sub>-CoHCF.

The change in the spin state observed for CoHCF after cycling is a clear sign of a change in the coordination of the iron in this sample upon repeated CV cycles.

The relative electrochemical stress in CoHCF caused a higher predominance of the so called “insoluble” species and the evident appearance of high spin Fe(III) in the  $^{57}\text{Fe}$  Mössbauer spectra, never observed in the  $\text{TiO}_2\text{-CoHCF}$  compound.

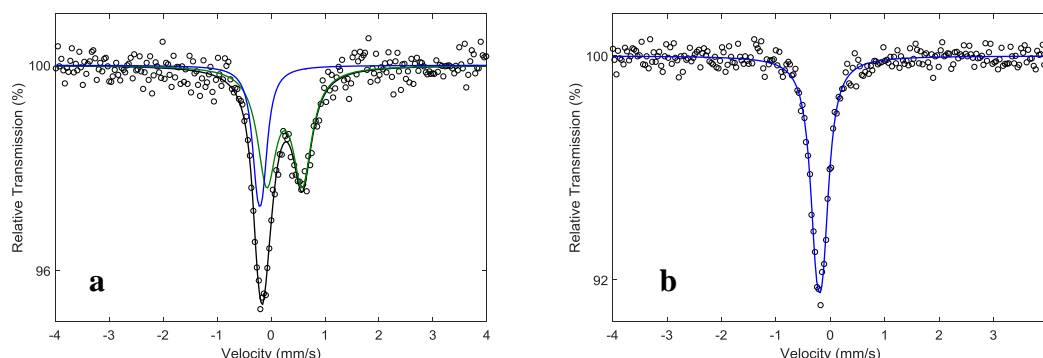


**Figure 68** Room temperature  $^{57}\text{Fe}$  Mössbauer spectra for samples CoHCF (a) and  $\text{TiO}_2\text{-CoHCF}$  (b) after 20 CV cycles from 1.1 to 0.0 V with a scan rate of  $1.0 \text{ mV s}^{-1}$ . The circles and the lines represent the experimental and fitted data, respectively.

**Table 14**  $^{57}\text{Fe}$  Mössbauer hyperfine parameters at room temperature of the measured samples.

Sample	$\Delta^*$ (mm/s)	$\delta^*$ (mm/s)	$\Gamma^*$ (mm/s)	$\text{RA}^*$ (%)	Site
Pristine CoHCF	0.43(1)	-0.15(1)	0.33(2)	82(5)	Fe(III) LS
	0.13(5)	-0.08(3)	0.4(1)	18(5)	Fe(II) LS
Pristine $\text{TiO}_2\text{-CoHCF}$	0.13(2)	-0.08(1)	0.37(2)	100	Fe(II) LS
CoHCF after 20 CV cycles	0.65(2)	0.36(2)	0.43(3)	71(3)	Fe(III) HS
	0.12(2)	-0.10(1)	0.25(3)	29(3)	Fe(II) LS
$\text{TiO}_2\text{-CoHCF}$ after 20 CV cycles	0.12(2)	-0.09(1)	0.29(2)	100	Fe(II) LS

### 6.3.6 Photocatalytic degradation of methylene blue with Anatase $\text{TiO}_2\text{-CoHCF}$ composite material

$\text{TiO}_2\text{-CoHCF}$  in 10:1 ratio compound has been directly used to evaluate its photocatalytic activity in photoelectrochemical degradation of methylene blue (MB) in aqueous solutions under UV irradiation. For comparison, native anatase  $\text{TiO}_2$  was also tested.

MB has been chosen as a model to test the photocatalytic activity of surfaces in an aqueous medium in according with the International Standard ISO 10678.

The tests were performed by following the methodology reported in the previous cited ISO standard. The degradation reaction kinetics are studied by monitoring the variation of the normalized dye absorption spectra in function of the irradiation time with UV light in the wavelengths range between 220 and 750 nm, as shown in Fig. 69.

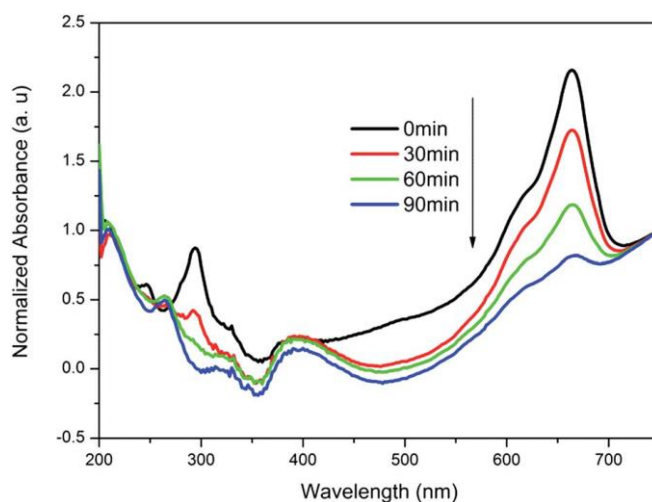


**Figure 69** CoHCF–TiO<sub>2</sub> 1:10 UV-Vis spectra in the  $\lambda$  range between 220 and 750 nm.

In the case of TiO<sub>2</sub>–CoHCF in 10:1 ratio, the decrease of the absorbance vs. time is faster than native TiO<sub>2</sub>; the value of  $dA/dt$  for TiO<sub>2</sub>–CoHCF is about 20% higher than the native TiO<sub>2</sub>.

The results revealed that the CoHCF doped TiO<sub>2</sub> showed higher photocatalytic activity than that of native TiO<sub>2</sub>.

## 6.4 Conclusion

New composite materials based on TiO<sub>2</sub>–MCHM have been synthesized and characterized with a correlated use of many experimental techniques in order to assess the formation of MCHM compounds, to investigate its bonding to TiO<sub>2</sub> and, finally, to characterize the associated modifications of the optical properties of titania.

Porous TiO<sub>2</sub> films were obtained at ambient temperature by using both TiCl<sub>4</sub> and anatase TiO<sub>2</sub> powder as precursor, and it appears to be a suitable electronic and structural mediator able to link stably with Metal Hexacyanometallates.

In particular, the cyclic voltammetry and the morphological inspection by TEM, confirm the formation of CoHCF and FeHCC cubic crystals linked to TiO<sub>2</sub> particles in the composites. IR, XPS, and XAS suggest the formation of a well-defined bond between the nitrogen of the cyano-group and the titanium of the titania substrate.

Vacancies in the structures play a key role in the promotion of the N–Ti bond. This model is supported, in particular, by the evolution of the Co/Fe stoichiometric ratio going from the 1:1 to 100:1 in the TiO<sub>2</sub>/CoHCF composites.

Indeed, in the 1:1 compound, the Co/Fe ratio is 1, characteristic of the so called “soluble” form; with increasing the TiO<sub>2</sub> fraction, the Co/Fe region approaches the limit value of the so called “insoluble” form, rich in vacancies of the Fe(CN)<sub>6</sub><sup>3-</sup> group. A similar trend occurs in the case of FeHCC.

UV-Vis spectra and the valence band measurement in the composites confirm a desirable reduction of the TiO<sub>2</sub> band gap.

It is worth noting the charge transfer in Anatase-doped Cobalt Hexacyanoferrate as highlighted by <sup>57</sup>Fe Mössbauer spectroscopy, indicating a change in the oxidation state at the iron centre on going from pure CoHCF to the TiO<sub>2</sub>-CoHCF composite.

The experimental evidence is supported by high-resolution XANES and EXAFS spectroscopy, the latter also indicating a consistent change (10%) of the Co-N first-shell bond distance, which in turn causes an equivalent variation of the cell parameter *a* of the lattice.

To the best of our knowledge, this is the first study in which a completely pure low-spin Fe(II) is obtained starting from a mix of low-spin Fe(II) and Fe(III), triggering of spin-crossover phenomena in Metal-Hexacyanoferrate based-molecular solids by an external stimuli other than photoexcitation.

The electron transfer induced in CoHCF by TiO<sub>2</sub> along the Co-NC-Fe-CN-Co chain in TiO<sub>2</sub>-CoHCF composites is confirmed by the unequivocal transformation of the typical quadrupole doublet of ferric iron of CoHCF into the single line spectrum of the ferrous species when CoHCF is nanodispersed with Anatase TiO<sub>2</sub>.

Galvanostatic measurements also confirm the electron transfer mechanism induced by TiO<sub>2</sub> highlighting the key role of the presence of TiO<sub>2</sub>.

The investigation of spin transitions induced by charge transfer in molecular solids is very important because these materials may become switchable components in molecular electronics and, thanks to the significant change in the spin state induced by the charge transfer, in spintronics as well.

The feasibility and versatility of the synthesis permits to obtain both bulk and thin films composite materials providing the starting point to exploit the suitability of such materials in photocatalytic and photovoltaic devices.

Practical use of these materials can be envisaged in other different areas, such as antibacterial treatments, protection of historical artifacts and self-cleaning surfaces.

- 
- <sup>1</sup> A. Fujishima and K. Honda, *Nature*, 1972, 238, 37.
- <sup>2</sup> G. Dai, L. Zhao, J. Li, L. Wan, F. Hu, Z. Xu, B. Dong, H. Lu, S. Wang and J. Yu, *J. Colloid Interface Sci.*, 2012, 365, 46.
- <sup>3</sup> F. R. Marciano, D. A. Lima-Oliveira, N. S. Da-Silva, A. V. Diniz, E. J. Corat and V. J. Trava-Airoldi, *J. Colloid Interface Sci.*, 2009, 340, 87.
- <sup>4</sup> D. Tahk, T. I. Kim, H. Yoon, M. Choi, K. Shin and K. Y. Suh, *Langmuir*, 2010, 26, 2240.
- <sup>5</sup> Graziani, L.; Quagliarini, E.; Osimani, A.; Aquilanti, L.; Clementi, F.; Yéprémian, C.; Lariccia, V.; Amoroso, S.; D'Orazio, M., *Build. Environ.*, 2013, 64, 38.
- <sup>6</sup> M. C. Tsai, M. H. Yang, Y. W. Chang, J. K. Tzeng, C. Y. Lee, H. T. Chiu, H. C. Chen and I. N. Lin, *Mater. Chem. Phys.*, 2013, 143, 60.
- <sup>7</sup> Fujishima, A.; Zhang, X.; Tryk, D. A., *Surf. Sci. Rep.*, 2008, 63, 515.
- <sup>8</sup> D. P. Serrano, G. Calleja, R. Sanz and P. Pizarro, *J. Mater. Chem.*, 2007, 17, 1178.
- <sup>9</sup> I. A. Rutkowska, A. Andrearczyk, S. Zoladek, M. Goral, K. Darowicki and P. J. Kulesza, *J. Solid State Electrochem.*, 2011, 15, 2545.
- <sup>12</sup> M. Pelaez, N. T. Nolan, S. C. Pillai, M. K. Seery, P. Falaras, A. Kontos, P. S. M. Dunlop, J. W. J. Hamilton, J. A. Byrne, K. O'Shea, M. H. Entezari, D. D. Dionysiou, *Appl. Catal. B*, 2012, 125, 331.
- <sup>13</sup> M. Berrettoni, M. Ciabocco, M. Fantauzzi, M. Giorgetti, A. Rossi, E. Caponetti, *RSC Adv.*, 2015, 5, 35435.
- <sup>14</sup> A. Fujishima, T. N. Rao, D. A. Tryk, *J. Photochem. Photobiol.* 2010, 1, 1.
- <sup>15</sup> X. Wang, A. Kafizas, X. Li, S. J. A. Moniz, P. J. T. Reardon, J. Tang, I. P. Parkin, J. R. Durrant, *J. Phys. Chem C*, 2015, 119, 10439.
- <sup>14</sup> M. Berrettoni, M. Giorgetti, S. Zamponi, P. Conti, D. Ranganathan, A. Zanotto, M. L. Saladino and E. Caponetti, *J. Phys. Chem. C*, 2010, 114, 6401.
- <sup>15</sup> P.J. Kulesza, M.A. Malik, S. Zamponi, M. Berrettoni, R. Marassi, *J. Electroanal. Chem* 397 (1995) 287-292.
- <sup>16</sup> S. Zamponi, M. Giorgetti, M. Berrettoni, P.J. Kulesza, J.A. Cox, A.M. Kijak, *Electrochim. Acta* 51 (2005) 118–124.
- <sup>17</sup> M. Giorgetti, M. Berrettoni, S. Zamponi, P.J. Kulesza, J.A. Cox, *Electrochim. Acta*, 51 (2005) 511-516.
- <sup>18</sup> A.I. Rykov, J. Wang, T. Zhang, K. Nomura, *Hyperfine Interact* 218 (2013) 53-58.
- <sup>19</sup> Sh.G. Beheir, K. Benyamin, F.M. Mekhail, *J. Radioanal. Nucl. Chem.* 232 (1998) 147-150.
- <sup>20</sup> M. Wilamowska, A. Lisowska-Oleksiak, *Solid State Ion.* 188 (2011) 118–123.
- <sup>21</sup> A. Widmann, H. Kahlert, I. Petrovic-Prelevic, H. Wulff, J. V. Yakhmi, N. Bagkar and F. Scholz, *Inorg. Chem.*, 2002, 41, 5706.
- <sup>22</sup> N.R. de Tacconi, K. Rajeshwar, R.O. Lezna, *Electrochimica Acta* 45 (2000) 3403–3411.
- <sup>23</sup> I.A. Rutkowska, M. Skunik, K. Miecznikowski, P.J. Kulesza, *ECS Trans.* 13 (2008) 185-198.
- <sup>24</sup> M. Khoudiakov, A. L. Parise and B. S. Brunshwig, *J. Am. Chem. Soc.*, 2003, 125, 4637.
- <sup>25</sup> N. R. de Tacconi, K. Rajeshwar and R. O. Lezna, *Electrochim. Acta*, 2000, 45, 3403.
- <sup>26</sup> M. Ciabocco, M. Berrettoni, D. F. Martino Chillura and M. Giorgetti, *Solid State Ion.*, 2014, 259, 53.
- <sup>27</sup> J. T. Culp, J-H. Park, F. Frye, Y-D. Huha, M. W. Meisel and D. R. Talham, *Coord. Chem. Rev.* 2005, 249, 2642.
- <sup>28</sup> O. Sato, T. Iyoda, A. Fujishima and K. Hashimoto, *Science* 1996, 272, 704.
- <sup>29</sup> J.-D. Cafun, G. Champion, M.-A. Arrio, C. Cartier dit Moulin and A. Bleuzen, *J. Am. Chem. Soc.* 2010, 132, 11552.
- <sup>30</sup> D. C. Jiles, *J. Phys. D: Appl. Phys.* 1995, 28, 1537.
- <sup>31</sup> Y. Ogawa, S. Koshihara, K. Koshino, T. Ogawa, C. Urano, and H. Tagaki, *Phys. Rev. Lett.*, 2000, 84, 3181.
- <sup>32</sup> T. Matsuda, H. Tokoro, K. Hashimoto, and S. I. Ohkoshi, *Dalton Trans.*, 2006, 5046
- <sup>33</sup> A. Bhattacharjee, S. Saha, S. Koner, V. Ksenofontov, S. Reiman, P. Gütlich, *J. Magn. Magn. Mater.* 2006, 302, 173.
- <sup>34</sup> M. Giorgetti, G. Aquilanti, M. Ciabocco, M. Berrettoni, *Phys. Chem. Chem. Phys.* 2015, 17, 22519.
- <sup>35</sup> S.-I. Ohkoshi and H. Tokoro, *Acc. Chem. Res.* 2012, 45, 1749.
- <sup>36</sup> A. Dei, *Angew. Chem. Int. Ed.* 2005, 44, 1160.
- <sup>37</sup> S. Ohkoshi, K. and J. Hashimoto, *Photochem. Photobiol. C* 2001, 2, 71.

- 
- <sup>38</sup> Tsang-Hsiu Wang, A.M. Navarrete-López, S. Li, D.A. Dixon, *J. Phys. Chem.* 114 (2010) 7561–7570
- <sup>39</sup> M. P. Seah, *Surf. Interface Anal.*, 2001, 31, 721.
- <sup>40</sup> N. Fairley, CasaXPS, version 2.3.15; 1999-2003.
- <sup>41</sup> D. A. Shirley, *Phys. Rev. B*, 1972, 5, 4709.
- <sup>42</sup> M. P. Seah, Quantification in AES and XPS. In: Briggs D, Grant JT (eds) *Surface Analysis by Auger and X-Ray Photoelectron Spectroscopy*. IM Publication Surface Science Spectra, Manchester, 2003.
- <sup>43</sup> J. H. Scofield, *J. Electron. Spectrosc.*, 1976, 8, 129.
- <sup>44</sup> R. F. Reilman, A. Msezane and S. T. J. Manson, *J. Electron. Spectrosc. Relat. Phenom.*, 1976, 8, 389.
- <sup>45</sup> M. Fantauzzi, A. Pacella, J. Fournier, A. Gianfagna, G. B. Andreozzi and A. Rossi, *Anal. Bioanal. Chem.*, 2012, 404, 821.
- <sup>46</sup> M. P. Seah and W. A. Dench, *Surf. Interface Anal.*, 1979, 1, 2.
- <sup>47</sup> B. Ravel and M. Newville, *J. Synchrotron Radiat.*, 2005, 12, 537.
- <sup>48</sup> T.J.B Holland and S.A.T. Redfern, *Mineral. Mag* 1997, 61, 65.
- <sup>49</sup> K.K. Kasem, D. Hanninger, A. Croxford, F. Phetteplace, *Mater. Sci. Pol.* 28 (2010) 439-449.
- <sup>50</sup> K. Oku, K. Wagatsuma and H. Matsuta, *J. Electron Spectrosc. Relat. Phenom.*, 1997, 83, 31.
- <sup>51</sup> X. Cui, L. Hong and X. Lin, *J. Electroanal. Chem.*, 2002, 526, 115.
- <sup>52</sup> M. Olla, G. Navarra, B. Elsener and A. Rossi, *Surf. Interface Anal.*, 2006, 38, 964.
- <sup>53</sup> M. Fantauzzi, A. Pacella, D. Atzei, A. Gianfagna, G. B. Andreozzi and A. Rossi, *Anal. Bioanal. Chem.*, 2010, 396, 2889.
- <sup>54</sup> D. Atzei, D. De Filippo, A. Rossi and R. Caminiti, *Spectrochim. Acta A*, 1993, 49, 1779.
- <sup>55</sup> D. Atzei, D. De Filippo, A. Rossi, R. Caminiti and C. Sadun, *Spectrochim. Acta A*, 1995, 51, 11.
- <sup>56</sup> D. Atzei, A. Rossi and C. Sadun, *Spectrochim. Acta A*, 2000, 56, 1875.
- <sup>57</sup> H. Haraguchi, K. Jujiwara and K. Puwa, *Chem. Lett.*, 1975, 409.
- <sup>58</sup> T. R. I. Cataldi, G. E. De Benedetto and A. Bianchini, *Electroanal. Chem.*, 1998, 448, 111.
- <sup>59</sup> W. Macyk, K. Szaciłowski, G. Stochel, M. Buchalska, J. Kuncewica and P. Łabuz, *Coord. Chem. Rev.*, 2010, 254, 2687.
- <sup>60</sup> R. Sanjinés, H. Tang, H. Berger, F. Gozzo, G. Margaritondo and F. Lévy, *J. Appl. Phys.*, 1994, 75, 2945.
- <sup>61</sup> K. Takegara and H. Harima, *Phase Transition*, 2002, 75, 799.
- <sup>62</sup> M. Giorgetti, *ISRN Mater. Sci.*, 2013, 2013, 1.
- <sup>63</sup> M. Berrettoni, M. Giorgetti, J. A. Cox, D. Ranganathan, P. Conti and S. Zamponi, *J. Solid State Electrochem.*, 2012, 16, 2861.
- <sup>64</sup> M. Giorgetti, L. Guadagnini, D. Tonelli, M. Minicucci and G. Aquilanti, *Phys. Chem. Chem. Phys.*, 2012, 14, 5527.
- <sup>69</sup> M. Berrettoni, M. Ciabocco, M. Fantauzzi, M. Giorgetti, A. Rossi, and E. Caponetti, *R. Soc. Chem. Adv.* 2015, 5, 35435.
- <sup>70</sup> M. Giorgetti, and M. Berrettoni, *Inorg. Chem.*, 2008, 47, 6001.
- <sup>71</sup> T. Yokohama, T. Otha, O. Sato, and K. Hashimoto, *Phys. Rev. B.*, 1998, 58, 8257.
- <sup>72</sup> V. Escax, G. Champion, M. A. Arrio, M. Zacchigna, C. Cartier Dit Moulin, and A. Bleuzen, *Angew. Chem. Int. Ed.*, 2005, 44, 4798.
- <sup>73</sup> T. E. Westre, P. Kennepohl, J. G. DeWitt, B. Hedman, K. O. Hodgson, and E. I. Solomon, *J. Am. Chem. Soc.*, 1997, 119, 6297.

## 7. Conclusions and future prospects

This thesis focused on the synthesis, characterization and analytical and technological applications of interesting inorganic compounds, called Prussian Blue analogs or Metal Hexacyanometallates, MHCMs.

Prussian Blue (PB) analogs open framework materials represent a class of extremely versatile compounds thanks to their unique physicochemical characteristics, that are primarily a result of the perovskite-like face-centered cubic crystal structure.

Four such compounds were considered in this thesis and in particular Indium and Nickel Hexacyanoferrate, for their notable properties as ion-exchangers and ionic sieves, allowing for cation selective extractions, also for the rare earth elements selective recovery, as shown in the thesis.

Subsequently, nanosized Cobalt Hexacyanoferrate was tested as a sensor for electroanalysis, the test system was the oxidation of L-cysteine, providing improved sensitivity and high stability and making it appropriate for electroanalytical applications.

Finally, the synthesis and characterization of novel  $\text{TiO}_2$ -Metal Hexacyanometallates composite materials were deeply investigated. The obtained experimental results highlighted that the electronic properties of  $\text{TiO}_2$  are substantially modified as confirmed in particular by UV-Vis and XP-valence band data.

It is worth noting that this is one of the first examples of the triggering of spin-crossover phenomena in Metal-Hexacyanoferrate based-molecular solids by an external stimuli other than photoexcitation and most of all one of the first studies in which a completely pure low-spin Fe(II) is obtained starting from a mix of low-spin Fe(II) and Fe(III).

In future studies, Metal Hexacyanometallates will provide the possibility to develop new technological applications both for antimicrobial packaging and ready-to-use electrodes as potentiometric and even amperometric sensors for analytical devices.

Particular importance of application of Prussian Blue analogs based sensors is expected in certain areas of clinical diagnostics, where high sensitivity and selectivity as well as the possibility of miniaturization are required.

## APPENDIX A

### Synthesis of Iron Hexacyanocobaltate (FeHCC) particles and antibacterial efficiency investigation

#### A1. Introduction

Environmental disinfection plays a crucial role in the prevention of infectious disease. In recent years, bacteria have been responsible for a large number of disease outbreaks in a variety of settings. Moreover, the increase in microorganism resistance to commonly applied chemotherapeutics and disinfectants constrain the development of new agents for disinfection.<sup>1</sup> The ability to control and/or destroy microorganisms is therefore of enormous importance to many organizations and industries, such as healthcare, food and drink, water treatment industries.

A possible approach to reduce the microbial contamination on food surfaces and in food preparation environments is the use of nanomaterials.

Antimicrobial nanocomposite systems are appealing, since materials in the nanoscale range have a high surface area to volume ratio as compared to their bulk counterparts. Nanomaterials are thus more efficient, since they are able to attach more copies of microbial assemblage and cells.<sup>2</sup> Antimicrobial nanoparticles that have been synthesized and tested for applications in packaging and food storage boxes include silver oxide nanoparticles,<sup>3</sup> zinc oxide, magnesium oxide nanoparticles<sup>4</sup> and nisin particles produced from the fermentation of a bacteria.<sup>5,6</sup>

Titanium dioxide is one of the most studied materials in the field of antibacterial applications, anyway its antibacterial activity is efficient only upon irradiation by ultraviolet (UV) light at levels that would provoke severe injure to human cells. In the TiO<sub>2</sub> nanocomposites, biocidal efficiencies depend on their light absorbance. Therefore, most TiO<sub>2</sub> compounds exhibit no antimicrobial effect in the dark condition.

Hence, there is a growing need to find alternative methods<sup>7</sup> for formulating new types of safe and cost effective antibiotics for eliminating and controlling the spread of such pathogens in foods or food processing environments.

Metal Hexacyanometallates have been never investigated in the field of antibacterial applications except for the Metal Hexacyanoferrate precursor, potassium ferricyanide, as reported in literature.<sup>8</sup> This compound is strongly able to inhibit the *E. coli* growth and survival under anaerobic fermentative conditions.

*Escherichia coli* is a group of hazardous biofilm-forming pathogenic bacteria which can cause several foodborne illnesses including diarrhea and hemolytic uremic syndrome (HUS), leading to severe kidney failure.<sup>9</sup> Contaminations and outbreaks caused by *E. coli*, specifically O157:H7 strain, have been reported in various food products, such as vegetable juices, dairy products, sausages, and nuts.<sup>10</sup>

Among the Metal Hexacyanometallates, Iron Hexacyanocobaltates (FeHCC) have not been widely studied in literature, it is reported in papers dealing with Cs sorption probed by Mössbauer spectroscopy<sup>11</sup> and its removal in waste solutions through a process involving the precipitation of cesium.<sup>12</sup> The redox activity is very likely to come from high spin iron atoms in FeHCC. Electrochemistry of Iron Hexacyanocobaltate compound was poorly investigated but it is known that the redox activity of high spin iron centre  $Fe^{2+}/Fe^{3+}$  occur.<sup>13</sup> Probably due to their oxidation capability, Iron Hexacyanocobaltate substrates exhibit a self-cleaning function, as shown in this study, by being able to decompose various types of organic matter and also act as disinfectants by injuring both the cell envelope and intracellular components of the microorganisms in contact with those substances. In fact a cell wall damage followed by cytoplasmic membrane injure leading to a direct intracellular attack can be proposed as the sequence of events when microorganisms come in contact with Iron Hexacyanocobaltate.

On this matter, the antibacterial activity is clearly observed in darkness, unlike the well-known  $TiO_2$  photocatalyst, efficient only upon irradiation by ultraviolet (UV) light.

It is worth underlining the FeHCC elevate stability even in different pH and in high humidity conditions, as FeHCC is extremely not soluble in water, avoiding any solubilization problem.

To the best of our knowledge, no data are available on the high antibacterial efficiency of Iron Hexacyanocobaltate, therefore this study, in collaboration with the University of Palermo, represents a preliminary approach and is aimed at reporting the fabrication of Iron Hexacyanocobaltate by a facile co-precipitation method and offering supportive evidences to indicate that this compound can inhibit the Gram negative *Escherichia Coli* and the Gram positive *Staphylococcus aureus* growth and even kill the bacterial cells by destroying the membranous configuration.

The investigation of the powerful antimicrobial properties of this compound could be interesting in order to develop new technological applications for antimicrobial packaging. Hence this study is the first step of a series of studies that will lead to establishment of antimicrobial packaging system.

## **A2. Experimental**

### **A2.1. Reagents and materials**

All chemicals used in this work were reagent grade and were used as received from Sigma-Aldrich ( $\text{FeCl}_2$  and  $\text{K}_3\text{Co}(\text{CN})_6$ ). Deionized water was used throughout this work. All experiments were carried out at room temperature and in air, except the dehydration of the sample carried on in the oven at  $80^\circ\text{C}$ .

### **A2.2. Chemical synthesis**

Iron Hexacyanocobaltate was prepared as described in literature.<sup>14</sup> Briefly, Iron Hexacyanocobaltate was simply synthesized by co-precipitation method mixing 0.05 M water solution of  $\text{FeCl}_2$  drop wise to an equivalent amount of  $\text{K}_3[\text{Co}(\text{CN})_6]$  and stirring at room temperature. The precipitate was allowed to stand for a night and air-dried at ambient conditions to improve the polymerization. Subsequently, the sample was carefully washed with deionized water to remove the unreacted salts and centrifuged to separate the solid product. Finally, the precipitate was dried at  $80^\circ\text{C}$ .

### **A2.3. Instrumentation**

XRD measurements were performed on a Rigaku Mo Ka X-ray source equipped with a Huber goniometer. Cell parameter,  $a$ , referred to the cubic structure, was calculated by the unit cell program.

TEM experiments were performed on a high resolution transmission electron microscope (HR-TEM) JEOL JEM-2100 operating at 200 kV. Elemental analysis was carried out using an energy dispersive X-ray detector (EDS), Oxford mod. 6498, with a  $30\text{ mm}^2$  area.

Infrared spectra (IR) were recorded with a Jasco FT/IR-4600 PLUS spectrometer working in transmission mode. At least 32 scans were typically taken between  $4000\text{ cm}^{-1}$  and  $500\text{ cm}^{-1}$  with a resolution of  $1\text{ cm}^{-1}$ . Powder spectra were recorded by using KBr pellets, containing about 1% w/w of the sample. The pellets were produced by compressing with 5 ton for about 20 s the powders in a stainless steel mold of 13 mm in diameter; no pressure effects have been observed by using a manually operated hydraulic press (Specac Ltd., Orpington Kent, UK). The spectrum of pure KBr was taken as a background reference.

#### **A2.4. Determination of the antibacterial activity**

The Gram-negative bacterium *Escherichia coli* K12 and the Gram positive *Staphylococcus aureus* ATCC25923 were used in this study and were maintained as described elsewhere.<sup>15,16</sup>

*E. coli* and *S. aureus* are facultative anaerobe microorganisms that can live both in presence and in the absence of oxygen.

To evaluate the antibacterial effect of potassium ferricyanide (KHCF) and Iron Hexacyanocobaltate (FeHCC) on bacterial survival, bacteria was grown aerobically at 37°C in a Luria Bertani (LB) broth. After overnight incubation, 1:100 inoculum was prepared in salt medium (46 mM K<sub>2</sub>HPO<sub>4</sub>, 23 mM KH<sub>2</sub>PO<sub>4</sub>, 0.4 mM MgSO<sub>4</sub>, 8 mM (NH<sub>4</sub>)<sub>2</sub>SO<sub>4</sub>, 8 μM FeSO<sub>4</sub>, 22 mM glucose, pH 7.4) or in LB medium, and bacteria were grown anaerobically in stationary capped tubes filled entirely with growth medium or aerobically in vigorously shaken tubes in a medium-tube volume of 1:10.

KHCF and FeHCC aqueous suspensions were added at different concentrations. The terminology is conserved for analogy with solutions, anyway it is worth noting that suspensions are used throughout this work.

Bacterial survival was determined by the colony counting method. Serial dilutions per each sample were prepared in liquid growth medium and spread across the surface of a LB agar plate. After overnight incubation at 37°C, the number of colony forming units (CFU) was counted and CFU/ml was deduced, considering number of CFU/volume plated (ml) X dilution factor used. The percentage of bacterial survival was determined considering the CFU at the time of the inoculum at 100% (t=0h). Each experiment was performed at least in triplicate.

Total bacterial growth was monitored using a Spark™ 10M multimode microplate reader measuring the OD<sub>600</sub> that is an indirect way to measure bacterial growth.

Since potassium ferricyanide (KHCF) and Iron Hexacyanocobaltate (FeHCC) adsorb, their absorbance was subtracted to the absorbance of the samples. The experiment was performed in triplicate.

Kirby Bauer method, as described by Lo Grasso et al.,<sup>17</sup> was used to assess antibacterial activity of the compounds in solid medium; briefly, a mixture of FeHCC was prepared and directly spotted on a LB agar plate containing an overlay of *E. coli*.

Antibacterial activity was measured as the inhibition halo formed around the spot. The experiment was performed in duplicate.

### **A2.5. Dual staining for assessment of loss of membrane integrity**

*E. coli* and *S. aureus* cultures were grown in 24 well culture plates and incubated with the selected compounds in anaerobic and aerobic conditions. Aliquots of 100  $\mu$ l were transferred into Eppendorf tubes, washed twice with phosphate buffer saline (PBS) and incubated with 1  $\mu$ l of an Acridine Orange (100  $\mu$ g/ml)-Ethidium Bromide (100  $\mu$ g/ml) mixture (1:1, v/v). Cells were immediately observed under a fluorescent microscopy (Carl Zeiss) with excitation (488 nm) and emission (550 nm) at 630X magnification.

### **A2.6. Intracellular reactive oxygen species (ROS) measurement**

The generation of intracellular ROS was monitored using dichloro-dihydro-fluorescein diacetate (DCFH-DA) that passively enters into the cells where it reacts with ROS to form the highly fluorescent compound dichlorofluorescein (DCF). For quantitative estimation of ROS, 100  $\mu$ l of treated-bacteria were washed twice with PBS and then incubated with 50  $\mu$ M of DCFH-DA at 37°C for 1h. The reaction mixture was discarded and replaced by 100  $\mu$ l of PBS; the green fluorescence intensity was detected using Spark™ 10M multimode microplate reader at an excitation wavelength of 485 nm and an emission wavelength of 528 nm. The values were averaged from three different wells and expressed as a percentage of fluorescence intensity relative to the control cells after normalization with the OD<sub>600</sub> values.

## **A3. Results and Discussion**

### **A3.1. Chemical characterization of FeHCC**

Figure 70 shows the XRD pattern for the FeHCC investigated compound, confirming the success of the synthesis. XRD patterns of FeHCC are consistent with the typical *fcc* lattice of MHCMS. FeHCC cell parameter, *a*, referred to the cubic structure, calculated by the unit cell program,<sup>18</sup> is 10.10 Å, very close to the cell parameter of many other Metal Hexacyanometallates.

A close inspection of the reflection peaks indicates a presence of the rhombohedral distortion, split of the peaks.

The rhombohedral structure is the result of a distortion of the characteristic, *fcc* crystal structure of PBAs along the body diagonal triggered by the asymmetric electrostatic potential induced within the cubic framework.

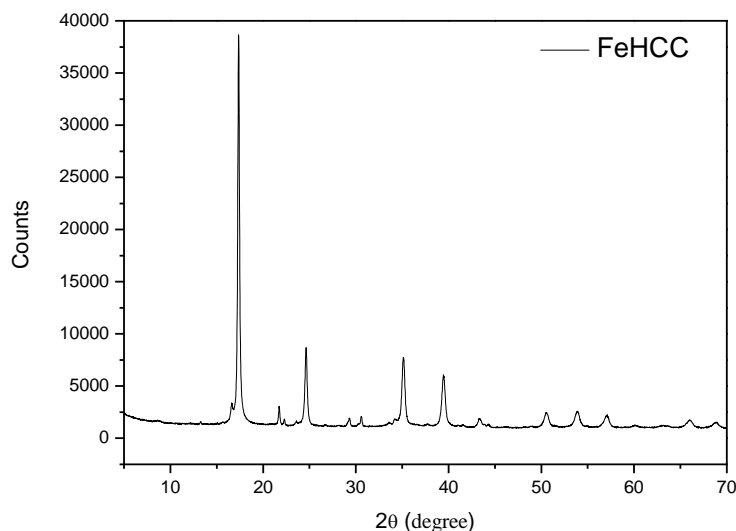


**Figure 70** XRD pattern of FeHCC compound.

IR spectroscopy provides useful information on the structure of the studied compounds.<sup>19</sup> It is well known that cyanide at its C end behaves as a very strong ligand resulting in low spin electronic configuration for the metal in the molecular block  $[M(CN)_6]$ . At the N end it forms bond with more ionic character and, in consequence, the outer metal is usually found in a high spin state.<sup>20</sup> The IR spectra of the studied compounds are composed of three absorption bands from vibrations related to the octahedral  $[Co(CN)_6]$  structural unit,  $\nu(CN)$ ,  $\delta(CoCN)$ ,  $\nu(CoC)$ , and those from the crystal water,  $\nu(H_2O)$  and  $\delta(HOH)$ .<sup>21</sup>

The stretching vibration of coordinated water in Metal Hexacyanometallates is usually observed as sharp bands around  $3550\text{ cm}^{-1}$  but strongly overlapped with the broad absorption band due to that motion from the hydrogen bonded waters. In cobalticyanides the  $\nu(CoC)$  vibration usually falls below  $400\text{ cm}^{-1}$  and it was not observed with the IR spectrophotometer used.

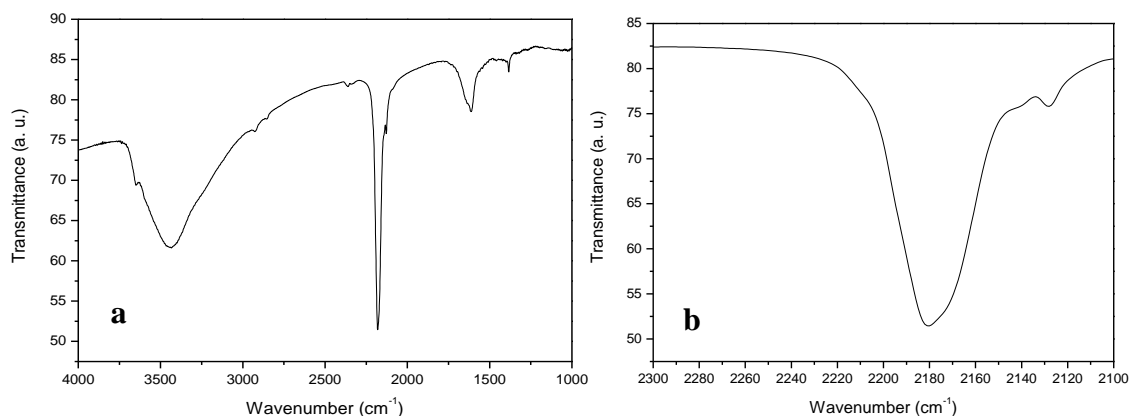


**Figure 71** IR spectra of the FeHCC powder in the region a) from  $4000$  to  $1000\text{ cm}^{-1}$  and b) of the CN group stretching.

FeHCC sample was also characterized by transmission electron microscope (TEM). To obtain TEM images of the electroactive film, the surface was scraped off by using the tip of a scalpel. Then the obtained powders was mixed with ethanol and the resulting dispersion was dropped on a net copper sample container in order to be analyzed with the Jeol JEM-2100 electronic microscope working at 200 KV. Figure 72 show the typical cubic aggregate of FeHCC of about 50÷100 nm in size.

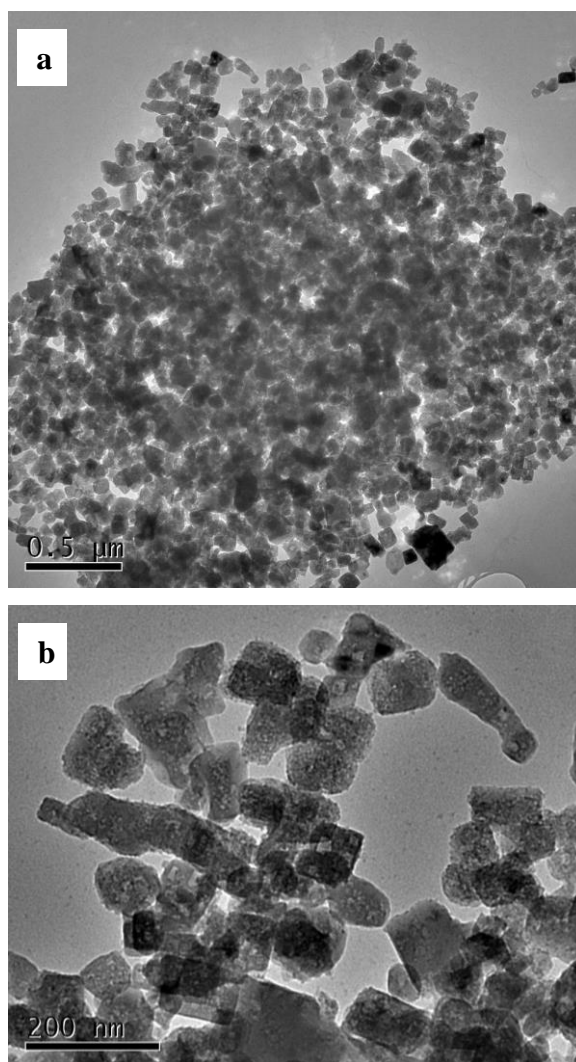


**Figure 72** TEM images of the FeHCC cubic aggregates.

### **A3.2. Antibacterial activity of FeHCC against *E. Coli* in anaerobiosis**

In most foods, surface growth of microorganisms is the major shelf-life limiting factor.<sup>22</sup> As already demonstrated in Bagramyan et al.,<sup>23</sup> *E. Coli* was able to survive in the salt medium under anaerobic conditions and its growth was strongly inhibited in the presence of 1.0 mM KHCF.

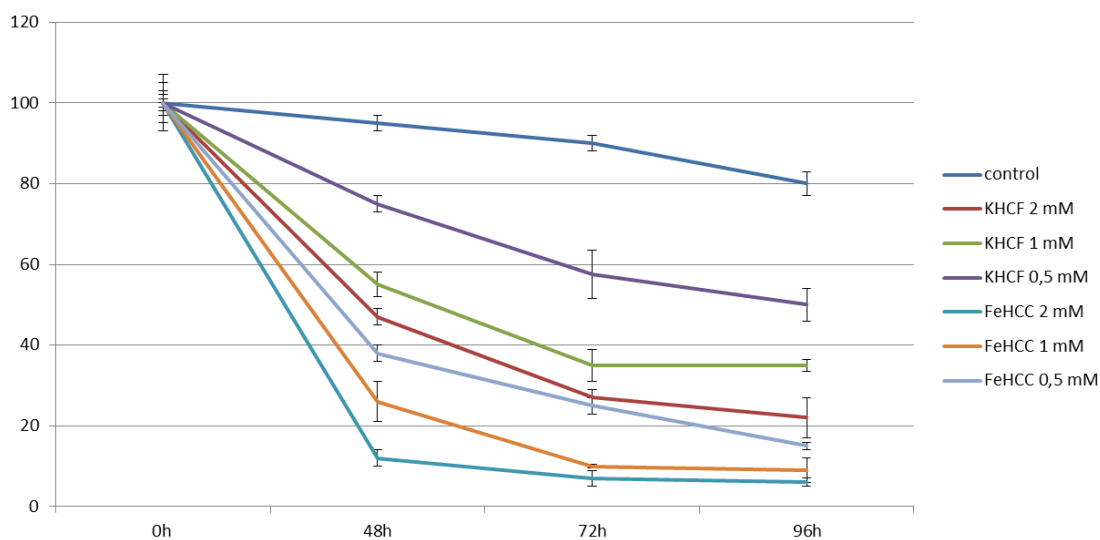
Hence, the bactericidal activity of both the Metal Hexacyanoferrate precursor, potassium ferricyanide, and the mixed Metal Hexacyanometallate, Iron Hexacyanocobaltate, FeHCC, was evaluated, by following the conditions described by Bagramyan et al.<sup>23</sup> Different concentrations (2.0, 1.0 and 0.5 mM) of FeHCC and KHCF were used.

Figure 73 reports the preliminary experimental results relative to the growth inhibitory test carried out both with KHCF and FeHCC under anaerobic conditions.

The data proved that the studied compounds reduced bacterial survival, anyway each presented different performances in terms of time and rate of action. The bacterial survival percentage in presence of KHCF and FeHCC demonstrated that FeHCC is more potent than KHCF in killing bacteria.

It has been noticed that with the increase in concentration of FeHCC, the inhibition rate has also been increased. The highest concentration of FeHCC has been found to completely inhibit the growth of pathogens. On the other hand the high concentration of KHCF also demonstrated inhibition of bacterial culture as the contact time increased, even though it seems to attain a steady state value at a relatively high percentage of bacterial survival.

Hence, the preliminary analysis confirm that FeHCC can inhibit *E. Coli* growth and even completely kill the bacterial cells, demonstrating effective toxicity against Gram-negative strains and it is interesting to note that the activity of composites was maintained over time.



**Figure 73** Percentage of bacterial survival under anaerobic fermentative conditions in presence of 2.0, 1.0 and 0.5 mM of KHCF and FeHCC. Control indicates the survival of *E. Coli* in the salt medium (no additions). Data are average from triplicate experiments. Error bars represent standard deviations of duplicate incubations. Statistical significance was determined by the unpaired Student's t-test.

### **A3.3. Antibacterial activity of FeHCC against *E. Coli* in aerobiosis**

Given this positive result and considering the physicochemical properties of FeHCC, we evaluated whether this compound was also able to work in aerobic conditions and in a rich medium, such as LB, where bacterial growth is much more prosperous.

This medium was chosen since our idea is to apply these nanoparticles as films to protect food that can be considered as a rich medium for bacterial growth. Thus, the experiment was performed incubating *E. coli* in the poor medium, Salt Medium, and in the rich medium, LB medium, in aerobiosis and anaerobiosis. In presence of oxygen, bacteria produce ATP by using aerobic respiration with the consequence of a much higher growth, while in anaerobiosis they perform anaerobic fermentation.

In LB the cell number is significantly higher with respect to SM medium, in all cases, confirming the higher growth rate of bacteria in LB.

In aerobiosis, 1.0 mM FeHCC produced a decrease in bacterial growth, but did not show a high antibacterial property in SM; in LB there was no a significant decrease in bacterial growth both in aerobiosis and anaerobiosis (Fig. 74, upper panels).

In this experiment, to better understand the mechanism of action of FeHCC after challenge with the nanoparticles, dual staining with acridine orange and ethidium bromide (AO/EB) was performed and cells were visualized under fluorescence microscope.

AO is a neutral dye that permeates passively into both live cells with an intact membrane and dead cells with a damaged membrane. Ethidium bromide, a charged dye, is taken up only if the cells have lost membrane integrity.

Cells with intact membranes appear uniformly green, whereas cells with damaged membranes also incorporate ethidium bromide and therefore stain orange.

Interestingly, as shown in Figure 74 (lower panels), control cells stained only with acridine orange both in aerobic and anaerobic conditions, while in treated cells is evident that the number of cells with damaged membranes increased.

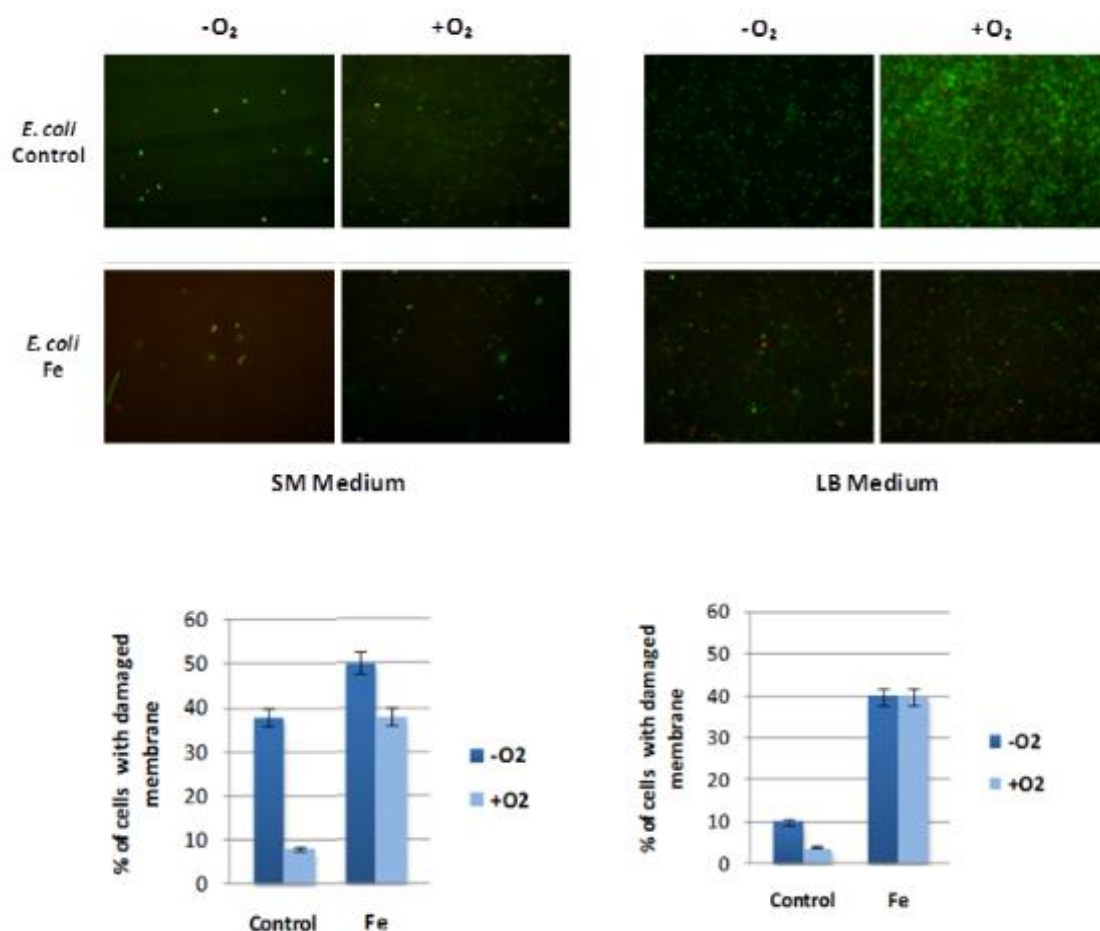


**Figure 74** Fluorescence micrographs of dual staining with acridine orange and ethidium bromide. Upper panels: Bacteria cells treated in aerobic and anaerobic conditions for 72 h with 10  $\mu$ M of selected compounds were stained with AO/EB and visualized under fluorescence microscope at 680X magnification. The figure is representative of images obtained from at least 3 different fields for each group and from three independent experiments. Lower panels: Histogram representing the quantification of cells with damaged membranes.

In addition, to test if in aerobiosis the antibacterial activity was dependent upon the production of reactive oxygen species (ROS) that can lead to membrane destabilization and, therefore, to cell death, ROS were measured and fluorescence micrographs of cells were done.

After incubation with FeHCC composites, ROS formed in the samples were detected at 523 nm emission wavelength by using a fluorescence spectrophotometer.

The results (Fig.75) confirmed the generation of free radicals in *E. coli* cells indicating the ability of FeHCC composites to break the bacterial cell membrane. An increase in the ROS synthesis leads to the formation of highly reactive radicals associated with cellular destruction.

Excess generation of reactive oxygen species can attack membrane lipids, which leads to a breakdown of membrane function. Certain transition metals might disrupt the cellular donor ligands that coordinate Fe, especially, the solvent-exposed [4Fe4S] clusters of proteins. The direct or indirect destruction of [4Fe4S] clusters by metals causes the release of additional Fenton-active Fe into the cytoplasm, resulting in increased ROS formation.

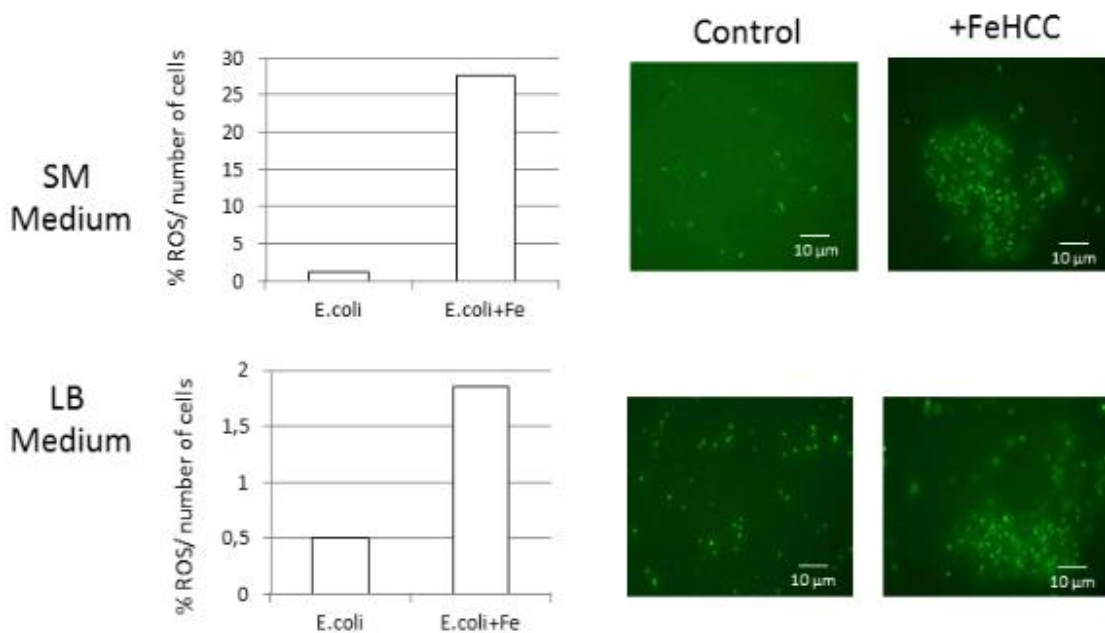


**Figure 75** Quantification of ROS production in aerobiosis conditions in SM and LB medium (left side) and Fluorescence micrographs after staining with dichloro-dihydro-fluorescein diacetate, DCFH-DA, (right side).

This analysis demonstrated that FeHCC induced ROS production in both the media suggesting an interaction between nanoparticles and cells.

This evidence together with the fact that after incubation a red precipitate is visible in the tubes induced us to think about an interaction of FeHCC with cell membranes.

Figure 76 shows the TEM images of the cells, after the treatment time with the FeHCC compound.

TEM analysis is a suitable tool for investigation of the morphology and microstructure of the cells and was performed to gain insight into mechanisms and to observe the alterations caused in the structure of E. Coli cells.

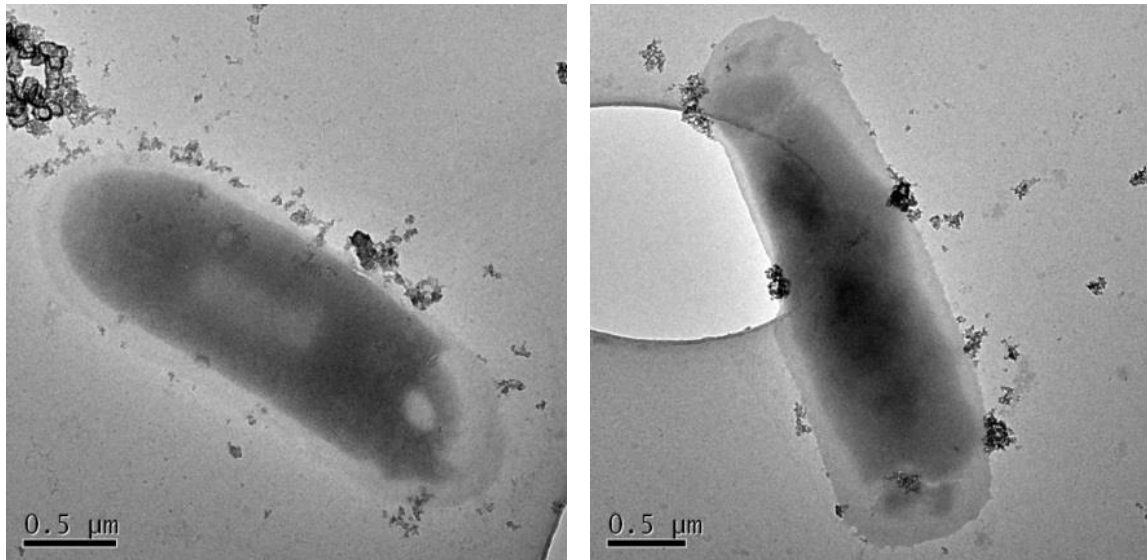


**Figure 76** TEM images of collected cells from liquid culture of *E. coli* after the incubation with FeHCC.

TEM images of the bacterial suspension showed the interaction of nanoparticles with the cell envelope of *E. coli*. FeHCC probably binds to negatively charged LPS membrane, affecting the membrane potential with a consequent disorganization of the outer membrane and cell death.<sup>24</sup>

The cell structure of FeHCC-exposed bacteria was damaged drastically, inner cell components displayed partial damage and leakage, and the cytoplasmic membrane appeared to be separated from the outer membrane.

Significant changes in the morphology occurred. It can be noted that more particles more bacterial disorganization and disaggregation occurred. We surmise, as already hinted by others,<sup>25</sup> that the death process involves electrostatics and is related to the high density of cationic charges present on the surface. The bacterial membranes possess a large number of negative charges and it is therefore natural that they adsorb on cationic substrates.

Based on the reported results, we can propose that the direct extracellular binding of the nanoparticles to the outer envelope of bacteria leads to formation of reactive oxygen species and availability of iron and, consequently, membrane destabilization, decreased permeability and cytoplasmic membrane injure leading to cell damage and reduction of microbial growth.

On this matter, the antibacterial activity is clearly observed in darkness, unlike the well-known TiO<sub>2</sub> photocatalyst, is efficient only upon irradiation by ultraviolet (UV) light.

#### **A3.4. Antibacterial activity of FeHCC against Gram positive and Gram negative bacteria in a rich medium**

After this preliminary result, the Minimal Inhibitory Concentration (MIC) in the rich liquid medium (LB) against *E. coli* and *S. aureus* was evaluated using the serial dilution method in both aerobiosis and anaerobiosis conditions.

The concentrations of FeHCC used were of 1.0, 10, 20, 40 and 50 mM.

As shown in fig. 77A and B, FeHCC was able to reduce the bacterial load of both *E. Coli* and *S. Aureus* in a dose-dependent manner.

Specifically, in this medium bacterial growth is very prosperous and 1.0 mM of compound is not effective at all on bacterial growth. 10 mM of nanoparticles reduce the bacterial load of *S. Aureus* to 75 % and of *E. Coli* to 90%.

The addition of 20 mM of FeHCC reduced to 60% and 75% the growth of *S. Aureus* and *E. Coli*, respectively.

40 mM of FeHCC was enough to kill almost the totality of *S. Aureus*, while the bacterial vital cells of *E. Coli* were still the 60% in respect to the control.

50 mM of FeHCC were sufficient to reduce the bacterial load of *E. Coli* to 2%. This result confirmed that Gram positive bacteria are more susceptible to FeHCC.

Similarly, in anaerobiosis, we obtained the same effect, a dose-dependent inhibition of *S. Aureus* growth with 40 mM able to kill almost all the bacteria (99.5%), differently 50 mM of FeHCC were not enough to get the same result with *E. Coli*.

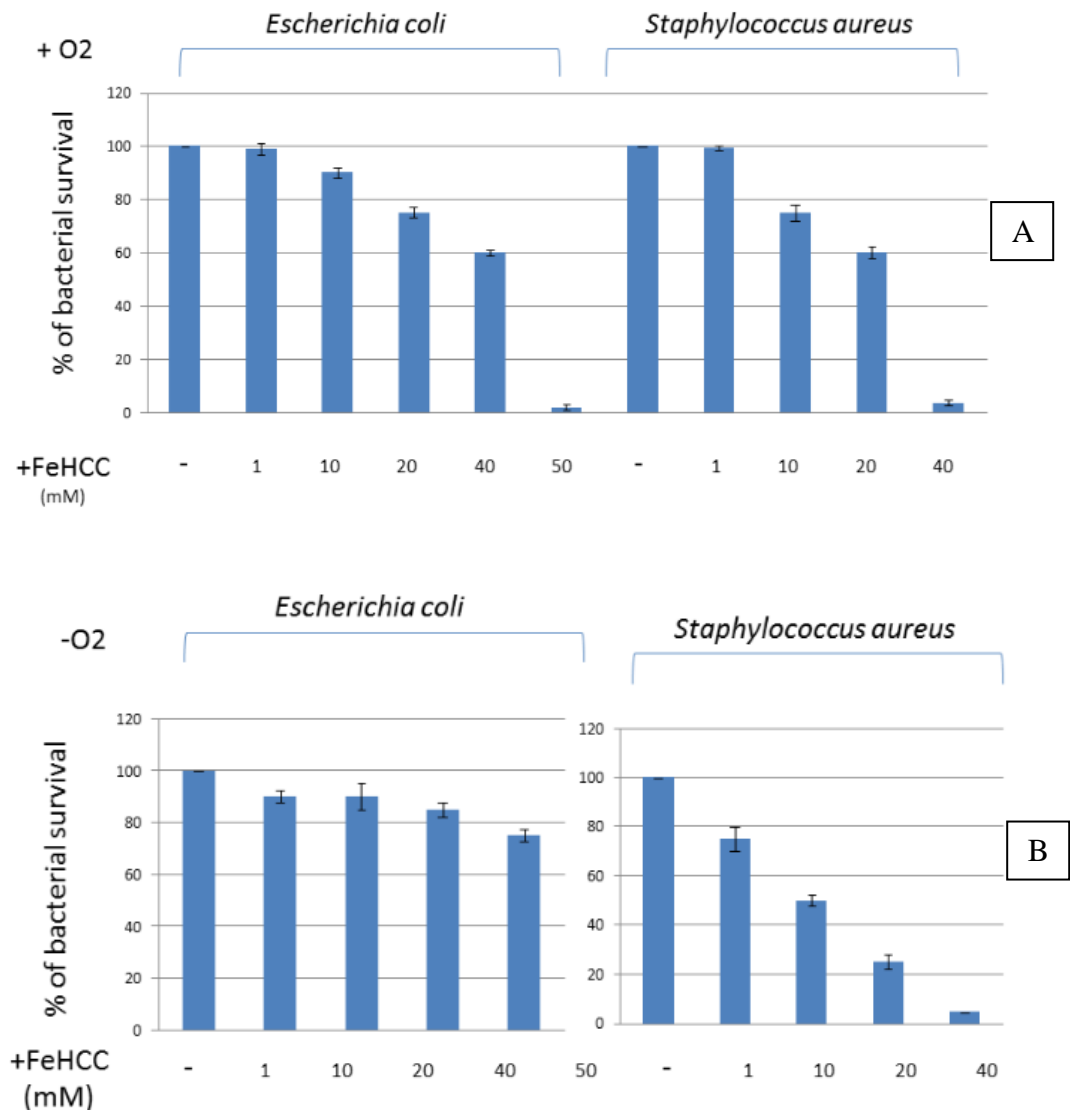


**Figure 77** Percentage of bacterial survival under aerobic (A) and anaerobic (B) conditions in presence of 1, 10, 20, 40 and 50 mM of KHCF. - indicates the survival of *E. Coli* and *S. Aureus* in LB medium (no additions). Data are average from triplicate experiments. Error bars represent standard deviations of duplicate incubations. Statistical significance was determined by the unpaired Student's t-test.

#### **A4. Conclusion**

The synthesis and characterization of Cobalt Hexacyanocobaltate (FeHCC) and the preliminary experimental results about its interesting antibacterial property are reported.

FeHCC particles were prepared by a facile co-precipitation technique. The physico-chemical characterization of the particles was carried out by XRF, XRD, FT/IR and TEM in order to study the elemental composition, crystal structure and particles morphology.

The antibacterial activity of the synthesized samples was tested against common foodborne pathogenic bacteria such as the Gram-negative bacterium *Escherichia Coli* and Gram-positive bacterium *Staphylococcus aureus*.

Antibacterial efficiency were determined by TEM images. The preliminary experimental results suggested that the FeHCC particles strongly inhibit the growth of the selected bacteria and it is worth underlining the FeHCC elevate stability even in high humidity and in different pH conditions.

The results of the investigation demonstrated that exposure of bacteria to FeHCC particles lead to disruption of cell membranes. The antimicrobial action of FeHCC is observed in both anaerobic and aerobic conditions.

The investigation of the powerful antimicrobial properties of this compound could be interesting in order to develop new technological applications for antimicrobial packaging. Hence, information from this investigation could represent the first step of a series of studies that will lead to establishment of antimicrobial packaging system to protect food and extend their shelf life. Anyway further studies in terms of chemical migration are needed to evaluate the safety of these films.

- 
- <sup>1</sup> M. Charnley, M. Textor, C. Acikgoz, *React. Funct. Polym.* 2011, 71, 329.
  - <sup>2</sup> P.G. Luo, F.J. Stutzenberger, *Advances in Applied Microbiology* 63 (2008) 145–181.
  - <sup>3</sup> Ivan Sondi, Branka Salopek-Sondi, *Journal of Colloid and Interface Science* 275 (2004) 177–182
  - <sup>4</sup> Jones, N., Ray, B., Koodali, R. T. and Manna, A. C., *FEMS Microbiology Letters*, 279, 71-76 (2008).
  - <sup>5</sup> Gadang, V. P., Hettiarachchy, N. S., Johnson, M. G., & Owens, C. (2008). *Journal of Food Science*, 73(8), 389–394.
  - <sup>6</sup> Touseef Amna, M. Shamshi Hassan, Ayman Yousef, Amrita Mishra, Nasser A. M. Barakat, Myung-Seob Khil, Hak Yong Kim, *Food Bioprocess Technol* (2013) 6:988–996
  - <sup>7</sup> Joseph, C. S., Prashanth, K. V. H., Rastogi, N. K., Indiramma, A. R., Reddy, S. Y., Raghavarao, K. S. M. S. (2011). *Food Bioprocess Technology*, 4, 1179–1185.
  - <sup>8</sup> Karine Bagramyan, Anna Galstyan, Armen Trchounian, *Bioelectrochemistry* 51, 2000. 151–156
  - <sup>9</sup> Montville and Matthews, 2008, *Food Microbiology: An Introduction*, 2nd ed
  - <sup>10</sup> Lu and Jun, 2012
  - <sup>11</sup> A.I. Rykov, J. Wang, T. Zhang, K. Nomura, *Hyperfine Interact* 218 (2013) 53-58.
  - <sup>12</sup> Sh.G. Beheir, K. Benyamin, F.M. Mekhail, *J. Radioanal. Nucl. Chem.* 232 (1998) 147-150.
  - <sup>13</sup> A. Widmann, H. Kahlert, I. Petrovic-Prelevic, H. Wulff, J.V. Yakhmi, N. Bagkar, F. Scholz, *Inorg. Chem.* 41 (2002) 5706.
  - <sup>14</sup> Mario Berrettoni, Michela Ciabocco, Marzia Fantauzzi, Marco Giorgetti, Antonella Rossi and Eugenio Caponetti, *RSC Adv.*, 2015, 5, 35435
  - <sup>15</sup> Giardina A, Alduina R, Gottardi E, Di Caro V, Süßmuth RD, Puglia AM. *Microb Cell Fact.* 2010 Jun 9;9:44. doi: 10.1186/1475-2859-9-44
  - <sup>16</sup> L Randazzo, G Montana, R Alduina, P Quatrini, E Tsantini, B Salemi, *Journal of Cultural Heritage*, 2015, 16 (6), 838-847
  - <sup>17</sup> Lo Grasso L, Maffioli S, Sosio M, Bibb M, Puglia AM, Alduina R. *J Bacteriol.* 2015 Aug 1;197(15):2536-44. doi: 10.1128/JB.00262-15
  - <sup>18</sup> T. J. B. Holland and S. A. T. Redfern, *Mineral. Mag.*, 1997, 61, 65.
  - <sup>19</sup> K. Nakamoto, in: *Infrared and Raman Spectra of Inorganic and Coordination Compounds*, John-Wiley and Sons, New York, Chichester, Brisbane, Toronto, Singapore, 1986, p. 484.
  - <sup>20</sup> A.G. Sharpe, in: P. Maitlis, F.A.G. Stone, R. West (Eds.), *The Chemistry of Cyano Complexes of the Transition Metals*, Academic Press, New York, 1976.
  - <sup>21</sup> J. Roque, E. Reguera, J. Balmaseda, J. Rodríguez-Hernández, L. Reguera, L.F. del Castillo, *Microporous and Mesoporous Materials* 103 (2007) 57–71
  - <sup>22</sup> Paik, J. S.; Dhanasekharan, M.; Kelly, M. J. *Packag Technol Sci* 1998, 11, 179.
  - <sup>23</sup> Karine Bagramyan, Anna Galstyan, Armen Trchounian, *Bioelectrochemistry* 51, 2000, 151–156
  - <sup>24</sup> R. Kügler, O. Bouloussa, F. Rondelez, *Microbiology* (2005), 151, 1341–1348
  - <sup>25</sup> Tiller GE, Hannig VL, Dozier D, Carrel L, Trevarthen KC, Wilcox WR, Mundlos S, Haines JL, Gedeon AK, Gecz J, *Am J Hum Genet* 68(6):1398-407